Combined Time and Frequency Domain Approaches to the Operational Identification of Vehicle Suspension Systems

Damien Maher, B. Eng.

A thesis submitted to Dublin City University in partial fulfilment of the requirements for the degree of

Doctor of Philosophy

Supervisor:

Dr. Paul Young,
School of Mechanical and Manufacturing Engineering,
Dublin City University,
Dublin 9,
Ireland.

January 2011

I hereby certify that this material, which I now submit for assessment on the programme of study leading to the award of Doctor of Philosophy is entirely my own work, that I have exercised reasonable care to ensure that the work is original, and does not to the best of my knowledge breach any law of copyright, and has not been taken from the work of others save and to the extent that such work has been cited and acknowledged within the text of my work.

Signed:

(Candidate) ID No.:

Date:

List of Publications

The following is a list of relevant publications and presentations by the author:

- D. Maher and P. Young, 'A combined time and frequency domain approach to the operational identification of vehicle suspension systems', In preparation.
- D. Maher and P. Young, 'An insight into linear quarter car model accuracy', *Vehicle System Dynamics: International Journal of Vehicle Mechanics and Mobility*, DOI 10.1080/00423111003631946, 2010.
- D. Maher and P. Young, 'Shock Absorber Identification for Quarter Car Simulation', *Advances in Mechanics: Irish Mechanics Society Symposium*, University College Dublin, 20–21 May, 2010.
- D. Maher and P. Young, 'Modelling of Road vehicle suspensions systems for performance evaluation', *2^{nd} International Operational Modal Analysis Conference*, Copenhagen, Denmark, 30 April–2 May, 2007.
- D. Maher and P. Young, 'Modelling of Road vehicle suspensions systems for performance evaluation', *The 23^{rd} International Manufacturing Conference*, Belfast, Northern Ireland, 30 August–1 September, 2006.

Other Publications and Presentations:

- D. Maher, J. Cleary, J. Healy, G. Carroll, D. Diamond, 'A field deployable autonomous wet chemistry analyser for in situ water quality monitoring', *SPIE Microtechnologies: Smart Sensors, Actuators and MEMS*, Prague, Czech Republic, 18–20 April, 2011 (Submitted).
- D. Maher, J. Healy, J. Cleary, G. Carroll, D. Diamond, 'Microfluidic chip development for an autonomous field deployable water quality analyser', *21^{st} Micro mechanics and micro systems Europe workshop*, Enschede, Netherlands, 26–29 September, 2010.
- J. Cleary, D. Maher, J. Healy, C. Slater, G. Carroll, D. Diamond, 'A microfluidic sensor for monitoring of nutrients in natural waters', *EUROPTRODE X–10^{th} European Conference on Optical Chemical Sensors and Biosensors*, Prague, Czech Republic, 28–31 March, 2010.

- J. Cleary, D. Maher, C. Slater, D. Diamond, 'In situ monitoring of environmental water quality using an autonomous microfluidic sensor', *IEEE Sensors Applications Symposium*, pp 36–40, Limerick, Ireland, 23–25 February, 2010.

- D. Maher, J. Cleary, J. Healy, C. Fay, G. Carroll, D. Diamond, 'Commercialisation of an Autonomous Phosphate Analyser', '*Environmental Scientists Association of Ireland, Environ 2010*', Limerick, Ireland, 17–19 February, 2010.

Contents

List of figures **ix**

List of tables **xiv**

Nomenclature **xvi**

Acronyms **xix**

Abstract **xxi**

1 Introduction **1**

1.1 Background 2

1.2 Research objectives 4

2 Literature review **6**

2.1 System identification 7

2.1.1 Characterisation 8

2.1.2 Model selection 9

2.1.3 Parameter estimation 9
2.1.4 Model validation 9
2.2 Linear system identification 10
2.2.1 Linear and nonlinear systems 11
2.2.2 Time domain methods 11
2.2.3 Frequency domain methods 13
2.2.4 Modal analysis 20
2.2.5 Operational modal analysis 23
2.3 Nonlinear system identification 27
2.3.1 Linearisation 27
2.3.2 Time domain methods 29
2.3.3 Frequency domain methods 32
2.3.4 Parameter estimation: least squares estimators 34
2.4 Force–response system identification 39
2.4.1 Vehicle suspension system identification 42
2.5 Response only system identification 47
2.5.1 Response only vehicle suspension system identification 49
2.6 Vehicle suspension system experimental test and simulation 57
2.6.1 Suspension experimental testing 58
2.6.2 Suspension simulation 63
2.7 Summary 69

3 Experimental design **70**

3.1 Experimental test development 70
3.1.1 Quarter car test rig 71
3.1.2 Isolated component testing 74
3.1.3 Shock absorber force measurement 75
3.1.4 Quarter car rig modal test 76
3.1.5 Data acquisition and analysis 78
3.2 Simulation development 82
3.2.1 Quarter car simulation 82
3.2.2 Data acquisition and analysis 85

4 Suspension system identification 88

4.1 Tyre identification 88
4.1.1 Characterisation 89
4.1.2 Model selection 90
4.1.3 Parameter estimation and model validation 92
4.2 Shock absorber identification 95
4.2.1 Characterisation 96
4.2.2 Model selection 98
4.2.3 Parameter estimation and model validation 99
4.3 Spring identification 101
4.3.1 Characterisation and model selection 102
4.3.2 Parameter estimation and model validation 103
4.4 Quarter car simulation 103

4.4.1 Linear quarter car simulation 104

4.4.2 Nonlinear quarter car simulation 107

4.4.3 Linear versus nonlinear quarter car simulation 107

4.4.4 Effect of tyre damping 110

5 Operational suspension system identification 112

5.1 Boundary perturbation technique 113

5.2 Application of the boundary perturbation technique to simulated data 116

5.2.1 Time domain approach 118

5.2.2 Frequency domain approach 127

5.3 Experimental quarter car rig identification 136

5.3.1 Characterisation and model selection 138

5.3.2 Operational parameter estimation 140

5.3.3 Operational model validation 148

6 Discussion 150

6.1 Force–response suspension system identification 150

6.1.1 Suspension component identification 151

6.1.2 Quarter car rig simulation 154

6.2 Operational suspension system identification 156

6.2.1 Nonlinear quarter car simulation 157

6.2.2 Quarter car rig identification 161

6.3 Summary 168

7 Conclusions **170**

7.1 Future work 171

Bibliography **173**

Appendices

A Tyre identification **192**

B Shock Absorber Identification **205**

C Matlab algorithms **218**

D QcAT - Quarter car Analysis Tool **224**

E Universal File Formats **232**

F Engineering drawings **238**

List of Figures

1.1 Automotive suspension system major components 3

2.1 Single input/output system 7

2.2 Steps in the system identification process 8

2.3 Representation of a system H 11

2.4 Linear SDOF system 12

2.5 Single input/output linear system 16

2.6 SDOF system frequency response function 17

2.7 Two input/single output system 18

2.8 Two input/single output system with uncorrelated inputs 18

2.9 Conditioned input/conditioned output model 19

2.10 Operational modal analysis 23

2.11 Singular values of the PSD matrix of the response 26

2.12 Block diagram model of the duffing oscillator 33

2.13 Inverse block diagram model of the duffing oscillator 33

2.14 System with output noise 38

2.15 Tyre driving point FRF's in radial direction 40

2.16 Force state map; (a) displacement–velocity; (b) velocity–acceleration . 44

2.17 Curve fit to the nonlinear restoring force in the suspension 50

2.18 Backlash describing function and NIFO results 52

2.19 Vehicle transmissibility and coherence functions 54

2.20 Change in internal damping force of a sway bar link 55

2.21 Paré quarter car test rig 59

2.22 Langdon quarter car test rig 60

2.23 Ruotavia quarter car test rig 62

2.24 Non–dimensional measured displacement of the wheel centre 62

2.25 Two DOF linear quarter car model 64

3.1 Quarter car suspension experimental test rig 71

3.2 CAD drawings of the quarter car experimental test rig 72

3.3 Quarter car experimental test rig detail 73

3.4 Wheel and tyre balancing rig 74

3.5 ESH® servo–hydraulic testing machine 75

3.6 Custom shock absorber force measurement set–up 76

3.7 Isolated and operational shock absorber force measurement set–up . . 77

3.8 Quarter car rig mode visualisation tool showing (13.7 Hz) 78

3.9 Quarter car rig EMA driving point FRF's 79

3.10 The measurement chain for vibration analysis 80

3.11 Dual channel spectrum averaging 81

3.12 Quarter car simulation 2 and 4 lobe cam input spectra 84

3.13 Quarter car rig tyre footprint at 2 mm and 9 mm deflections 85

3.14 QcAT analysis tab screen shot 86

3.15 Experimental testing hardware/software implementation 87

4.1 Tyre dynamic test setup 89

4.2 Tyre work diagrams for sinusoidal excitation at 2 Hz and 5 Hz 90

4.3 Proposed point contact tyre model 91

4.4 Proposed tyre model fit to measured data 95

4.5 Shock absorber experimental test setup 96

4.6 Shock absorber characteristic and work diagrams at 2 Hz and 5 Hz . 97

4.7 Linear, piecewise linear and nonlinear model MSE ($A = 1$mm) 100

4.8 Nonlinear shock absorber model fit for $f_e = 4$ Hz and $A = 4$ mm . . . 100

4.9 Spring work diagrams for sinusoidal excitation at 4 Hz and 7 Hz . . . 102

4.10 Quarter car model simulated and quarter car rig measured spectra . . 105

4.11 Quarter car simulated and measured data time history comparison . . 106

4.12 Linear and trilinear shock absorber models at 6.8 Hz and 11.2 Hz . . 108

4.13 Linear and nonlinear quarter car simulation evaluation at 6.8 Hz . . . 108

4.14 Linear and nonlinear quarter car simulation evaluation at 11.2 Hz . . 109

4.15 Tyre damping comparison at 10.4 Hz 110

5.1 SDOF system subject to base excitation 113

5.2 Two DOF nonlinear quarter car model 116

5.3 Nonlinear quarter car simulation restoring force surface 119

5.4 Nonlinear quarter car simulation RFS (10% backlash) 121

5.5 Quarter car simulation with Bouc–Wen shock absorber RFS 123

5.6 Bouc–Wen quarter car model simulated and estimated time histories . 125

5.7 Bouc–Wen quarter car model simulated and estimated time histories . 126

5.8 Three input single output R–MISO setup 129

5.9 Nonlinear quarter car model R–MISO 130

5.10 Nonlinear quarter car model R–MISO analysis results (5 % noise) . . 130

5.11 Nonlinear quarter car model R–MISO RFP curve–fit (5 % noise) . . . 132

5.12 Bouc–Wen quarter car simulation R–MISO model check results . . . 134

5.13 Bouc–Wen quarter car simulation R–MISO analysis results 135

5.14 Bouc–Wen quarter car simulation R–MISO RFP curve–fit 136

5.15 Quarter car rig accelerometer locations for operational testing 137

5.16 Quarter car rig 72 lobe pseudo random cam 137

5.17 Quarter car rig with known added mass attached to the sprung mass 138

5.18 Quarter car rig restoring force surface (10 averages) 139

5.19 Quarter car rig restoring force surface (400 averages) 139

5.20 Quarter car rig boundary perturbation analysis with added mass . . . 141

5.21 Normalised unsprung mass displacement in the x, y and z–directions . 142

5.22 Quarter car rig R–MISO model check results 145

5.23 Quarter car rig R–MISO analysis results 145

5.24 Quarter car rig R–MISO weighted RFP curve–fit 146

5.25 Quarter car rig nonlinear damping model 147

5.26 Operational simulation comparison with measured data 149

6.1 Shock absorber input and output spectra for excitation at 4 Hz . . . 152

6.2 Observed shock absorber friction phenomena 152

6.3 Stick–slip transition velocity and optimised trilinear c_5 parameter . . 153

6.4 Linear and nonlinear quarter car simulation evaluation at 11.2 Hz . . 155

6.5 Quarter car rig boundary perturbation analysis with added mass . . . 163

6.6 Quarter car rig R-MISO analysis results 165

List of Tables

2.1 Drops in coherence and the associated nonlinearities 54

3.1 Measured quarter car component parameters 82

4.1 Nonlinear tyre model MSE 93

4.2 Revised nonlinear tyre model MSE 94

4.3 Shock absorber spring dynamic stiffness k_s [N/mm] 102

4.4 Linear spring model MSE at discrete frequencies and amplitudes . . . 103

4.5 Linear quarter car simulation parameters 104

5.1 Quarter car simulation parameters 117

5.2 Nonlinear quarter car simulation setup parameters 118

5.3 Estimated parameters; both nonlinearities included 119

5.4 Estimated parameters; only dominant friction nonlinearity included . 120

5.5 Estimated parameter error for varying backlash 121

5.6 Estimated parameters with backlash included in the model 122

5.7 Bouc–Wen quarter car simulation parameters 123

5.8 Estimated Bouc–Wen quarter car model parameters 124

5.9 Estimated Bouc–Wen quarter car model parameters with backlash . . 126

5.10 Estimated Bouc–Wen quarter car model parameters 127

5.11 Signal processing parameters used for R–MISO analysis 129

5.12 Estimated mass normalised nonlinear quarter car model parameters . 133

5.13 Signal processing parameters used for Bouc–Wen R–MISO analysis . 134

5.14 Quarter car rig boundary perturbation analysis results 142

5.15 Signal processing parameters for quarter car rig R–MISO analysis . . 144

5.16 Quarter car rig R–MISO analysis inputs 144

5.17 Quarter car rig estimated component parameters 146

5.18 Quarter car rig operational damping model parameters 148

6.1 Quarter car rig resonance frequencies 166

Nomenclature

A	Excitation amplitude	[m]
B, α, β, γ	Bouc–Wen hysteretic model parameters	[–]
$E[\cdot]$	Expected value	[–]
F	Force	[N]
F_c	Coulomb friction force	[N]
F_d	Damper force	[N]
F_{st}	Static friction force	[N]
F_s	Spring force	[N]
F_t	Tyre force	[N]
G_{xy}	Cross–spectrum between signals x and y (1 sided)	[unit(x)*unit(y)/Hz]
H_1	H1 frequency response function estimator	[–]
H_{xy}	FRF between input x and output y	[–]
L_{xy}	FRF between input x and output y for conditioned inputs	[–]
N	Number of samples	[–]
R_{xx}	Autocorrelation of signal x	[unit(x)^2]
R_{xy}	Cross–correlation between signals x and y	[unit(x)*unit(y)]
S_{xx}	Autospectrum of signal x(two sided)	[unit(x)^2/Hz]
S_{xy}	Cross–spectrum between signals x and y (2 sided)	[unit(x)*unit(y)/Hz]
T	Period	[s]
V, Σ, U	SVD factors	[–]
Δf	Frequency interval	[–]
Λ	Composite frequency response function	[–]
$\ddot{x}$	Acceleration	[m/s^2]
$\ddot{x}_s$	Sprung mass acceleration	[m/s^2]
$\ddot{x}_u$	Unsprung mass acceleration	[m/s^2]

$\dot{x}$	Velocity	[m/s]
$\dot{x}_s$	Sprung mass velocity	[m/s]
$\dot{x}_u$	Unsprung mass velocity	[m/s]
$\dot{z}$	LuGre friction model bristle velocity	[m/s]
η	Hysteretic energy loss per cycle	[–]
γ^2_{xy}	Coherence function between signals x and y	[–]
$\gamma^2_{y:x}$	Multiple coherence between all inputs x and output y	[–]
$\hat{[\cdot]}$	Estimated value	[–]
κ, ξ, ϑ	Hyperbolic tangent shock absorber model parameters	[–]
$[\cdot]^*$	Complex conjugate	[–]
$[\cdot]^H$	Hermitian transpose	[–]
$[\cdot]^T$	Transpose	[–]
μ_s	Shock absorber friction force	[N]
μ_x	Mean of x	[–]
μ_y	Mean of y	[–]
ν	Bouc–Wen evolutionary variable	[–]
σ^2_x	Variance of x	[–]
σ_0	LuGre friction model bristle stiffness	[N/m]
σ_1	LuGre friction model bristle damping	[N s/m]
τ	Time delay	[s]
ζ_{eq}	Equivalent damping ratio	[–]
c	Damping coefficient	[N s/m]
c_1, c_2, c_3	Trilinear damping model coefficients	[N s/m]
c_4, c_5	Trilinear damping model coefficients	[m/s]
c_{eq}	Equivalent damping coefficient	[N s/m]
c_s	Shock absorber damping coefficient	[N s/m]
c_t	Tyre nonlinear stiffness coefficient	[–]
c_u	Tyre damping coefficient	[N s/m]
e	Model error	[–]
f	Frequency	[Hz]
f_e	Excitation frequency	[Hz]
f_n	Nonlinear restoring force	[N]
f_o	Tyre force offset	[N]
h	Hysteretic damping coefficient	[N/m]
i, j, k	Index	[–]
j	Imaginary Unit $j^2 = -1$	[–]
k	Stiffness	[N/m]

k_n	Shock absorber cubic stiffness	[N/m^3]
k_s	Shock absorber spring stiffness	[N/m]
k_u	Tyre stiffness	[N/m]
m	Mass	[kg]
m_s	Sprung mass	[kg]
m_u	Unsprung mass	[kg]
n	Bouc–Wen hysteretic model order	[–]
t	Time	[s]
v_s	Stribeck velocity	[m/s]
x	Displacement	[m]
x_s	Sprung mass displacement	[m]
x_u	Unsprung mass displacement	[m]
z	LuGre friction model bristle deflection	[m]

Acronyms

ARMA Auto–Regressive Moving Average.

ARX Auto–Regressive with eXogenous inputs.

CNC Computer Numerical Control.

CRP Conditioned Reverse Path.

DOF Degree–Of–Freedom.

DPE Direct Parameter Estimation.

EFDD Enhanced Frequency Domain Decomposition.

EMA Experimental Modal Analysis.

ER Electrorheological.

ERA Eigensystem Realisation Algorithm.

FDD Frequency Domain Decomposition.

FRF Frequency Response Function.

GUI Graphical User Interface.

ITD Ibrahim Time Domain.

LSCE Least Squares Complex Exponential.

LVDT Linear Variable Differential Transformer.

MDOF Multiple Degree–Of–Freedom.

MISO Multiple Input/Single Output.

MR Magnetorheological.

MSE Mean Squared Error.

NARMAX Nonlinear Auto-Regressive Moving-Average with eXogenous inputs.

NARX Nonlinear Auto-Regressive with eXogenous inputs.

NIFO Nonlinear Identification through Feedback of the Outputs.

OMA Operational Modal Analysis.

PSD Power Spectral Density.

QcAT Quarter car Analysis Tool.

R–MISO Reverse Multiple Input/Single Output.

RFP Rational Fraction Polynomials.

RFS Restoring Force Surface.

RMS Root Mean Square.

SCC Synthesis Correlation Coefficient.

SDOF Single Degree–Of–Freedom.

SISO Single Input/Single Output.

SSI Stochastic Subspace Identification.

SVD Singular Value Decomposition.

Abstract

Combined Time and Frequency Domain Approaches to the Operational Identification of Vehicle Suspension Systems

Damien Maher

This research is an investigation into the identification of vehicle suspension systems from measured operational data. Methods of identifying unknown parameter values in dynamic models, from experimental data, are of considerable interest in practice. Much of the focus has been on the identification of mechanical systems when both force and response data are obtainable. In recent years a number of researchers have turned their focus to the identification of mechanical systems in the absence of a measured input force.

This work presents a combined time and frequency domain approach to the identification of vehicle suspension parameters using operational measurements. An end–to–end approach is taken to the problem which involves a combination of focused experimental design, well established force–response testing methods and vehicle suspension experimental testing and simulation. A quarter car suspension test rig is designed and built to facilitate experimental suspension system testing. A novel shock absorber force measurement set–up is developed allowing the measurement of shock absorber force under both isolated and operational testing conditions. The quarter car rig is first disassembled and its major components identified in isolation using traditional force–response testing methods. This forms the basis for the development of an accurate nonlinear simulation of the quarter car test rig. A comprehensive understanding of the quarter car experimental test rig dynamics is obtained before operational identification is implemented. This provides a means of validating the suspension parameters obtained using operational testing methods.

A new approach to the operational identification of suspension system parameters is developed. The approach is first developed under controlled simulated conditions before being applied to the operational identification of the quarter car experimental test rig. A combination of time and frequency domain methods are used to extract sprung mass, linear stiffness and nonlinear damping model parameters from the quarter car experimental test rig. Component parameters identified under operational conditions show excellent agreement with those identified under isolated laboratory conditions.

Chapter 1

Introduction

This research is an investigation into the development of vehicle suspension simulations from measured operational data. Methods of identifying unknown parameter values in dynamic models from experimental test data are of considerable interest in practice. In design studies system identification methods can be applied to experimental test data gathered from isolated testing of a specific component of interest. Alternatively, they can be applied to operational data to facilitate on-line monitoring and reliability studies.

System identification is a well established area of research. Much of the focus has been on the identification of mechanical systems when force and response data are obtainable. In many applications it can be impractical or impossible to measure excitation forces. For example, during vehicle suspension operation, the input force from the road surface to the tyre or the shock absorber force are difficult to identify experimentally. In recent years a number of researchers have turned their focus to the identification of mechanical systems in the absence of a measured input force. One particular example is the rise of Operational Modal Analysis (OMA) techniques for the identification of mechanical systems. The advantage of using operational testing is that the system can be tested in its operating environment under actual loading conditions and often without interfering with the system operation.

Design engineers have always had to come to a compromise between development time and product quality and performance. This is especially true for the automotive industry. There is a constant demand for improved vehicle quality, safety, efficiency and performance. From the point of view of suspension systems, each new car strives

to have better handling and also greater passenger comfort. This drive for greater performance and shorter development times has created a demand for dedicated test and simulation equipment. In the development of vehicle suspension systems much development is exhaustively done by ride work [1, 2]. During ride work a vehicle is driven over a number of test tracks. The suspension performance is evaluated and the shock absorber tuned to improve the performance. With the increased availability of powerful computers, many organisations are increasingly relying on numerical simulations in place of expensive ride work for product evaluation [3, 4].

Numerical simulation is considerably less expensive in terms of cost and time. The parameters for these simulations would classically be obtained using isolated component testing. This requires disassembly of the suspension system and isolated testing of the individual suspension components. The identification of simulation parameters from operational testing would provide a convenient method of developing suspension simulations. It would also provide a cost effective and simple method of continuous system monitoring as the instrumentation is non intrusive and does not require the vehicle to be taken out of service.

With the increasing use of powerful computer systems in motor vehicles coupled with the falling cost of robust and accurate accelerometers [5], the collection of suspension vibration data during vehicle operation could easily be implemented. Continuous monitoring of suspension operation would provide large amounts of data for analysis both at regular service intervals and also by the on-board computer. These data could be analysed to determine suspension system parameters and allow for accurate assessment of suspension system performance. Vehicle manufacturers could track changes in suspension performance over the lifetime of the vehicle and use the acquired design knowledge in future system developments.

1.1 Background

A vehicle suspension system is the term given to the system of springs, shock absorbers and linkages connecting a vehicle chassis to its wheels. Suspension systems dynamics are often viewed from two perspectives, ride and handling. A vehicle's ride quality is a measure of how well it evens out the irregularities of a bumpy road. Vehicle handling is a measure of how well the car corners, brakes and accelerates safely. The suspension is designed to maximise the friction between the tyres and

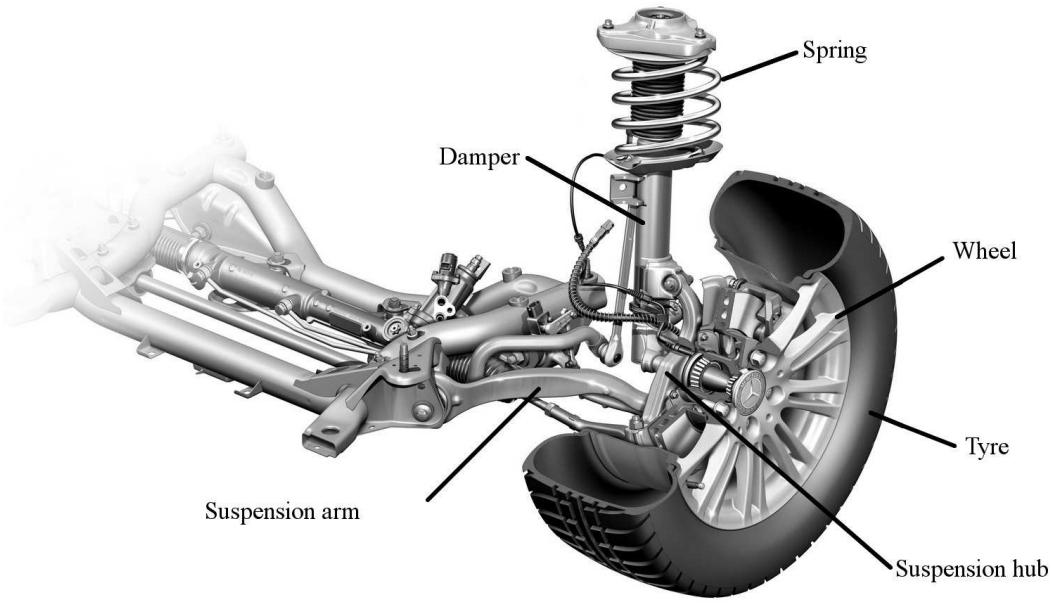

Figure 1.1: Automotive suspension system major components

the road surface to ensure good handling. It is also designed to maximise the comfort of passengers by reducing the acceleration of the car body and, hence, forces on passengers. Suspension design is a compromise brought about by the demands of these conflicting goals. Suspension experimental testing and simulation play a major role in this design process.

Vehicle suspension systems can be classified into two main categories, independent and dependent. The terms refer to the ability of opposite wheels to move relative to each other. Dependent suspension systems have some form of rigid connection between opposite wheels such as a beam axle or live axle which holds the wheels in place. Independent systems allow opposite wheels to react independently to road conditions. They provide superior ride and handling characteristics but are more expensive to manufacture. This work will focus on independent suspension systems and in particular the MacPherson Strut system.

The MacPherson Strut system is a widely used system in cars because of its light weight and compact size [6, 7, 8]. The major components of the system are shown in Figure 1.1. The shock absorber consisting of spring and damper elements serves to protect the vehicle from impact forces and high acceleration resulting from road irregularities [9]. The spring force generated depends on wheel travel. The spring temporarily stores energy imparted to the system by the road surface. The purpose of the damper is to control the rate of energy release from the spring. It improves

road holding by preventing the wheels from bouncing off the road. The dampers resistance to sudden movements results in impact forces. The selection of springs and dampers properties represent a compromise between the demands of ride and handling [9]. It is common to design nonlinearity into the system to achieve the desired ride and handling properties.

The tyre transfers forces and moments from the road surface to the suspension system. Tyre stiffness is typically ten to twenty times that of the suspension spring. The suspension arm and shock absorber are connected to the vehicle chassis using rubber joints or rubber bushings. Road obstacles such as pot holes or transverse joints in the road surface, excite the suspension system in a wide frequency range which can come into the audible region [9]. Rubber bushings provide noise and vibration insulation by reducing the transmission of high frequency vibrations to the chassis.

1.2 Research objectives

This work will develop techniques for the identification of vehicle suspension system parameters in the absence of *a priori* knowledge of the system or the input force at the tyre patch. A focused and comprehensive approach to the problem will be implemented, beginning with the development of an experimental testing setup. This will take the form of a vehicle suspension experimental test rig, designed to simulate on–road vehicle conditions in the laboratory. Traditional force–response identification techniques will first be implemented on the major suspension rig components. This will involve the disassembly of the rig to allow individual components to be tested in isolation. Component models developed under isolated conditions will provide the parameters for the development of a suspension system simulation.

The background knowledge gained during force–response testing of the quarter car rig will provide the basis to pursue and develop the operational suspension system identification techniques. Operational techniques will first be developed under controlled simulation conditions. They will then be applied to the experimental identification of the suspension experimental test rig. Only acceleration measurement of the unsprung and sprung masses will provide the measured data for operational testing. It is believed that in the presence of unmeasured excitation force, a boundary perturbation technique can be used to identify the component parameters in

the system. This involves conducting two experimental tests, one a known added mass attached to the vehicle sprung mass. The operational testing methods will be developed to allow an instrumented vehicle to be tested in service without interfering with vehicle operation. The identified suspension parameters from operational testing will be compared with those obtained using isolated testing to assess the validity of the proposed approach.

Chapter 2

Literature review

This review provides an overview of the published work critical to the understanding of this research in the context of mechanical engineering research today. To begin, a review of mechanical system identification is presented. System identification is the process of estimating input–output dynamic systems models, and their parameters using measured data. The subject of system identification is extremely broad and much research has been published in the literature on this topic. Therefore, the topic has been broken down. Linear system identification procedures are first examined followed by a review of popular nonlinear system identification techniques. Examples from the literature on the application of linear and nonlinear system identification methods to both experimental and simulated data are also presented.

Focus then turns to the identification of vehicle suspension systems. The existing literature is viewed from two angles, force–response identification and response only identification, or operational identification. A critical review of research focusing on the characterisation, mathematical modelling, parameter estimation and simulation of suspension systems is documented. Experimental testing setups used by other authors in the characterisation and identification of vehicle suspension systems are examined along with simulation approaches. Finally the conclusions of this literature review are summarised and the objectives of this investigation outlined.

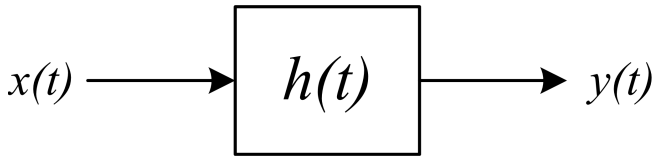

Figure 2.1: Single input/output system

2.1 System identification

A system can be defined as any collection of interacting elements for which there are cause and effect relationships among the variables [10]. This study is devoted to dynamic systems, meaning the variables are time dependent. Consider the standard diagrammatic form of a Single Input/Single Output (SISO) system shown in Figure 2.1, where $x(t)$ is the input function of time, $y(t)$ is the response function of time and $h(t)$ is a function which maps $x(t)$ to $y(t)$. Given any two of these quantities it is possible, in principle, to determine the third. Simulation refers to the process of determining $y(t)$ given $x(t)$ and an appropriate description of $h(t)$, deconvolution is the process of determining $x(t)$ given $y(t)$ and $h(t)$, and, finally, system identification involves the construction of an appropriate representation of $h(t)$, given $x(t)$ and $y(t)$. In essence, it is the process of developing a mathematical model of a dynamic system based on measured data from the system.

The majority of mechanical system analysis procedures are based on linearity (*e.g* modal analysis) [11]. It is, therefore, essential that some form of test for the presence of nonlinearities be carried out in the early stages of the identification process. The identification and quantification of nonlinearities in mechanical systems is important when models are being developed for the prediction of system performance [12]. System identification methods can be classified into two types, parametric and non–parametric. Parametric methods aim to determine the parameters of an assumed model of the system under investigation. Non–parametric methods aim to produce the best functional representation of the system without *a priori* assumptions of the system model. Regardless of system type, the steps in the identification process are generally the same. System identification is a complex process as shown in Figure 2.2 [13]. The identification process can be broken down into the following broad categories, characterisation, model selection, parameter estimation and model validation. Each of this categories will now be discussed in more detail.

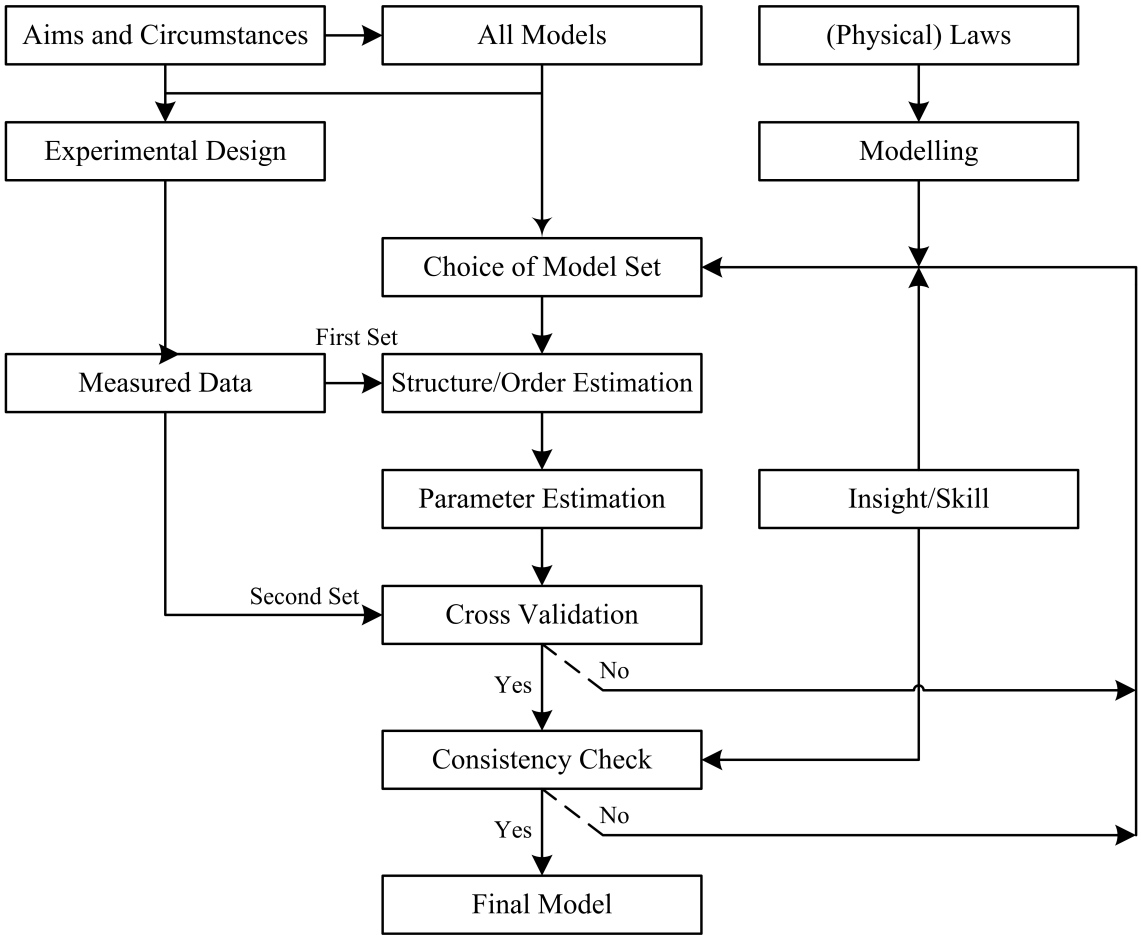

Figure 2.2: Steps in the system identification process (reproduced from [13])

2.1.1 Characterisation

The first step in the identification procedure is the detection of nonlinearity. Nonlinearity is present when there is no simple proportional relation between cause and effect. Once it has been established that a nonlinearity exists, further investigation is required to establish the location and type of nonlinearity present. A nonlinear system is said to be characterised when the location, type and functional form of all damping, stiffness and kinematic nonlinearities in the system are known. Characterisation is the first step in the identification procedure as it provides prior information about the system's nonlinear structure which is needed to select an appropriate input–output model form [14]. Once a system has been characterised, various identification and parameter estimation algorithms can be applied to estimate the model parameters with varying degrees of accuracy.

2.1.2 Model selection

The second step in the identification procedure is model selection. Model selection involves the identification of a set of candidate models which may be suitable for modelling the system (*e.g* time domain models, frequency domain models, parametric, non–parametric, graphical). A combination of *a priori* system knowledge and engineering intuition and insight are required for the selection process [15]. After a set of models has been determined, a specific model or models in the set are selected. The selection of a model is usually based on the results of some preliminary experimental measurements of the system. Specially designed experiments are often used to record the input–output data required for system identification. The experimental design aims to ensure that the measured data from such tests provide maximum information about the system. In some cases the user may have no influence on the setup of the system to be identified and the measured data may have to be recorded from the system in its normal operating environment, as commonly observed in the vibration analysis of civil engineering structures.

2.1.3 Parameter estimation

Once the model form is selected, the parameters of the model are estimated. Data from experimental tests conducted on the system are used for the parameter estimation process. Assessment of the model quality is typically based on how the model performs when it attempts to reproduce the measured data [15]. To be genuinely useful a parameter estimation procedure should provide (i) parameters, (ii) error estimates on the parameters, and (iii) a statistical measure of the goodness of fit [16]. Results from the parameter estimation step may need to be fed back into the system identification process and the model order or type revised.

2.1.4 Model validation

Once the results from the parameter estimation step are satisfactory, the proposed model must be validated. New measurement sets may be used to test the model for a wider range of input signals. The inputs signals must be within the limits of the model specified during the model selection process. Uncertainty on the estimates increases with the number of estimated parameters for a given amount of measured

data [17], therefore, simpler models are preferred to complex models if they provide an acceptable level of accuracy. The acceptable level of accuracy is specific to the application and to the intended model use. For example the level of accuracy required for flight flutter test on commercial aircraft is much greater than that required for machine tool anti–vibration mounts.

It is quite likely, in some cases, that the initial model may not pass the validation test. The model may be deficient for a number of reasons [15],

- the experimental data are not informative enough to aid the selection of an appropriate model;
- the parameter estimation algorithm failed to find the best model;
- the selected model is not appropriate to describe the system.

A major part of the system identification process is addressing these issues in an iterative manner, guided by prior information and the outcomes of previous attempts. In this research the identification process will be applied to the analysis of vehicle suspension systems. Addressing this process in an iterative manner will involve the use of aspects of both linear and nonlinear system identification techniques presented in the following sections.

2.2 Linear system identification

In practice, almost every system is nonlinear. As the theory of nonlinear systems can be very involved, they are often approximated by linear models, assuming that in the operating region, the system can be linearised. This approximation allows the use of simple models without jeopardising properties which are important to the modeller. It has been noted that the majority of system identification methods are based on linearity [11]. At this point a brief review of the strict definition of linear and nonlinear systems is warranted. This is followed by a look at popular linear system identification techniques in the literature.

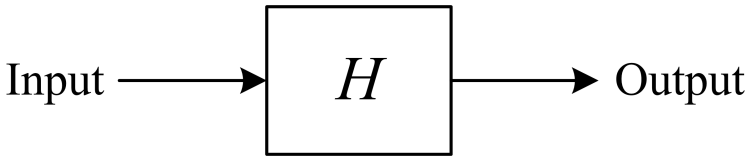

Figure 2.3: Representation of a system H

2.2.1 Linear and nonlinear systems

Consider the system shown in Figure 2.3. The input is changed in some way by the system H to produce the output. The system is linear if, for any inputs $x_1 = x_1(t)$ and $x_2 = x_2(t)$ and any constants c_1 and c_2,

$$H\left[c_1x_1 + c_2x_2\right] = c_1H\left[x_1\right] + c_2H\left[x_2\right]. \tag{2.1}$$

This equation has two properties which are required for linear systems, the additive property and the homogeneous property. Should the system not satisfy either of these properties, the system is considered nonlinear and is defined as follows; A system, H, is nonlinear if, for any inputs $x_1 = x_1(t)$ and $x_2 = x_2(t)$ and any constant c, the system input/output relations are not additive,

$$H\left[x_1 + x_2\right] \neq H\left[x_1\right] + H\left[x_2\right] \tag{2.2}$$

and/or are not homogeneous,

$$H\left[cx_1\right] \neq cH\left[x_1\right]. \tag{2.3}$$

These nonlinear operations in equations 2.2 and 2.3 produce non–Gaussian output data when the input data are Gaussian. In the case of a linear system, Gaussian input data produces Gaussian output data. In reality all systems exhibit some degree of nonlinearity. It has been shown in [18] (in a case study to identify a nonlinear vehicle shock absorber) that errors resulting from the analysis of nonlinear systems using linear system analysis techniques, can be significant.

2.2.2 Time domain methods

Direct Parameter Estimation (DPE) is a method developed by Mohammad *et al.* [19] for directly estimating the physical parameters, i.e., mass, stiffness and damping, of

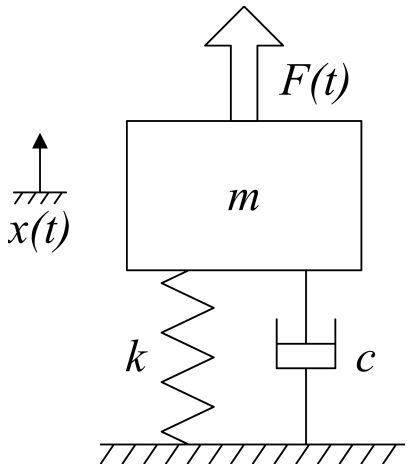

Figure 2.4: Linear SDOF system

linear and nonlinear structures using measured time data. The structure is modelled using a lumped parameter system. A least squares estimation procedure is used to allow the estimation of the system parameters given only the excitation at a single point. The implementation of the DPE technique is described here for a linear Single Degree–Of–Freedom (SDOF) system, and is extended to nonlinear system identification in § 2.3.2. Consider the linear SDOF oscillator shown in Figure 2.4. The differential equation of motion of the system is given by,

$$m\ddot{x}(t) + c\dot{x}(t) + kx(t) = F(t). \tag{2.4}$$

If N samples of acceleration $\ddot{x}(t)$, velocity $\dot{x}(t)$, and displacement $x(t)$, are recorded the problem can be formulated as follows,

$$\begin{bmatrix} \ddot{x}_1 & \dot{x}_1 & x_1 \\ \ddot{x}_2 & \dot{x}_2 & x_2 \\ \vdots & \vdots & \vdots \\ \ddot{x}_N & \dot{x}_N & x_N \end{bmatrix} \begin{Bmatrix} m \\ c \\ k \end{Bmatrix} = \begin{bmatrix} F_1 \\ F_2 \\ \vdots \\ F_N \end{bmatrix}. \tag{2.5}$$

This equation has the general form,

$$[A]\{x\} = [B]. \tag{2.6}$$

Coefficients of x are estimated by minimising the length of residual vector (e),

$$\|e\| = \|Ax - B\| = e^T e. \tag{2.7}$$

A least squares solution to this problem can be found using singular value decomposition(SVD) of A (discussed in detail in § 2.3.4),

$$A = U\Sigma V^T \tag{2.8}$$

$$x = V\,(1/\Sigma)\,(U^T B) \tag{2.9}$$

leading to optimal least squares estimates of the model coefficients m, c and k in equation 2.4.

Estimation of a continuous time system, as described by equation 2.4, requires that measured time data be available for each term in the model equation. Records are required for acceleration $\ddot{x}(t)$, velocity $\dot{x}(t)$, displacement $x(t)$ and force $F(t)$. An alternative approach is to adopt a discrete time representation of equation 2.4. If the input force and output displacement signals are sampled at regular intervals of time Δt, records of data $f_i = f(t_i)$ and $x_i = x(t_i)$ are obtained for $\{i = 1, 2, ..., N\}$. The derivatives $\ddot{x}(t_i)$ and $\dot{x}(t_i)$ can be approximated by the discrete forms [11],

$$\dot{x}(t_i) \approx \frac{x(t_i) - x(t_i - \Delta t)}{\Delta t} = \frac{x_i - x_{i-1}}{\Delta t} \tag{2.10}$$

$$\ddot{x}(t_i) \approx \frac{x_{i+1} - 2x_i + x_{i-1}}{\Delta t^2}. \tag{2.11}$$

Substitution into equation 2.4 yields,

$$x_i = a_1 x_{i-1} + a_2 x_{i-2} + b_1 f_{i-1} \tag{2.12}$$

where a_1, a_2 and b_1 are constant coefficients and functions of the original parameters m, c and k and the sampling interval $\Delta t = t_{i+1} - t_i$. In time series literature, this model is termed an Auto–Regressive with eXogenous inputs (ARX) model. The advantage of this model lies in the fact that only the states x and f need be measured to estimate the model parameters, a_1, a_2 and b_1, and, hence, identify the system.

2.2.3 Frequency domain methods

The term 'spectral analysis' is used to describe the analysis of data in the frequency domain. The use of the frequency domain to describe the characteristics of vibration systems finds favour in many engineering applications, where the response of the system to an input is a function of frequency as well as the magnitude of the input.

The Fourier Transform is a particular case of the transform relating the time and frequency domains.

Fourier Transform

For the case where x(t) is a continuous function and,

$$\int_{-\infty}^{\infty} |x(t)|\, dt < \infty \tag{2.13}$$

the Fourier Transform exists such that,

$$X(f) = \int_{-\infty}^{\infty} x(t) e^{-j2\pi ft} dt \qquad -\infty < f < \infty. \tag{2.14}$$

In a similar mapping the Inverse Fourier Transform is,

$$x(t) = \int_{-\infty}^{\infty} X(f) e^{j2\pi ft} df \qquad -\infty < t < \infty \tag{2.15}$$

while in the case of a vibration system $x(t)$ is a real valued function and the resultant transform is a complex valued function. The Finite Fourier Transform assumes that the input function is periodic with the time for one period being T, the sample length. The transform is defined over this period as,

$$X_T(f) = X(f,T) = \frac{1}{T} \int_0^T x(t) e^{-j2\pi ft} dt. \tag{2.16}$$

In the case of data acquired through sampling, $\{x_0, x_1, ..., x_{N-1}\}$, rather than a continuous record the Discrete Fourier Transform, which exists only at discrete frequencies f_k is,

$$X_k = X(k\Delta f) = \frac{1}{N} \sum_{n=0}^{N-1} x_n e^{-j\frac{2\pi kn}{N}} \qquad k = 0, 1, 2, ..., N-1 \tag{2.17}$$

where the fundamental frequency is $f_0 = 1/T$ and the discrete frequencies are kf_0 and $f_k - f_{k-1} = f_0 = \Delta f$.

Spectra

The autospectrum of a time record is a measure of its power content as a function of frequency as defined by,

$$S_{xx}(f) = \lim_{T\to\infty} \frac{1}{T} E\left[X_k^*(f,T)\, X_k(f,T)\right]. \tag{2.18}$$

The cross–spectrum between two signals is,

$$S_{xy}(f) = \lim_{T\to\infty} \frac{1}{T} E\left[X_k^*(f,T)\, Y_k(f,T)\right] \tag{2.19}$$

where E is an averaging operation over the number of records available, with each individual record having its own index k. S is valid for all f, both positive and negative, and in the case where time records are real then $S(-f) = S(f)$ leading to the definition of the single sided estimate,

$$G_{xy}(f) = \lim_{T\to\infty} \frac{2}{T} E\left[X_k^*(f,T)\, Y_k(f,T)\right]. \tag{2.20}$$

In reality $T \to \infty$ may only be approximated. The expected operator, E, is replaced by averaging a number of records, increasing T without increasing the transform length. This lengthening of the sampling time helps to ensure that the sampled data are representative of the original sample. The statistical accuracy of the estimate is also improved by increasing the number of averages [20].

Frequency Response Function

Frequency Response Functions (FRF) are one of the most widely used methods of visualising the input–output properties of a system. FRF's can be used to rapidly detect the presence of nonlinearities in a system. FRF distortions can be used to provide information about system nonlinearity [11]. Symptoms of nonlinearity include changes in FRF structure for different levels of excitation and response at multiples of the forcing frequency in the presence of a pure sinusoidal excitation [21].

Consider an ideal linear SISO system without noise, as show in Figure 2.5. The FRF, $H(f)$, between the Fourier Transform of the input $X(f)$ and the Fourier Transform

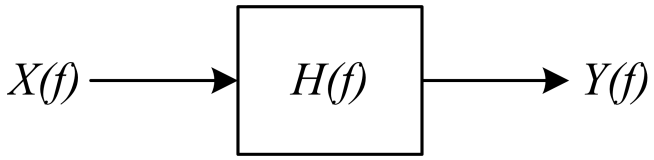

Figure 2.5: Single input/output linear system

of the output $Y(f)$ is given by,

$$H(f) = \frac{Y(f)}{X(f)}. \tag{2.21}$$

In the presence of noise the FRF is commonly estimated using spectral relations. The calculation of autospectra and cross–spectra, as an intermediate step, allows averaging operations to be carried out to minimise random errors. The most commonly used estimator is known as the H_1 estimator. It minimises the effect of noise on the response and is given by,

$$H_1(f) = \frac{S_{xy}(f)}{S_{xx}(f)} \tag{2.22}$$

where S_{xy} is the cross–spectra between the input and output and S_{xx} is the autospectra of the input.

The FRF is a complex valued function of frequency. Figure 2.6 shows the magnitude and phase representation of the FRF for the linear system shown in Figure 2.4. The natural frequencies, damping ratios and mode shapes of a system can be determined from the system FRF, and are discussed in more detail in § 2.2.4.

Coherence function

The coherence function describes the extent of the linear relationship between the input and the output signals and is defined as,

$$\gamma_{xy}^2 = \frac{|S_{xy}(f)|^2}{S_{xx}(f)S_{yy}(f)} \qquad 0 \leq \gamma_{xy}^2 \leq 1. \tag{2.23}$$

If a perfect linear relationship exists between $x(t)$ and $y(t)$, at some frequency f_k, then the coherence function, γ_{xy}^2, will be equal to unity at that frequency. If $x(t)$ and $y(t)$ are such that $S_{xy}(f_k) = 0$ at frequency f_k, then the coherence function will be zero at that frequency. Coherence is widely recognised and accepted as a

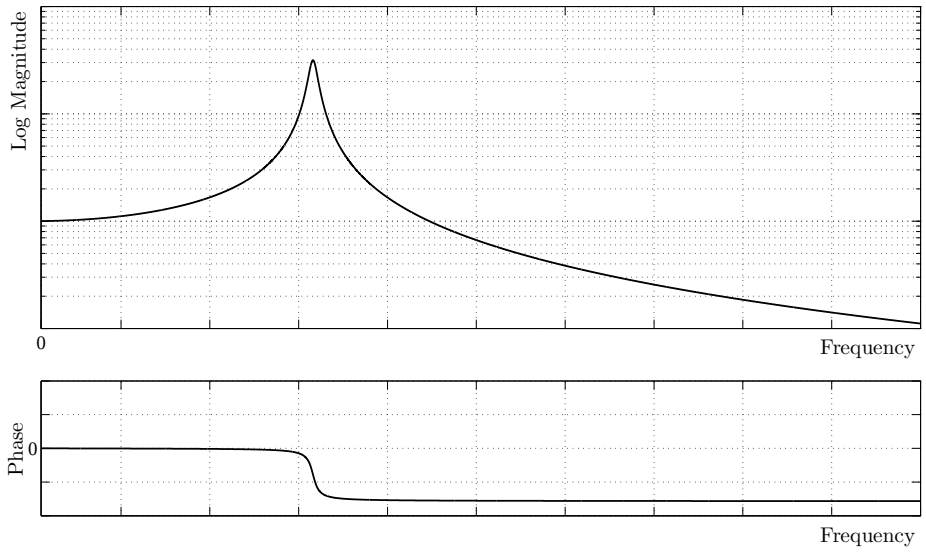

Figure 2.6: SDOF system frequency response function

measure of the 'goodness of fit' of a proposed linear model to measured data. It is also arguably the most widely used test of nonlinearity [11]. When the coherence function falls substantially from unity, the use of a linear model to describe the system becomes questionable [22]. In practice four main reasons exist as to why a computed coherence function may not equal unity at all frequencies [18]. They are,

1. Extraneous noise in the input and output measurements;
2. Bias and random errors in spectral density function estimates;
3. The output $y(t)$ is due in part to an input other than the measured $x(t)$;
4. Nonlinear system operations between $x(t)$ and $y(t)$.

Good data acquisition practice, signal processing and physical understanding of the system under test can eliminate the coherence drops due to the first three reasons. In the presence of nonlinear operations the linear theory breaks down as the difference between signal noise and nonlinearities cannot be shown [22]. Modified spectral techniques have been developed which allow nonlinear relationships to be investigated, these will be discussed in § 2.3.3.

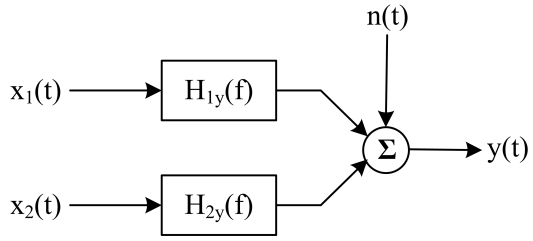

Figure 2.7: Two input/single output system

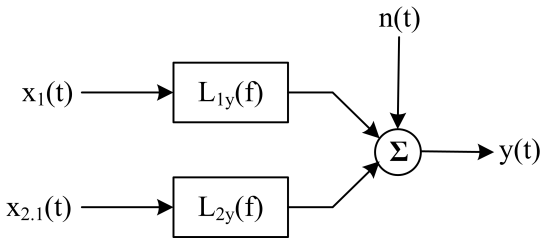

Figure 2.8: Two input/single output system with uncorrelated inputs

Multiple input single output systems

The analysis of Multiple Input/Single Output (MISO) systems is well documented in the works of Bendat and Piersol [23, 24]. MISO system analysis will be described here for the special case of a two input single output system, shown diagrammatically in Figure 2.7. In the special case of uncorrelated inputs ($S_{12} = 0$ and $\gamma_{12}^2 = 0$), spectral techniques can be applied to each leg independently to give an indication of the linear relationship between each input and the output. If the two inputs $x_1(t)$ and $x_2(t)$ are partially correlated ($0 < \gamma_{12}^2 < 1$), some of the contents of the output, which will appear to be due to the first input, will in fact be due to the second input. A similar effect will occur in the analysis of the second path. In this case, these influences must be removed before the analysis can be completed. This is achieved using conditioned spectral analysis. The system in Figure 2.7 can be remodelled as shown in Figure 2.8. In this case, the inputs are uncorrelated conditioned records, developed from the original input records, *i.e.*, $x_{2.1}(t)$ is a conditioned input and represents the input $x_2(t)$ with the linear effects of $x_1(t)$ removed from $x_2(t)$. The frequency response function $L_{1y}(f)$ is the optimal linear system to predict $y(t)$ from $x_1(t)$. Likewise $L_{2y}(f)$ is the optimal linear system to predict $y(t)$ from $x_{2.1}(t)$. L_{1y}

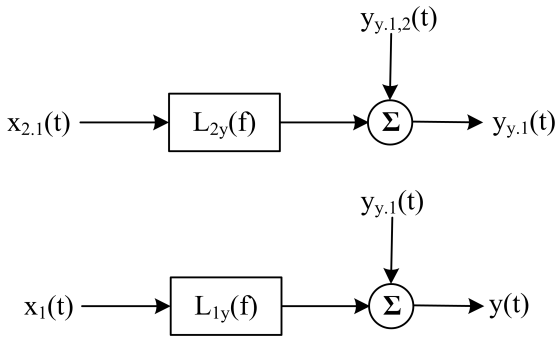

Figure 2.9: Conditioned input/conditioned output model

and L_{2y} are defined as,

$$L_{1y}(f) = \frac{S_{1y}}{S_{11}} \tag{2.24}$$

$$L_{2y}(f) = \frac{S_{2y.1}}{S_{22.1}} \tag{2.25}$$

where $S_{2y.1}$ is the conditioned cross–spectrum between $x_{2.1}(t)$ and $y(t)$ and $S_{22.1}$ is the autospectrum of $x_{2.1}(t)$, defined as follows, for finite T,

$$S_{2y.1}(f) = \frac{1}{T} E\left[X^*_{2.1}(f)\, Y(f)\right] \tag{2.26}$$

$$S_{22.1}(f) = \frac{1}{T} E\left[X^*_{2.1}(f)\, X_{2.1}(f)\right]. \tag{2.27}$$

The H coefficients in Figure 2.7 can be related to the L coefficients in Figure 2.8 using the following equations [23],

$$H_{1y}(f) = L_{1y}(f) - L_{12}(f) H_{2y}(f) \tag{2.28}$$

$$H_{2y}(f) = L_{2y}(f) \tag{2.29}$$

where $L_{12}(f)$ is the FRF between $X_1(f)$ and $X_2(f)$. The two input/single output model of Figure 2.8 with mutually uncorrelated inputs $x_1(t)$ and $x_{2.1}(t)$ is equivalent to the two separate SISO models in Figure 2.9. The ordinary coherence between $x_1(t)$ and $y(t)$ is defined as,

$$\gamma^2_{1y} = \frac{|S_{1y}(f)|^2}{S_{11}(f) S_{yy}(f)} \tag{2.30}$$

while for the second record, the coherence is defined as,

$$\gamma^2_{2y.1} = \frac{|S_{2y.1}(f)|^2}{S_{22.1}(f)S_{yy.1}(f)} \tag{2.31}$$

and is referred to as the partial coherence between the conditioned records, $x_{2.1}(t)$ and $y_{y.1}(t)$. The multiple coherence function can now be defined as,

$$\gamma^2_{y:x}(f) = 1 - \left[1 - \gamma^2_{1y}\right]\left[1 - \gamma^2_{2y.1}\right]. \tag{2.32}$$

The multiple coherence function is a measure of the linear dependence between a collection of inputs and an output, independent of the correlation between the inputs [24].

2.2.4 Modal analysis

Modal analysis is a well established and powerful technique for the analysis of linear systems. It is the most popular method of performing linear system identification in structural dynamics [25]. Classic vibration theory explains the existence of natural frequencies, damping factors, and mode shapes for linear systems. Consider the general mathematical representation of a SDOF system defined in equation 2.4; taking the Fourier Transform and rearranging gives,

$$X(\omega) = H(\omega)\,F(\omega) \tag{2.33}$$

where

$$H(\omega) = \frac{1}{-m\omega^2 + jc\omega + k}. \tag{2.34}$$

Equation 2.33 shows that the system response, $X(\omega)$ is directly related to the forcing function, $F(\omega)$, through the quantity $H(\omega)$. $H(\omega)$ is the system FRF and the denominator of equation 2.34 when equated to zero, is known as the characteristic equation. The characteristic values of this equation are known as the complex roots of the equation or the complex poles or modal frequencies of the system. The FRF can be written as a function of the complex poles of the system as follows,

$$H(\omega) = \frac{1/m}{(j\omega - \lambda)(j\omega - \lambda^*)} \tag{2.35}$$

where,

$$\lambda = \sigma + j\omega_d$$
$$\lambda^* = \sigma - j\omega_d$$

and ω_d is the damped natural frequency. This analysis can be extended to Multiple Degree–Of–Freedom (MDOF) systems. MDOF linear systems can always be represented as a superposition of a number of SDOF linear systems. Consider the MDOF form of equation 2.4[1],

$$\boldsymbol{M}\ddot{\boldsymbol{x}}(t) + \boldsymbol{C}\dot{\boldsymbol{x}}(t) + \boldsymbol{K}\boldsymbol{x}(t) = \boldsymbol{F}(t) \tag{2.36}$$

in the case of a two Degree–Of–Freedom (DOF) system,

$$\boldsymbol{M} = \begin{bmatrix} m_1 & 0 \\ 0 & m_2 \end{bmatrix}, \boldsymbol{C} = \begin{bmatrix} c_1 + c_2 & -c_2 \\ -c_2 & c_2 \end{bmatrix}, \boldsymbol{K} = \begin{bmatrix} k_1 + k_2 & -k_2 \\ -k_2 & k_2 \end{bmatrix}$$

$$\boldsymbol{F} = \begin{Bmatrix} f_1(t) \\ f_2(t) \end{Bmatrix}, \boldsymbol{x} = \begin{Bmatrix} x_1(t) \\ x_2(t) \end{Bmatrix}$$

in the MDOF case,

$$\boldsymbol{H}(\omega) = \left[-\boldsymbol{M}\omega^2 + j\omega\boldsymbol{C} + \boldsymbol{K}\right]^{-1} = \frac{\boldsymbol{N}(\omega)}{d(\omega)} \tag{2.37}$$

where the numerator polynomial matrix, $\boldsymbol{N}(\omega)$, and the characteristic polynomial $d(\omega)$ are given by,

$$\boldsymbol{N}(\omega) = adj\left(-\boldsymbol{M}\omega^2 + j\omega\boldsymbol{C} + \boldsymbol{K}\right)$$
$$d(\omega) = det\left(-\boldsymbol{M}\omega^2 + j\omega\boldsymbol{C} + \boldsymbol{K}\right).$$

Equation 2.37 can be written in the modal model form,

$$\boldsymbol{H}(\omega) = \sum_{r=1}^{n} \frac{\boldsymbol{R}_r}{j\omega - \lambda_r} + \frac{\boldsymbol{R}_r^*}{j\omega - \lambda_r^*} \tag{2.38}$$

[1]To aid clarity and simplify notation, matrices and vectors in the remainder of this section and in section 2.2.5 are identified using bold face type, i.e. $[M] = \boldsymbol{M}$, $\{x\} = \boldsymbol{x}$

where

$$
\begin{aligned}
r &= \text{mode number} \\
\boldsymbol{R}_r &= \text{residue matrix of mode } r = Q_r \boldsymbol{\Psi}_r \boldsymbol{\Psi}_r^T \\
\boldsymbol{\Psi}_r &= \text{mode shape vector of mode } r \\
Q_r &= \text{modal scaling factor} \\
\lambda_r &= \text{system pole} \\
n &= \text{number of modes.}
\end{aligned}
$$

The modal model (equation 2.38) expresses the structure's dynamic behaviour as a linear combination of n resonant modes. The n modes are defined by a resonant frequency ω_r, a damping ratio $\zeta_r = \sigma_r / |\lambda_r|$ and a mode shape vector $\boldsymbol{\Psi}_r$. The modal properties of the structure depend on the material properties, boundary conditions and geometry of the structure. Experimental Modal Analysis (EMA) is the process of determining the modal parameters (ω_r, $\boldsymbol{\Psi}_r$, λ_r) from measured experimental data. The process has three stages [26],

Modal data acquisition involves the measurement of the data required for the modal parameter estimation phase. The frequency response function is the most common and important measurement to be made.

Modal parameter estimation is a special case of system identification where the *a priori* model of the system is known to be in the form of modal parameters.

Modal data presentation/validation is the process of providing a physical view or interpretation of the modal parameters.

Traditionally EMA methods applied to nonlinear structures require the assumption of 'weak nonlinearities' or a nonlinear model structure which is similar, for small perturbations, to the underlying linear system. Rice and Fitzpatrick noted that it known to be limited in the case of non lightly damped structures [27]. In the presence of nonlinearity, the curve fitting algorithms of modal analysis will result in the identification of a linear system which best describes the nonlinear system. Nonlinear system FRF's will change with a change in excitation amplitude and as a result, the linearisation carried out by the curve fitting algorithm will only be valid for a given excitation level.

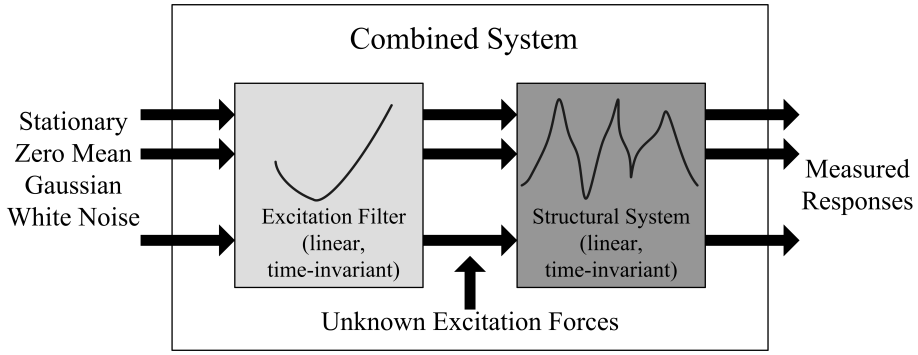

Figure 2.10: Operational modal analysis

2.2.5 Operational modal analysis

Operational Modal Analysis (OMA) is a relatively new concept in the field of mechanical testing. OMA involves conducting modal analysis without knowing the input forces acting on the structure. The input force is assumed to be normally distributed Gaussian white noise. Originally developed for extracting the modal parameters of civil engineering structures, it is now becoming popular for mechanical structures [28]. The advantage of using OMA is that structures can be tested in their operating environment under actual loading conditions. This allows for the identification of more realistic modal models for in–operation structures [29]. It also has the advantage of using ambient excitation. This is useful for large structures which are difficult to excite or require expensive specialist equipment to excite them.

The principle behind OMA is shown schematically in Figure 2.10. The measured responses are the responses of the combined system. The modal model of the system is extracted from the estimated model of the combined system. In other words, the response which comes from the system must be separated from the response due to the excitation. If the system is excited using white noise, the output spectrum contains full information of the structure as all modes are excited equally. However, this is generally not the case. In general, the excitation has a spectral distribution which results in modes being weighted by the spectral distribution of the input force. Computational noise and measurement noise also contribute to the response. In addition, rotating parts create harmonic vibrations which show themselves as sharp peaks in the measured response.

The Frequency Domain Decomposition (FDD) technique used for OMA is an extension of the classical frequency domain method often referred to as the peak picking

technique. Unlike classical methods, it can identify closely spaced modes with high accuracy even in the presence of strong noise contamination. It can also identify harmonic components in the response signal [30]. The FDD method, however, cannot be used to make damping estimates. The Enhanced Frequency Domain Decomposition (EFDD) technique is an extension of the FDD technique. It allows for the estimation of both natural frequency and damping for a particular mode. Once a peak has been identified, the SDOF Power Spectral Density (PSD) function in the area of the identified peak is taken back to the time domain using the Inverse Discrete Fourier Transform. The resonant frequency is obtained by counting the zero crossings, and the damping by the logarithmic decrement of the corresponding SDOF normalised auto correlation function [31].

The FDD methods are based on the formula for input/output PSD relationships for stochastic process. Starting with equation 2.33 and multiplying by its Hermitian transpose leads to,

$$\boldsymbol{G}_{yy}(\omega) = \boldsymbol{H}(\omega)^* \boldsymbol{G}_{xx}(\omega) \boldsymbol{H}(\omega)^T \tag{2.39}$$

where $\boldsymbol{G}_{xx}(\omega)$ is the input PSD matrix. $\boldsymbol{G}_{yy}(\omega)$ is the output PSD matrix, and $\boldsymbol{H}(\omega)$ is the FRF matrix. From classical modal analysis theory, the FRF can be written in partial fraction form, in terms of poles, λ and residues $\boldsymbol{R}$ as shown in equation 2.38. Using equation 2.39 and the Heaviside partial fraction theorem for polynomial expansions, the following expression can be obtained for the output PSD matrix $\boldsymbol{G}_{yy}(\omega)$, assuming the input is a zero mean white noise distribution, *i.e.*, its PSD is a constant matrix ($\boldsymbol{G}_{xx}(\omega) = C$),

$$\boldsymbol{G}_{yy}(\omega) = \sum_{r=1}^{n} \frac{\boldsymbol{A}_r}{j\omega - \lambda_k} + \frac{\boldsymbol{A}_r^*}{j\omega - \lambda_r^*} + \frac{\boldsymbol{B}_r}{-j\omega - \lambda_r} + \frac{\boldsymbol{B}_r^*}{-j\omega - \lambda_r^*} \tag{2.40}$$

where $\boldsymbol{A}_r$ and $\boldsymbol{B}_r$ are the r^{th} mathematical residues. Considering a lightly damped model and that the contribution of the modes at a particular frequency is limited to a finite number (usually 1 or 2), then the response spectral density matrix can be written as the following final form [31],

$$\boldsymbol{G}_{yy}(\omega) = \sum_{r \in sub(\omega)} \frac{d_r \boldsymbol{\Psi}_r \boldsymbol{\Psi}_r^T}{j\omega - \lambda_r} + \frac{d_r^* \boldsymbol{\Psi}_r^* \boldsymbol{\Psi}_r^{*T}}{j\omega - \lambda_r^*} \tag{2.41}$$

where $r \in sub(\omega)$ is the set of modes that contribute at the particular frequency and where $\boldsymbol{\Psi}_r$ is the mode shape and d_r is a scaling factor for the r_{th} mode. This form of the output PSD matrix can be decomposed using the SVD technique into a

set of singular values and corresponding singular vectors,

$$\boldsymbol{G}_{yy}(\omega) = \boldsymbol{\Phi}\boldsymbol{\Sigma}\boldsymbol{\Phi}^{H} \tag{2.42}$$

where $\boldsymbol{\Sigma}$ is the singular value matrix and $\boldsymbol{\Phi}$ the singular vectors unitary matrix, given by,

$$\boldsymbol{\Sigma} = \begin{bmatrix} s_1 & 0 & 0 & . & . & 0 \\ 0 & s_2 & 0 & . & . & . \\ 0 & 0 & s_3 & . & . & . \\ . & . & . & . & . & 0 \\ . & . & . & . & s_r & 0 \\ 0 & . & . & 0 & 0 & 0 \end{bmatrix} \tag{2.43}$$

$$\boldsymbol{\Phi} = \begin{bmatrix} \{\phi_1\} & \{\phi_2\} & \{\phi_3\} & . & . & \{\phi_r\} \end{bmatrix} \tag{2.44}$$

where ϕ_i are approximations of the individual mode shapes, while the resonant frequencies can be obtained form the singular values. r singular values and r singular vectors are obtained at each frequency. Plotting these values versus frequency allows a peak picking method to be used to determine resonant frequencies. At a particular frequency if only one mode is dominant then only one singular value will be dominant at this frequency. This allows for the identification of coupled modes. Figure 2.11 shows the singular values of the output PSD matrix for a simulated building [30]. The simulation was designed to have two sets of closely spaced modes. The FDD technique allowed the identification of all modes (18.7, 20.9, 38.2, 55.05 and 55.12 Hz), including closely spaced modes, in the frequency range of the test.

Devriendt and Guillaume introduced an approach to identify modal parameters from output only transmissibility measurements [29, 32]. The approach makes no assumption regarding the spectral nature of the excitation forces. Transmissibilities are obtained by taking the ratio of two response spectra, *i.e.* $T_{ij} = X_i(\omega)/X_j(\omega)$. Assuming a single force at an input DOF, k, it can be shown that,

$$\boldsymbol{T}^{k}_{ij}(\omega) = \frac{\boldsymbol{X}_i(\omega)}{\boldsymbol{X}_j(\omega)} = \frac{\boldsymbol{H}_{ik}(\omega)\boldsymbol{F}_k(\omega)}{\boldsymbol{H}_{jk}(\omega)\boldsymbol{F}_k(\omega)} = \frac{\boldsymbol{N}_{ik}(\omega)}{\boldsymbol{N}_{jk}(\omega)} \tag{2.45}$$

with $\boldsymbol{N}_{ik}(\omega)$ and $\boldsymbol{N}_{jk}(\omega)$ the numerator polynomials occurring in the transfer function models $\boldsymbol{H}_{ik}(\omega) = \boldsymbol{N}_{ik}(\omega)/d(\omega)$ and $\boldsymbol{H}_{jk}(\omega) = \boldsymbol{N}_{jk}(\omega)/d(\omega)$. The common denominator polynomial, $d(\omega)$, whose roots are the system poles disappear by taking the ratio of the two response spectra. Note that the transmissibilities defined in

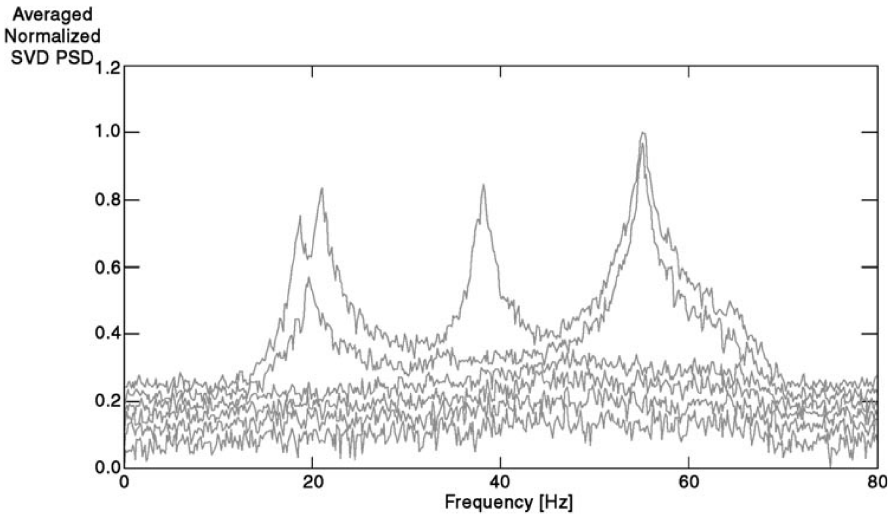

Figure 2.11: Singular values of the PSD matrix of the response (reproduced from [30])

equation 2.45 depend on the location of the input DOF k of the unknown force. This fact was used by the authors to identify the modal parameters as outlined below.

Consider the modal model between input DOF k, and output DOF i (equation 2.38) [2],

$$\boldsymbol{H}_{ik}(\omega) = \sum_{r=1}^{n} \frac{\boldsymbol{\Psi}_{ir} L_{kr}}{j\omega - \lambda_r} + \frac{\boldsymbol{\Psi}^*_{ir} L^*_{kr}}{j\omega - \lambda^*_r}. \tag{2.46}$$

It can be shown, using equation 2.46, that the limiting value of the transmissibility function in equation 2.45 for ω going to the system's poles, λ_r, converges to,

$$\lim_{\omega \to \lambda_r} \boldsymbol{T}^k_{ij}(\omega) = \frac{\boldsymbol{\Psi}_{ir} L_{kr}}{\boldsymbol{\Psi}_{jr} L_{kr}} = \frac{\boldsymbol{\Psi}_{ir}}{\boldsymbol{\Psi}_{jr}} \tag{2.47}$$

and becomes independent of the location of the input DOF k of the unknown force. Subtraction of two transmissibility functions with the same output DOF's (i, j) but different input DOF's (k, l) yields,

$$\lim_{\omega \to \lambda_r} \left(\boldsymbol{T}^k_{ij}(\omega) - \boldsymbol{T}^l_{ij}(\omega) \right) = \frac{\boldsymbol{\Psi}_{ir}}{\boldsymbol{\Psi}_{jr}} - \frac{\boldsymbol{\Psi}_{ir}}{\boldsymbol{\Psi}_{jr}} = 0. \tag{2.48}$$

This means that the system poles, λ_r, are zeros of the function $\Delta \boldsymbol{T}^{kl}_{ij}(\omega) = \boldsymbol{T}^k_{ij}(\omega) -$

[2] The residue matrix here is expressed in terms of a modal participation factor. At response DOF p and force DOF q the residue of mode r is given by $\boldsymbol{R}_{pqr} = Q_r \boldsymbol{\Psi}_{pr} \boldsymbol{\Psi}_{qr} = L_{qr} \boldsymbol{\Psi}_{pr}$

$\boldsymbol{T}_{ij}^{l}(\omega)$ and consequently, poles of its inverse,

$$\frac{1}{\Delta \boldsymbol{T}_{ij}^{kl}(\omega)} = \frac{1}{\boldsymbol{T}_{ij}^{k}(\omega) - \boldsymbol{T}_{ij}^{l}(\omega)} \tag{2.49}$$

The above theoretical results show that it is possible, by using transmissibilities, to obtain a rational function $1/\Delta \boldsymbol{T}_{ij}^{kl}(\omega)$, with zeros equal to the system poles. This function can be obtained by combining two transmissibility functions with the same output DOF's but different locations of the input DOF's. This is directly the result of the fact that transmissibilities vary with the location of the applied forces, but become independent of them at the system poles (equation 2.47). The approach was extended to deal with the presence of harmonic excitations in [33].

2.3 Nonlinear system identification

Unlike linear systems, no general analysis method exists for nonlinear systems which can be applied to all systems in all cases [11, 34]. This is due to the highly individualistic nature of nonlinear systems and the fact that the basic principles which form the basis of modal analysis are no longer valid in the presence of nonlinearity [35]. In the presence of 'strong' nonlinearities, the only approach is to address the nonlinearities directly and develop a mathematical description of their behaviour [36]. As a result, an increasing number of nonlinear system identification methods have been developed over the last three decades. These identification methods will be divided into a number of broad categories, namely linearisation, time domain methods and frequency domain methods.

2.3.1 Linearisation

In the field of mechanics, investigators have represented physical laws using rather simple equations. For many physical systems the governing equations are not so simple, therefore, certain assumptions are employed to represent the governing equations in a form which is more easily understood. Thus the process of linearisation has become an intrinsic part of the rational analysis of physical systems [37]. Historically, linearisation methods were the first methods used for the purposes of nonlinear system identification. Equivalent linearisation is a technique first proposed by Caughey

[38]. This technique involved the minimisation of the mean squared error between the measured response of a nonlinear oscillator subject to Gaussian excitation and a linearised system.

One of the most widely used methods of visualising the input/output properties of a linear system is to construct the system FRF. Harmonic balance provides one of the neatest methods of deriving a nonlinear system FRF [11]. It is a means of finding the optimal quasi–linearisation of a nonlinear system. Consider the equation of motion,

$$m\ddot{x} + c\dot{x} + f_n(x) = F(t) \tag{2.50}$$

where $f_n(x)$ represents a nonlinear restoring force. Harmonic balance provides a means of obtaining k_{eq} for a given operating condition, such that,

$$f_n(x) \approx k_{eq}x. \tag{2.51}$$

Consider a phase shifted sinusoidal excitation of the form, $Fsin(\omega t - \phi)$, and assuming a trial solution of the form, $Xsin(\omega t - \phi)$, yields the nonlinear form $f_n(Xsin(\omega t))$. Expanding this function as a Fourier series yields,

$$f_n(Xsin(\omega t)) = a_0 + \sum_{n=1}^{\infty} a_n cos(n\omega t) + \sum_{n=1}^{\infty} b_n sin(n\omega t). \tag{2.52}$$

The Fourier expansion is a finite sum if f_n is a polynomial. The fundamental terms are the only parts of interest for the purpose of harmonic balance. Elementary Fourier analysis applies and

$$a_0 = \frac{1}{2\pi}\int_0^{2\pi} f_n(Xsin(\omega t))\, d(\omega t) \tag{2.53}$$

$$a_1 = \frac{1}{\pi}\int_0^{2\pi} f_n(Xsin(\omega t))\, cos(\omega t)\, d(\omega t) \tag{2.54}$$

$$b_1 = \frac{1}{\pi}\int_0^{2\pi} f_n(Xsin(\omega t))\, sin(\omega t)\, d(\omega t). \tag{2.55}$$

If the stiffness function is purely odd, i.e. $f_n(-x) = -f_n x$, then $a_0 = a_1 = 0$. Considering terms up to the fundamental in this case gives,

$$f_n(Xsin(\omega t)) \approx b_1 sin(\omega t) = k_{eq} Xsin(\omega t) \tag{2.56}$$

leading to the following expression for k_eq,

$$k_{eq} = \frac{b_1}{X} = \frac{1}{\pi X} \int_0^{2\pi} f_n(X sin(\omega t)) sin(\omega t) d(\omega t). \tag{2.57}$$

The FRF takes the form,

$$\Lambda(\omega) = \frac{1}{-m\omega^2 + jc\omega + k_{eq}} \tag{2.58}$$

where $\Lambda(\omega)$ is often referred to as a composite FRF due to the nature of its derivation. k_{eq} represents the mean value of the stiffness experienced by the system over one cycle. For this reason harmonic balance is sometimes referred to as an averaging method [11]. The formulae presented here show the implementation of the harmonic balance method for nonlinear stiffness, however, the method has no restrictions on the form of the nonlinearity.

Rice presented a linearisation technique for weakly nonlinear components [39]. The underlying differential equation governing a vibrating system was identified by changing equivalent linear stiffness and damping coefficients measured over a range of response levels. The method was verified using experimental testing of an aircraft panel connector. The identified model showed excellent results when subject to a range of excitation which were different to those used for the identification process.

2.3.2 Time domain methods

Masri and Caughey laid the foundations of a nonlinear system identification technique known as Restoring Force Surface (RFS) method [40]. Given the equation of motion of a SDOF system as described using Newton's second law,

$$m\ddot{x}(t) + f(x(t), \dot{x}(t)) = F(t) \tag{2.59}$$

where m is the mass and $f(x, \dot{x})$ is the internal restoring force which returns the system to its equilibrium position when disturbed. The function, $f(x, \dot{x})$, is seen to only depend on x and $\dot{x}$ and, therefore, can be represented by a surface over the phase plane, *i.e.*, (x, $\dot{x}$) plane. Rearranging equation 2.59 gives,

$$f(x(t), \dot{x}(t)) = F(t) - m\ddot{x}(t). \tag{2.60}$$

If the mass m, input force $F(t)$ and output acceleration $\ddot{x}(t)$ are measured, all the terms on the right hand side of the equation are known and hence so is f. For discrete sampled data, the i^{th} sample instant of equation 2.60 is given by,

$$f_i = f_i(x_i, \dot{x}_i) = F_i - m\ddot{x}_i. \tag{2.61}$$

If the velocities $\dot{x}_i$ and displacements x_i are know at each instant, $i = 1, 2, ..., N$, a triplet $(x_i, \dot{x}_i, f_i)$ is specified. This triplet of values gives a point on the phase plane and also the height of the restoring force above the phase plane. The scattering of points above the phase plane can be interpolated to form a continuous surface. Masri and Caughey fitted a parametric model to the restoring force in the form of a double Chebyshev series, although superior techniques in terms of ease of use, speed and accuracy have been developed since the original work [11].

RFS's provide a relatively simple method of visualising the nonlinearity in a system. A similar method, termed 'force–state mapping' was developed by Crawley and O'Donnell [41]. The RFS method has received much attention in research and significant improvements have been brought about since the original paper [42, 43, 44, 45, 46]. It is argued in [47] that none of the other nonlinear system identification methods provide a model as recognisable and usable by the engineer.

DPE introduced in § 2.2.2 can be extended to the identification of nonlinear systems. The implementation of the DPE technique is described here for a nonlinear SDOF system. Its application to a more complex MDOF nonlinear system can be found in reference [19], where it is applied to two and three DOF simulated and experimental data. Consider the differential equation of motion of a SDOF Duffing oscillator,

$$m\ddot{x}(t) + c\dot{x}(t) + kx(t) + k_3x^3(t) = F(t). \tag{2.62}$$

If N samples of acceleration $\ddot{x}(t)$, velocity $\dot{x}(t)$ and displacement $x(t)$ are recorded, the problem can be formulated as follows,

$$\begin{bmatrix} \ddot{x}_1 & \dot{x}_1 & x_1 & x_1^3 \\ \ddot{x}_2 & \dot{x}_2 & x_2 & x_2^3 \\ \vdots & \vdots & \vdots & \vdots \\ \ddot{x}_N & \dot{x}_N & x_N & x_N^3 \end{bmatrix} \begin{Bmatrix} m \\ c \\ k \\ k_3 \end{Bmatrix} = \begin{bmatrix} F_1 \\ F_2 \\ \vdots \\ F_N \end{bmatrix} \tag{2.63}$$

The inclusion of the nonlinear form x^3 in this formulation allows the coefficient

of the nonlinearity to be estimated along with the linear coefficients m, c and k. Masri *et al.* used a variation of the DPE technique to identify the state equation in complex nonlinear systems [48]. The method determines the analytical solution $\hat{g}$, that approximates the unknown system state equation, g. The form of $\hat{g}$ includes a suitable set of basis functions that are relevant to the problem at hand. Consider the Duffing oscillator defined in equation 2.62. A suitable choice of basis functions in this case might be,

$$basis = (F, Fx, F\dot{x}, PS) \tag{2.64}$$

where PS represents the list of basis terms in the power series expansion of,

$$PS = \sum_{i=0}^{i_{max}} \sum_{j=0}^{j_{max}} x^i \dot{x}^j. \tag{2.65}$$

Least squares techniques were used to estimate the coefficients of $\hat{g}\left(x, \dot{x}, F\right)$. Coefficients in $\hat{g}$ exceeding a predefined value, for example 10^{-6}, are retained. The identification scheme finds the correct model form and unneeded terms in the basis function are found to be extraneous. The method was also applied to the identification of a hysteretic system, simulated using a Bouc–Wen model.

The linear variant of the time series approach, Auto–Regressive Moving Average (ARMA) models, have long been used for modelling and prediction purposes, the classic reference for this material being the work by Box and Jenkins [49]. The ARX model introduced in § 2.2.2 can be extended to nonlinear systems, such as the Duffing oscillator represented by equation 2.62 to yield,

$$x_i = a_1 x_{i-1} + a_2 x_{i-2} + b_1 f_{i-1} + c x_{i-1}^3. \tag{2.66}$$

This model is termed a Nonlinear Auto-Regressive with eXogenous inputs (NARX) model. The regressive function, x_i, contains a cubic term and is, therefore, nonlinear. This model can be generalised to include all terms of order n_p or less to yield,

$$x_i = F^{(n_p)}\left(x_{i-1}, ..., x_{i-n_x}; f_{i-1}, ..., f_{i-n_f}\right). \tag{2.67}$$

This model form can represent a wide class of nonlinear systems when the nonlinearities are polynomial in nature [35]. The model can be extended to account for the more realistic case of noise on the measured data, where the measured signal consists of the true signal and a noise signal, $x_m(t) = x(t) + \epsilon(t)$. This yields an extension of the general model in equation 2.67, referred to as a Nonlinear Auto-Regressive

Moving-Average with eXogenous inputs (NARMAX),

$$x_i = F^{(n_p)}\left(x_{i-1}, ..., x_{i-n_x}; f_{i-1}, ..., f_{i-n_f}; r_{i-1}, ..., r_{i-n_r}\right) \tag{2.68}$$

where the system noise is assumed to be the result of passing a zero mean white noise sequence, $\{r_i\}$, through a digital filter with coefficients q_1, q_2, etc,

$$\epsilon_i = r_i + q_1 r_{i-1} + q_2 r_{i-2} + ... \tag{2.69}$$

The NARMAX modelling technique is very versatile and the use of a noise model makes it a powerful system identification tool. In most cases, it can exploit well established linear least squares parameter estimation techniques [50]. The non–parametric nature of the method, however, does not provide direct physical insight into the system under investigation and in the case of multi input/multi output use, the number of model terms can quickly become enormous [47].

The time domain version of the Hilbert Transform has been applied to the problem of nonlinear system identification. The method is presented in the work of Feldman [51, 52]. The proposed methods, FREEVIB and FORCEVIB, aim to identify instantaneous modal parameters (natural frequencies and damping characteristics, and their dependencies on vibration amplitude and frequency). The methods however are only truly suited to signals with a single dominant frequency. Extending the method to two component signals is discussed in [53].

2.3.3 Frequency domain methods

Nonlinear spectral methods have been developed for the identification of nonlinear systems. Algorithms were first introduced by Bendat and Piersol for SDOF square law and quadratic systems [54, 55]. Rice and Fitzpatrick extended the approach to deal with SDOF systems with arbitrary nonlinearities [22]. The authors also introduced the concept of constructing an inverse model of the nonlinear system. This procedure (commonly referred to as the 'reverse path' or 'Reverse Multiple Input/Single Output (R–MISO)' method) reverses the role of the input and outputs of the system, and allows nonlinear SISO models to be converted into equivalent MISO linear models. Consider the case of the duffing oscillator described in equation 2.62. This system can be represented by the block diagram shown in Figure 2.12. Note that the nonlinear term is contained in the feedback loop. By using the R–MISO

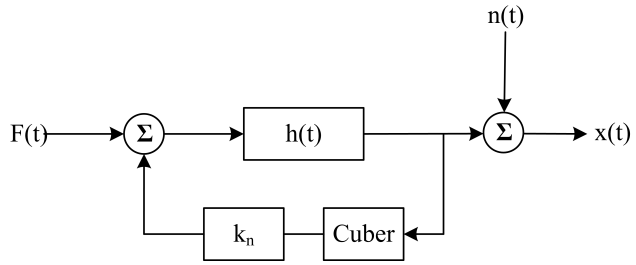

Figure 2.12: Block diagram model of the duffing oscillator

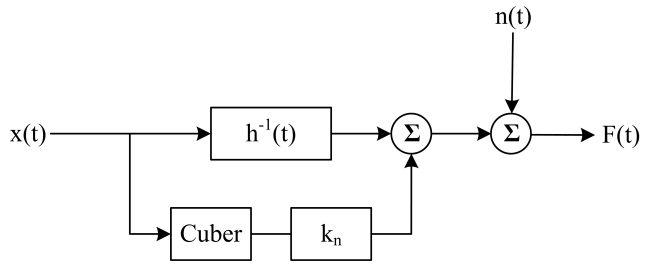

Figure 2.13: Inverse block diagram model of the duffing oscillator

approach, the system can be setup in the form shown in Figure 2.13. This is now a two input/single output problem with inputs $x(t)$ and $x^3(t)$ and output $F(t)$ and can be solved using the linear MISO techniques outlined in § 2.2.3.

An extension of this method for the case of MDOF systems was proposed in [27]. Richards and Singh presented a similar spectral method termed the Conditioned Reverse Path (CRP) method [56]. Only slight differences exist in the formulation of the R–MISO and CRP are not elaborated on here, in–depth discussion on the similarities and differences between the methods can be found in [57] and [58].

Nonlinear Identification through Feedback of the Outputs (NIFO) is a spectral method for the identification of nonlinear systems proposed in [59]. For a general lumped parameter nonlinear vibrating system with different type of nonlinearities at different degrees of freedom, the impedance model is given by,

$$[B_L(\omega)]_{N_0\times N_0}\{X(\omega)\}_{N_0\times 1}+\sum_{i=1}^{N_n}\mu_i(\omega)\{B_{ni}\}_{N_0\times 1}X_{ni}(\omega)=\{F(\omega)\}_{N_0\times 1}. \quad (2.70)$$

The linear impedance matrix, $[B_L(\omega)]$, represents the contribution of the underlying linear lumped spring–mass–damper elements. The summation terms account for the contribution of the lumped nonlinearities. The term $\mu_i(\omega)$ determines the strength of the associated nonlinearity, $\{B_{ni}\}$ determines the nonlinearity location and the

scalar spectrum $X_{ni}(\omega)$ is the Fourier spectrum of the nonlinear function of the output time histories, and determines the types of nonlinearity in the system.

The nonlinearities create unmeasured, internal feedback forces in the underlying linear model of the system. Rearranging equation 2.70 gives,

$$\begin{aligned} [B_L(\omega)]\{X(\omega)\} &= \{F(\omega)\} - \sum_{i=1}^{N_n} \mu_i(\omega)\{B_{ni}\} X_{ni}(\omega) && (2.71) \\ &= \{F(\omega)\} - \{F_n(\omega)\} && (2.72) \end{aligned}$$

where $\{F(\omega)\}$ represent the external forces on the system while, $\{F_n(\omega)\}$, represents the internal forces in the system due to the nonlinearities.

Pre–multiplying equation 2.71 by the FRF of the underlying linear system, and separating measured and unmeasured quantities gives,

$$\begin{aligned} \{X(\omega)\} = [\ [H_L(\omega)] \quad & [H_L(\omega)]\,\mu_1(\omega)\{B_{n1}\} \quad ... \\ & [H_L(\omega)]\,\mu_{N_n}(\omega)\{B_{nN_n}\}] \begin{pmatrix} \{F_\omega\} \\ -X_{n1}(\omega) \\ \vdots \\ -X_{N_n}(\omega) \end{pmatrix}. \end{aligned} \quad (2.73)$$

This formulation allows internal nonlinear feedback forces to act together with measured external inputs to produce the measured outputs. The system inputs and outputs can be measured and the nonlinear functions can be calculated from the measured input and outputs. Equation 2.73 forms the basis for the NIFO parameter estimation method.

2.3.4 Parameter estimation: least squares estimators

A large portion of the nonlinear analysis techniques outlined above use parameter estimation methods based on the least squares technique. The least squares estimators are among those with the best developed theoretical foundations; they are very popular and intensively used [17]. This section gives a brief overview of least squares estimation techniques.

Linear least squares

Linear least square techniques can be applied to models which are linear in the parameters. Linear in the parameters implies that there is a linear relationship between the parameters of the model and its output. The complexity of the optimisation problem is significantly reduced when linear least squares techniques can be applied. Consider a variable p forms a linear relationship with N independent variables q_i, $(i = 1, 2, ..., N)$ such that,

$$p = \{a\}^T \{q\} \tag{2.74}$$

where

$$\{a\} = \{a_1, a_2, ..., a_N\}^T$$
$$\{q\} = \{q_1, q_2, ..., q_N\}^T .$$

$\{a\}$ is a constant vector while $\{q\}$ is a time dependent variable vector. Given M different observations, equation 2.74 can be used M times to form the matrix equation,

$$\{p\} = [Q] \{a\} \tag{2.75}$$

where the design matrix $[Q]$ is given by,

$$[Q] = [\{q(1)\}, \{q(2)\}, ..., \{q(M)\}]^T .$$

When the number of samples, M, exceeds the number of variables in $\{a\}$, the equations are said to be overdetermined and a least squares solution can be found such that the sum of the squared errors between the predicted values and observations is minimised. The error vector between the predicted and the observed can be defined as,

$$\{e\} = \{p\} - [Q] \{a\} . \tag{2.76}$$

The cost function is given by,

$$\begin{aligned} K(\{a\}) &= \{e\}^T \{e\} \\ &= \{p\}^T \{p\} - \{a\}^T [Q]^T \{p\} - \{p\}^T [Q]^T \{a\} + \{a\}^T [Q]^T [Q] \{a\} . \end{aligned} \tag{2.77}$$

Minimising the cost function is achieved by taking its derivative with respect to vector $\{a\}$ and assigning it to zero, such that,

$$\frac{\partial K\left(\{a\}\right)}{\partial\{a\}} = -2\left[Q\right]^T\{p\} + 2\left[Q\right]^T\left[Q\right]\{a\} = 0 \tag{2.78}$$

leading to the well known normal equations for the best parameter estimates $\{\hat{a}\}$,

$$\left[Q\right]^T\left[Q\right]\{\hat{a}\} = \left[Q\right]^T\{p\} \tag{2.79}$$

which can be trivially solved,

$$\{\hat{a}\} = \left(\left[Q\right]^T\left[Q\right]\right)^{-1}\left[Q\right]^T\{p\}. \tag{2.80}$$

When it is known that errors from different locations are of different extents, it is possible to weight the errors in the least squares analysis to optimise the outcome. Given a known weighting matrix $[W]$ the cost function for the linear least squares problem (equation 2.77) becomes,

$$K\left(\{a\}\right) = \{e\}^T\left[W\right]\{e\} = \left(\{p\} - \left[Q\right]\{a\}\right)^T\left[W\right]\left(\{p\} - \left[Q\right]\{a\}\right). \tag{2.81}$$

Minimisation of the cost function as before yields the weighed least squares estimate,

$$\{\hat{a}\} = \left(\left[Q\right]^T\left[W\right]\left[Q\right]\right)^{-1}\left[Q\right]^T\left[W\right]\{p\}. \tag{2.82}$$

Robust estimation

In practice, direct solution of the normal equations in not recommended as problems can arise when the matrix, $\left[Q\right]^T\left[Q\right]$, is close to singular. This can result when correlation exists between the matrix columns, due to correlations between model terms (a matrix is singular if two columns are equal). The solution using normal equations is also susceptible to round off error [16]. Robust estimators have been developed which transform the design matrix into a form in which its columns are uncorrelated. One such method is based on the use of Singular Value Decomposition (SVD) and is the method of choice for solving most linear least squares problems [16]. For any matrix $[Q]$ of dimensions (M, N), where $M \geq N$, it is possible to

factorise it using SVD to obtain,

$$[Q] = [U]\,[\Sigma]\,[V]^T \tag{2.83}$$

where U, V are orthogonal matrices of dimensions (M, N) and (N, N) respectively, and $[\Sigma]$ is a diagonal matrix of dimensions (N, N). The diagonal elements of $[\Sigma]$, ($\varphi_{jj} \geq 0$ for $j \leq N$), are called singular values, and are arranged in descending order of significance. The number of non–zero singular values in $[\Sigma]$ is the rank of the matrix $[Q]$. If $[Q]$ has only $r < N$ linearly independent columns, then the rank is r and $N - r$ singular values are zero. The use of SVD allows the calculation of,

$$[Q]^\dagger = [V]\,[\mathrm{diag}\,(1/\varphi_{jj})]\,[U]^T \tag{2.84}$$

where $[Q]^\dagger$ is referred to as the pseudo–inverse of $[Q]$ such that,

$$[Q]^\dagger\,[Q] = [I]\,,\ \text{but,}\ \ [Q]\,[Q]^\dagger \neq [I]\,. \tag{2.85}$$

This can be used with equation 2.74 to obtain,

$$\{\hat{a}\} = [Q]^\dagger\,\{p\} = [V]\,[\mathrm{diag}\,(1/\varphi_{jj})]\,[U]^T\,\{p\}\,. \tag{2.86}$$

If any singular value, φ_{jj}, in $[\Sigma]$ is zero (in practice, due to measurement error, less than a tolerance limit, ε, close to zero), its reciprocal in equation 2.86 should be set to zero, instead of infinity. This effectively removes any linear dependence between the vectors in $[Q]$. The value of ε is chosen such that, any singular values whose ratio to the largest singular value is less than N times the machine precision, should be modified in this fashion [16].

Parameter uncertainty

In practice different samples of data will contain different noise components and as a result will give different parameter estimates. The parameter estimates, therefore, represent a random sample from a population of possible estimates, characterised by a probability distribution. If the expected value of the parameter estimates coincide with the true parameter values, the estimates are said to be unbiased.

Consider the system shown in Figure 2.14 where the measured output is corrupted

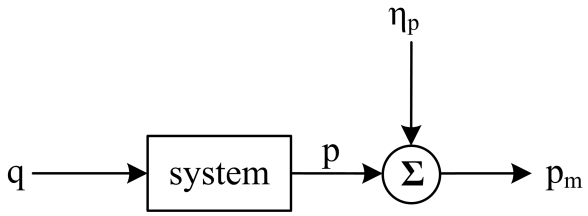

Figure 2.14: System with output noise

by noise. In this case equation 2.75 becomes,

$$\{p_m\} = [Q]\{a\} + \{\eta_p\} \tag{2.87}$$

where p_m, the measured signal, equals the true signal p plus the noise signal η_p. Assuming the measurement noise is uncorrelated white noise with zero mean, $E[\eta_p] = 0$, the estimated parameters, $\hat{a}$, will be unbiased. In the case of unbiased estimates the variance of the parameter distribution is provided by the covariance matrix [11],

$$C = \sigma_\zeta^2 \left([Q]^T [Q] \right)^{-1} = \sigma_\zeta^2 [V] [\Sigma]^{-2} [V]^T \tag{2.88}$$

where σ_ζ^2 is the variance of the noise on the measurements. If the noise on the measured signals is coloured, the estimates will be biased regardless of the amount of data measured. In this case the bias can be eliminated by including a noise model in the parameter estimation process.

Nonlinear least squares

Nonlinear least squares techniques are employed when the model depends nonlinearly on the set of M unknown parameters, $\{a\} = \{a_1, a_2, ..., a_M\}^T$. Problems of this form require iterative solution. The iterative search routines have three basic steps [17],

- selection of a set of starting values;
- generation of an improved set of parameters;
- selection of a stop criterion.

One popular method of solving nonlinear least squares methods is the Levenberg–Marquardt method. The method works well in practice and has become the standard

of nonlinear least squares routines [16]. Consider the cost function,

$$K(a) = e^T e = (p - q(a))^T (p - q(a)) \tag{2.89}$$

new estimates of the model parameters are generated using,

$$\delta a_{k+1} = \left(J_k^T J_k + \lambda I\right)^{-1} J_k^T (p - q(a)) \tag{2.90}$$

where the Jacobian matrix J is given by,

$$J = \frac{\partial q}{\partial a}. \tag{2.91}$$

The method uses the λ parameter to vary between the Gauss–Newton method and the gradient method. The latter is used far from the minimum, switching continuously to the former as the minimum is approached. The basic structure of the algorithm can be broken down as follows [17]:

1. Select a set of starting parameters and a large starting value of λ;
2. Calculate the Jacobian J;
3. Calculate δa_{k+1} using equation 2.90;
4. Is the step successful: $K(\hat{a}_{k+1}) < K(\hat{a}_k)$?
   - if yes: decrease λ and proceed to 5
   - if no: increase λ and restart at 3
5. If the stop criterion is not met, go to 2, otherwise stop.

2.4 Force–response system identification

EMA identification methods are the most widely used linear system identification techniques in the literature. Application of EMA techniques to system identification problems have been wide and varied; and the applications, trends and challenges are extensively documented [60, 61].

One particular work of interest to this investigation was conducted by Zegelaar [62]. It presented the EMA of a tyre under two boundary conditions, a free tyre and a

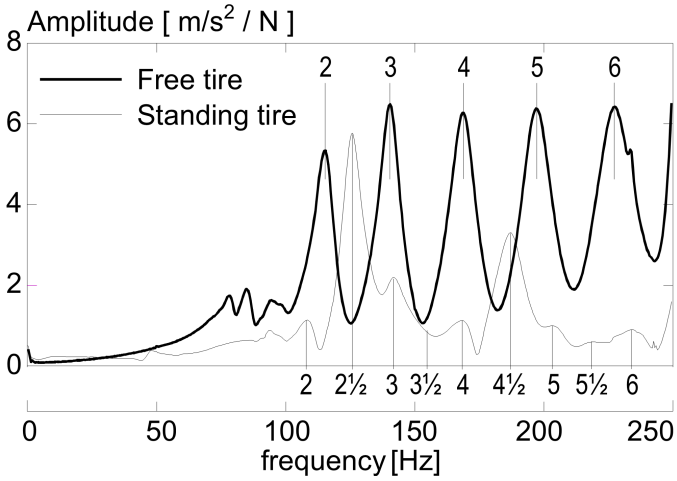

Figure 2.15: Tyre driving point FRF's in radial direction (reproduced form [62])

tyre standing on a road. Although the frequencies of the predicted higher order modes were less than the measured modes, in general the EMA results compared well with those from a flexible ring tyre model under both boundary conditions. In the free tyre state, smooth symmetric mode shapes of the tyre were identified. The second boundary condition applied a 4000 N preload to the tyre to represent its actual operating conditions. It was observed that the mode shapes and frequencies were different, and also, a number of modes were identified at frequencies half way between the successive free tyre modes. Figure 2.15 shows the results of the EMA for both boundary conditions. Although the free tyre test provided an accurate representation of the tyre behaviour, these results suggest that identification of components in their operating environment may provide a more applicable representation.

The reverse path or R–MISO spectral method has been applied to a broad range of nonlinear systems. Fitzpatrick and Rice implemented the method on SDOF and MDOF numerically simulated vibrating system [12, 27], Meskell and Fitzpatrick experimentally identified the parameters of a SDOF system with both coulomb and viscous damping [63] and its application to the modelling and identification of nonlinear squeeze film dynamics was presented in [64, 65, 66]. In an extensive revision of his previous book on 'Nonlinear System Analysis and Identification from Random Data', Bendat presented complex MDOF applications of the method for oceanographic, automotive and biomedical systems [18]. The methods have become very popular for ocean engineering applications, due to the nonlinear nature of the excitation mechanisms. Liagre and Niedzwecki used R–MISO techniques to

experimentally identify the dynamic parameters of an deep water compliant offshore structure [67]. A mathematical model of the structure was developed. The ordinary coherence inputs between each potential inputs and the output were computed and the most relevant inputs retained for the identification of related parameters. The method identified linear stiffness and damping parameters as well as trilinear stiffness and quadratic damping type nonlinearities. Parker applied R–MISO techniques to the identification of cushioning materials for protective packaging applications [68]. The R–MISO approach to the problem provided a more accurate description of the protective material cushioning characteristics used by packaging designers in their calculations for the protection of a product. Garibaldi used CRP methods to quantify the nonlinear behaviour of a clamped beam with a local nonlinearity at one end [34]. A two input/single output model was used. The inputs were the displacement at the end of the beam and a nonlinear term of the form $(sign\,(x(t)\,|x(t)|^m))$. The exponent, m, was found by graphing the multiple coherence levels for a range of trial analyses and determining the exponent level which maximised the coherence. The linear frequency response function developed using theCRP method provided a more accurate description of the system behaviour than linear H_1 and H_2 FRF estimators.

Meskell *et al.* used force–state mapping to develop a nonlinear lumped parameter model of a coupled fluid structure system [69]. The experimental setup consisted of a tube array in a wind tunnel. One of the tubes was connected to a flexible aluminium support structure outside the wind tunnel. The identification of the support structure using R–MISO spectral analysis can be found in [63]. The tube was displaced and the free decay recorded for a flow velocity in the range of 0–8.5 m/s. The equation of motion of the tube after averaging out turbulent excitation effects is,

$$m\ddot{x}(t) + c_s\dot{x}(t) + k_s x(t) = E\,(x, \dot{x}, U_\infty)\,. \tag{2.92}$$

Rearranging the equation of motion yields,

$$\ddot{x}(t) = \frac{1}{m}\left(E\,(x, \dot{x}, U_\infty) - c_s\dot{x}(t) - k_s x(t)\right) = F\,(x, \dot{x}, U_\infty) \tag{2.93}$$

therefore, the total force due to the support structure $(c_s\dot{x}(t) - k_s x(t))$ and fluid–elastic force $(E\,(x, \dot{x}, U_\infty))$ can be plotted above the phase plane $(x, \dot{x})$. Assessment of the force–state maps for varying fluid velocities allowed an assumption to be made that the fluid–elastic force could be represented as the sum of linear and cubic stiffness and damping terms. The main features of the identified model were a

destabilising linear damping term and stabilising cubic damping term. The identified model showed good correlation with measured results.

Kerschen *et al.* examined the identification of a nonlinear beam with piecewise linear stiffness and bilinear stiffness using RFS methods. The restoring force was modelled using a mathematical representation of the form,

$$f\left(x,\dot{x}\right)=\sum_{i=0}^{m}\sum_{j=0}^{n}\alpha_{ij}x^{i}\dot{x}^{j}. \tag{2.94}$$

The values of α_{ij} were obtained using least squares parameter estimation. A significance factor given by,

$$s_{\theta}=100\frac{\sigma_{\theta}^{2}}{\sigma_{x}^{2}} \tag{2.95}$$

was introduced to determine which terms in equation 2.94 were significant and which could be safely discarded. σ_x^2 corresponds to the variance of the sum of all the terms in the model and σ_θ^2 is the variance of the considered term. The piecewise linear and bilinear systems under test consisted of a clamped beam, which when its transverse motion exceeded a certain limit, made contact with a steel bush. The study looked at theoretical and experimental identification of the beam. Third order polynomial and piecewise linear models were applied and both gave good results. As acceleration, velocity and displacement signals were required for the analysis, careful signal processing was required to obtain the three signals from measurement acceleration.

2.4.1 Vehicle suspension system identification

The identification of vehicle suspension systems poses a significant challenge. Vehicle suspension systems are known to be highly nonlinear systems, and it is untenable to model them as linear systems [70]. The combination of high damping, hysteresis, friction among others, results in a system which can be difficult to identify. Many analytical techniques currently available are limited to the steady state response of weakly nonlinear oscillators [35], while many frequency domain methods are quite limited when applied to highly damped systems [71].

RFS methods have been widely applied in research, most noticeably in the area of nonlinear automotive components [1, 21, 70, 72, 73, 74, 75]. Its application in

the absence of measured input excitations has also been reported [76]. One of the reasons for its popularity is the ability to quickly provide a visual representation of the restoring force in the system. Cafferty *et al.* presented the characterisation of an automotive shock absorber, subject to random excitation, using the RFS method [21]. The use of random excitation is noted as having a number of benefits including,

- No control over the input is required beyond setting the excitation amplitude and frequency limits;
- Data can be acquired in a short space of time, eliminating the possibility of non–stationary data through warming of the shock absorber;
- The significant dynamical behaviour of the system will be described by the 'backbone' of the restoring force surface as frequency dependent behaviour and memory effects will be averaged (only a single force value exists for every point on the phase plane);
- A more uniform covering of the phase–plane can be achieved (compared to harmonic excitation methods) allowing the use of simpler surface interpolation algorithms.

The ability of random excitation to estimate the 'backbone' of the shock absorber, by averaging memory effects, allowed the use of a tenth order polynomial model form and linear least square parameter estimation. The shock absorber was also modelled using a hyperbolic tangent model of the form,

$$F_d = \kappa \left\{ tanh\left(\xi \dot{x} + \vartheta\right) - tanh\left(\vartheta\right) \right\} \tag{2.96}$$

parameter estimation of κ, ξ and ϑ required the use of nonlinear least squares. Although, the polynomial model gave more accurate results, the hyperbolic tangent model has the advantage of giving linear damping at high piston velocities and is, therefore, unconditionally stable.

Duym proposed that velocity and acceleration ($f(\dot{x}, \ddot{x})$) be used in place of velocity and displacement ($f(\dot{x}, x)$) when applied to force–state mapping of shock absorbers subject to broadband excitation signals [72]. A visual comparison of the two force–state map approaches is shown in Figure 2.16. Two experiments were carried out on a shock absorber, the first with multisine excitation containing 16 sines with frequencies from 1.25–16.25 Hz and the second for a beating signal (5.0–5.2 Hz).

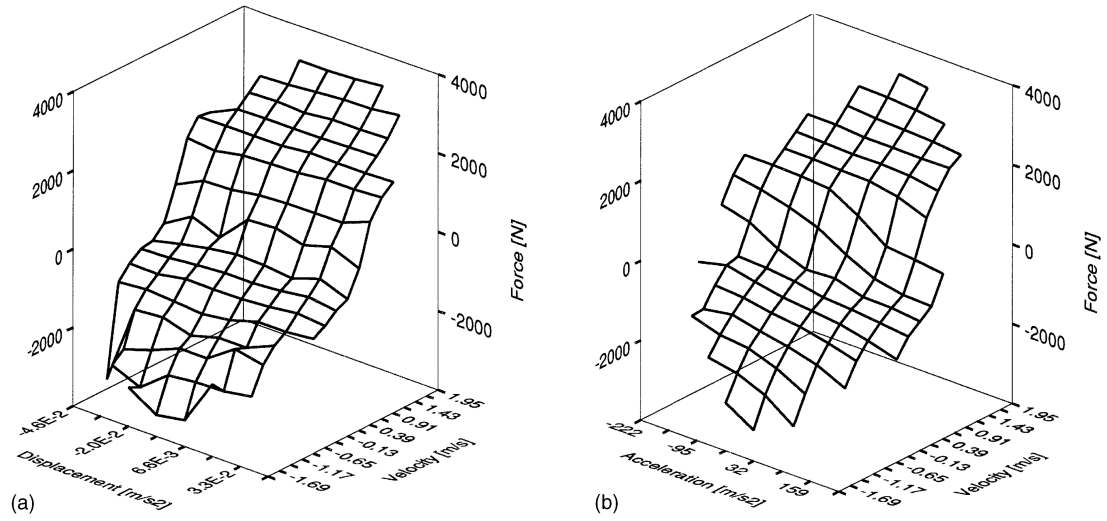

Figure 2.16: First–order force state map for a 16 by 8 grid for (a) displacement–velocity and (b) velocity–acceleration (reproduced from [72])

Zeroth order and first order Taylor series expansions were fitted to the $f(\dot{x}, \ddot{x})$ and $f(\dot{x}, x)$ phase planes. The Root Mean Square (RMS) error between the measured results and the fitted models was significantly lower for the $f(\dot{x}, \ddot{x})$ map for multisine excitation (broadband). However, the traditional $f(\dot{x}, x)$ force–state map showed slightly lower RMS errors for the beating case (narrowband).

Identification of vehicle shock absorbers are almost always carried out under isolated testing conditions. Numerous examples exist in the literature of shock absorber identification using force–response methods. Most use harmonic excitation [77], but arguments have been made for the use of random [21, 78, 79], sine–on–sine [80], swept sine[2, 81], constant velocity [82] and actual recorded road data [83]. Ko *et al.* examined shock absorber characteristic variation with wear. This involved the removal of used shock absorbers from vehicle suspensions to facilitate isolated testing [84]. The identification of Magnetorheological (MR) dampers for vehicle suspension applications has also proved popular[85, 86, 87, 88]. All applications involved isolated testing of the dampers on mechanical test stands under different applied magnetic fields. Yao *et al.* used the identified MR damper model in a quarter car suspension simulation [87]. The semi–active MR damper outperformed the passive component in terms of controlling sprung mass acceleration, suspension deflection and tyre deflection. Sung *et al.* conducted extensive experimental testing and identification of Electrorheological (ER) shock absorbers [89]. The work involved dynamometer characterisation of the shock absorber, control system development in a quarter car

test rig, before on the road full vehicle testing. Hardware in the loop simulation for the identification of a vehicle shock absorber was presented in [78]. In the simulation the actual shock absorber is used and was excited by a hydraulic actuator. Its damping and force response were measured directly and fed back to the simulation in real time. This approach allowed accurate simulation without the need for the identification of complex nonlinear components.

Gobbi *et al.* investigated suspension vibration and harshness by measuring forces and moments at the chassis suspension joints [90]. The ruotavia test rig (Figure 2.23) was used in this study. Special six axis load cells, presented in detail in reference [91], were used to measure the forces and moments at the joints. The suspension was excited by passing over a cleat on the rotating drum surface. Constant speed and varying speed analysis was carried out. For the constant speed analysis, averaging of the measured signals was carried out using auto and cross–correlation functions to synchronise the individual cleat passages in the recorded time histories. This approach allowed calculation of an accurate spectrum of the bushing force at the suspension joints. The varying speed analysis, conducted between 8 km/hr and 48 km/hr, revealed that the plots of maximum force are not monotonically increasing functions. The maximum RMS peaks in the vertical and horizontal forces occur approximately at 20–25 km/hr and 30–35 km/hr, respectively. The authors included suspension system support structure interaction in their dynamic model, a technique not previously reported in literature. The support structure was excited using hammer excitation at the suspension connection joints and the one degree of freedom models were developed from the accelerances measured. In a related study [92], Gobbi *et al.* further analysed the results to obtain modal damping via the Hilbert Transform. A time history of joint force in the longitudinal direction was band pass filtered around the frequency of interest. The Hilbert Transform of the filtered signal was computed and the damping of the system in the longitudinal direction was calculated from the slope of the decay envelope.

Nozaki and Inagaki presented a method of analysing coil springs and shock absorbers independently without removing them from the vehicle [93]. The vehicle body was excited using a vertical up and down motion at speeds in the 0–0.3 m/s range. At the point where the body displacement of zero was crossed, the spring reaction was zero. By measuring the tyre vertical load at this point, it was possible to obtain the damping force value of the shock absorber itself, excluding the effect of the spring. By varying the body excitation speed, a shock absorber force characteristic diagram

was generated. The spring constant was found from the vehicle body displacement and the tyre vertical load when a static force was applied to the vehicle body. The method was verified theoretically and experimentally, but requires dedicated hardware and software developed specifically for the application.

Kim and Ro proposed a method of developing accurate simple models of complex mechanical systems [94]. The authors constructed an accurate complex model of a double wishbone suspension system in ADAMS® and used it to produced a two DOF reduced order model. The reduced order model was produced from the linearised ADAMS® model. It was found to be very accurate when compared with the complex ADAMS® model. The authors compared the two DOF reduced order model to a two DOF quarter car model (see § 2.6.2), with component data (sprung mass, unsprung mass, spring stiffness, shock absorber damping, tyre stiffness) measured from the actual suspension system, and found significant differences in the output of both models. A set of revised component parameters were developed from the reduced order model for use in the two DOF quarter car model. The goal was to develop a set of parameters such that the response of the quarter car model was as close as possible to the reduced order model. This revised quarter car model produced results which showed only slight difference from the reduced order model and hence the complex ADAMS® model.

Kim *et al.* investigated the relationship between quarter car model component parameters and the suspension kinematic structure [7]. A complex ADAMS® model of the suspension system was used in place of an experimental setup. A double wishbone suspension was first examined. A parameter identification technique was used to build a more efficient mathematical model, called the identified model, than the nominal model (a model based on measured component data). The parameters identified using this technique replaced the sprung mass, unsprung mass, spring stiffness, shock absorber damping and tyre stiffness parameters of the nominal model in a two DOF quarter car model. The identified model better represented the response of the complex ADAMS® model than the nominal model. A complex ADAMS® model of a MacPherson strut was then built. The model parameters were the same as those used for the double wishbone ADAMS® model. The parameter identification technique was again applied and a new identified model was produced. Results showed that the identified model of the MacPherson strut differed significantly from the identified model of the double wishbone. This showed that although the suspension parameters remained the same, a change in the kinematic structure resulted in

a significant change in the parameters of the identified model. The authors termed parameters owing to the suspension structure as 'invisible' uncertainties (i.e. not shown in the component data).

Langdon developed an adaptive control method for the identification of a quarter car test rig [95]. The quarter car system (or plant) was treated as an unknown. The input to the unknown plant was also applied to an 'Adaptive Linear Combiner' which is an adaptive finite impulse response filter. The adaptive part of the filter is the time varying weight vector, which can be continuously changed to meet some performance criteria. The output of the plant is called the desired signal. The output of the adaptive filter is subtracted from the desired signal to form an error. A least mean squares algorithm uses the approximated error gradient to incrementally adjust the values of the adaptive filter weights. The model, created by this method, is purely empirical and is a finite impulse response filter that replicates the input to output relationship of the physical system. The model error was 16.9 % for the unsprung mass response and 9.9 % for the sprung mass response when the method was applied to the quarter car rig. This system identification algorthim was used as part of an adaptive control algorithm to assist in the control of the quarter car rig excitation to replicate a desired response.

Allison and Sharpe investigated the longitudinal vibrations of vehicle suspension systems [96]. A quarter car suspension system was run on a smooth rolling road at constant velocity while being subject to a sequence of longitudinal forcing frequencies in the 10–100 Hz range. A model of the tyre and suspension system was developed. The tyre model used the rigid ring model with a bristle model to represent tyre road interaction. The planer motion of the tyre hub is resisted by a spring and viscous damper in both the longitudinal and vertical directions. Measured and simulated FRF's in the longitudinal direction, after model optimisation, showed good correlation in the lower frequency ranges (<40 Hz) but it was believed that high frequency behaviour of the rig, unaccounted for in the model, served to produce discrepancies at higher frequencies.

2.5 Response only system identification

Kerschen *et al.*, in their comprehensive review of nonlinear system identification [35], discussed some key aspects which will drive the development of nonlinear sys-

tem identification in years to come. One point made by the authors is the need to move towards *in–situ* testing of structures in place of laboratory testing of representative structures. They also stated that the use of operating loads and ambient excitation is an area which merits further investigation, with the goal of reducing the dependence on measured excitation forces. This view is shared by a number of other authors including Schiehlen and Hu, who highlighted the need to identify shock absorbers under real operating conditions [78]. While Adams and Allemang stressed that system characterisation is best achieved using *in–situ* experimental characterisation procedures [59], a view shared by Bendat and Piersol when nonlinear components exist in the system [24]. Basseville argued that there is a strong industrial need for techniques extracting system models under real operating conditions [97], due to the fact that modal models obtained in a laboratory may fail to predict the correct operational system behaviour. One of the key arguments for the use of OMA in place of EMA is that when a structure is removed from its operating environment and tested under laboratory conditions, the laboratory experimental conditions can differ significantly from the real life operating conditions [29]. This allows for the identification of more realistic modal models for in–operation structures. Although the modal analysis approach remains inherently linear, in–operation techniques would allow linearisation to be carried out around the actual loading conditions and external restraints [97].

The application of OMA techniques to mechanical systems has received much attention in the past number of years. Application areas of OMA have been wide and varied, from identification of a wind turbine wing using acoustic excitation [31], to the vibro–acoustical analysis of a helicopter cabin [98], to operational identification of a machine tool dynamic parameters [99], while numerous applications have been reported for civil engineering applications; one recent and interesting analysis was presented in [100]. Möller *et al.* compared EMA and OMA of a plate structure with an electric motor attached [28]. The results showed that it was possible to extract all modes in the frequency range of interest using OMA. Peeters *et al.* presented the dynamic characterisation of a complete truck by OMA [101]. During truck development, it is common to subject the vehicle to vibration testing, in the form of either four post shaker tests or test track measurements. The authors conducted a study on the feasibility of exploiting operational data from these tests to enhance the vehicle development process. The paper compared finite element modes of a full truck with modes identified by OMA. The truck was excited using a 4 post shaker system. Only acceleration responses at 78 degrees of freedom were measured. Al-

though OMA did not identify many of the finite element model modes, it was argued that the modes identified using OMA are the modes most relevant in describing the truck in its normal operating environment.

More complex applications of OMA have been carried out in cases where the assumption of white noise as an input is clearly invalid. Brincker *et al.* [102] used OMA to test a car body in the presence of engine excitation. The response data were analysed using two different techniques: a non–parametric technique based on FDD, and a parametric technique working on the raw data in time domain, a data driven Stochastic Subspace Identification (SSI) algorithm. Both techniques identified 16 modes under 85 Hz and the result were validated by comparing the two methods. This work highlights how OMA can be used in the presence of harmonic excitations, in this case from the engine in operation. Although harmonics would be present in the response spectra, methods of identification and elimination of harmonics have been developed for use with OMA. Mohanty and Rixen presented a modified EMA parameter estimation techniques (Least Squares Complex Exponential (LSCE), Eigensystem Realisation Algorithm (ERA) and Ibrahim Time Domain (ITD)) for use with OMA in the presence of harmonic excitations [103, 104, 105]. The methods allowed the harmonic content in the measured signal to be accounted for, but all required knowledge of the harmonic frequencies. The methods were verified experimentally using a beam structure excited using multi–harmonic loads superimposed on random excitation. Accurate identification was achieved even when the harmonic content was very close to the resonant frequencies of the beam.

2.5.1 Response only vehicle suspension system identification

The identification of vehicle suspension systems in the absence of input measurements has received much less attention compared with force–response methods. Haroon, Adams and Luk presented a technique for estimating linear system parameters using nonlinear restoring forces in the absence of an input measurement [106]. The method employed a technique termed nonlinear restoring force extraction. The nonlinear restoring force was identified by fitting a hysteretic model of the form,

$$\frac{f_{nl}(\Delta\dot{x}, \Delta x)}{m_2} = \Delta\dot{x} - 2.5\Delta x \tag{2.97}$$

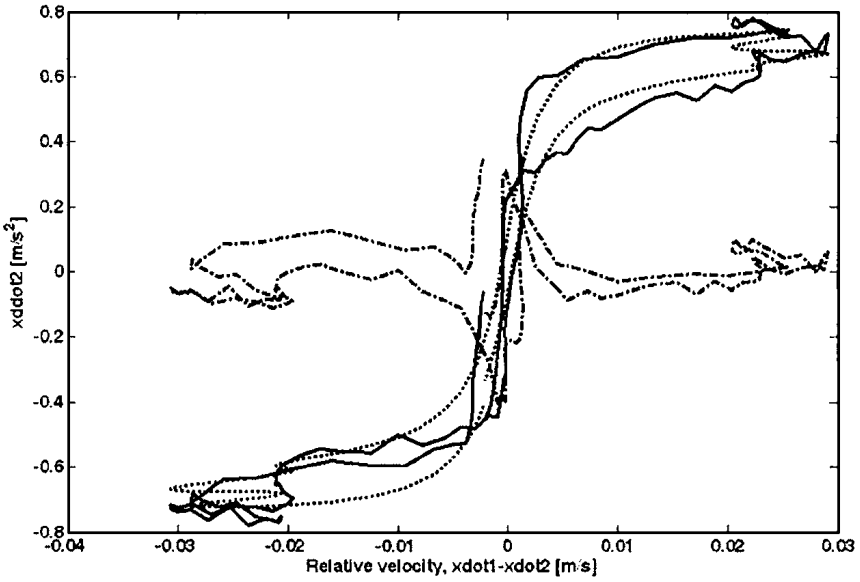

Figure 2.17: Curve fit to the nonlinear restoring force in the suspension. Nonlinear damping restoring force (——), curve fit (− − −), and error(−.−) (reproduced from [106])

$$\Delta\dot{x} = arctan\left[400(\dot{x}_1 - \dot{x}_2)\right]/2.2 \tag{2.98}$$

to the measured restoring force data. The curve fit is shown in Figure 2.17. The identified model was subtracted from the total restoring force of the system to leave an estimate of the linear restoring force. DPE was used with a boundary perturbation technique to estimate the linear system parameters from the estimated linear restoring force. The approach was applied to experimental tyre vehicle suspension system data, gathered using shaker testing on the front corner of a vehicle. Validation of the experimental results was not achieved as the analysis lacked *a priori* information about the actual mass and linear stiffness in the system. The identified mass (326.16 kg) and stiffness (79126 N/m for chirp excitation and 71021 N/m for random excitation) parameters were assumed to be 'reasonable', despite the fact that it was noted the estimated stiffness was higher than typical values for an average passenger car.

Haroon *et al.* demonstrated that nonlinear mechanical system models can be identified from experimental vehicle data in the absence of input data at the tyre patch [76]. Chirp excitation using a hydraulic shaker was applied to a front wheel of a test vehicle and the frequency and amplitude dependence of nonlinearities were characterised using restoring force methods. An output only formulation of the NIFO

parameter estimation technique was used to identify the system. Consider the equation of motion of the sprung mass of a two DOF suspension model in the frequency domain (ignoring damping),

$$\left(-m_s\omega^2 + k_2\right) Y_2(\omega) = k_2 Y_1(\omega) + \mu_1 Y_{n1}(\omega) + \mu_2 Y_{n2}(\omega) \tag{2.99}$$

where Y_1 and Y_2 are the Fourier Transforms of the unsprung and sprung mass displacements, Y_{n1} and Y_{n2} are the Fourier Transforms of two particular restoring forces of interest and μ_1 and μ_2 are the corresponding coefficients determining the nonlinear weighting. Rearranging equation 2.99 and noting that the transmissibility between the unsprung mass and sprung mass of the underlying linear two DOF system, T_{21}, is equal to,

$$T_{21} = \frac{k_2}{(-m_s\omega^2 + k_2)} \tag{2.100}$$

leads to,

$$Y_2(\omega) = \left[\begin{array}{ccc} T_{21}(\omega) & \frac{\mu_1}{k_2} T_{21}(\omega) & \frac{\mu_2}{k_2} T_{21}(\omega) \end{array} \right] \left[\begin{array}{c} Y_1(\omega) \\ Y_{n1}(\omega) \\ Y_{n2}(\omega) \end{array} \right]. \tag{2.101}$$

Least squares parameter estimation is used to calculate the three coefficient functions in the row matrix for each frequency point. The approach was applied to the experimental identification of a single wheel of a full vehicle. Sine sweep excitation was used to characterise the nonlinearities in the system. Changes in characteristic and work diagrams for varying input frequency and amplitude were examined. NIFO was applied to random data for varying input amplitude ranging from 0.5–7.0 mm RMS displacements at the tyre patch. Two nonlinearities were included, coulomb friction damping and backlash in stiffness. As they were dominant in different operating ranges, NIFO was applied to each separately. The backlash describing function and NIFO results are shown in Figure 2.18. The NIFO technique provided good estimates of the linear transmissibility functions in each case (the linear transmissibility was assumed to be equal to the transmissibility at the lowest excitation level).

Three different nonlinear system identification approaches were applied to experimental test data from the front right suspension of a full vehicle in [70]. The system was excited with a swept sine using a hydraulic shaker. Acceleration measurements were taken at the suspension knuckle and the top of the shock absorber. First a visualisation of the nonlinearity in the shock absorber was obtained using RFS meth-

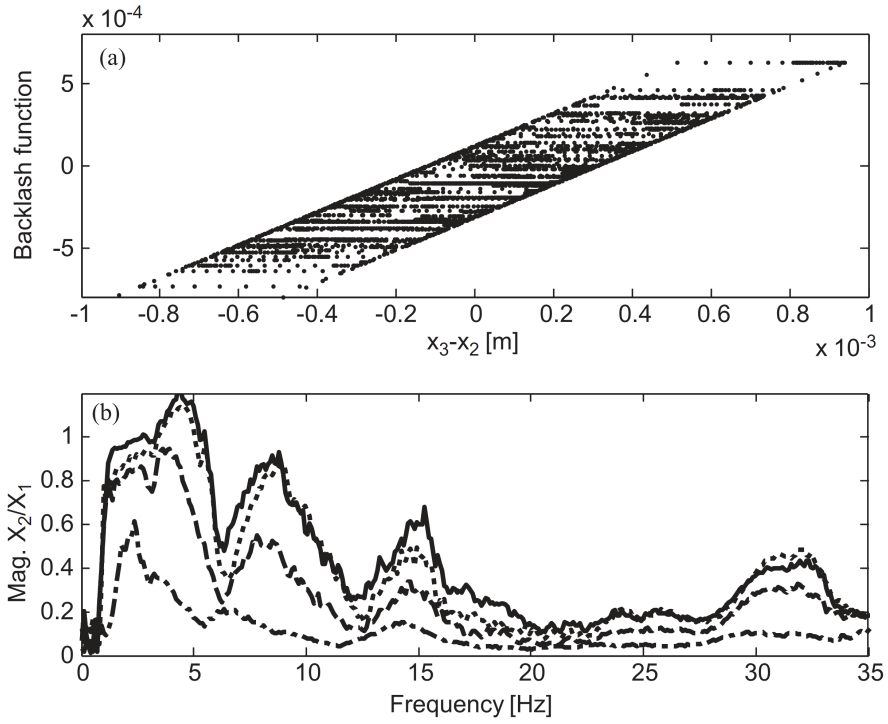

Figure 2.18: (a) Backlash describing function between the spindle and body in the strut used in NIFO parameter estimation procedure and (b) magnitudes of measured transmissibility functions between the spindle and body for: (. . .), 0.5mm; (− − −), 1.0mm; and (−.−), 7.0mm input levels with the NIFO estimate (——) of a near zero level input using the 1.0mm data. (reproduced from [76])

ods. The output only formulation of the NIFO technique was then applied to the problem. This approach allowed the frequency dependence of the shock absorber to be captured. It was noted that the method required specific knowledge of the nonlinearity form before the identification step. Only reasonable success was achieved with this approach and no actual parameters estimates were reported. Errors were attributed to unidentified nonlinearities in the system. The final approach aimed to average out frequency effects using random excitation. Linear and nonlinear optimisation routines were used to fit a ninth order polynomial model and a hyperbolic tangent form (equation 2.96) to the force–velocity curve. Both models gave accurate results but the hyperbolic tangent model has the advantage of giving linear damping at high piston velocities and is, therefore, unconditionally stable. The output only NIFO technique was also implemented by Hickey *et al.* [74]. Characteristic and work diagrams were used to characterise the nonlinearities in a vehicle suspension system. Although actual parameter estimates were obtained using the NIFO approach for simulated data, the authors stopped short of reporting actual parameters in the experimental case. Again errors were attributed to unidentified nonlinearities.

McGee *et al.* proposed a frequency domain approach for the identification of nonlinearities in vehicle suspension systems in the absence of a known input force [107]. The authors used transmissibility functions and ordinary coherence functions between the sprung and unsprung masses to develop the method. In systems with polynomial nonlinearities, such as quadratic or cubic stiffness, additional frequency response components due to nonlinear interactions are present at frequencies other than the excitation frequencies. These additional frequencies are often referred to as harmonic distortion. The authors identified the harmonic distortion frequencies for different polynomial nonlinearities. They examined the transmissibility functions and ordinary coherence functions of quarter car models with polynomial nonlinearities. Nonlinear frequency permutations, which created drops in the ordinary coherence function served to characterize the associated nonlinearities. Experimental validation was carried out using two methods. The first involved the use of a hydraulic shaker table under one wheel of a mid–sized vehicle. This setup allowed for the measurement of the input force. Quadratic stiffness, cubic stiffness and coulomb friction were identified using the transmissibility function, frequency response function and ordinary coherence functions produced. The second method used on–road testing at three different driving speeds on a rough road and an urban highway. The nonlinearities were again identified using autospectra, transmissibility functions and ordinary coherence functions. Figure 2.19 shows transmissibility and coherence functions, between sprung mass response and unsprung mass response, for a full vehicle road test at 35 mph. The sprung (f_1) and unsprung mass (f_2) resonances were identified at 1.4 Hz and 11.5–13.5 Hz, respectively. The drops in coherence and the associated nonlinearitites are listed in Table 2.1. This work successfully characterised the nonlinearities in a vehicle suspension system but stopped short of parameter estimation.

Operational damage detection is an area which has been pursued by a small number of authors. Haroon and Adams used response only measurement to detect and track the progress of mechanical damage in vehicle suspension components [75]. The authors discussed the merits of data interrogation methodologies to identify loads and faults in suspension systems, leading to reduced maintenance costs and future development of more durable suspension systems. RFS's were used to characterise the frequency dependence of nonlinear internal loads in the system, while changes in the restoring forces with the onset and progression of damage were used for damage detection. Swept sine excitation was provided by hydraulic actuators over the 0–15 Hz range. The method was demonstrated using full vehicle and quarter car tests

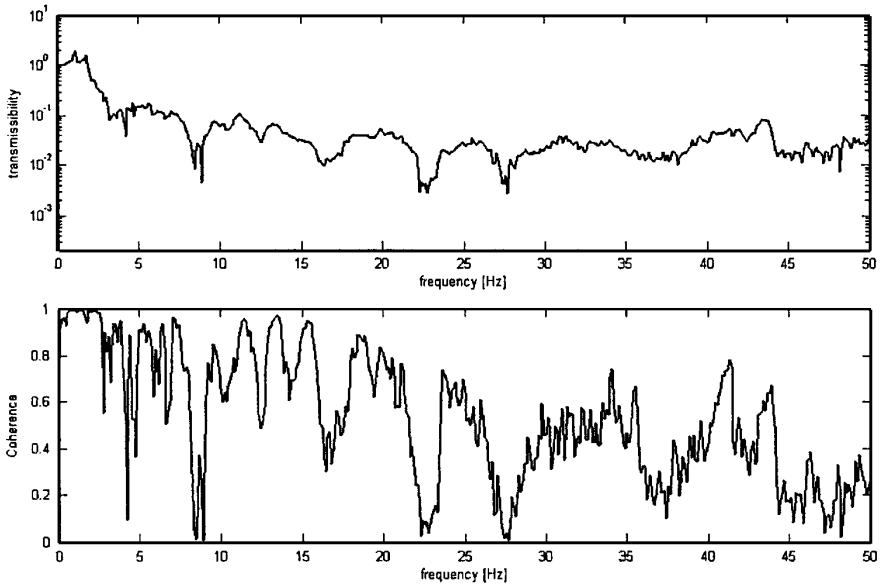

Figure 2.19: Transmissibility and coherence function between sprung mass response and unsprung mass response for a vehicle speed of 35 mph on an urban highway (reproduced from [107])

Frequency [Hz]	Description	Nonlinearity
14.2	Frequency Permutation, $f_1 + f_2$	Quadratic stiffness
16.2	Frequency Permutation, $f_2 + 2f_1$	Cubic stiffness in suspension
22.5	Frequency Permutation, $2f_2 - f_1$	Cubic stiffness in suspension
27.5	Frequency Permutation, $2f_2 + f_1$	Cubic stiffness in suspension
22–50	Consistently worsening trend in coherence	Coulomb friction in suspension

Table 2.1: Drops in coherence and the associated nonlinearities for a vehicle speed of 35 mph on an urban highway (reproduced from [107])

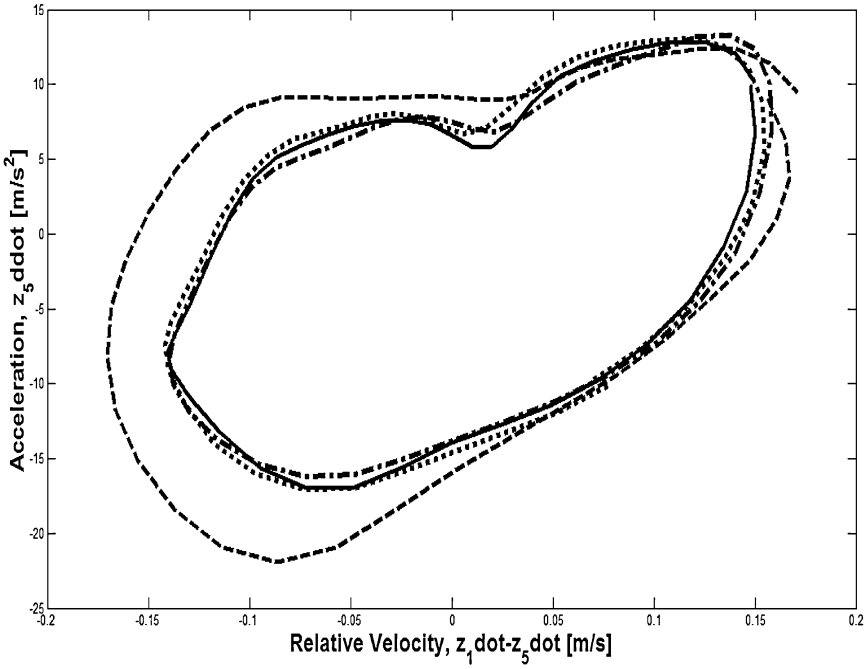

Figure 2.20: Change in internal damping force of the sway bar link with usage (34 Hz); Baseline 1 (——), baseline 2 (−.−.−), after 10 hours of testing (− − −) and after 24 hours of idle time (. . .) (reproduced from [108])

with different damage types. In related studies [108, 109, 110] the authors used RFS's and transmissibility measurements across a damaged automotive component to develop empirical damage evolution models. Although a combination of full vehicle suspension testing and more traditional isolated component testing was used, the input forces were not measured during data acquisition. One interesting test conducted during this work involved the examination of the change in internal restoring force in the vertical damping of a full vehicle sway bar link. A baseline restoring force was calculated before the system was excited using sinusoidal excitation for 10 hours. Data were collected at the end of the test and again after the system sat idle for 24 hours. The results are shown in Figure 2.20. The results suggest that under continuous operation the restoring force in the system changes. This result indicates that even the most accurate model of such a system developed in isolation may not accurately represent its actual behaviour during prolonged operation.

The provision of information to support condition based maintenance in place of calender based maintenance for rail carriages was examined in [111]. This work focused on monitoring three parameter changes indicative of common faults in railway vehicles (wheel conicity and damper condition). A Rao–Blackwellized particle filter based method was used for parameter estimation. Particle filtering is a simulation

based method for general nonlinear non–Gaussian state estimation, which attempts to approximate the complete probability density function of the state to be estimated. Only acceleration and gyroscopic measurements were used to implement the method. The method was found to give excellent results in simulations when the rail track roughness was known, but parameter estimates related to wheel condition were significantly biased when the track roughness was unknown and required estimation. Experimental tests were found to give reasonable results for the damping parameters although the parameter estimates related to wheel condition were again significantly biased.

A sensing methodology to determine automotive damper condition under normal operation has been presented in [112, 113]. The authors noted in their literature review that no precise method exists to continuously evaluate dampers under normal operating conditions. Two approaches were taken, analysis of the suspension system as a whole and a study of the damper internal working principles. The former used acceleration transmissibilities across the shock absorber to assess suspension system condition, the latter used measurements of the damper internal chamber pressure, temperature and wheel acceleration to determine damper condition. Both methods were successfully validated using operational vehicle testing.

Rozyn and Zhang estimated the sprung mass of a simulated vehicle driven over an unknown and unmeasured road profile [114]. The method used measured response only, from three accelerometers mounted on the sprung mass of the vehicle. Free decay response of the system were computed using auto–correlation functions while the vehicle was in motion, allowing for the use of modal analysis techniques. The equivalent linear stiffness of the suspension system is required to implement the method. Simulation results using a three DOF vehicle model showed relative errors in the estimated mass and inertial parameters of less than 6 %. Although the technique showed good results for simulated data, no experimental validation of the method was carried out.

Best identified a vehicle tyre model using GPS (Global Positioning System) and inertial measurements during vehicle operation [115]. Instrumented vehicles performed 10 step steer events at constant velocities. The authors used an extended Kalman filter for system identification, to derive individual load dependent tyre models. Results showed successful tyre model identification.

Hermans and Van Der Auweraer used OMA methods to solve a noise problem in a

passenger car [116]. A booming interior noise problem occurred at a frequency close to 80 Hz. Operational testing was carried out on a rough asphalt road at 50 km/hr along with a detailed laboratory modal test. EMA identified a bending mode in the rear suspension at 74.6 Hz and this compared favourably with a mode identified at 71.9 Hz using OMA.

The fact that the input force was not required for system identification in the works outline above, allowed *in–situ* testing of the suspension components to be used in all cases. Schiehlen and Hu highlighted the need to identify characteristics of vehicle shock absorbers under real conditions [78]. They developed a piecewise linear model of a shock absorber experimentally tested using stochastic models of road roughness. The identification was repeated using stepped sine excitation. It was found that the stepped sine excitation produced smaller errors when compared with measured data, but the authors stressed that these parameters are not optimal in the real operating environment of the shock absorber. They noted that experiments and simulations in the real environment are very important for the parameter identification of a model. The implementation of operational identification methods for vehicle suspension systems has become even more achievable in recent years with the increase in electronic diagnosis equipment in vehicles [112]. The instrumentation and sensing systems required to implement system identification method already exist in modern vehicles, load sensors form part of braking distribution systems [113], while accelerometers are a key component in vehicle stability, crash sensing and adaptive suspension systems [117].

2.6 Vehicle suspension system experimental test and simulation

This literature review to date has presented system identification techniques applied to linear and nonlinear systems. Part of the review focused on the identification of vehicle suspension systems. System experimental test and simulation play an important part in the identification process. This section presents a review of the experimental test and simulation of suspension systems. Current methods of conducting such experimental testing are outlined along with a description of hardware setups currently in use. This will lead to a discussion on suspension simulation methods. Popular simulation methods used in research are compared.

2.6.1 Suspension experimental testing

The goals of and approach to suspension experimental testing depend on the nature of the industry for which the test is being conducted. For vehicle manufacturers Noise, Vibration and Harshness (NVH) along with durability would be the major concerns. For racing or performance applications vehicle stability and handling would be more important than NVH. For all applications, experimental testing provides a method of tuning and testing suspension setups to specific applications.

Multi post hydraulic test rigs

Vehicle manufacturers use multi–post testing systems. A multi–post testing system is an experimental device that allows the simulation/recreation of driving conditions (*e.g.*, racing track or test track conditions) in the controlled environment of the laboratory. A four post system, for example, consists of a servo–hydraulic actuator (post) under each vehicle wheel. The unrestrained vehicle is excited through its tyres in order to determine some of the dynamic characteristics of the vehicle, its suspension and its tyres. Inputs are controlled accurately and are repeatable. This feature enables the effect of small changes to the vehicle and its suspension to be quantified with precision. Seven and eight post testing rigs are used by racing teams or when aerodynamics effects need to be included in simulations. Aeroload actuators become necessary to tune the suspension at the correct ride height by including aerodynamic effects. Input data for multi–post test systems are gathered by driving instrumented vehicle around a test track. The response of the vehicle is then replicated on the multi–post system using Iterative Control System (ICS) software [118]. This software allows the engineer to play back a track profile on the multi–post system and assess the effect of suspension changes.

Multi–post test rigs are expensive to install, run and maintain. The rigs are multiple input/multiple output systems which require a high degree of control knowledge and understanding to use properly [95]. Multi–post test rigs are not very popular in the literature of suspension research. A much more popular experimental testing setup is the quarter car test rig, which will now be examined.

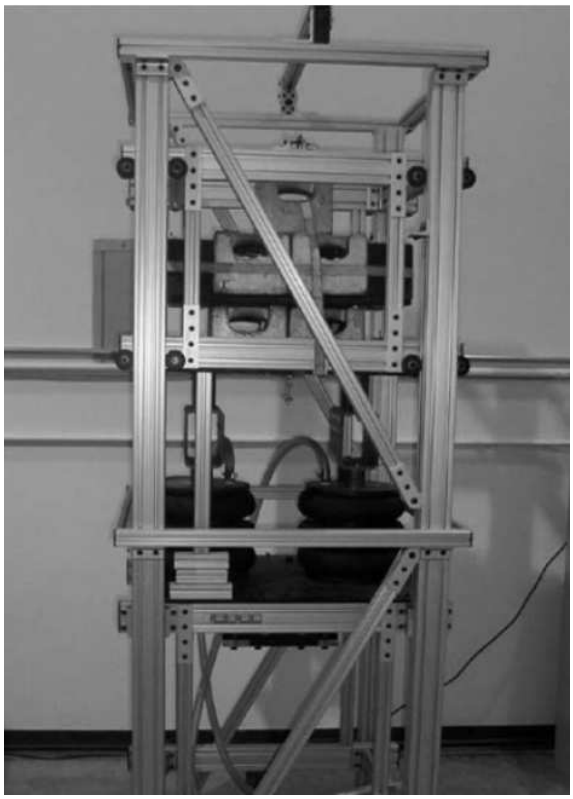

Figure 2.21: Paré Quarter Car Test Rig (reproduced from [119])

Quarter car test rigs

Quarter car test rigs are designed to provide realistic suspension movement whilst eliminating the need to have a full vehicle present for testing purposes. Quarter car test rigs vary in size, shape and complexity. The primary experimental purpose of a rig determines its design. Rigs designed for testing tyre vibration differ significantly from those designed to test semi–active shock absorbers. The following section highlights the different types of quarter car rigs used in research. It has been noted that very few applications are presented in the literature referring to full suspension indoor testing [92].

Excitation is normally provided by hydraulic shaking systems or rolling roads. Some test rigs simplify or eliminate complex components of suspension systems. Rigs employing hydraulic shaker excitation sometimes eliminate the wheel and tyre from the system. An example of this type of rig can be seen in Figure 2.21. The rig was designed by Paré [119] and used in research into semi–active control methods by Ahmadian and Paré [120] and Ahmadian, Goncalves and Sandu [121]. The rig consisted of a sprung mass constrained to move in the vertical direction using eight

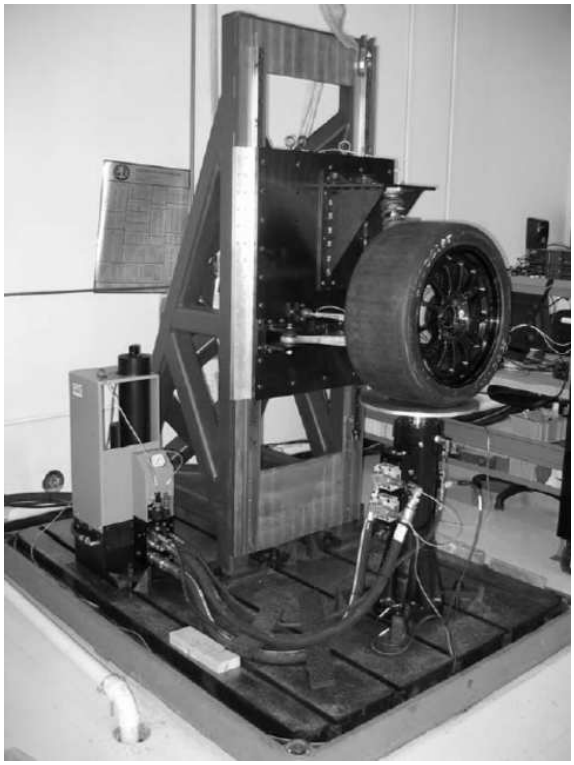

Figure 2.22: Langdon Quarter Car Test Rig (reproduced from [95])

linear bushings. This was connected to the unsprung mass using two air springs in parallel. Excitation was provided to the unsprung mass using a hydraulic shaking system through eight rubber mounts designed to have a stiffness close to that of a tyre. This type of rig is primarily used for active and semi–active control system development and validation. In this type of testing, the performance metric would be the acceleration of the sprung mass as this is directly related to the force experienced by passengers. For this reason the inclusion of the tyre is not critical, as the primary concern is the transmission of vibration between the unsprung mass and the sprung mass. Further examples of similar rig setups can be found in references [96, 122]. This type of rig does not include the effects of suspension geometry. No suspension arms are used in the rig setup. Both the sprung and unsprung masses are constrained to move in the vertical direction. The effects of rolling tyre vibrations cannot be examined with this type of rig.

Langdon designed a tyre coupled quarter car test rig [95]. The rig was used in research by Ziegenmeyer, to estimate the disturbance inputs to the tyre [123]. This rig, shown in Figure 2.22, consisted of a full suspension system, including wheel and tyre, from a racing car. Excitation is provided to the tyre patch using a hydraulic shaker. This type of rig allows for the use of an actual suspension system with

the flexibility of a hydraulic excitation system. The suspension arm and shock absorber are attached to a rigid metal plate which is constrained to move in the vertical direction using two linear guides. The support structure and base were tested to ensure no resonances of these structures existed in the frequency range of interest of the study. The rig was used to develop a control algorithm to determine the excitation required to replicate a response recorded during a road test. Tyre coupled hydraulic rigs are the most popular in literature and many different types and design variations exist [124, 125, 126, 127, 128, 129]. Another popular approach is to use a hydraulic actuator on one corner of a full vehicle [70, 75, 76, 106]. A wide range of excitations can be used with this type of test setup. The excitations are repeatable and accurate. The effects of the rolling tyre are not included with this type of system. The system can only be excited in the direction of the hydraulic shaker. In reality, when the tyre encounters a road disturbance it is excited in the vertical, transverse and fore–aft directions.

A 'rolling road' type quarter car rig was used by Giorgetta *et al.* [130] and Gobbi *et al.* [90, 92, 131]. The rig, based at the Laboratory for the Safety of Transport at the Politecnico di Milano, consists of a 2.6 m diameter steel drum which provides a running contact surface for vehicle wheels. The drum is driven by an electric motor. The suspension arm and shock absorber are attached to a sled system which is free to move in the vertical direction on two cylindrical rails. The rig can be seen in Figure 2.23. It is primarily used to test suspension vibration performance when running over cleats on the drum surface. The excitation provided to the system with this type of rig will always be periodic. It does, however, allow for the effect of the rolling tyre to be included in the analysis. This is very applicable in NVH studies as tyres have been shown to be the leading cause of vehicle noise above 80 km/hr [132]. Another advantage of this type of rig is that realistic inputs are provided to the system. As the rig passes over a cleat on the drum surface it is excited in the vertical, transverse and fore–aft directions. Figure 2.24 shows results from a rolling road rig mapping the wheel displacement in the vertical and fore aft directions. This is an important feature when examining the dynamics of the unsprung mass in more than one plane. Allison and Sharp used a rolling road type rig to investigate suspension longitudinal vibrations in vehicle suspensions [96]. Haga developed half car rolling road test rig. The rig consisted of two rolling drums which provided the input to a full rear suspension and axle assembly of a passenger car [133].

Figure 2.23: Ruotavia quarter car test rig (reproduced from [130])

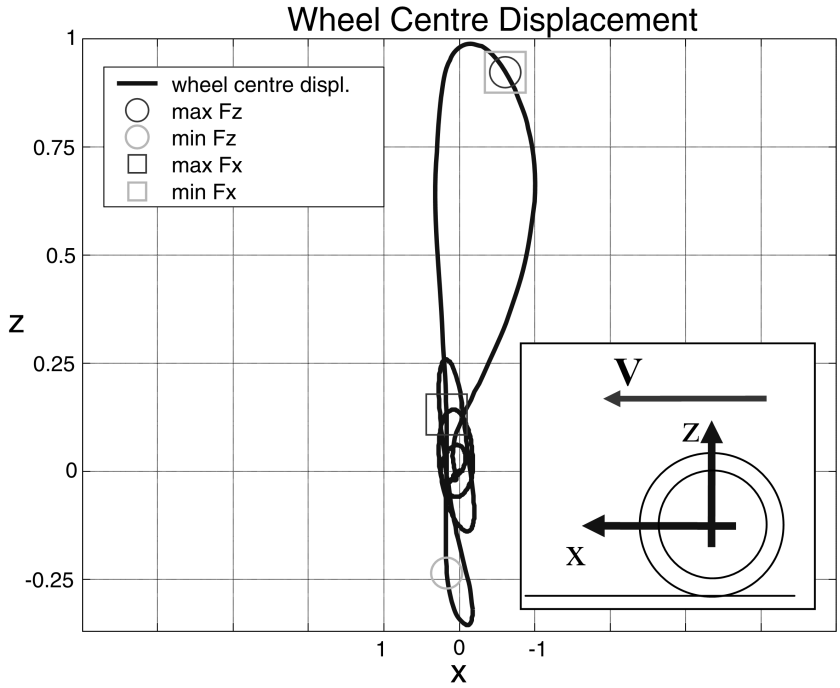

Figure 2.24: Non–dimensional measured displacement of the wheel centre (reproduced from [92])

2.6.2 Suspension simulation

Prior to the widespread use of computer technology, for complex systems, the only model at a design engineers disposal was a replica of the real thing. For complex systems nowadays the model is almost certain to be a mathematical model. The mathematical modelling of a dynamic system is the formulation of mathematical relationships which describe all the features of the system that are considered essential [134]. Features which are considered essential depend on the purpose of the model and also their effect on the behaviour of the system being modelled. For suspension performance analysis, a model to evaluate ride comfort may only take account of the vertical acceleration of the sprung mass, whereas an in–depth handling model may take wheel and tyre movement and vibration in the vertical, transverse and fore–aft directions into account.

In the literature, the analytical quarter car model is said to be the most widely used suspension system model [7, 94, 135, 136]. With the current trend of using four independent suspension systems on a single vehicle, the linear quarter car model offers quite a reasonable representation of the actual suspension system [7, 94, 137].

Quarter car model

A diagram of the classic linear two degree of freedom quarter car model can be seen in Figure 2.25. The model consists of a sprung mass which represents the mass of a quarter of the vehicle chassis and the unsprung mass which represents the mass of a single wheel, tyre, shock absorber and suspension knuckle. The sprung and unsprung masses are connected using linear spring and viscous damping elements to represent the stiffness and damping of the shock absorber. The tyre is modelled as a linear spring in parallel with a viscous damper (point contact tyre model). Despite its simplicity, the linear quarter car model is very popular in the literature of suspension research. It has for a long time been the *par excellence* model used in suspension design [138]. It has the following advantages over more complex models [139]:

- Few design parameters;
- Few performance parameters;

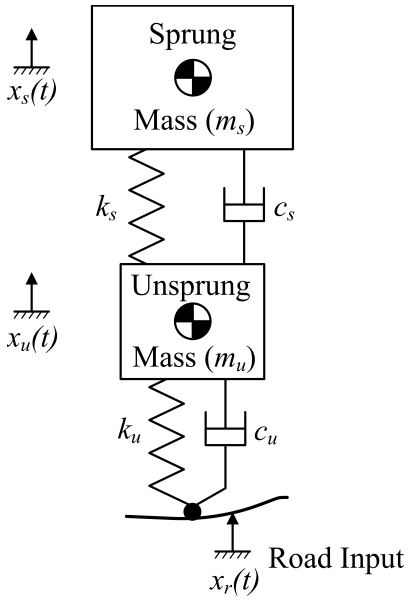

Figure 2.25: Two DOF linear quarter car model

- The relationship between design and performance is easily understood;
- Single input system, leading to ease of computation of performance;
- Ease of application of control theory to derive control laws.

It does not, however, give any representation of the geometrical effects of having four wheels and offers no possibility of studying the excitation of vehicle body roll and pitch motions. Two lesser used analytical models, the four degree of freedom half car model and seven degree of freedom full car model are used when these parameters are of interest [4, 114, 140, 141].

Quarter car model accuracy

Conflicting views were found in the literature on the accuracy of the linear quarter car model. Despite its widespread use, little dedicated research was found on the validity of the relatively simple model in predicting the movement of complex suspension systems.

A number of authors have cast doubts over the effectiveness of the linear quarter car model in predicting suspension movement in certain circumstances. Kim and Ro wrote that the two mass quarter car model is effective in predicting the two

dominant modes, sprung mass bouncing and wheel hopping [94]. They did, however, have some reservations about the component data used in such simulations. The authors constructed a complex multibody model and used it to produce a two degree of freedom reduced order model. They estimated the component parameters for the reduced order model and found them to be very far from the measured component data. They also referred to work carried out by Kim *et al.* [7], in which it was shown that suspension kinematic structure has an influence on the effectiveness of the simple linear quarter car model. Türkay and Akçay used a linear quarter car model to study the response of a vehicle to random road inputs [142]. Their results showed how imprecise knowledge of the excitation road spectra would impact subsequent active suspension design. They recognised that the linear quarter car model is 'too simple for performing a comprehensive analysis of the ride motion of the vehicle' but also noted that significant insight into the problem was obtained using this simple model. Etman *et al.* compared the optimum parameters of a stroke dependent truck damper for both a linear quarter car model of the front side of a truck and a 34 degree of freedom multibody full truck model [143]. It was concluded that the step from the quarter car model to the full scale model was 'pretty large', due to the fact that a great deal of the dynamic behaviour of the truck was not included in the quarter car model. They did, however, note that a reasonable resemblance of the global response behaviour was present between the two models.

A popular view among authors is that the linear quarter car model is used due to its simplicity and that the qualitative information it provides in the initial stages of design, outweighs the inaccuracy [138, 139, 144, 145]. Elmadany and Abduljabbar stated that it captures the most basic features of the real vehicle problem. They followed this by saying that when a detailed model of vehicle motion is required, more elaborate models (two or three dimensional models) must be used which take account of features omitted from the quarter car model [146]. An important property of the quarter car model is that it properly represents the problem of controlling wheel load variations and contains suspension system forces which are properly applied between unsprung and sprung masses [139]. This fact has given rise to the widespread use of quarter car models in the development of active and semi–active suspension control strategies.

Tyre modelling

The pneumatic tyre serves an important purpose in suspension systems with respect to the isolation of road induced vibration. There are a variety of tyre models in the literature with different levels of complexity. Tyre model complexity is determined by the frequency range of interest of the study [147].

In the low to intermediate frequency range the most widely used and simple tyre model is the point contact model [148, 149]. It consists of a linear spring in parallel with a linear viscous damper. This is considered to give relatively good approximations of tyre forces generated when a tyre is in contact with small amplitude, long wavelength road profiles. The enveloping behaviour of tyres as they roll over small obstacles cannot be accounted for in such a model as it does not consider the tyre geometry and elasticity in the contact zone. This model, although quite crude, is acceptable for ride analysis [138]. More complex tyre models are required for Noise, Vibration and Harshness (NVH) investigations [147, 149] and for handling, braking and traction studies. Such models must account for road tyre adhesion (both longitudinal and lateral) as well as rolling friction [138].

Conflicting views were also found on the issue of tyre damping in quarter car models. The view that tyre damping is typically small, and is ,therefore, insignificant compared with shock absorber damping is shared by a number of authors [141, 150, 151, 152]. The placement of tyre damping in the quarter car model has also been given as a reason to neglect its effects [139]. It was noted in [153] that tyre damping is often neglected in suspension simulations due to the fact that it is difficult to estimate.

On the other hand, some authors argue that the role of tyre damping in vehicle dynamics is overshadowed by factors which are presumed to be more important [154, 155]. It is often neglected, even in view of the fact that the tyre damping ratio is generally accepted to be between 0.03 and 0.10, depending on tyre size and type [156]. Levit and Zorka published a paper on the influence of tyre damping in quarter car active suspension models [155]. The authors urged that considerable care be taken in setting tyre damping to zero when developing quarter car models for control applications. Non–zero tyre damping was shown to couple the motions of the sprung and unsprung masses at all frequencies and lead to substantially different transfer functions for RMS body acceleration. Türkay and Akçay studied the effect

of tyre damping on the performance limitations of quarter car active suspension models subject to random road excitation. Results showed that tyre damping can have a significant influence on the closed loop performance of the active suspension system [156]. Maher and Young investigated the effect of tyre damping on the accuracy of the quarter car model subject to sinusoidal excitation [157]. Simulation results were compared with measured results from a quarter car test rig. Isolated testing of the quarter car rig shock absorber, spring and tyre provided the simulation parameters. Tyre damping was shown to lower the magnitude of the peaks in the unsprung mass acceleration and was also found to increase the accuracy of the simulation when compared with measured results.

Shock absorber modelling

A shock absorber is one of the most important elements in a suspension system. It is a complex nonlinear element [158, 159]. Duym highlighted that attempts in the past to simulate vehicle behaviour showed poor correlation with measured values due to the fact that shock absorbers were modelled as pure linear elements [1]. He stated that linear modelling of shock absorbers have been rejected and replaced by a two–slope or three–slope model which represents the most important nonlinearity in the characteristic diagram. Duym, however, also noted that the presence of hysteresis in the characteristic diagram can falsify simulation results obtained using the two–slope model. Basso noted that damping force is a nonlinear function of many parameters and its modelling is extremely difficult [82]. He stated that due to these modelling difficulties it is often preferable to characterise the shock absorber restoring force, not only in terms of damping force, but also in terms of internal friction force and elastic effects due to the possible presence of a spring.

Shock absorber modelling has been the focus of much research in the last two decades. An exhaustive review of modelling techniques can be found in [1]. Models can generally be divided into three categories, physical, rheological and non–parametric. Physical models are developed from knowledge of the internal structure of the shock. They are accurate over a wide range of operating conditions. They are, however, difficult to develop and most require a large number of parameters which can only be determined using expensive in–depth testing of the shock. Physical models also tend to be computationally intensive and are not suited to dynamic simulations. They have also seen limited application to the analysis of vehicle ride

and handling [160].

Rheological models are developed using a collection of elements such as dash pots, springs, friction and backlash. They can be tedious to develop but provide a model which has a broad operating range. They can be computationally intensive as with physical models [77]. Non–parametric models are developed from measured quantities such as force and velocity. They are easier to develop than the methods above but can only describe the shock absorber in a limited range of operation. For dynamic simulations, the force–velocity relationship of the suspension damper can be approximated by a sequence of connected straight line segments. The majority of analysis involving vehicle dynamics, road holding, handling and control employ either linear or piecewise linear and symmetric damping properties [160]. The contribution of hysteresis, asymmetry and gas spring effect are often assumed negligible [160].

Spring modelling

A helical spring such as that found in an automobile are often treated as simple massless force elements. Lee and Thompson stated that helical springs typically used in automotive suspension systems can be treated as massless force elements at low frequencies (below 40 Hz). In the same paper the authors stated that above about 40 Hz the dynamic stiffness is found to increase sharply due to internal resonance [161]. This highlights the fact that the purpose of the suspension model will determine the type of spring model to be used. Many dynamic spring models have been developed; most are complex, taking lateral and shear deformations of the wire into account. The equations which govern the dynamics of helical springs become twelve simultaneously partial differential equations containing inertial terms which are difficult to solve. An in–depth review of the development of helical spring modelling theory can be found in [161]. Verros *et al.* noted that the restoring force of a car suspension exhibits nonlinear characteristics. They modelled the spring as a trilinear element and stated that this is a sufficiently accurate representation of the spring characteristic [144].

2.7 Summary

This literature review provides a summary of well established identification methods and current trends in nonlinear system identification. It is clear that the identification of nonlinear systems poses a significant challenge, due to their individualistic nature and the lack of general analysis methods which can be applied to all systems in all cases.

Vehicle suspension systems are known to be highly nonlinear [70]. A wide variety of identification procedures have been applied to this identification problem, mostly using traditional force–response identification methods. The identification of vehicle suspension systems in the absence of input measurements has received much less attention among the research community. Numerous works focused on detection of changing suspension parameters due to wear or damage [109, 111, 112, 113], others characterised the nonlinearities in suspension system [107], but neither approach provided estimates of actual parameter values. The work of Haroon *et al.* [106] estimated actual suspension parameters, but a lack of *a priori* knowledge of the system under test prevented a thorough validation of the method.

This investigation will approach the problem of operational vehicle suspension system identification from a new angle. A vehicle suspension test rig will be designed to facilitate laboratory experimental testing (Chapter 3). A traditional force–response approach will be used to identify the individual components of the suspension system. A simulation of the suspension rig will be developed and validated using measured experimental data from the rig (Chapter 4). Successful identification of the quarter car test rig using traditional methods will provide the foundation to pursue the operational identification of the system (Chapter 5). Operational data in the form of acceleration measurements will be used for this purpose. This end–to–end approach to the operational identification of vehicle suspension systems will provide a structured approach to the problem using a combination of focused experimental design, well established force–response testing methods, vehicle suspension experimental testing and simulation.

Chapter 3

Experimental design

The importance of experimental testing and simulation to the system identification process is highlighted in the literature review (Chapter 2). The design and development of both the experimental testing set–up and simulation set–up for this investigation is outlined here. The chapter is divided into two sections. Firstly the experimental testing set–up design and development is described in Section 3.1. The experimental design focuses around the development of a vehicle suspension test rig. The rig is designed to facilitate the end–to–end approach to operational suspension identification, proposed in the literature review. The data acquisition and signal processing hardware and software are also described. Section 3.2 examines the suspension simulation development and data visualisation. The development of a quarter car experimental test and simulation analysis tool, or Quarter car Analysis Tool (QcAT), is detailed in this section.

3.1 Experimental test development

The popularity of quarter car test rigs for suspension system experimental test and analysis, was highlighted in the literature review (§ 2.6.1). It was noted that the goals of the proposed testing dictates the overall rig design. This investigation aims to replicate the case of on–road full vehicle testing. Therefore, to provide the most realistic excitation (multi–directional) and to include the effects of a rolling tyre, a rolling road type quarter car rig is developed.

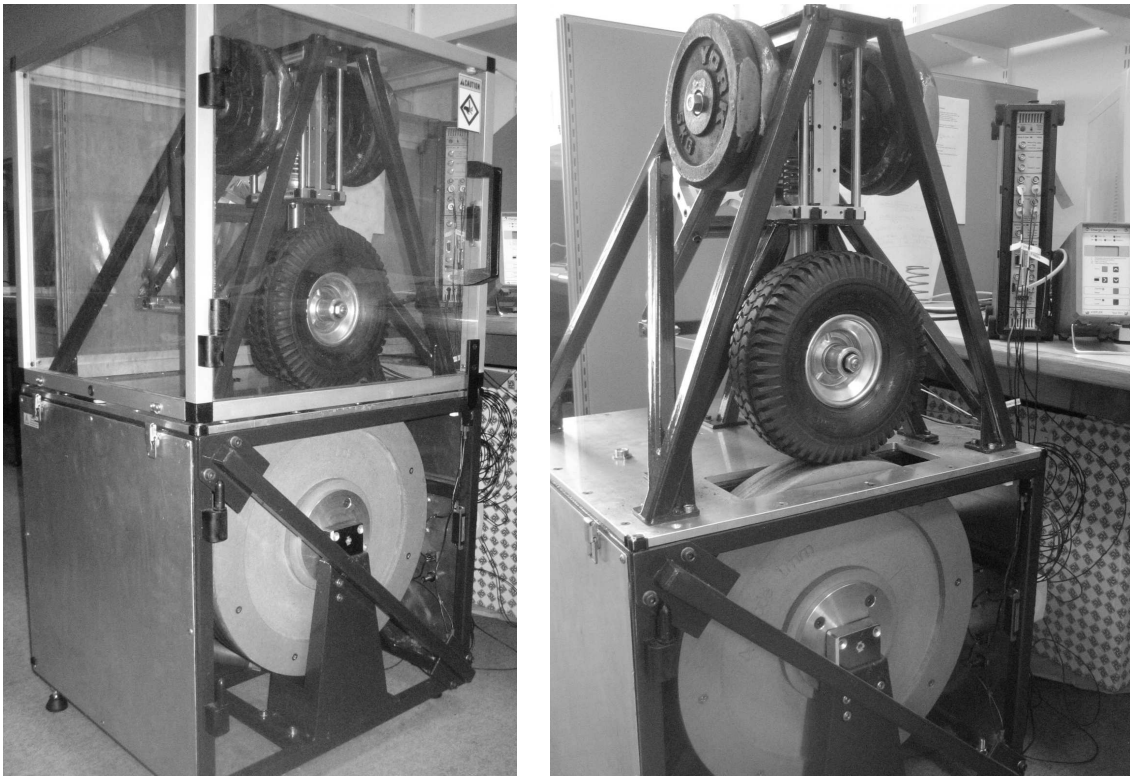

(a) Complete test rig (b) Rig with safety cover removed

Figure 3.1: Quarter car suspension experimental test rig

3.1.1 Quarter car test rig

Figures 3.1 shows the experimental test rig purpose built for this research. The rig is designed to mimic a MacPherson Strut type car suspension (engineering drawings showing dimensions of the assembled rig can be found in Appendix F). It has two main parts; the suspension system and the suspension support structure. The suspension system (Figure 3.2) consists of a 260 mm diameter tyre and steel wheel rim. The wheel is mounted on a 12 mm diameter stub axle supported by the suspension hub. The hub is attached to a link representing the vehicle chassis (chassis link) using either a dual horizontal link set–up or an A–arm (The suspension hub and horizontal links are shown in Figure 3.3a). The rig has interchangeable steel and rubber bushings at the A–arm to chassis link connection points. A shock absorber connects the suspension hub to the sprung mass. The shock absorber is an air damper unit (Festo® pneumatic cylinder, model number DSNU–PPV–A) with coil–over spring and is mounted vertically. Due to the relatively low damping requirements of the rig, commercially available car and motorcycle shock absorbers are unsuitable for this application. Flow control valves are placed on the damper

Figure 3.2: CAD drawings of the quarter car suspension experimental test rig showing the suspension system

inlet/outlet ports. Control of the air flow in to and out of the cylinder allows the characteristics of the damper to be adjusted.

The suspension system support structure consists of a base constructed of 25 mm mild steel square section to provide a rigid base for the suspension system. A dual truss support structure is mounted to the rig base. It supports parallel THK® HRW21 precision linear guides as shown in Figure 3.3b. The sprung mass is constrained to one degree of freedom (vertical) using this guide system, in a similar manner to other rigs detailed in the literature review [92, 95, 119]. The base also houses the motor, motor controller, cams and gearing system. The motor is a CMG® SLA 71B–4 three phase electric motor (Figure 3.3c). The motor is run using a Hitachi® SJ200 Inverter. Motor speed is controlled and monitored using a feedback control system implemented using a National Instruments® USB–6009 multifunction I/O module and Matlab® control software. The motor speed is monitored using a Kübler® type 2400 rotary encoder (Figure 3.3c). The encoder has a resolution of 500 pulses per revolution and it also has 1 pulse per revolution home signal. The encoder signal is acquired using the USB–6009 at a rate of 48 kHz. The home signal pulse is used to correlate time series measurements performed at the same cam and wheel speeds, allowing for time domain averaging.

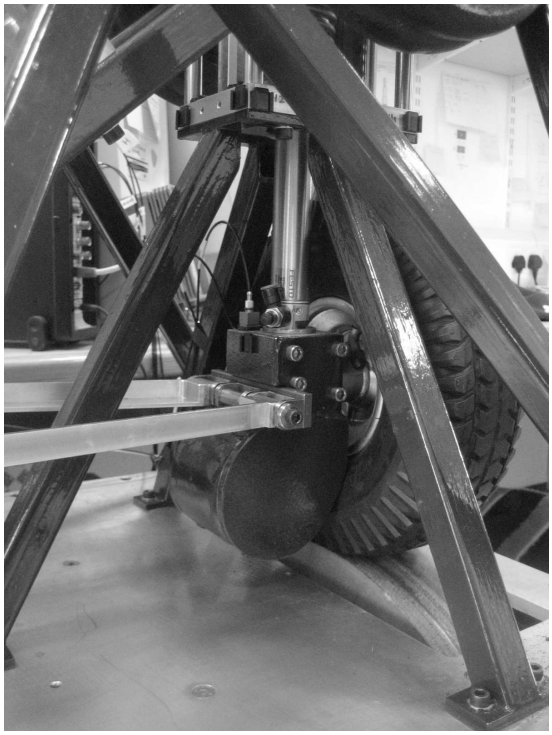

(a) Suspension hub

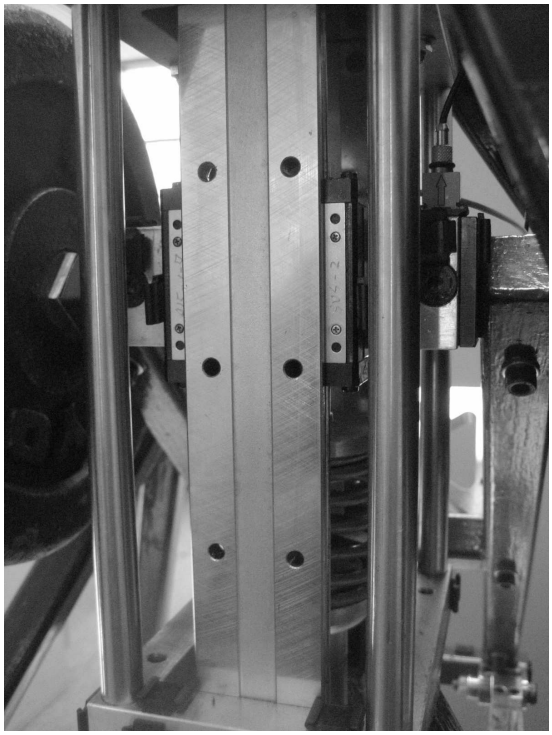

(b) Linear Guide

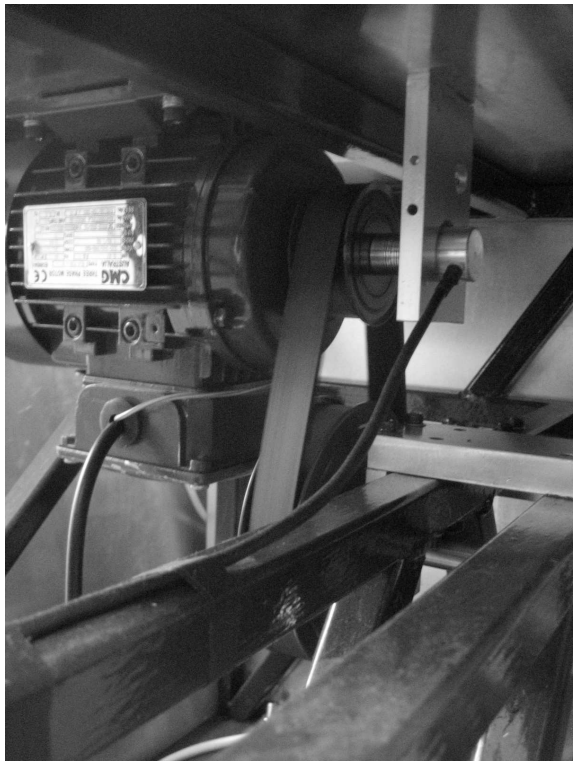

(c) Motor and Encoder

Figure 3.3: Quarter car experimental test rig detail

Figure 3.4: Wheel and tyre balancing rig

The cams used to excite the suspension system are Computer Numerical Control (CNC) machined from medium density fibreboard. The rig can be set–up to use a 2 lobe sine cam, 4 lobe sine cam or a 72 lobe pseudo random cam. The 2 lobe and 4 lobe cams provide 2.5 mm and 1 mm peak to peak sine amplitudes, respectively. The pseudo random cam has 72 lobes with Matlab® generated random amplitudes between ±2.5 mm. All cams have a mean diameter of approximately 460 mm.

A purpose built wheel and tyre balancing rig, shown in Figure 3.4, is used to balance the wheel and tyre assembly of the quarter car rig. The wheel is balanced using a single plane balancing method known as the four run method [162]. The four run method is a relatively simple but effective method of mass balancing. After an initial baseline run, three trial masses are added individually at known locations on the rotor and the vibration results from the four runs are used to determine a correction vector. The magnitude of the correction vector is proportional to the mass required for balance and its argument is equal to the angle at which the mass needs to be applied to the rotor.

3.1.2 Isolated component testing

An ESH® servo–hydraulic testing machine is used to perform isolated testing on individual suspension components. A picture of the ESH® machine can be seen in Figure 3.5, showing the shock absorber and tyre testing set–ups. The machine can produce sinusoidal, triangular or square wave oscillations in the 0.01–30 Hz

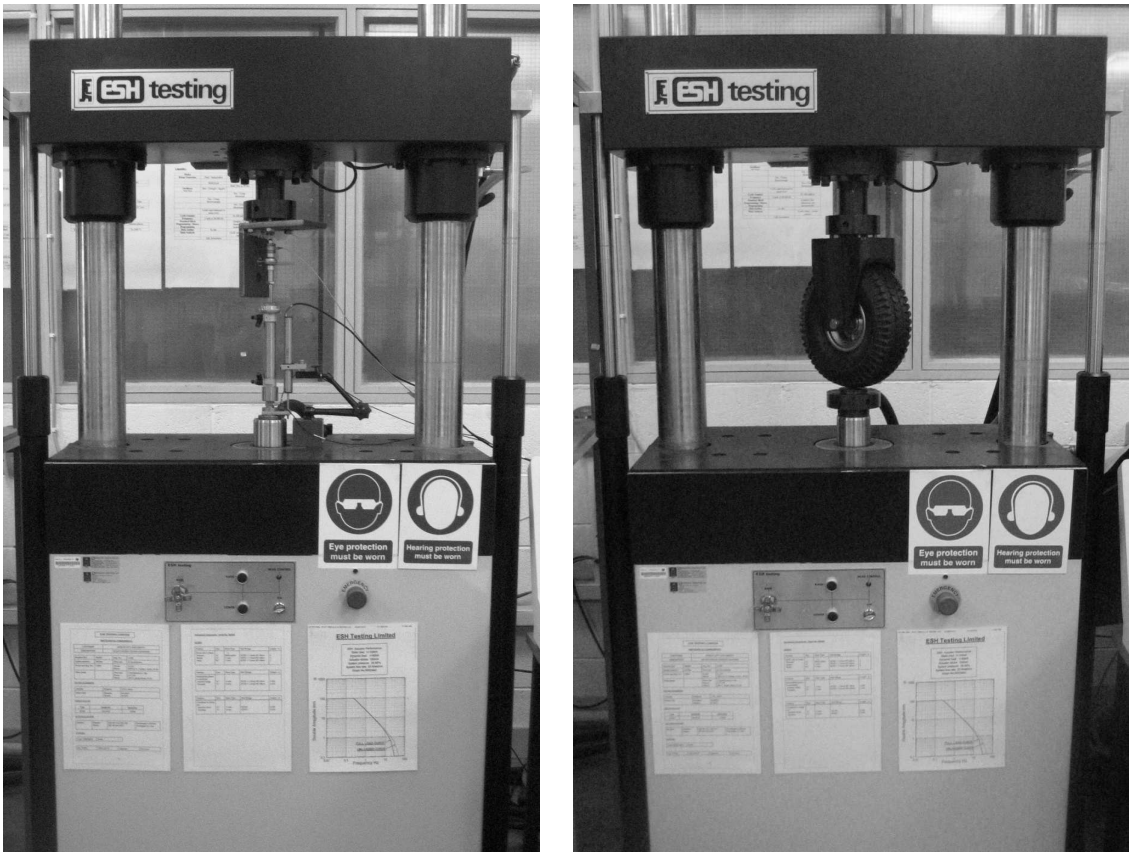

(a) Shock absorber test set–up (b) Tyre test set–up

Figure 3.5: ESH® servo–hydraulic testing machine

frequency range. The machine is used for both static and dynamic identification of the shock absorber, tyre and spring.

3.1.3 Shock absorber force measurement

A novel force measurement system is developed allowing the measurement of shock absorber force during isolated and operational testing using an identical force transducer set–up. A force measurement set–up of this nature has, to the author's knowledge, not been previously reported in the literature. The set–up uses a Kistler® 9021A load washer sandwiched between two 5 mm thick steel washers, as shown in Figure 3.6. A high precision rod end provides the shock absorber attachment to the sprung mass. The complete set–up is mounted on a steel shaft running through the rod end, steel washers and load washer. A preload of 6 kN is applied to the load washer using the preload nut. The complete set–up is dynamically calibrated using a Brüel & Kjær® Type 8200 force sensor on the ESH® machine. The calibration

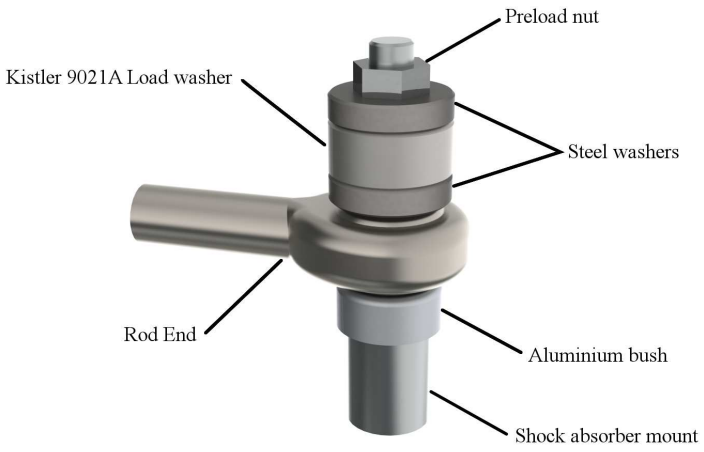

Figure 3.6: Custom shock absorber force measurement set–up (See Appendix F for detailed engineering drawings)

set–up is shown in Figure 3.7b. The shock absorber force measurement set–up is mounted to the shock absorber shaft while the Brüel & Kjær® Type 8200 is connected in series with the shock absorber and ESH® machine piston. The Type 8200 provides a direct measurement of the shock absorber force allowing calibration of the load washer set–up. Figure 3.7a shows the 9021A load washer mounted on the quarter car rig, using the same calibrated mounting method. Full engineering drawings of the shock absorber force measurement setup can be found in Appendix F.

3.1.4 Quarter car rig modal test

A modal analysis of the quarter car rig and support structure is carried out to identify the resonant frequencies of the rig. Twenty three measurement points are used and measurements are taken in three directions at each point to give a sixty nine Degree–Of–Freedom (DOF) model of the rig. The rig is excited in the x, y and z directions at measurement point 1, located at the A–arm to chassis link connection point. In terms of a full vehicle, the x, y and z directions are defined as the, transverse, fore–aft and vertical directions, respectively. The structure is excited using hammer impact excitation. The hammer used is a Brüel & Kjær® type 8202 impact hammer. A rubber tip is used for this analysis due to the relatively low frequency range of interest (0–100 Hz). A Matlab® based mode visualisation tool is developed to animate operating deflection shapes of the rig. This tool aids in the

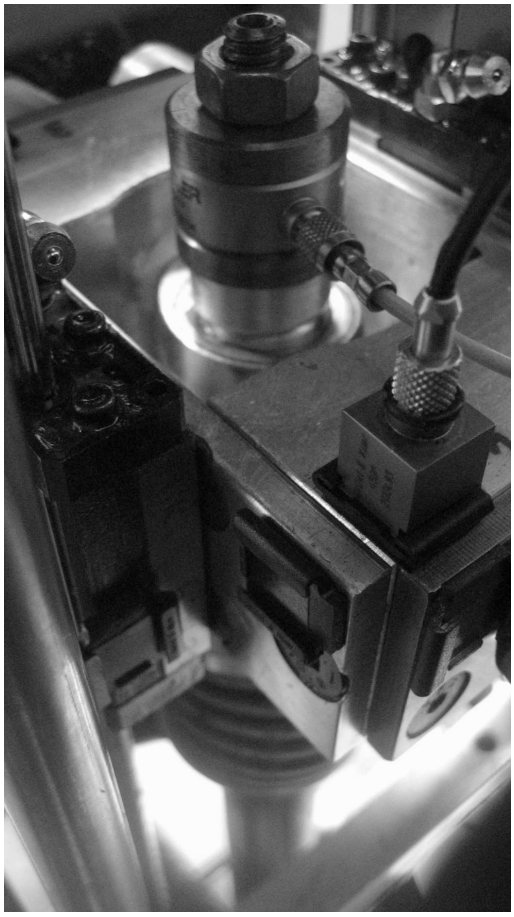

(a) Force measurement set–up mounted on the shock absorber during operational testing

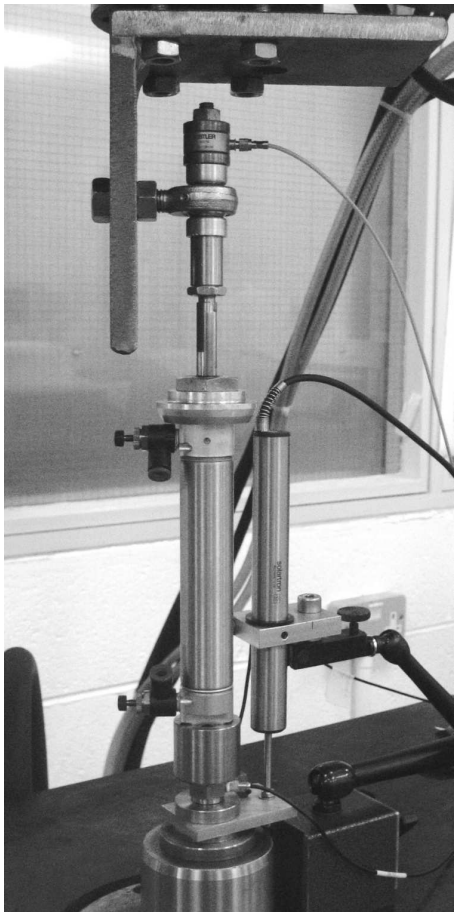

(b) Force measurement set–up mounted on the shock absorber during isolated testing

Figure 3.7: Isolated and operational shock absorber force measurement set–up

visualisation of vibration modes and identification of resonance sources. A screen shot of a typical resonance animation is shown in Figure 3.8. The 13.7 Hz mode in this example, is seen to be due to a tyre bounce motion with the unsprung mass and sprung mass motions coupled (measurement points 1 and 2 are at the A–arm to chassis link connections, points 3, 4, 5 and 6 are on the sprung mass and point 7 is on the unsprung mass).

Figure 3.9 shows driving point receptance plots for hammer impact excitation taken on the sprung mass and unsprung mass in the x and z directions. Significant resonances are seen at frequencies of 13, 25, 33, 48, 71, 78 and 91 Hz. The modes of vibration of the quarter car rig support structure are consistent with modes of vibration typically observed during full vehicle 'body–in–white' modal tests [163, 164]. In the work of Verboven *et al.* [163] a full modal analysis of a car chassis was carried

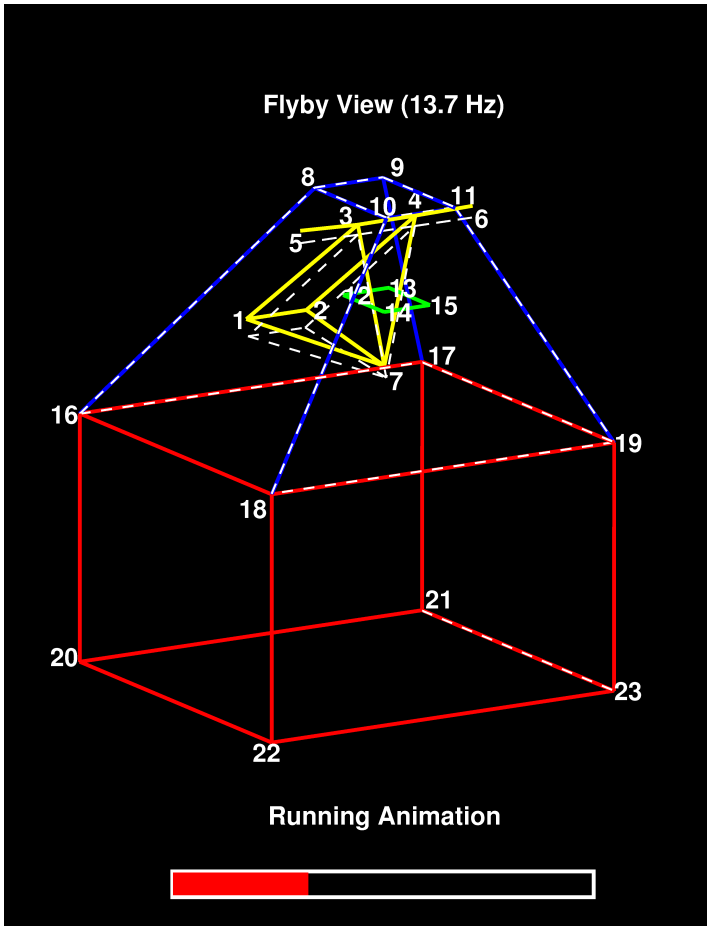

Figure 3.8: Quarter car rig mode visualisation tool showing a flyby view of a rig resonance at 13.7 Hz (the undeformed structure is shown in dashed white lines)

out. Dominant modes of vibration are observed at approximately 26, 35, 42, 51, 68, 78 and 82 Hz. The presence of modes of vibration in the quarter car rig, which are similar to those identified in full vehicle tests, contributes to a realistic system identification scenario.

3.1.5 Data acquisition and analysis

Experimental measurements on the rig are carried out using Pulse®. The Pulse® hardware/software family is Brüel & Kjærs® platform for noise and vibration analysis. Data acquisition is carried out using Brüel & Kjærs® type 3109 input/output module, which communicates with a computer via a Brüel & Kjær® type 7533 LAN interface module. The type 3109 module has four input channels for multichannel vibration measurements and two output channels for system excitation. It allows in-

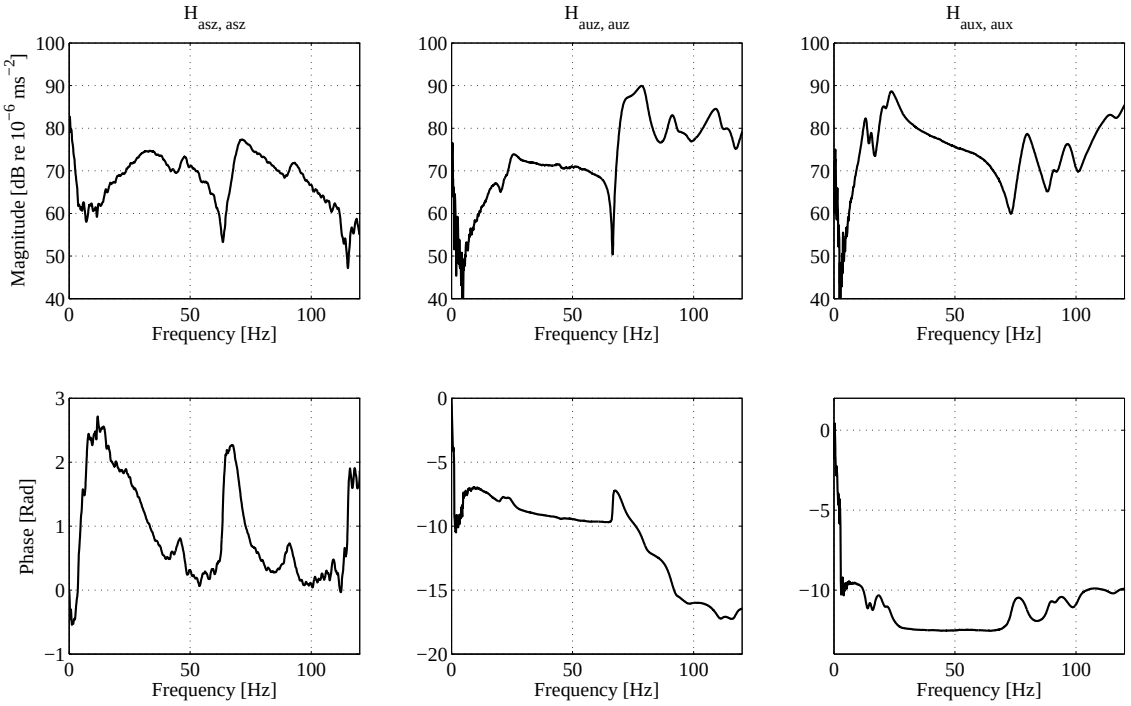

Figure 3.9: Quarter car rig experimental modal analysis driving point FRF's; significant resonances are seen at frequencies of 13, 25, 33, 48, 71, 78 and 91 Hz (Subscripts are defined as follows: asz, sprung mass acceleration in the z direction; auz, unsprung mass acceleration in the z direction; aux, unsprung mass acceleration in the x direction).

dependent input ranges to be set for each channel, optional input autorange, built–in digital signal processors, automatic DC–offset compensation and overload detection for out–of–band frequencies.

Transducers

Brüel & Kjær® type 4508 accelerometers are used for acceleration measurement. They provide a wide frequency range of operation (0.3–8000 Hz) combined with a low mass and high sensitivity (100 mV/g). This model of accelerometer is widely used in the automotive and aeronautical industries for modal analysis and structural analysis measurements. The accelerometers are of the piezoelectric type. Piezoelectric sensors develop a charge when subjected to a force. The accelerometers have an integrated charge amplifier to convert the piezoelectric output signals to voltages. They are mounted using Brüel & Kjær® UA–1407 mounting clips. The clips

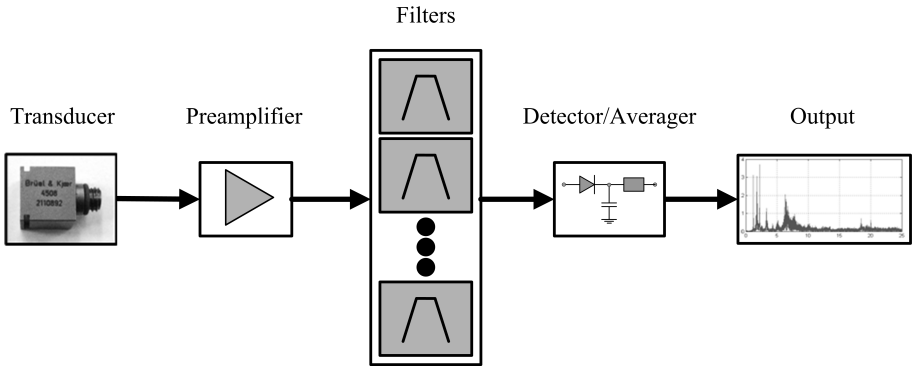

Figure 3.10: The measurement chain for vibration analysis (adapted from [165])

are secured using cyanoacrylate. This set–up gives an upper limiting measurement frequency of 2 kHz. Displacement measurements are carried out using a Solartron Metrology® DC25 Linear Variable Differential Transformer (LVDT). The DC25 has a ±25 mm operating range and a sensitivity of 17.12 mV/V/mm.

Force measurements are conducted using a Kistler® piezoelectric load washer, type 9021A. The load washer has a sensitivity of -4.3 pC/N and a maximum load rating of 35 kN. A Kistler® type 5011 charge amplifier is used in conjuction with the load washer to convert the electrical charge yielded by the sensor into a proportional voltage signal. A Brüel & Kjær® type 8200 force sensor is also used for force measurement. Type 8200 is a small, permanently pre–loaded transducer usable in the force range 1000 N tensile to 5000 N compressive. The 8200 has a sensitivity of 4.0 pC/N. It is mounted in series with a Brüel & Kjær® type 2646 inline charge converter.

Vibration measurement

Vibration measurement and analysis starts with a time–varying, real world signal from a transducer or sensor. The measurement chain for vibration analysis is shown in Figure 3.10. The preamplifier amplifies and conditions the transducer signal. The filtering of the signal may involve the use of low–pass (anti–alias), high–pass, band–pass or integration filters. In frequency analysis, for example, a bank of band–pass filters is used and the signal is passed through each filter simultaneously. The resulting output is used to develop a frequency spectrum of the signal. The final stage in the measurement chain is the detector/averager. This converts the vibration signal into a level which can be shown on the display.

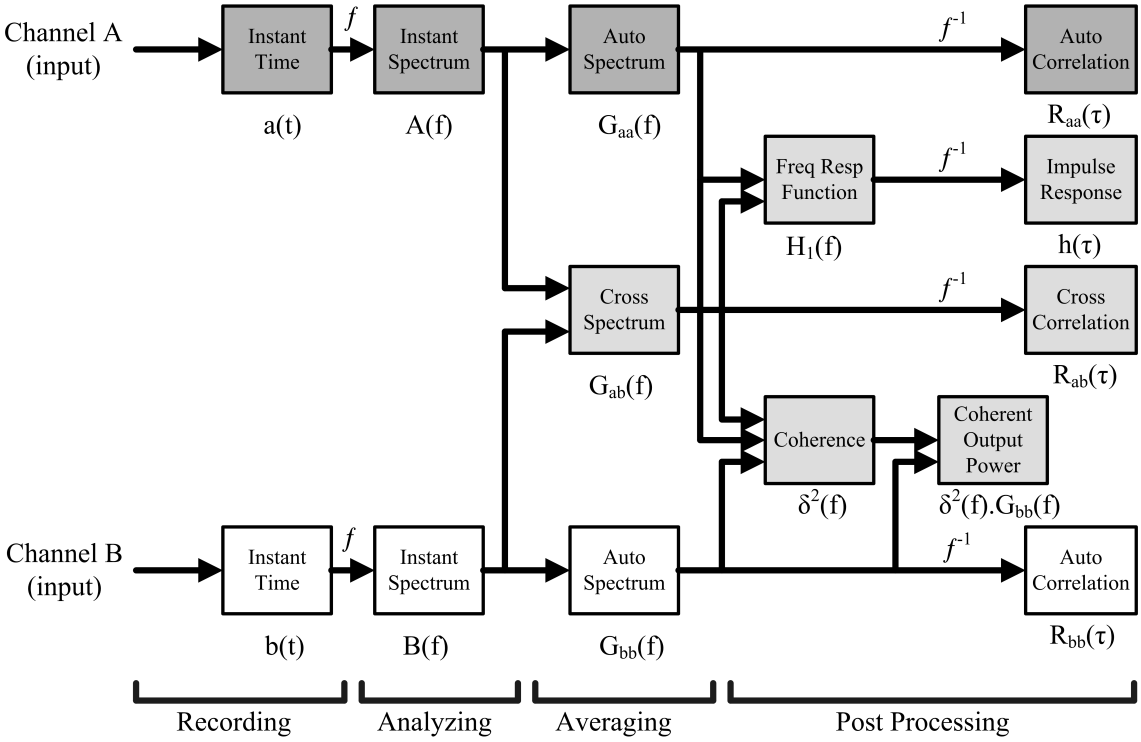

Figure 3.11: Dual channel spectrum averaging (adapted from [166])

Dual channel measurements

A dual channel measurement is the simultaneous measurement of the cross–spectrum between two input channels, and a measurement of the autospectrum of the two channels. A diagram of a dual channel spectrum averaging is shown in Figure 3.11. The analog input signals of channels A and B are filtered, sampled, and digitized to give a series of digital sequences or time history records. The sampling rate and the record lengths determine the frequency range and the resolution of the analysis. A Fourier Transform is performed on both time history records. Multiplication and averaging are performed and two autospectra are generated along with a cross–spectrum [166]. All the other functions can be computed by post processing of these measured spectra. This is important for practical applications as only one measurement needs to be made regardless of how many post processed functions are used [166].

Parameter	Description	Measured Value
m_u	Unsprung mass	8.02 kg
m_s	Sprung mass	25.24 kg
k_u	Tyre stiffness	89020 N/m
k_s	Spring stiffness	5690 N/m
c_s	Shock absorber damping	334 N s/m

Table 3.1: Measured quarter car component parameters

3.2 Simulation development

The two DOF linear quarter car model, as shown in Figure 2.25, is used for the purposes of suspension system simulation in this work. It will be used as a starting point for the development of a more accurate simulation as individual component testing is carried out. The advantages and limitations of this widely used model are outlined in the literature review (§ 2.6.2). Table 3.1 defines the component parameters used in the linear quarter car model. The sprung and unsprung mass are measured from the quarter car test rig. The mass values were chosen during rig design to provide realistic unsprung and sprung mass natural frequencies (derived in § 3.2.1). The experimental identification of the remaining parameters is presented in detail in Chapter 4 and Appendices A and B and therefore, will not be discussed any further at this point.

3.2.1 Quarter car simulation

Consider the quarter car model shown in Figure 2.25 subject to a displacement input x_r. A force balance performed on the sprung and unsprung masses yields the following equations of motion,

$$m_u\ddot{x}_u + c_s\left(\dot{x}_u - \dot{x}_s\right) + c_u\left(\dot{x}_u - \dot{x}_r\right) + k_s\left(x_u - x_s\right) + k_u\left(x_u - x_r\right) = 0 \tag{3.1}$$

$$m_s\ddot{x}_s - c_s\left(\dot{x}_u - \dot{x}_s\right) - k_s\left(x_u - x_s\right) = 0. \tag{3.2}$$

The equations of motion are implemented in block diagram form in Simulink® to allow numerical solution. The undamped natural frequencies of the quarter car model are calculated by letting damping go to zero, and putting the equation of

motion in matrix form,

$$\begin{bmatrix} m_s & 0 \\ 0 & m_u \end{bmatrix} \begin{Bmatrix} \ddot{x}_s \\ \ddot{x}_u \end{Bmatrix} + \begin{bmatrix} k_s & -k_s \\ -k_s & k_s + k_u \end{bmatrix} \begin{Bmatrix} x_s \\ x_u \end{Bmatrix} = \begin{Bmatrix} 0 \\ k_u x_r \end{Bmatrix}. \tag{3.3}$$

Assuming a sinusoidal excitation of the form $x_r = Xsin(\omega t)$, it can be shown that $\ddot{x}_s = -\omega^2 x_s$, therefore, equation 3.3 becomes,

$$\begin{bmatrix} -\omega^2 m_s + k_s & -k_s \\ -k_s & -\omega^2 m_u + k_s + k_u \end{bmatrix} \begin{Bmatrix} x_s \\ x_u \end{Bmatrix} = \begin{Bmatrix} 0 \\ k_u x_r \end{Bmatrix}. \tag{3.4}$$

Calculating the determinant of the square matrix and setting it equal to zero yields,

$$\omega^4 (m_u m_s) - \omega^2 (m_s k_s + m_s k_u + m_u k_s) + \left(k_s^2 + k_s k_u - k_s\right) = 0. \tag{3.5}$$

Subbing in the values in Table 3.1 and solving for ω, yields natural frequencies of

$$\omega_s = 2.39 \text{ Hz} \tag{3.6}$$

$$\omega_u = 17.29 \text{ Hz}. \tag{3.7}$$

These frequencies are referred to as the body bounce (ω_s) and wheel hop (ω_u) frequencies.

Simulation input

The 2 and 4 lobe cams manufactured for the quarter car rig provide an approximately sinusoidal displacement excitation to the tyre patch. To develop simulation displacement excitation time histories, the cam surfaces are profiled using a Mitutoyo® Absolute ID–S 1012M digimatic indicator with a resolution of 0.01 mm. Each cam surface is measured at 72 equally spaced points around the circumference. Four separate measurement sets are taken and averaged to develop a 72 point profile of the cam surface. This 72 point profile is used, along with user selected values for cam rotation frequency and sample rate, to generate a simulation displacement excitation to match that of the experimental test rig.

Figure 3.12 shows the input spectrum generated by the 2 and 4 lobe cams rotating at a frequency of 2.3 Hz. Significant peaks are observed in the 2 lobe cam spectrum at 2.3 Hz and 4.6 Hz, and at 2.3 Hz, 9.2 Hz and 18.4 Hz in the 4 lobe cam spectrum.

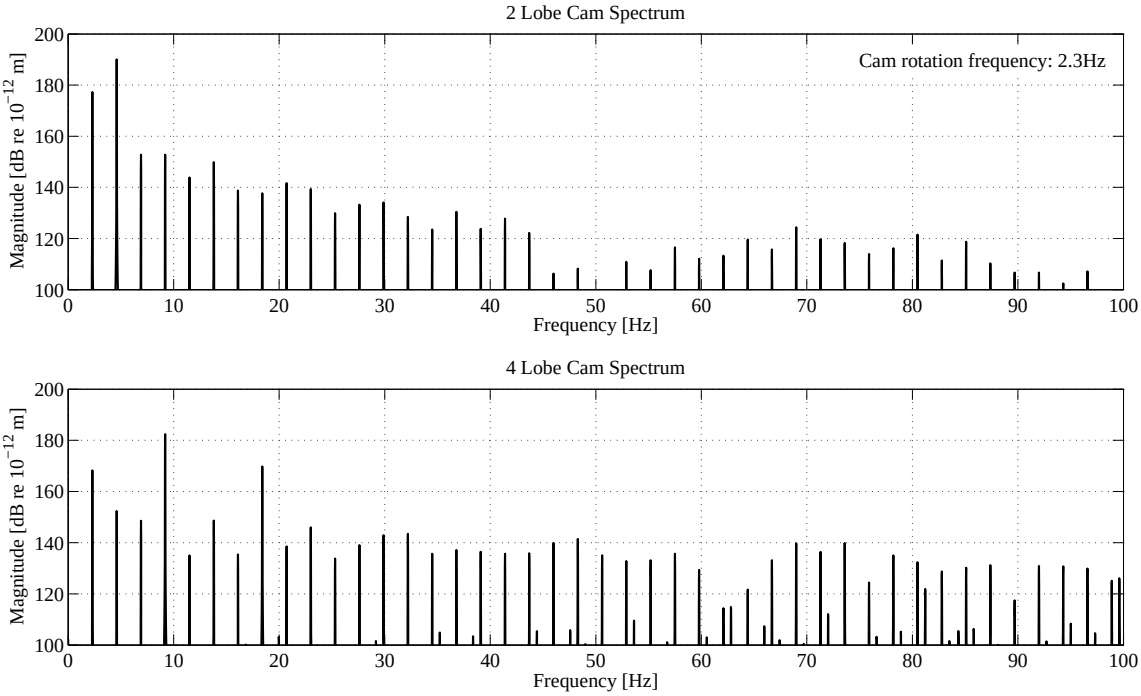

Figure 3.12: Quarter car simulation 2 and 4 lobe cam input spectra corresponding to a cam rotation frequency of 2.3 Hz

All other peaks are greater than 30 dB below the respective dominant peaks.

As the tyre rotates on the surface of the cam, it acts as a mechanical filter, effectively smoothing the cam input. The extent of the smoothing depends on two factors; the rolling radius of the tyre and tyre enveloping. Tyre enveloping is the tendency of a pneumatic tyre to partially engulf short wavelength road irregularities. The tyre rubber tends to drape over the the major asperities of the road surface [167]. Tyre enveloping damps and reduces the effects of road irregularities and, hence, decreases the force input to the suspension hub. In quarter car simulations, where point contact tyre models are often used, problems can arise when road irregularities are encountered which are shorter than the tyre footprint length. The point contact tyre model produces large errors in its load prediction as it follows the road profile exactly and produces a load proportional to the surface contour. An actual tyre travelling over the same surface produces much less load variation due to the tyre partially or fully enveloping these irregularities [168]. Tests are carried out to determine the size of the contact patch under static loading. The tests involve compressing an inked tyre in the ESH® machine onto a sheet of white paper. The length of the contact patch is measured from the tyre footprint at 1 mm intervals, between 1 mm and

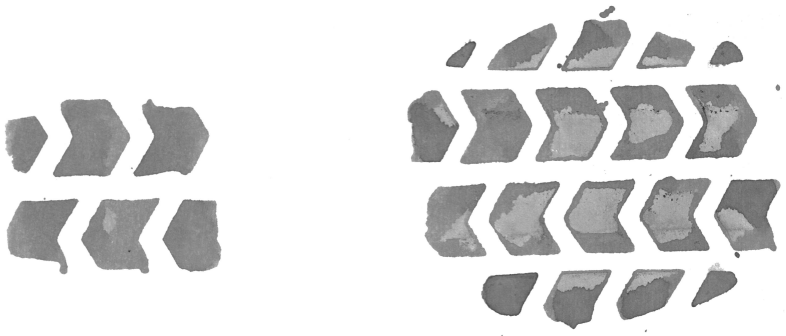

(a) Tyre footprint: 2 mm Deflection

(b) Tyre footprint: 9 mm Deflection

Figure 3.13: Quarter car rig tyre footprint at 2 mm and 9 mm deflections

10 mm static deflection. The tyre footprint for 2 mm and 9 mm static deflections are shown in Figure 3.13. Knowledge of the tyre footprint at a range of static loads allowed for the development of a moving average filter to represent tyre enveloping. The input signal to the tyre is smoothed using this filter to represent the tyre enveloping and mechanical filter properties of the tyre [169, 170]. The length of the moving average filter is dependent on the tyre loading conditions during suspension simulation and is calculated from the known tyre footprints under static deflection.

3.2.2 Data acquisition and analysis

Quarter car Analysis Tool (QcAT) is a custom experimental test and simulation analysis tool developed in Matlab®. QcAT gives the user control of the complete data acquisition–analysis–presentation process from a single Graphical User Interface (GUI). The acquisition tab allows the user to enter experimental and simulation parameters. QcAT implements ActiveX control of both Pulse® and Labview® to set data acquisition and experimental test rig parameters. A basic motor control loop uses the USB–6009 I/O module to set the motor speed via a control voltage to the inverter. The actual motor speed is calculated using the optical encoder signal and adjusted until the actual speed matches the user defined value. After acquisition measurement data are exported to Matlab® in Universal File Dataset 58b format for further analysis. Universal file formats are used as a *de facto* standard by the

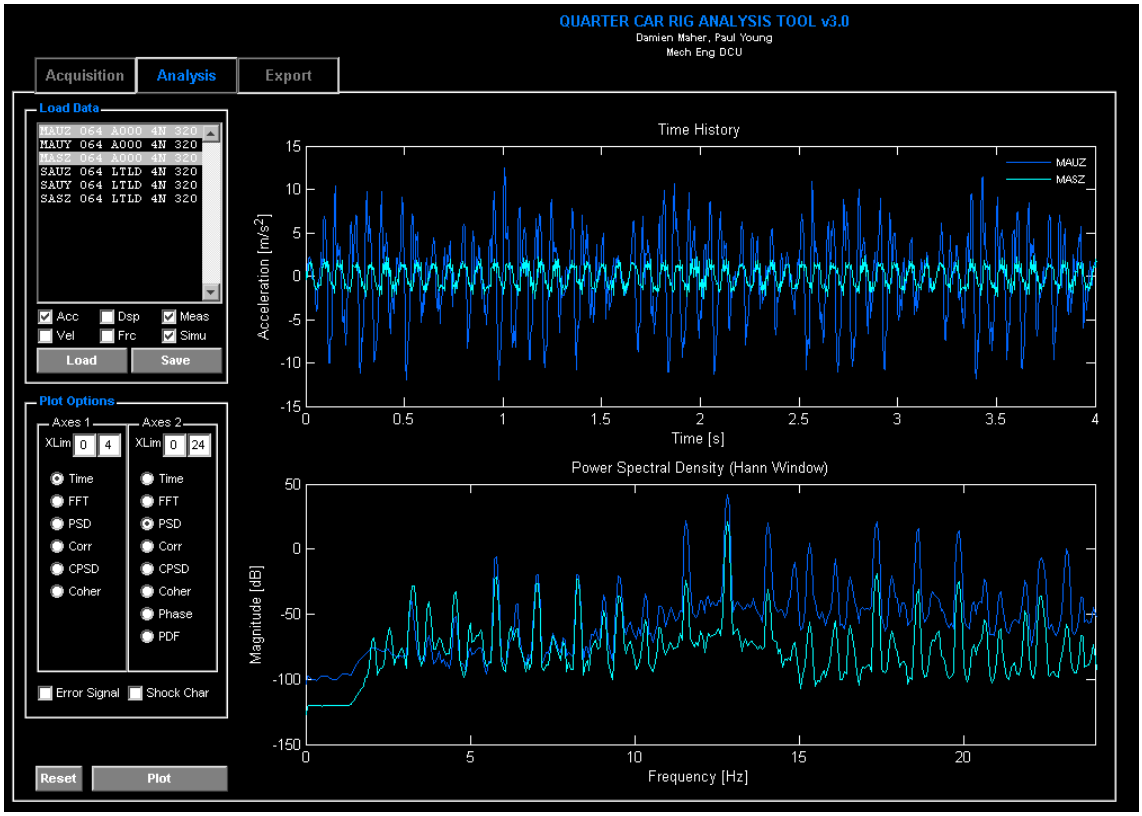

Figure 3.14: QcAT analysis tab screen shot

experimental dynamics community. Details of the Universal File Dataset 58b format can be found in Appendix E. The QcAT analysis tab is shown in Figure 3.14. The analysis tab allows time and frequency domain visualisation of the data. Historic data can be loaded into the analysis tab, and because of the standard universal file format used, details of the analysis type and experimental set–up parameters are available to the user. The presentation of data acquired and analysed in QcAT is achieved using the export screen. Multiple data sets can be loaded and exported for presentation purposes. A more detailed description of the feature of QcAT, along with a development history is reported in Appendix D. A diagram summarising the hardware/software implementation is shown in Figure 3.15.

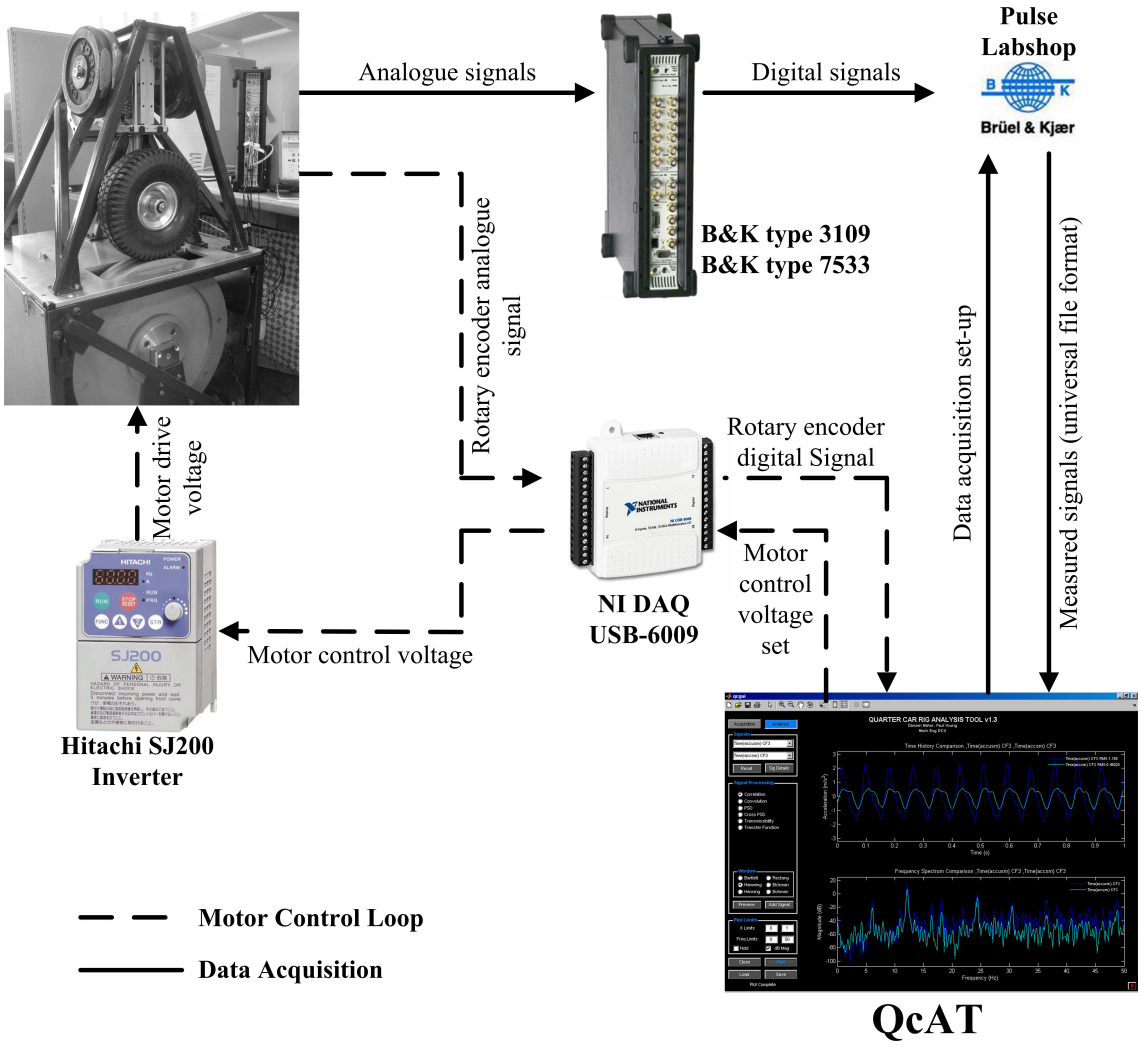

Figure 3.15: Experimental testing hardware/software implementation

Chapter 4

Suspension system identification

The literature review in Chapter 2 examined suspension system identification from two angles, the more traditional force–response approach and the relatively new response only or operational approach. Chapter 3 outlined the development of an experimental testing setup with the flexibility to allow both isolated suspension component testing and also operational suspension system testing. In this chapter the identification of the suspension system using the force–response approach is presented. Sections 4.1, 4.2 and 4.3 document the identification of the tyre, shock absorber and spring, respectively. This is carried out by disassembling the quarter car rig and testing each of the components in isolation using the ESH® servo–hydraulic testing machine. The identified component parameters, from the isolated testing, form the basis for the development of a quarter car simulation of the quarter car rig. Section 4.4 presents the development and evaluation of both linear and nonlinear quarter car models.

4.1 Tyre identification

This section gives an overview of the tyre identification procedure and a detailed account is documented in Appendix A. The tyre is tested both statically and dynamically in isolation using the ESH® testing machine. The test setup can be seen in Figure 4.1. Tests are carried out at four different inflation pressures, 1.1 Bar, 1.5 Bar, 1.8 Bar and 2.0 Bar. A preload is applied to the tyre before each test to replicate operational conditions. Testing is carried out at selected frequencies between 1

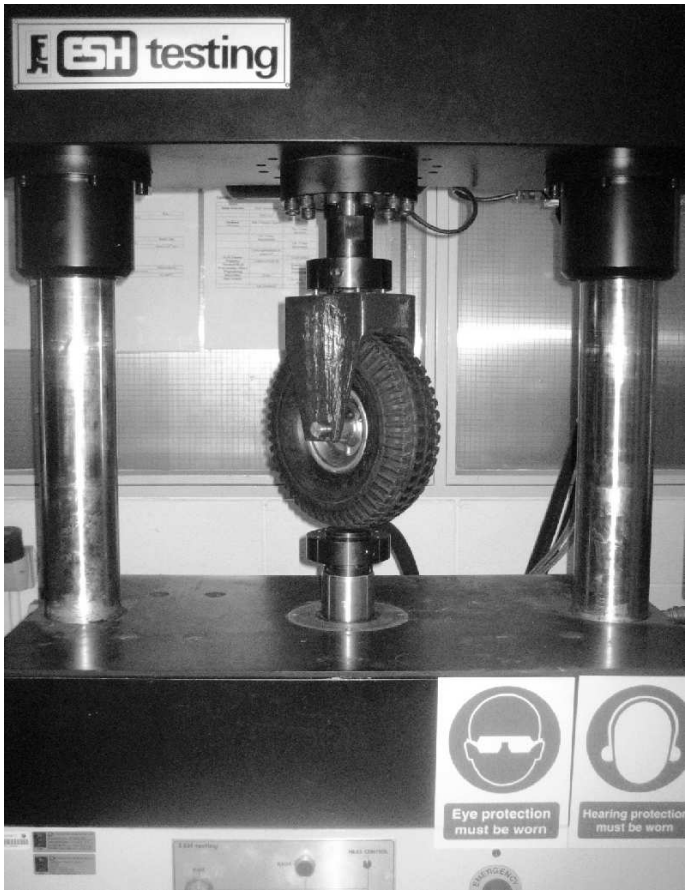

Figure 4.1: Tyre dynamic test setup

Hz and 14 Hz, and at selected amplitudes between 1 mm and 4 mm.

4.1.1 Characterisation

Static tyre compression test results show the tyre to be almost linear for deflections up to 10 mm. Static linear stiffness values of 63.32 N/mm and 81.42 N/mm are calculated for the 1.1 Bar and 2.0 Bar tests, respectively. Under dynamic sinusoidal loading, of the form $x = A\sin(2\pi f_e t)$, where f_e and A are the excitation frequency and amplitude, respectively, the tyre shows a hardening/softening spring characteristic at all test frequencies and amplitudes. This behaviour is due to the preload applied to the tyre prior to dynamic testing. Two typical work diagrams (force–displacement) are shown in Figure 4.2. The test on the left is run at an inflation pressure of 1.1 Bar, with a sinusoidal input excitation amplitude of 2 mm and excitation frequency of 5 Hz. The test on the right is run at an inflation pressure of 2.0 Bar, with input amplitude and frequency equal to 3 mm and 2 Hz, respectively.

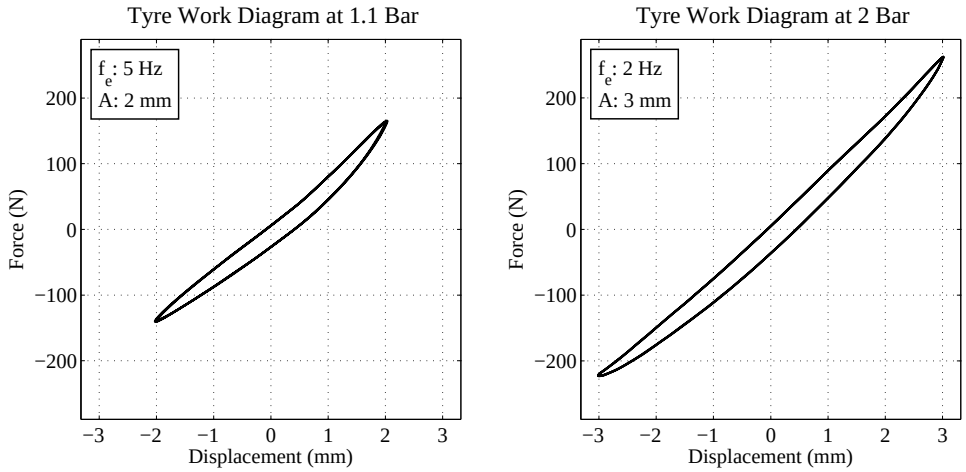

Figure 4.2: Tyre work diagrams at $f_e = 5$ Hz, $A = 2$ mm, 1.1 Bar (left) and $f_e = 2$ Hz, $A = 3$ mm, 2.0 Bar (right)

Hysteresis loops are also observed in the work diagrams. The area enclosed by the loop denotes the energy dissipated by the tyre in one cycle of motion. The damping mechanism of the tyre is investigated by examining the frequency dependence of the energy dissipation. Results show that in general the energy loss per cycle does not increase significantly with increasing frequency and at higher frequencies it decreases slightly with increasing frequency. The energy loss per cycle is also approximately proportional to the square of the excitation amplitude. These observations are consistent with hysteretic damping [171, 172, 173] and lead to the assumption that the major damping mechanism of the tyre is hysteretic damping.

4.1.2 Model selection

Based on these initial observations, a point contact tyre model is developed. The literature review noted that the relatively simple point contact tyre model is widely used for low to intermediate frequency range studies [148, 149] and is acceptable for ride analysis [138]. The proposed point contact tyre model consists of a hysteretic damper in parallel with a nonlinear spring, as shown in Figure 4.3. The tyre stiffness

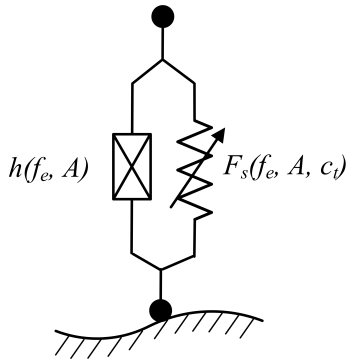

Figure 4.3: Proposed point contact tyre model (nonlinear spring in parallel with a hysteretic damper)

is modelled as a hardening/softening nonlinear spring system. The nonlinear spring force, F_s, is given by,

$$F_s = k_n(x + c_t x^2) \tag{4.1}$$

where k_n is the tyre stiffness, x is the tyre deflection and c_t is the coefficient of the hardening/softening nonlinearity. The hardening/softening spring characteristic observed in Figure 4.2 is due to the preload applied to the tyre. It should be noted that the nonlinearity in the tyre is modelled using an asymmetric nonlinear term (x^2). This nonlinear functional form is chosen for its ability to represent the tyre stiffness nonlinearity without *a priori* knowledge of the presence of a preload on the tyre.

Consider a linear spring and hysteresis damper connected in parallel. The force displacement relation, assuming approximately harmonic excitation, can be expressed as [173],

$$F = (k + ih)x \tag{4.2}$$

where h is called the hysteresis damping constant and,

$$k + ih = k\left(1 + i\frac{h}{k}\right) = k(1 + i\eta). \tag{4.3}$$

The term $k + ih$ is known as the complex stiffness and $\eta = h/k$ is a constant indicating a dimensionless measure of damping. An equivalent viscous damping

ratio and viscous damping constant can be calculated for hysteretic damping using,

$$\zeta_{eq} = \frac{\eta}{2} \tag{4.4}$$

$$c_{eq} = \frac{\eta k}{\omega}. \tag{4.5}$$

Therefore, the equation for the force displacement relation of the tyre can be expressed as,

$$\begin{aligned} F_t &= F_s + F_d & (4.6)\\ &= k_n(x + c_t x^2) + c_{eq}(\dot{x}) & (4.7) \end{aligned}$$

where, the terms F_t, F_s and F_d represent the tyre force, the spring force and the damping force, respectively. The tyre damping is now represented here using the frequency dependent damping term c_{eq}.

4.1.3 Parameter estimation and model validation

Experimental data collected at a tyre inflation pressure of 1.8 Bar are used for the model parameter estimation. The nonlinear stiffness, k_n, shows both frequency and amplitude dependence, while c_t and η depend only on excitation amplitude. k_n shows an approximately linear relationship with frequency and amplitude. Least squares are used to fit first order polynomials to plots of k_n versus A and k_n versus f_e. This yields the following expression for k_n in terms of A and f_e,

$$k_n = -2.79A + 0.5f_e + 89.02. \tag{4.8}$$

The terms c_t and η are found to be dependent only on excitation amplitude, therefore, expressions for c_t and η in terms of excitation amplitude are obtained in a similar manner,

$$\begin{aligned} c_t &= 0.0085A + 0.0234 & (4.9)\\ \eta &= -0.0067A + 0.1071. & (4.10) \end{aligned}$$

The reader is referred to Appendix A for a more detailed description of the parameter estimation in equations 4.8, 4.9 and 4.10.

Tyre Inflation Pressure 1.8 Bar				
A	1mm	2mm	3mm	4mm
f_e	MSE	MSE	MSE	MSE
1hz	0.5	0.6	1.4	3.0
2hz	0.0	0.6	1.2	3.1
4hz	0.1	0.5	1.2	2.9
5hz	0.2	0.6	1.5	-
7hz	0.4	0.4	1.5	-
10hz	0.6	0.6	-	-
14hz	0.8	-	-	-

Table 4.1: Nonlinear tyre model MSE

The proposed model is implemented in Matlab®. Simulations are carried out and compared with experimental data. In order to have an objective measure of 'goodness of fit', the Mean Squared Error (MSE) is introduced,

$$MSE(\hat{x}) = \frac{100}{N\sigma_x^2}\sum_{i=1}^{N}(x_i - \hat{x}_i)^2 \tag{4.11}$$

where N is the number of data points and σ_x^2 is the variance of the measured data record. Experience with this norm suggests that a value less than 5 % indicates a good model while less than 1 % indicates excellence [70]. Table 4.1[1] shows simulation MSE for a range of excitation frequencies and amplitudes.

The simulation error is seen to increase with increasing excitation frequency and amplitude. A refinement of the model is introduced which takes account of a negative offset observed in measured data along the y–axis. This offset can be seen in Figure 4.2. This type of drift is a characteristic of asymmetric systems. Such systems are prone to bias their response toward a preferred or weak direction [174]. The absolute value of the offset, f_o, in Newtons, is found to increase with increasing excitation amplitude while remaining relatively independent of excitation frequency. Orthogonal least squares are used to fit a third order polynomial to a plot of measured offset versus excitation amplitude, yielding an expression for f_o which is a nonlinear function of excitation amplitude,

$$f_o(A) = -0.44A^3 - 0.61A^2 - 0.23A \tag{4.12}$$

[1]Missing data outside ESH machine capability

Tyre Inflation Pressure 1.8 Bar				
A	1mm	2mm	3mm	4mm
f_e	MSE	MSE	MSE	MSE
1hz	0.3	0.1	0.1	0.1
2hz	0.1	0.2	0.1	0.3
4hz	0.0	0.1	0.1	0.2
5hz	0.2	0.2	0.2	-
7hz	0.2	0.2	0.4	-
10hz	0.1	0.2	-	-
14hz	0.1	-	-	-

Table 4.2: Revised nonlinear tyre model MSE

The resulting expression for f_o is included in equation 4.1 to yield,

$$F_s(x) = k_n(x + c_t x^2) + f_o(A) \tag{4.13}$$

The modified nonlinear tyre model therefore becomes,

$$\begin{aligned} F_t &= F_s + F_d & (4.14)\\ &= k_n(x + c_t x^2) + f_o(A) + c_{eq}(\dot{x}). & (4.15) \end{aligned}$$

Evaluation of this modified nonlinear tyre model revealed a significant improvement over the original nonlinear tyre model. Table 4.2 shows the MSE for a range of excitation frequencies and amplitudes at a pressure of 1.8 Bar. The average MSE across all measurement frequencies and amplitudes is found to be 0.17 %, indicating an excellent model fit. The tyre model fit is shown for two example measurements in Figure 4.4.

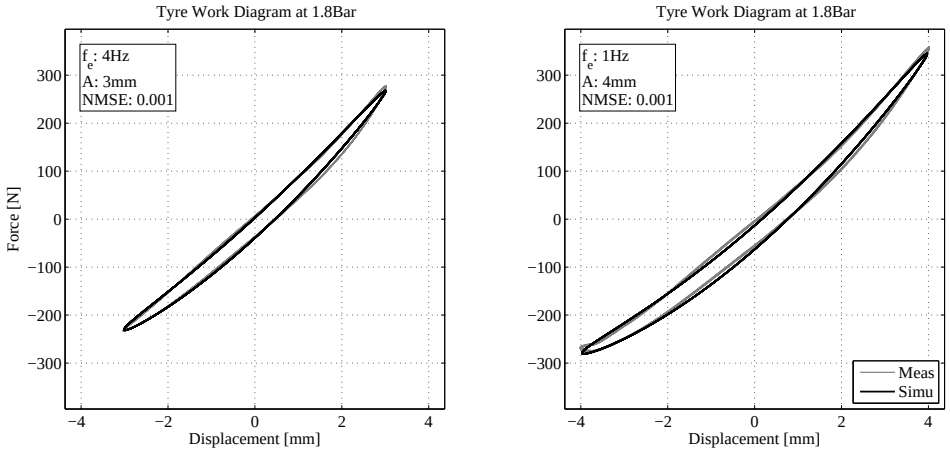

Figure 4.4: Proposed tyre model fit to measured data at $f_e = 4$ Hz, $A = 3$ mm, 1.8 Bar (left) and $f_e = 1$ Hz, $A = 4$ mm, 1.8 Bar (right)

4.2 Shock absorber identification

Identification of shock absorbers is usually carried out experimentally using mechanical test stands [78] and harmonic excitation [77, 158]. In this work, the shock absorber is tested in isolation using the ESH® machine. Figure 4.5 shows a close up of the shock absorber test setup, which is based on the methods used by Centro Ricerche FIAT (CRF) of Torino, Italy as presented in a case study by Worden and Tomlinson [11]. A detailed account of the shock absorber identification is documented in Appendix B. An overview of the identification process is outlined here. The literature review presented many works which highlighted the complex nonlinear nature of shock absorbers [78, 82, 158, 159]. Despite this, it has been common practice to model the damping of a shock absorber as a linear viscous damper, as in the linear quarter car model. This linear model is now commonly replaced with two and three slope models to account for the major nonlinearities of the shock absorber [1]. The shock absorber, used in this investigation, is a coil–over type. The spring is removed and the damper dynamically tested in isolation to characterise its behaviour.

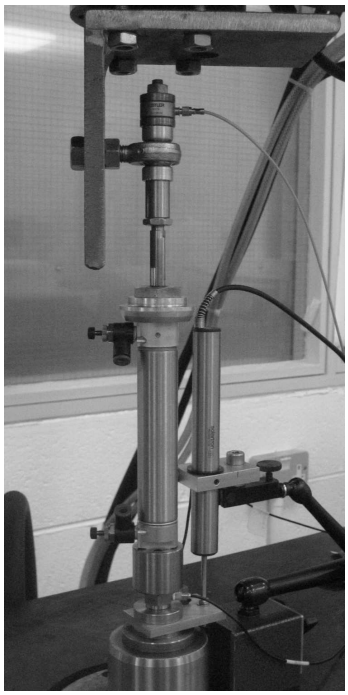

Figure 4.5: Shock absorber experimental test setup

4.2.1 Characterisation

Figure 4.6 shows typical characteristic (force–velocity) and work (force–displacement) diagrams for the damper subject to sinusoidal displacement excitation of the form $x = A\sin(2\pi f_e t)$. Initial observation of the characteristic diagrams indicate the presence of static friction in the damper. This can be seen as the shock absorber velocity increases from zero. Note the sharp increase in force (sticking) followed by a decrease in force (slipping). Due to the low velocity of the damper at 2 Hz 0.5 mm, the friction force dominates, a common property of coulomb friction [11]. The stick–to–slip transition is seen to occur at a force of approximately ±13 N. In the slipping phase, the damper force decreases as the velocity increases to its maxima of ±6.3 mm/s. The force as the velocity decreases from its maximum is lower than the corresponding force as the velocity increases to its maximum. This phenomenon, known as frictional lag, was observed experimentally by Hess and Soom [175]. Note that as the velocity returns to zero from the maxima, the damper again enters the stick state at approximately ±0.6 mm/s.

Pre–sliding displacement of approximately 83 μm can also be seen in the work diagram. This spring like behaviour in static friction may be due to relative displacement between the cylinder wall and the piston seal prior to slipping. The pre–sliding

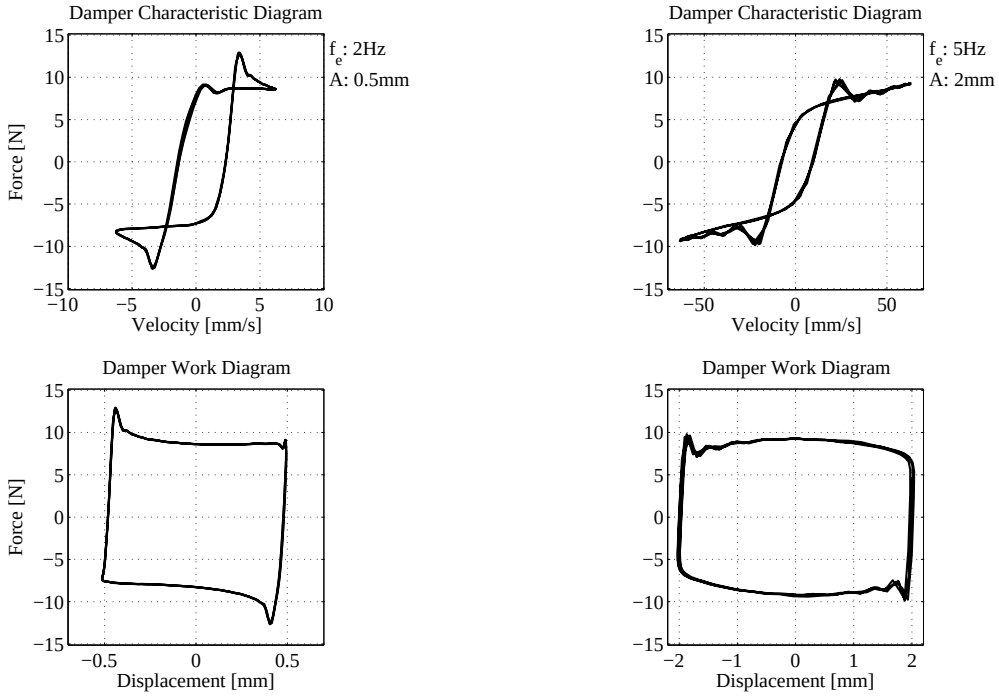

Figure 4.6: Shock absorber characteristic and work diagrams at $f_e = 2$ Hz, $A = 0.5$ mm (left) and $f_e = 5$ Hz, $A = 2$ mm (right)

displacement increases with excitation frequency to a value of approximately 153 μm at 14 Hz, 0.5 mm amplitude. It also increases with amplitude and a value of 110 μm is recorded at 2 Hz, 4 mm amplitude. This indicates that pre–sliding displacement is dependent on the acceleration of the damper piston in the sticking phase of motion. Overall, the damper shows similar characteristics to those observed by Guglielmino *et al.* for isolated testing of a prototype semi–active automotive friction damper [138].

The energy dissipation per cycle of the shock absorber, at the larger amplitudes of excitation (>2 mm), is seen to increase in an approximately linear fashion with excitation frequency, indicating that the damping mechanism is viscous damping. At the lower amplitudes (0.5 mm and 1 mm) the energy dissipation does not show strong dependence on excitation frequency. This is believed to be due to the dominance of friction damping at low excitation amplitudes.

4.2.2 Model selection

Based on the observations made during shock absorber characterisation, three shock absorber models are proposed. A simple linear model, a piecewise linear model and a full nonlinear model. The linear model takes the form of a linear viscous damping element, where the shock absorber force, F_d, is a function of the linear damping coefficient, c, and the shock absorber piston velocity, $\dot{x}$,

$$F_d = c\dot{x}. \tag{4.16}$$

The piecewise linear model is chosen to be trilinear. A trilinear model is selected based on the observation of three distinct regions in the characteristic diagrams in Figure 4.6, a viscous damping characteristic at high velocities in compression and rebound and a static friction zone at low shock absorber velocities. The equations representing the trilinear characteristic are given by [78],

$$F_d(\dot{x}) = \begin{cases} c_3(\dot{x} - c_5) + c_1c_5 & \text{for } \dot{x} > c_5, \\ c_1\dot{x} & \text{for } c_4 \leq \dot{x} \leq c_5, \\ c_2(\dot{x} - c_4) + c_1c_4 & \text{for } \dot{x} < c_4 \end{cases} \tag{4.17}$$

where c_1, c_2 and c_3, represent the damping coefficients of the three regions while c_4 and c_5 represent the transition velocities between the damping coefficients.

The nonlinear model aims to model the dynamic friction in the shock absorber, the symptoms of which are seen in the characteristic diagrams. Friction models can be classified as static or dynamic. Static friction models cannot sufficiently describe all the dynamic effects of friction, such as pre–sliding displacement, friction lag and variable break away force [176, 177]. A dynamic friction model is required to model the complex phenomena observed in the shock absorber characteristic diagram. One such model, called the LuGre model, was developed by Canudas de Wit *et al.* [178]. The LuGre model supports hysteretic behaviour due to friction lag, spring like behaviour in static friction and gives a varying break away force depending on the rate of change of the applied force. The LuGre model is a bristle

type friction model and is given by [178],

$$\frac{dz}{dt} = v - \sigma_0 \frac{|v|}{g(v)} z \tag{4.18}$$

$$g(v) = F_c + (F_{st} - F_c) e^{-(v/v_s)^2} \tag{4.19}$$

$$F = \sigma_0 z + \sigma_1 \dot{z} + f(v) \tag{4.20}$$

where z is the unmeasurable average deflection of the bristles, σ_0 is the bristle stiffness and σ_1 is the bristle velocity dependent damping coefficient. F_{st} and F_c represent the static friction force and the coulomb friction force, respectively. The term, v_s, is the stribeck velocity and the function $g(v)$ characterises the stribeck effect. The function $f(v)$ models the lubrication and viscous friction effects.

4.2.3 Parameter estimation and model validation

To assess the accuracy of the different models across the frequency range of interest, optimisation is carried out to find the model parameters for the linear, piecewise linear and nonlinear shock absorber models. The linear model is optimised using orthogonal least squares, while the piecewise and nonlinear models are optimised in Matlab® using the pattern search optimisation function *patternsearch*. The normalised mean squared error is used as a measure of quality of the model fit. Figure 4.7 shows the MSE for the three models for an excitation amplitude of 1 mm.

The linear and piecewise linear models show large MSE at low frequencies. The error is seen to decrease in both cases as excitation frequency increases. This is due to the increased piston velocity at higher excitation frequencies which serves to reduce the influence of the dominant static friction nonlinearity. The nonlinear model shows a good model fit, with the MSE below 4 % at all frequencies. Figure 4.8 shows the LuGre model with optimised parameters to fit the experimental data for an excitation frequency of 4 Hz and an amplitude of 4 mm. It accurately models the asymmetric behaviour of the damper in acceleration and deceleration and also includes hysteresis effects and pre–sliding displacement.

Initial investigations are carried out to identify the optimal parameters of the nonlinear model across the frequency and amplitude range of the experimental tests. To be truly useful, an expression is required which can identify the model parameter

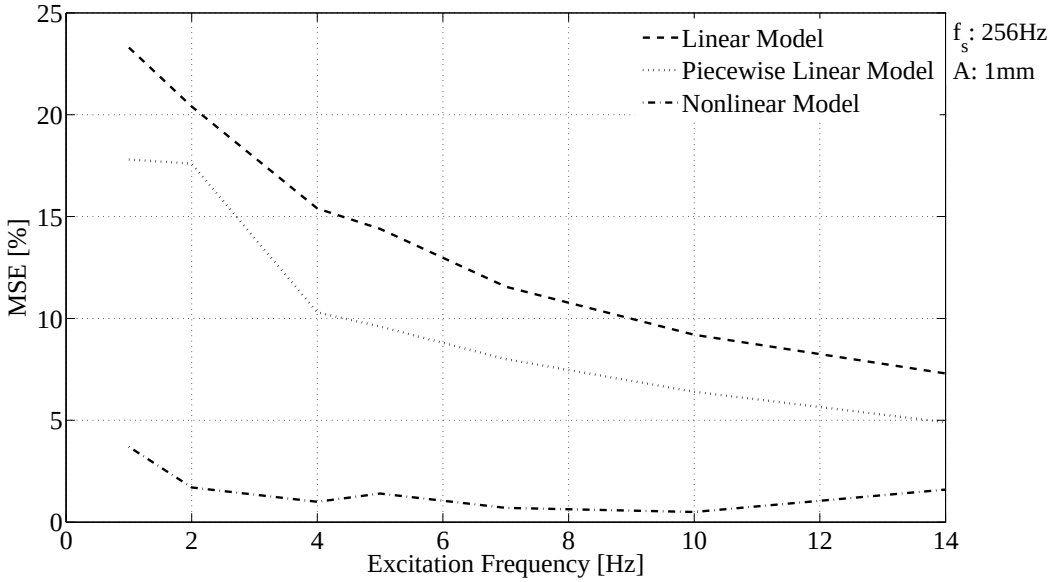

Figure 4.7: Linear, piecewise linear and nonlinear model MSE ($A = 1$mm)

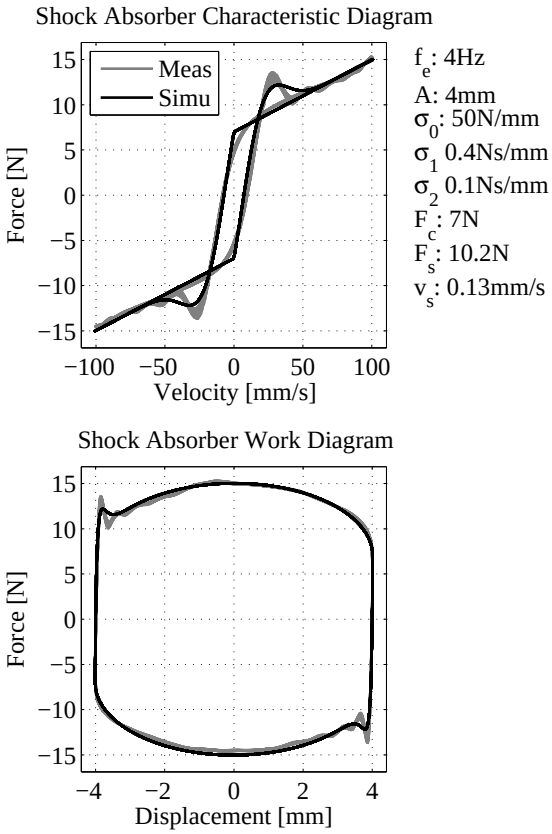

Figure 4.8: Nonlinear shock absorber model fit for $f_e = 4$ Hz and $A = 4$ mm

values not only at the discrete experimental test points, but at any user defined excitation frequency within the range of the experimental tests. The identification of such an expression proves extremely difficult. No easily identifiable pattern exists between optimised model parameters across the experimental test range. Dynamic friction models such as the LuGre model are known to be complex and hard to implement in practical engineering applications [179]. In this investigation optimisation of the LuGre model requires a significant amount of time. Each evaluation of the optimisation objective function requires a simulation to be run for comparison with the measured data. Due to the complex nature of the LuGre model, this simulation requires a sampling rate of 8192 Hz to prevent numerical integration errors. As a result optimisation of each LuGre model at each individual test frequency and amplitude takes a number of hours (The objective function was evaluated 3140 times to obtain the optimised model shown in Figure 4.8). This is compared with minutes for the piecewise linear model and seconds for the linear model, which can both use much lower simulation sampling rates.

The trilinear model parameters can be directly related to phenomena identified in the shock absorber characteristic diagrams. The friction which dominates at low velocities can be related to parameter c_1 which represents the trilinear damping at low velocities. The sticking to sliding transition velocity to parameters c_4 and c_5 while the viscous damping outside the static friction zone can be related to parameters c_2 and c_3. Although the parameters of the model are intuitive, it also proves difficult to identify expressions for the parameters across the frequency and amplitude range of the experimental tests.

4.3 Spring identification

Automotive helical springs are often treated as simple massless linear spring elements. Background reading has shown that at low frequencies (below 40 Hz), this assumption is a valid one [161]. Above 40 Hz, the dynamic stiffness has been found to increase sharply. This experimental test of the spring will aim to first verify this assumption and also investigate the damping effect of the spring in the 0–20 Hz range. The spring test setup is the same as that of the tyre dynamic test.

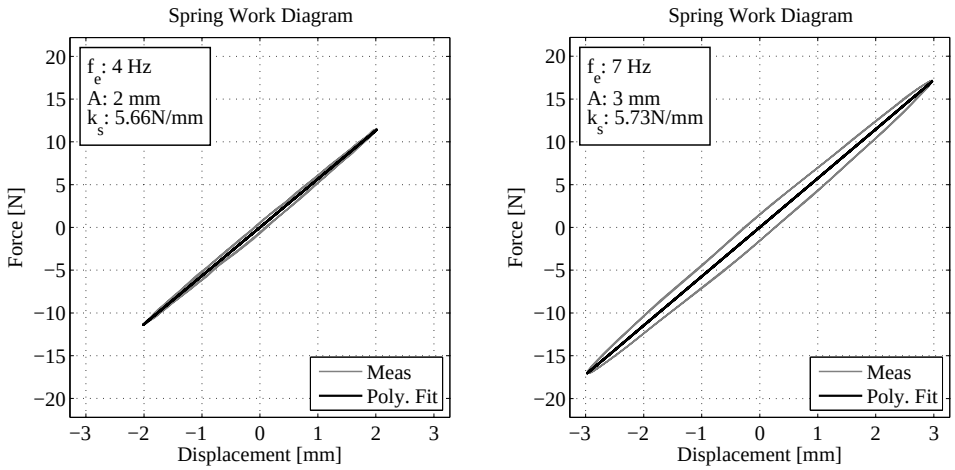

Figure 4.9: Spring work diagrams at $f_e = 4$ Hz, $A = 2$ mm (left) and $f_e = 7$ Hz, $A = 3$ mm (right)

A	1mm	2mm	3mm	4mm	6mm
f_e	k_s	k_s	k_s	k_s	k_s
1 Hz	5.61	5.66	5.67	5.67	5.67
2 Hz	5.61	5.66	5.67	5.67	5.67
4 Hz	5.64	5.66	5.68	5.68	-
5 Hz	5.64	5.68	5.69	-	-
7 Hz	5.69	5.72	5.73	-	-
10 Hz	5.77	5.79	-	-	-
14 Hz	5.94	-	-	-	-

Table 4.3: Shock absorber spring dynamic stiffness k_s [N/mm]

4.3.1 Characterisation and model selection

Two typical spring work diagrams are shown in Figure 4.9. The spring is seen to be almost linear in the range of the experimental test. First order polynomials are fitted to the measured data to estimate the spring stiffness. Table 4.3 shows spring stiffness, k_s, over a range of excitation frequencies and amplitudes.

Slight hysteresis is observed at the higher excitation frequencies and amplitudes. The energy dissipation per cycle, ΔW, at an excitation frequency of 7 Hz and an

A	1mm	2mm	3mm	4mm
f_e	MSE	MSE	MSE	MSE
1 Hz	-	0.5	1.3	0.6
2 Hz	6.2	0.1	0.5	0.0
4 Hz	0.0	0.0	0.0	0.0
5 Hz	0.3	0.1	0.0	-
7 Hz	0.5	0.0	0.0	-
10 Hz	0.4	0.0	-	-
14 Hz	0.4	-	-	-

Table 4.4: Linear spring model MSE at a range of excitation frequencies and amplitudes

amplitude of 3 mm, is among the highest with a value of 0.0133 J. Comparing this value with the corresponding value from the damper revealed that the energy loss in the spring is over 14 times less than that of the damper. At lower amplitudes and frequencies the energy dissipation of the spring is over 40 times less than that of the damper. It is therefore concluded that damping in the spring is negligible.

4.3.2 Parameter estimation and model validation

The spring stiffness does not show significant dependence on excitation frequency or amplitude. The mean dynamic spring stiffness is found to be 5.69 N/mm. The static stiffness of the spring as per the spring specifications is 4.9 N/mm, indicating that the stiffness of the spring increases under dynamic loading. Based on these results, the spring is modelled as a massless linear spring element with a stiffness of 5.69 N/mm. Table 4.4 shows the normalised mean squared error between measured spring force and simulated spring force. The linear spring model shows good correlation across the frequency and amplitude range of this testing.

4.4 Quarter car simulation

The result of the tyre, shock absorber and spring identification are now used to develop both linear and nonlinear quarter car models. The simulations are evaluated by comparing simulation results with measured data from the quarter car test rig. The quarter car rig is excited with an approximately sinusoidal excitation with peak to peak amplitude of 1 mm in the frequency range of 1.6–24.0 Hz. Fifty six

Parameter	Description	Measured value
m_u	Unsprung mass	8.02 Kg
m_s	Sprung mass	25.24 Kg
k_u	Tyre stiffness	89020 N/m
k_s	Spring stiffness	5690 N/m

Table 4.5: Linear quarter car simulation parameters

individual frequencies are used in this frequency range giving a frequency resolution, Δf, of 0.4 Hz. Tests are carried out at each frequency for 64 seconds and synchronous time averaged. Individual data segments are synchronised using the quarter car rig optical encoder signal, which is phase–locked to the rotation of the cam. Desynchronisation [180] and random phase shift errors (jitter) [181] in the synchronous averaging process are minimised using a technique known as Woody adaptive filtering [182]. The Woody adaptive filter is a special case and application of the cross–correlation technique. Signal segments are shifted to maximum cross correlations during averaging. The frequency spectrum of each averaged time history is calculated. The real and imaginary values are noted at the excitation frequency and are combined to give a response spectrum of the rig across the frequency range.

Due to the complex excitation frequency and amplitude dependence of the shock absorber, linear and piecewise linear models are fitted to the operational shock absorber characteristic at each frequency of interest. Fitting a model at each measurement frequency ensures that the linear and piecewise linear shock absorber models offer the best representation of the shock absorber characteristic at that individual frequency. The linear quarter car parameters fixed for the duration of this testing are shown in Table 4.5.

4.4.1 Linear quarter car simulation

The linear quarter car simulation uses a linear tyre model and the shock absorber is modelled as a linear spring and linear viscous damper in parallel. The simulated linear quarter car spectra and measured quarter car spectra are shown in Figure 4.10. The quarter car spectra show that the linear quarter car simulation provides a reasonable approximation of the magnitude of the unsprung mass acceleration across the full frequency range of the test. It does, however, over predict the magnitude of

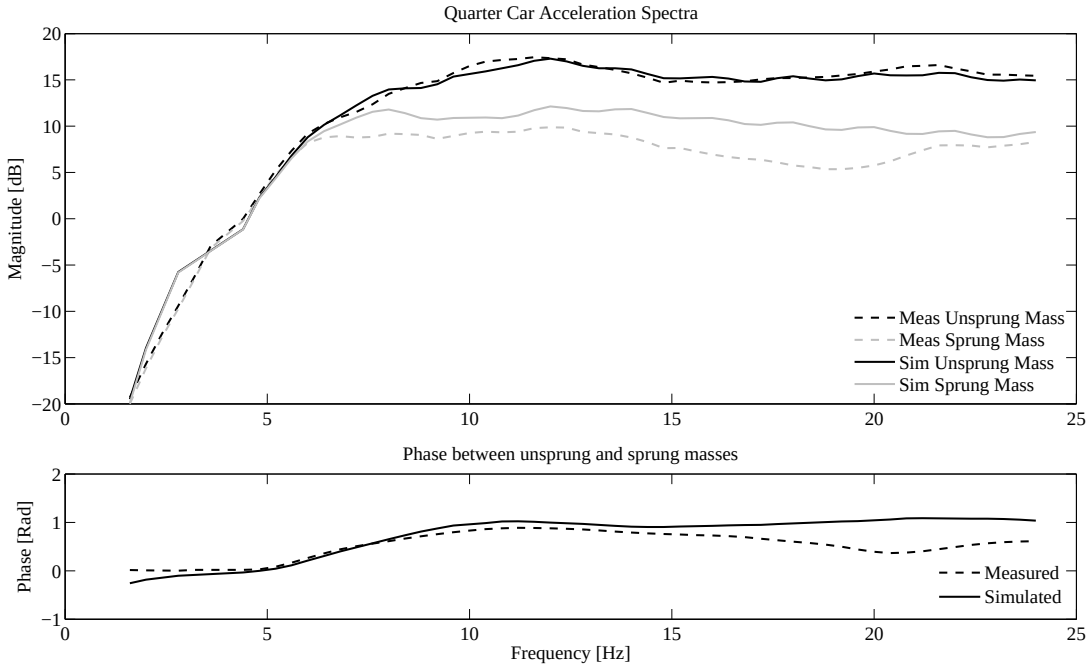

Figure 4.10: Linear quarter car model simulated and quarter car rig measured acceleration spectra between 1.6–24 Hz

the sprung mass acceleration above 5 Hz. Figure 4.11 shows simulated and measured acceleration time history comparisons at 5.2 Hz and 12.0 Hz. The Root Mean Square (RMS) signal amplitudes are also shown. The simulation accurately predicts both unsprung and sprung mass acceleration amplitudes at 5.2 Hz. The percentage errors in acceleration RMS are 3.7 % and 1.3 % for the unsprung mass and sprung mass, respectively. At 12.0 Hz the simulation under predicts the unsprung acceleration and over predicts the sprung mass acceleration. The percentage error is 19.1 % for the unsprung mass and 30.9 % for the sprung mass (Further discussion on these results can be found in § 6.1.2).

The presence of static friction in the damper is confirmed from the measured sprung and unsprung mass spectra. Notice how the measured sprung and unsprung mass spectra are almost identical below approximately 5 Hz. Correlation coefficients are calculated between the measured unsprung and sprung mass accelerations in the 1.6–24.0 Hz frequency range. The correlation coefficient is a measure of the strength of the relationship between the two signals. It is calculated using [24],

$$\rho_{xy}(\tau) = \frac{R_{xy}(\tau) - \mu_x \mu_y}{\sqrt{[R_{xx}(0) - \mu_x^2][R_{yy}(0) - \mu_y^2]}} \tag{4.21}$$

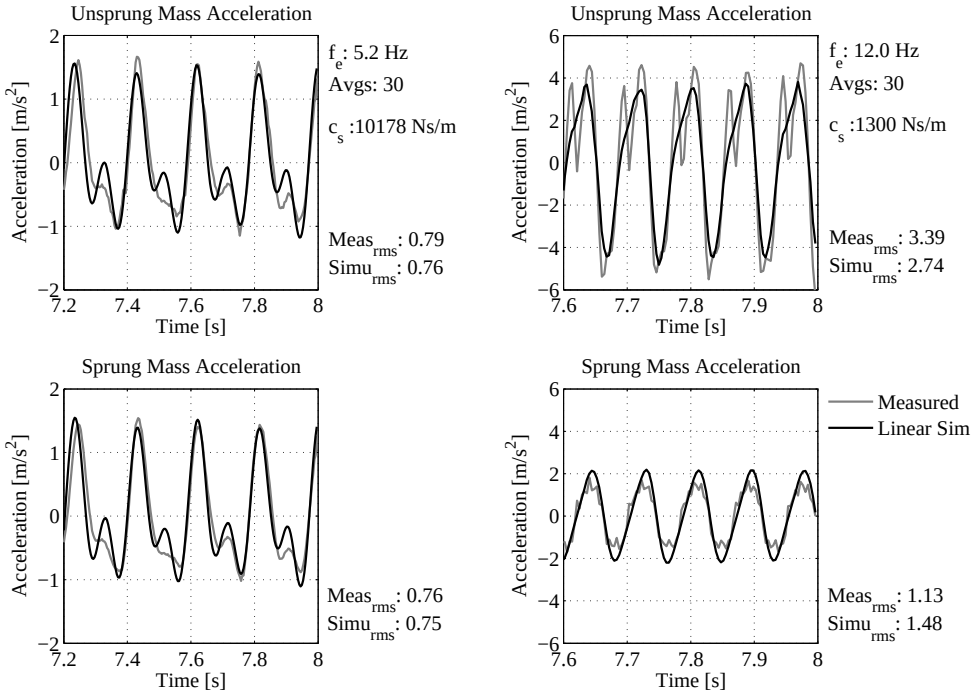

Figure 4.11: Linear quarter car model simulated and quarter car rig measured time history comparison at 5.2 Hz and 12.0 Hz

where $R_{xy}(\tau)$ is the cross–correlation between x and y at time τ, $R_{xx}(0)$ is the autocorrelation of x at $\tau = 0$, $R_{yy}(0)$ is the autocorrelation of y at $\tau = 0$, μ_x is the mean value of x and μ_y is the mean value of y. Correlation coefficients are calculated at $\tau = 0$. Correlation coefficients for measured accelerations are above 0.99 for excitation frequencies below approximately 5.0 Hz. This indicates that the unsprung and sprung masses movements are highly coupled below this frequency. The correlation coefficients at 5.2 Hz and 12.0 Hz are 0.98 and 0.51, respectively.

This provides an insight into why the linear model is more accurate at 5.2 Hz than at 12.0 Hz. The measurement at 5.2 Hz is very close to the static friction zone and as a result the dominant mode of damping in the shock absorber at this frequency is due to friction damping. A linear damping model gives a reasonable approximation of this damping at 5.2 Hz due to the small relative velocity across the shock absorber. At 12.0 Hz the damping is a combination of both friction damping and viscous damping due to the larger relative velocity and displacement across the shock absorber. A linear damping approximation at this frequency does not accurately describe the shock absorber characteristic. The effect of this static friction can be seen in the calculated linear damper coefficients. At 5.2 Hz the linear

damping coefficient is calculated to be 10178 N s/m compared with a value of 1300 N s/m at 12.0 Hz.

4.4.2 Nonlinear quarter car simulation

A nonlinear quarter car model is developed and tested at selected frequencies. The goal of this particular analysis is to quantify the accuracy improvement which may be obtained with the inclusion of nonlinear suspension component models in a quarter car simulation. The isolated identification of the shock absorber shows that the nonlinear LuGre model provides an accurate representation of the shock absorber across a broad frequency range (Figure 4.7). The LuGre model is known to be hard to implement in practical engineering applications [179]. In this investigation the complex nature of the model requires that a simulation sampling frequency of 8192 Hz be used to prevent numerical integration errors. This creates a number of practical problems due to long simulation run times and large data sets (A 128 second nonlinear quarter car simulation produces output time histories with in excess of 1 million data points). The trilinear model is chosen to model the shock absorber in this investigation. It provides a good compromise between the simplicity of a linear model and the complexity of the LuGre model.

The nonlinear quarter car model uses the nonlinear tyre model developed during isolated testing and also a trilinear damper model developed from operational testing. The frequencies selected for this test are 6.8 and 11.2 Hz. The optimised trilinear shock absorber model and equivalent linear shock absorber model for each of these frequencies are shown in Figure 4.12. The trilinear models are optimised using direct search methods. The optimisation is carried out in Matlab® using the *patternsearch* function. The MSE between the measured shock absorber force and the simulated shock absorber force is used as a measure of the model fit. The trilinear shock absorber models are shown to give significantly smaller error magnitudes than their linear equivalents.

4.4.3 Linear versus nonlinear quarter car simulation

The nonlinear simulation results are shown side by side with linear simulation results in Figures 4.13 and 4.14. The excitation frequency, damper parameters, measured

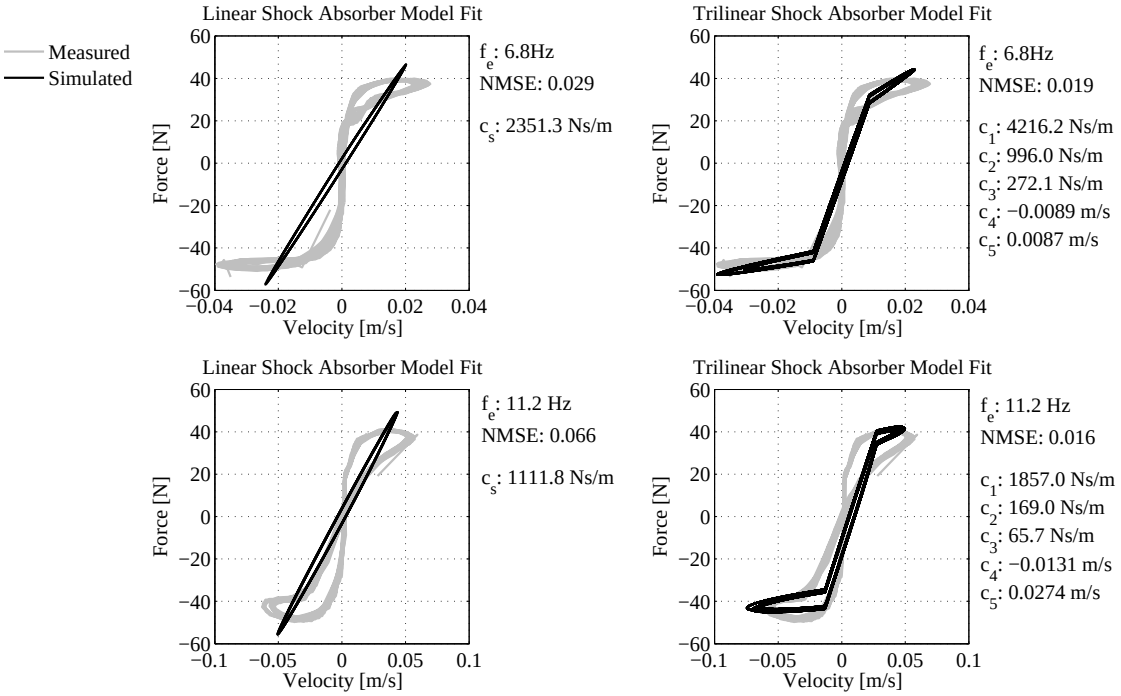

Figure 4.12: Linear and trilinear shock absorber models at 6.8 Hz and 11.2 Hz

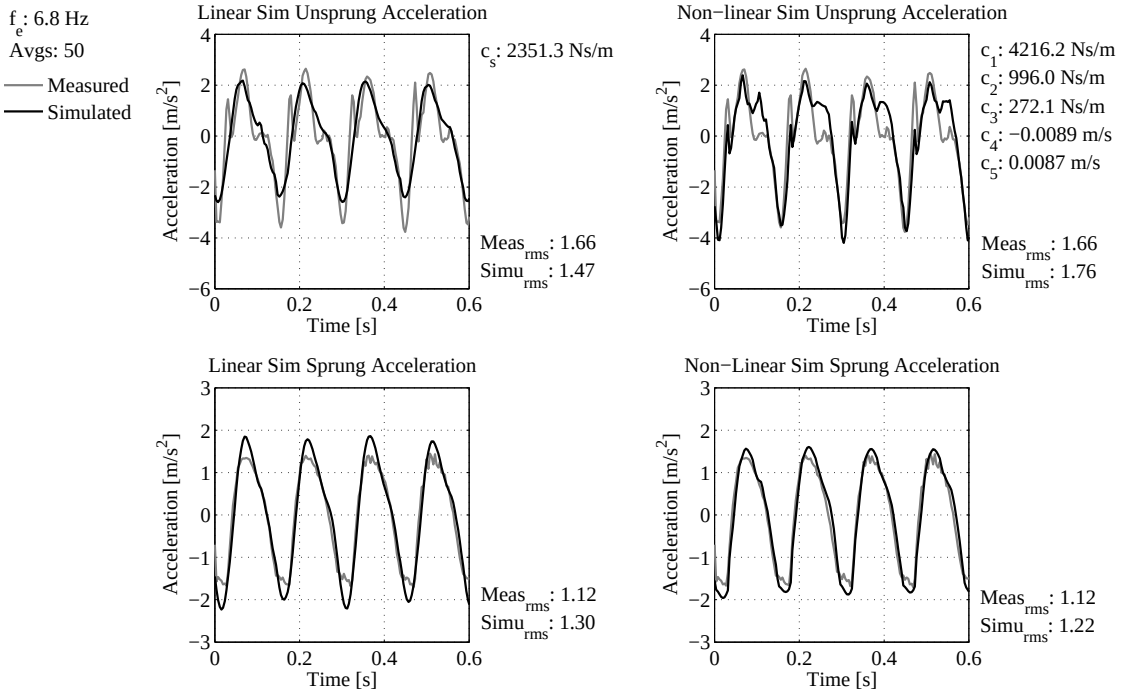

Figure 4.13: Linear and nonlinear quarter car simulation evaluation at 6.8 Hz

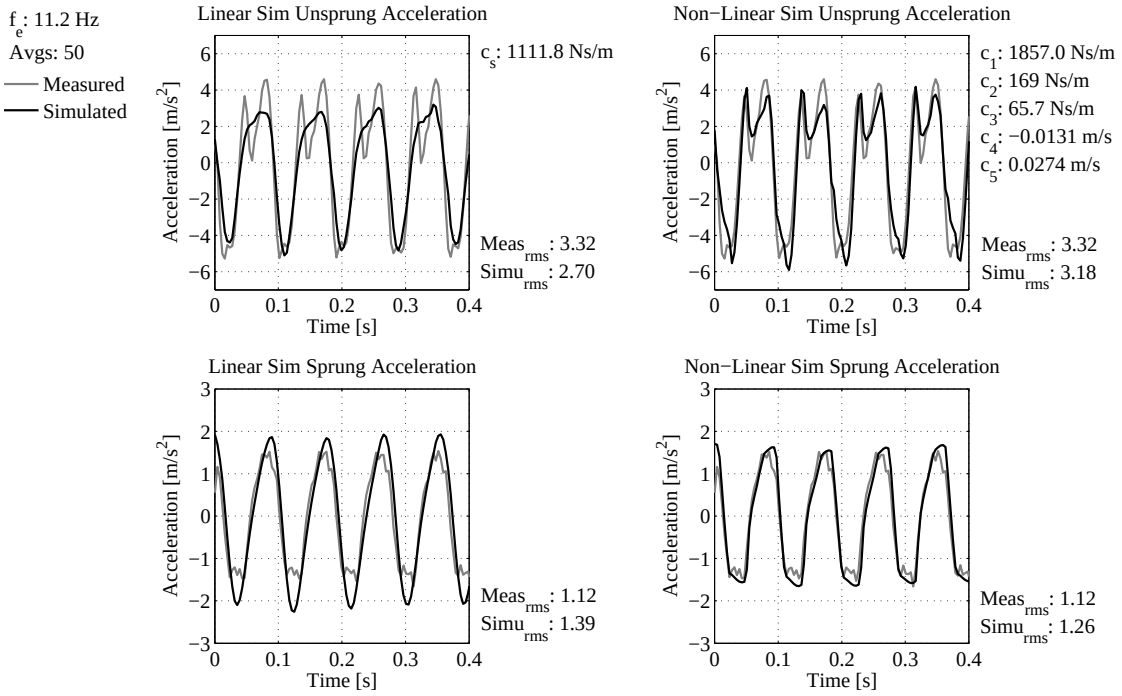

Figure 4.14: Linear and nonlinear quarter car simulation evaluation at 11.2 Hz

acceleration RMS and simulated acceleration RMS values are plotted with each Figure. In general, the results show that the nonlinear simulation provides a significant improvement over the linear simulation when compared with measured results from the quarter car rig. The nonlinear simulation accurately predicts both the unsprung and sprung mass accelerations in terms of magnitude and signal peak pattern. The linear simulation gives a reasonable approximation of the magnitude of the unsprung mass acceleration but over predicts the magnitude of the sprung mass acceleration. It also gives a poor estimate of the signal peak pattern. At 6.8 Hz the linear simulation shows a 11.4 % error in the unsprung mass acceleration and a 16.1 % error in the sprung mass acceleration. The nonlinear simulation showed errors of 6.0 % and 8.9 % for the unsprung and sprung mass accelerations, respectively. At 11.2 Hz the linear simulation shows an 18.7 % error in the unsprung mass acceleration and a 24.1 % error in the sprung mass acceleration. This is compared with 4.2 % and 12.5 % for the nonlinear simulation unsprung and sprung mass accelerations, respectively.

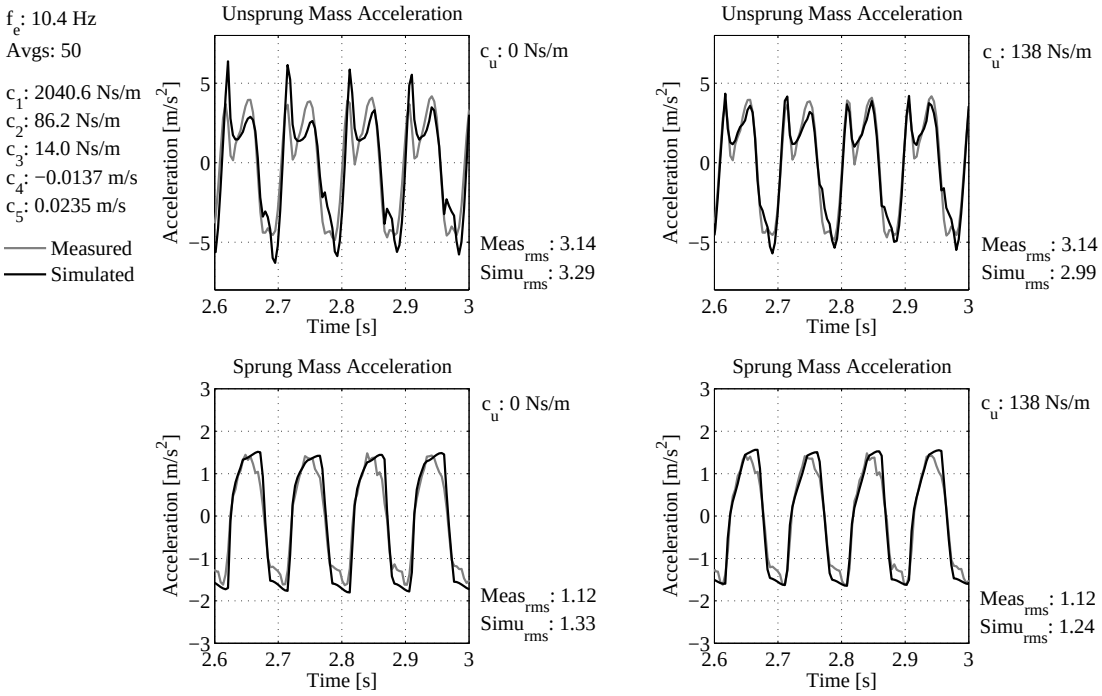

Figure 4.15: Comparison of nonlinear quarter car models without tyre damping (left) and with tyre damping (right) at 10.4 Hz

4.4.4 Effect of tyre damping

The literature highlighted differences of opinion among authors with regard to the importance of tyre damping in quarter car simulations. The damping of the tyre used in this experimental investigation is quantified using isolated tyre testing. To test the effect tyre damping has on simulation results, two quarter car simulations with optimised trilinear damper are run. Two tyre models are used. The first simulation uses a linear spring point contact model with no damping and the second uses a linear spring and viscous damper point contact model. The test is conducted at 10.4 Hz and the equivalent tyre viscous damping coefficient, c_u, is found to be 138 N s/m at this frequency (equation 4.5). The results from the two simulations are compared with measured results in Figure 4.15.

The simulation with tyre damping shows more damping in the peaks of the unsprung mass acceleration when compared with the simulation with no tyre damping. The simulation with no tyre damping and the simulation with tyre damping show maximum peak amplitudes of 6.4 m/s^2 and 4.3 m/s^2, respectively. This is compared with a measured maximum peak amplitude of 4.0 m/s^2. Both simulations show a

percentage error of 4.7 % in the RMS amplitude of the unsprung mass acceleration. The simulation with no tyre damping shows a percentage error of 17.8 % for sprung mass acceleration RMS amplitude while the simulation with tyre damping reduces this error to 10.7 %.

This chapter shows the development of linear and nonlinear quarter car simulations of the quarter car test rig. Force–response testing of the major components (tyre, damper, spring) provide the simulation parameters. Accurate linear and nonlinear models of the components are developed by disassembling the rig and testing the components in isolation. The nonlinear quarter car simulation, with nonlinear tyre and trilinear shock absorber, is seen to give good results when simulated data is compared with measured data from the quarter car test rig.

Chapter 5

Operational suspension system identification

Having identified the major quarter car rig components in isolation in Chapter 4, focus now turns to the operational identification of the system. The acquired signals for operational identification are sprung mass acceleration in the vertical direction and the unsprung mass accelerations in the transverse, fore-aft and vertical directions. These are signals which can easily be obtained by instrumenting a vehicle in service without interfering with vehicle operation. The boundary perturbation technique, used to identify suspension system components in the absence of a measured input force, is first introduced in section 5.1. The boundary perturbation technique is then developed under a controlled simulation environment. Results from the application of the technique to nonlinear quarter car simulations are presented in section 5.2. Both time and frequency domain approaches to the parameter estimation are documented. The robustness of the technique is examined for a number of simulation scenarios including noise polluted data, uncharacterised nonlinearities, hysteresis and unknown shock absorber model form. Focus then turns to the identification of the quarter car test rig in section 5.3. The results from both time and frequency domain approaches to the experimental identification of the quarter car rig are presented.

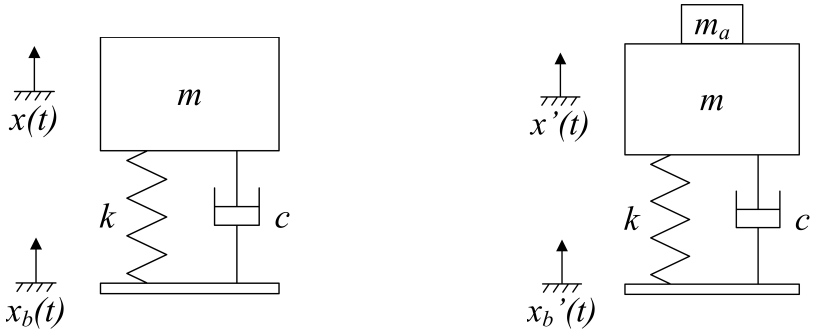

(a) Original system (b) Perturbed system

Figure 5.1: SDOF system subject to base excitation

5.1 Boundary perturbation technique

In the absence of a known excitation force on a system, a technique known as boundary perturbation can be used to identify the system using only measured system responses. The boundary perturbation technique is first introduced here using a Single Degree–Of–Freedom (SDOF) example before being discussed in the context of vehicle suspension systems. Consider a SDOF system subject to base excitation, as shown in Figure 5.1a. The equation of motion of the system is given by,

$$m\ddot{x} + c\left(\dot{x} - \dot{x}_b\right) + k\left(x - x_b\right) = 0. \tag{5.1}$$

Consider the case where parameters m, c and k are unknown and signals x and x_b, and their derivatives, are measured. Equation 5.1 cannot be solved directly for m, c and k but can be reformulated to yield,

$$\frac{c}{m}\left(\dot{x} - \dot{x}_b\right) + \frac{k}{m}\left(x - x_b\right) = \ddot{x}. \tag{5.2}$$

If N samples of each of the measured signals are recorded, this equation can be written as an over determined set of equations as follows,

$$\begin{bmatrix} (\dot{x} - \dot{x}_b)_1 & (x - x_b)_1 \\ (\dot{x} - \dot{x}_b)_2 & (x - x_b)_2 \\ \vdots & \vdots \\ (\dot{x} - \dot{x}_b)_N & (x - x_b)_N \end{bmatrix} \begin{Bmatrix} c/m \\ k/m \end{Bmatrix} = \begin{bmatrix} \ddot{x}_1 \\ \ddot{x}_2 \\ \vdots \\ \ddot{x}_N \end{bmatrix} \tag{5.3}$$

Equation 5.3 can be solved for the mass normalised damping (c/m) and mass normalised stiffness (k/m) parameters using standard least squares techniques. Now

consider the case where the same system is perturbed by a known mass m_a (Figure 5.1b) such that,

$$m^{'} = m + m_a. \tag{5.4}$$

If signals x' and x'_b (and their derivatives) are measured, the analysis above can be repeated to yield estimates of the new mass normalised damping $\left(c/m^{'}\right)$ and mass normalised stiffness $\left(k/m^{'}\right)$ parameters. Using the mass normalised stiffness parameters estimated from the original and perturbed systems, and equation 5.4, the following relationship can be established,

$$\frac{(k/m)}{(k/m^{'})} = \frac{m^{'}}{m} = \frac{(m + m_a)}{m} \tag{5.5}$$

leading to an expression for the estimated system mass,

$$\hat{m} = m_a \left(\frac{(k/m)}{(k/m^{'})} - 1 \right)^{-1}. \tag{5.6}$$

The estimated system mass ($\hat{m}$) can be used to estimate the system stiffness, $\hat{k}$, and system damping, $\hat{c}$.

Now consider a vehicle suspension system. When sprung mass and unsprung mass accelerations are measured during suspension operation, a simple technique which involves the addition of a known mass to the sprung mass of the vehicle is used to determine the parameters of the shock absorber. This technique involves no disassembly of the vehicle suspension system and no measurement of the force input from the road surface to the tyre patch. Two road tests of the vehicle are required, one with no added mass and one with the known added mass attached. Consider the linear quarter car model shown in Figure 2.25. The sprung mass equation of motion is given by,

$$m_s \ddot{x}_s - c_s \left(\dot{x}_u - \dot{x}_s \right) - k_s \left(x_u - x_s \right) = 0. \tag{5.7}$$

If N samples of $\ddot{x}_s$, $\dot{x}_s$, x_s, $\dot{x}_u$ and x_u are recorded, the problem can be formulated as follows,

$$\begin{bmatrix} \left(\dot{x}_u - \dot{x}_s\right)_1 & \left(x_u - x_s\right)_1 \\ \left(\dot{x}_u - \dot{x}_s\right)_2 & \left(x_u - x_s\right)_2 \\ \vdots & \vdots \\ \left(\dot{x}_u - \dot{x}_s\right)_N & \left(x_u - x_s\right)_N \end{bmatrix} \begin{Bmatrix} c_s/m_s \\ k_s/m_s \end{Bmatrix} = \begin{bmatrix} \ddot{x}_{s1} \\ \ddot{x}_{s2} \\ \vdots \\ \ddot{x}_{sN} \end{bmatrix} \tag{5.8}$$

Direct Parameter Estimation (DPE) methods are used to obtain estimates for sprung mass normalised damping (c_s/m_s) and stiffness (k_s/m_s). The analysis is repeated with a known mass, m_a, added to the sprung mass such that,

$$m_s^{'} = m_s + m_a. \tag{5.9}$$

New estimates of sprung mass normalised damping ($c_s/m_s^{'}$) and stiffness ($k_s/m_s^{'}$) are obtained. In the SDOF example above, the mass normalised stiffness is used to estimate the system mass. However, the mass normalised damping can also be used for this purpose. The concept of a significance factor is introduced here to determine which of the mass normalised parameters should be used to give the best estimate of the system mass. The significance factor is used to determine which term is most important in the model formulation. The significance factor of the individual model terms, θ, is defined as follows,

$$s_\theta = 100\frac{\sigma_\theta^2}{\sigma_y^2} \tag{5.10}$$

where, σ_y^2 is the variance of the estimated output with all model terms included and σ_θ^2 is the variance of the output with only the θ term included. Roughly speaking, s_θ can be interpreted as the percentage contribution to the model variance by the individual model term θ. Assuming (k_s/m_s) is the most significant term in this example, dividing (k_s/m_s) by $(k_s/m_s^{'})$, and using equation 5.9 leads to an estimate of the sprung mass, $\hat{m}_s$,

$$\frac{(k_s/m_s)}{(k_s/m_s^{'})} = \frac{m_s^{'}}{m_s} = \frac{(m_s + m_a)}{m_s} \tag{5.11}$$

$$\Rightarrow \hat{m}_s = m_a \left(\frac{(k_s/m_s)}{(k_s/m_s^{'})} - 1 \right)^{-1}. \tag{5.12}$$

The estimated sprung mass, $\hat{m}_s$, can be used to obtain estimates of the shock absorber damping, $\hat{c}_s$, and stiffness, $\hat{k}_s$, parameters. The analysis can be extended to include nonlinearities characterised using the Restoring Force Surface (RFS) method.

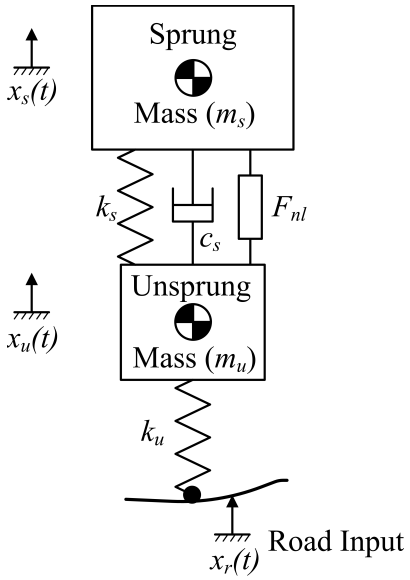

Figure 5.2: Two DOF nonlinear quarter car model

5.2 Application of the boundary perturbation technique to simulated data

A series of nonlinear quarter car simulations are conducted to develop the boundary perturbation technique under a controlled simulation environment. The nonlinear quarter car simulation setup, shown in Figure 5.2, is used for this purpose. The differential equations of motion describing the system are,

$$m_u\ddot{x}_u + c_s\left(\dot{x}_u - \dot{x}_s\right) + k_s\left(x_u - x_s\right) + k_u\left(x_u - x_r\right) + F_{nl}(x_u - x_s, \dot{x}_u - \dot{x}_s) = 0 \quad (5.13)$$

$$m_s\ddot{x}_s - c_s\left(\dot{x}_u - \dot{x}_s\right) - k_s\left(x_u - x_s\right) - F_{nl}(x_u - x_s, \dot{x}_u - \dot{x}_s) = 0 \quad (5.14)$$

where, the term F_{nl} represents the force due to the nonlinear elements in the shock absorber. For this investigation the shock absorber nonlinearities are chosen to be coulomb friction and cubic stiffness,

$$F_{nl} = \mu_s\left(sign\left(\dot{x}_u - \dot{x}_s\right)\right) + k_n\left(x_u - x_s\right)^3. \quad (5.15)$$

The simulations are chosen to have a dominant coulomb friction nonlinearity and a mild cubic stiffness. The parameter estimation is first carried out to identify both nonlinearities. The second situation looks at identifying just the dominant nonlinearity, ignoring the mild cubic stiffness. This approach examines the influence

Parameter	Value	Unit
m_u	10.0	kg
m_s	25.0	kg
k_u	9x10^4	N/m
k_s	5x10^3	N/m
ζ	10.0	%
k_n	5.0	%
μ_s	50.0	%

Table 5.1: Quarter car simulation parameters

of uncharacterised nonlinearities on the system identification. The application of the method to nonlinear quarter car simulations with memory, is then examined. Both a backlash parameter and a Bouc–Wen shock absorber model are employed for this purpose. For the Bouc–Wen simulations the exact shock absorber model form is assumed to be unknown. This represents a practical identification problem, where characterisation must be conducted to select an appropriate model form.

Simulated time data are obtained by integrating the equation of motion with a fourth order Runge–Kutta scheme [16]. The road input excitation to the tyre is simulated with a white noise signal band limited to 1–50 Hz, using a sixth order Butterworth filter [183]. The input signal Root Mean Square (RMS) amplitude is equal to 0.0005 m. The small amplitude is chosen based on observation and basic measurement of a smooth road surface. The sampling frequency used is 256 Hz and 524288 samples of data are taken for each simulation. The stochastic input excitation is different for each simulation and is unmeasured. Each simulation is repeated 100 times to yield an ensemble of parameter estimates. Table 5.1 shows the quarter car parameters used for the simulation. The static friction (μ_s) and cubic stiffness (k_n) nonlinearities are specified as a percentage of the total shock absorber force RMS magnitude. The added mass, used for boundary perturbation, is set at 10 % of the sprung mass magnitude for all simulations. Simulations are run with and without noise. For the simulations with noise, measured signals are noise polluted to a level of 5 % of their respective RMS value, with uncorrelated white noise. The simulation setup parameters, summarised in Table 5.2, are used for all simulations unless otherwise stated.

Sampling frequency, f_s	Time points, N	Simulation Runs	Input	Input Amplitude (RMS)	Input filter	Solution
256 Hz	524288	100	White Noise	0.0005 m	BP: 1–50 Hz	4^{th} order Runge–Kutta

Table 5.2: Nonlinear quarter car simulation setup parameters

5.2.1 Time domain approach

The boundary perturbation technique is first implemented using time domain parameter estimation. DPE is used to estimate the system parameters in each case. Shock absorber characterisation is carried out using RFS methods. In the absence of a measured shock absorber force, the sprung mass acceleration can be used, effectively giving a RFS scaled by the magnitude of the sprung mass [70, 76].

Nonlinear quarter car simulation

Figure 5.3 shows the RFS for the shock absorber in the quarter car simulation. The dominant static friction nonlinearity is clearly visible at zero velocity in the restoring force surface plot and the characteristic diagram. The effect of the mild cubic stiffness can be observed in the work diagram in Figure 5.3.

The boundary perturbation technique is first implemented with all the nonlinearities in the shock absorber included in the problem formulation. The ensemble mean and standard deviations of all parameter estimates, with and without noise, are shown in Table 5.3 (the Matlab® function *lssvd*, developed for boundary perturbation least squares parameter estimation is documented in Appendix C). To assess the effect of uncharacterised nonlinearities on the parameter estimation process, a second parameter estimation is carried out ignoring the cubic stiffness. The results are shown in Table 5.4. In the absence of noise, exact estimates are obtained for all parameters when all nonlinearities are included in the estimation process. When the cubic stiffness is ignored, accurate estimates of m_s, c_s and μ_s are obtained, while k_s showed an error of 9.6 %. The estimated linear stiffness has increased to componsate for the lack of a cubic stiffness term in the estimation process.

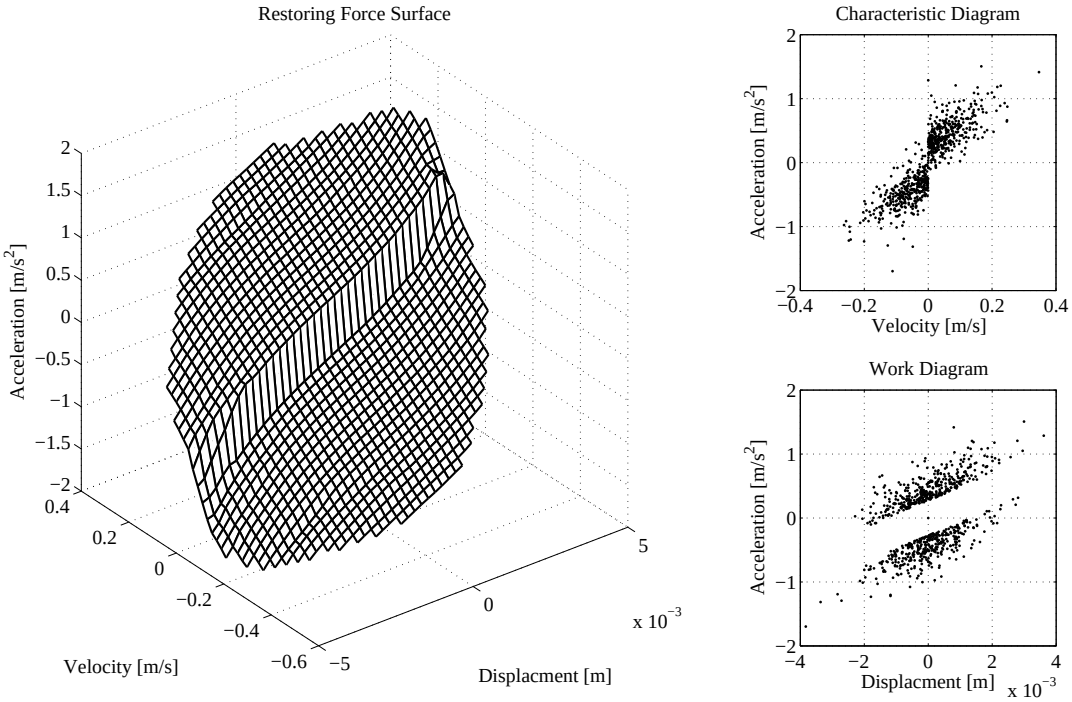

Figure 5.3: Nonlinear quarter car simulation restoring force surface

No Noise

Parameter	Actual	Estimated	Std Dev	% Error
m_s	25.0	25.0	0.0	0.0
k_s	5000.0	5000.0	0.0	0.0
c_s	70.7	70.7	0.0	0.0
μ_s	6.3	6.3	0.0	0.0
k_n	1.68x10^8	1.68x10^8	0.0	0.0

5% Noise

Parameter	Actual	Estimated	Std Dev	% Error
m_s	25.0	25.0	0.3	+0.2
k_s	5000.0	4959.9	69.0	+0.8
c_s	70.7	76.1	1.0	+7.7
μ_s	6.3	5.6	0.1	-10.7
k_n	1.58x10^8	1.59x10^8	2.3x10^6	+0.5

Table 5.3: Estimated parameters; both friction and cubic stiffness nonlinearities included

No Noise

Parameter	Actual	Estimated	Std Dev	% Error
m_s	25.0	25.0	0.4	+0.0
k_s	5000.0	5481.5	9.2	+9.6
c_s	70.7	70.6	0.1	-0.1
μ_s	6.3	6.3	0.0	+0.0

5% Noise

Parameter	Actual	Estimated	Std Dev	% Error
m_s	25.0	25.0	0.4	+0.1
k_s	5000.0	5449.9	79.1	+9.0
c_s	70.7	76.1	1.0	+7.7
μ_s	6.3	5.6	0.1	-10.7

Table 5.4: Estimated parameters; only dominant friction nonlinearity included

Nonlinear quarter car simulation with memory

In practical applications the characteristic of the shock absorber may not be readily identifiable as a spring-damper-friction model. Other more complex nonlinearities such as hysteresis may be present in the shock absorber. Hysteretic systems are among the more difficult nonlinear systems to investigate and identify [48]. To assess the effect of hysteresis on the parameter estimation procedure a nonlinear simulation is run with hysteresis (backlash) in damping. The backlash magnitude is expressed as a percentage of the RMS relative velocity across the shock absorber. Figure 5.4 shows the RFS for the nonlinear quarter car model with 10 % backlash. Table 5.5 shows the ensemble mean error and standard deviation of the estimates for varying backlash between 0 and 10 %. Another simulation is now run with 10 % backlash, but in this case a backlash parameter is included in the model formulation (backlash is introduced by processing the relevant signal before conducting the parameter estimation; when the input changes direction, an initial change in input has no effect on the output until the specified backlash deadband is overcome). The results of the revised parameter estimation are shown in Table 5.6. Table 5.5 shows that as backlash approaches 10 % large errors on the parameter estimates are seen. However, Table 5.6 indicates that the inclusion of a backlash term in the model allows excellent parameter estimates to be obtained even at high backlash levels.

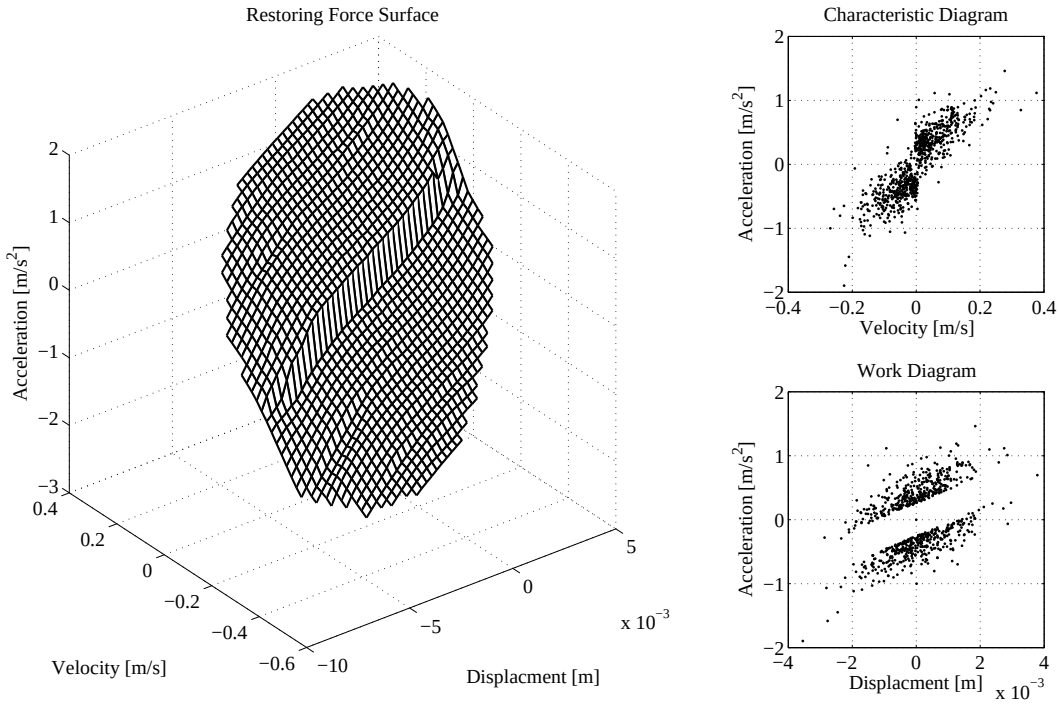

Figure 5.4: Nonlinear quarter car simulation RFS (10% backlash)

No Noise

	Backlash %				
Parameter	0.00	0.01	0.10	1.00	10.00
m_s	0.00	+0.00	+0.00	-0.07	-0.47
k_s	0.00	+0.01	+0.14	+1.28	+9.28
c_s	0.00	+0.01	+0.17	+1.63	+7.96
μ_s	0.00	-0.02	-0.22	-2.34	-12.82
k_n	0.00	-0.04	-0.38	-4.02	-26.91

5% Noise

	Backlash %				
Parameter	0.00	0.01	0.10	1.00	10.00
m_s	+0.15	-0.10	-0.96	-0.27	-0.25
k_s	-0.46	-0.70	-0.60	+0.17	+8.95
c_s	+8.04	+7.79	+7.78	+7.53	+9.11
μ_s	-10.38	-10.64	-10.60	-10.77	-14.24
k_n	+0.90	+0.44	+0.39	-2.37	-25.67

Table 5.5: Estimated parameter error for varying backlash between 0.0 %–10.0 %

No Noise

Parameter	Actual	Estimated	Std Dev	% Error
m_s	25.0	25.0	0.0	0.0
k_s	5000.0	5000.0	0.0	0.0
c_s	70.7	70.7	0.0	0.0
μ_s	6.3	6.3	0.0	0.0
k_n	1.68x10^8	1.68x10^8	0.0	0.0

5% Noise

Parameter	Actual	Estimated	Std Dev	% Error
m_s	25.0	24.9	0.4	-0.2
k_s	5000.0	4972.0	77.5	-0.6
c_s	70.7	75.9	1.1	+7.3
μ_s	6.3	5.7	0.1	-10.2
k_n	1.68x10^8	1.57x10^8	2.6x10^6	-0.9

Table 5.6: Nonlinear quarter car model with 10% backlash, estimated parameters with backlash included in the model formulation

Unknown shock absorber model structure

So far reasonable parameter estimates have been obtained in situations where the shock absorber model form is known, backlash is small (<1 %) or accounted for in the model and noise is low. A more complex identification problem is now examined. Consider a simulation with unknown shock absorber model structure exhibiting hysteretic behaviour. This replicates the practical situation where measured operational data must be used to characterise the suspension system. One method proposed in the literature of simulating hysteretic behaviour is the Bouc–Wen model. The Bouc–Wen model has the ability to capture the properties of a wide class of real nonlinear hysteretic systems [48]. The shock absorber is modelled as a linear spring and damper in parallel with a Bouc–Wen hysteretic element, as described by the following equation for the shock absorber force,

$$F = c_s\dot{x}(t) + k_s x(t) + \alpha\nu(t) \tag{5.16}$$

where, the evolutionary variable ν is governed by,

$$\dot{\nu}(t) = B\dot{x}(t) - \beta\left|\dot{x}(t)\right|\nu(t)\left|\nu(t)\right|^{n-1} - \gamma\dot{x}(t)\left|\nu(t)\right|^{n}. \tag{5.17}$$

Param	Value	Unit
m_u	10.0	Kg
m_s	25.0	Kg
k_u	9x10^4	N/m
k_s	5x10^3	N/m
ζ	10.0	%
B	800	-
β	1x10^4	-
γ	1x10^3	-
n	1	-
α	300	-

Table 5.7: Bouc–Wen quarter car simulation parameters

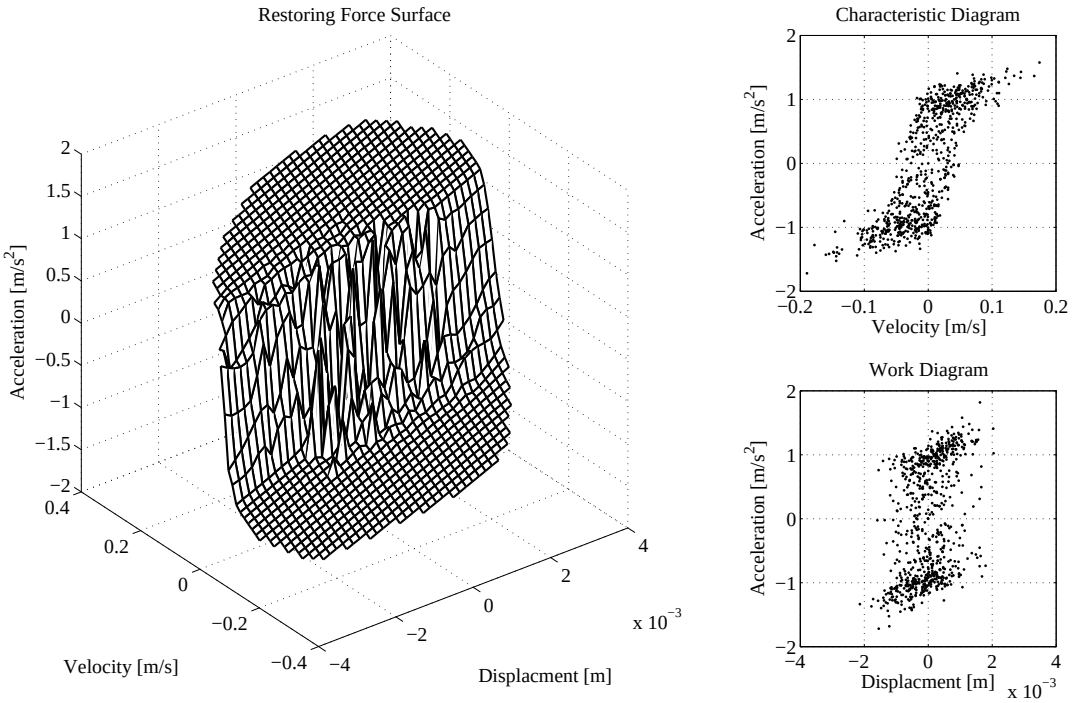

Figure 5.5: Quarter car simulation with Bouc–Wen shock absorber RFS

The shape of the hysteric loop is governed by the coefficients B, α, β, γ and n. Simulation parameters for the revised quarter car model are given in Table 5.7. Figure 5.5 shows the RFS for the Bouc–Wen quarter car simulation. The hysteresis in the system can be identified from the stochastic nature of the RFS at low velocities. The interpolated RFS attempts to average the separate hysteresis paths in compression and rebound. The RFS identifies the 'backbone' of the shock absorber, showing the significant dynamical behaviour of the system [21].

No Noise

Parameter	Actual	Estimate	Std Dev	% Error
m_s	25.0	24.9	1.5	-0.4
k_s	5000.0	11072.7	673.0	+121.5
c_s	70.7	244.0	14.2	+245.1
μ_s	-	5.8	0.4	-

5% Noise

Parameter	Actual	Estimate	Std Dev	% Error
m_s	25.0	25.0	1.8	+0.0
k_s	5000.0	11053.6	796.9	+121.1
c_s	70.7	243.9	17.1	+244.9
μ_s	-	5.8	0.4	-

Table 5.8: Estimated Bouc–Wen quarter car model parameters

From analysis of the RFS it is clear that a simple spring–mass–damper model will not accurately represent the shock absorber. In fact the selection of an appropriate model to represent the shock absorber characteristic in this case proves extremely difficult. The shock absorber has not only a non–polynomial type characteristic, but its RFS is also not an explicit function of just its present states. As an initial investigation, the nonlinear quarter car model, with static friction is used to model the system. This is a reasonable first model selection based on one interpretation of the RFS. The discontinuity in the system at low velocities resembles that of a coulomb friction characteristic. Due to the complex nature of the Bouc–Wen model a simulation sampling rate of 2048 Hz is required to prevent numerical integration errors. The simulation signals are downsampled to 256 Hz before analysis. The estimated parameters with and without noise are shown in Table 5.8. The simulated and estimated time histories are compared, for the case with no noise, in Figure 5.6.

The model selection is refined to include the backlash evident in the characteristic diagram in Figure 5.5. The width of the hysteretic region, in m/s, when the acceleration is zero, is used as a measure of the backlash in the system. The backlash input signal for the parameter estimation process is generated from the relative velocity signal across the shock absorber. When the velocity changes direction, the backlash deadband must be overcome before the velocity continues in the opposite direction. The measured deadband is 0.07 m/s. An iterative approach is then applied to the

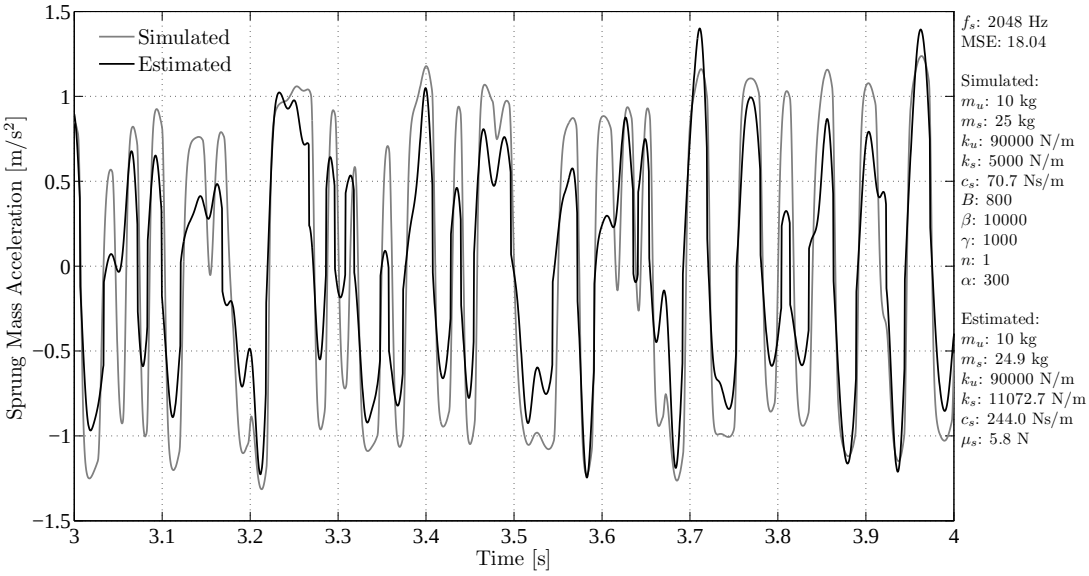

Figure 5.6: Bouc–Wen quarter car model simulated and estimated sprung mass acceleration time histories

identification of the optimal level of backlash in the model. This involves the identification of model parameters using the initial estimate of 0.07 m/s. The Mean Squared Error (MSE) between the identified model and the true Bouc–Wen quarter car simulation is evaluated for a range of backlash values. The backlash value, which minimises the MSE of the estimated model, is then taken as the new backlash value and the process is repeated until there is no significant decrease in the model MSE. The results of the analysis with an optimal backlash value of 0.038 m/s are shown in Table 5.9. The simulated and estimated time histories are compared, for the case with no noise and backlash, in Figure 5.7.

The boundary perturbation analyses carried out thus far, require that a shock absorber model form must be selected for use in the problem formulation. A different approach is examined here, which uses the nonlinear system identification methods presented by Masri *et al.* [48] (§ 2.3.2), adapted for the operational case. Using this method, the algorithm itself determines the required parameters to best represent the system. The set of basis functions for the analysis are chosen to be,

$$basis = (sign(\dot{x}_u - \dot{x}_s), PS) \tag{5.18}$$

where, PS represents the list of basis terms in the power series expansion of the

No Noise

Parameter	Actual	Estimate	Std Dev	% Error
m_s	25.0	25.3	1.3	+1.2
k_s	5000.0	7353.5	372.4	+47.1
c_s	70.7	208.6	11.2	+195.0
μ_s	-	11.7	0.6	-

5% Noise

Parameter	Actual	Estimate	Std Dev	% Error
m_s	25.0	25.1	1.3	+0.4
k_s	5000.0	7563.4	399.6	+51.3
c_s	70.7	206.8	11.3	+192.5
μ_s	-	11.5	0.6	-

Table 5.9: Estimated Bouc–Wen quarter car model parameters with backlash

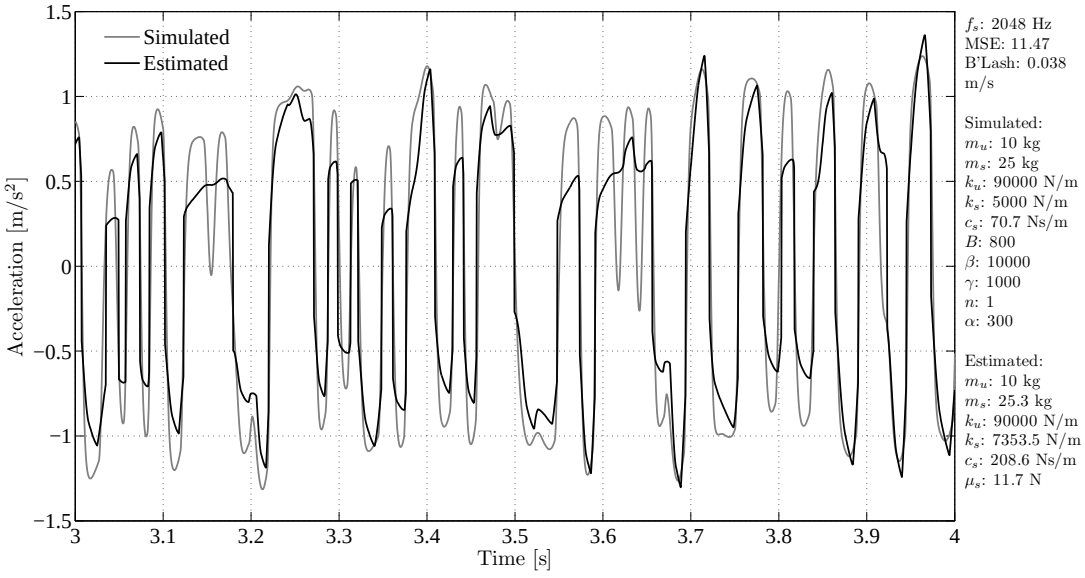

Figure 5.7: Bouc–Wen quarter car model simulated and estimated sprung mass acceleration time histories (with Backlash)

No Noise				
Parameter	Actual	Estimate	Std Dev	% Error
m_s	25.0	25.1	3.8	+0.6
k_s	5000.0	13664.7	2038.8	+173.3
c_s	70.7	360.7	51.7	+410.1

Table 5.10: Estimated Bouc–Wen quarter car model parameters, using revised time domain approach

doubly indexed series,

$$PS = \sum_{i=0}^{i_{max}} \sum_{j=0}^{j_{max}} (x_u - x_s)^i (\dot{x}_u - \dot{x}_s)^j \tag{5.19}$$

for i_{max} and j_{max} equal to 3. The results of the analysis are shown in Table 5.10.

In all simulated cases for the Bouc–Wen quarter car model, the actual (hysteretic) shock absorber model is not included in the estimation process. Therefore, the identification approach is effectively a non-parametric one. Sprung mass estimates are good in all cases, but the identified linear stiffness and damping parameters have effectively become equivalent linear stiffness and damping values, due to the non–parametric nature of the methods when applied to an unknown shock absorber model form.

5.2.2 Frequency domain approach

Time domain methods provide accurate estimates of sprung mass in all cases. Less success is obtained in the estimation of true values of stiffness and damping in the case when the exact shock absorber model form is unknown. The frequency domain approach applied here assumes that the mass has been calculated from the time domain procedures. The aim here is to obtain a more accurate estimate of the linear stiffness parameter in the suspension system.

The frequency domain approach aims to use Reverse Multiple Input/Single Output (R–MISO) to develop the linear Frequency Response Function (FRF) of the suspension system in order to identify the linear system parameters. In the case of the two Degree–Of–Freedom (DOF) quarter car model, the sprung mass equation of motion

(given in equation 5.13) can be rearranged as follows,

$$\ddot{x}_s = \frac{1}{m_s}\left[c_s\left(\dot{x}_u - \dot{x}_s\right) + k_s\left(x_u - x_s\right) + F_{nl}(x_u - x_s, \dot{x}_u - \dot{x}_s)\right]. \tag{5.20}$$

This equation shows that the acceleration of the sprung mass is equal to the mass normalised shock absorber force. In this case the inputs to the R–MISO analysis are chosen to be the relative displacement across the shock absorber $(x_u - x_s)$ and nonlinear functions of $(x_u - x_s)$ and $(\dot{x}_u - \dot{x}_s)$ representing the shock absorber nonlinearity form. The R–MISO output is $\ddot{x}_s$. This approach allows for the calculation of a linear FRF between $x_u - x_s$ and $\ddot{x}_s$, after the nonlinearities due to the shock absorber have been removed from the problem, using conditioned spectral analysis.

The nonlinear function inputs are selected by examining the ordinary coherence between a set of possible inputs and the output. The area under the ordinary coherence function in the frequency range of interest is calculated and expressed as a percentage of perfect coherence. Functions with a coherence level above a selected tolerance percentage are included in the problem formulation. The selected set of input functions is then ordered based on the magnitude of their ordinary coherence with the output. The proposed R–MISO formulation is then checked to ensure the problem is well-defined. The following four conditions must be satisfied [23],

- Ordinary coherence between any pair of input records should not equal unity;
- Ordinary coherence between any input and the output should not equal unity;
- Multiple coherence between any input and the other inputs, excluding the given input, should not equal unity;
- Multiple coherence between the inputs and the outputs should be sufficiently high (> 0.5).

Nonlinear quarter car simulation

As in the time domain case, the method is first applied to the quarter car simulation with static friction and cubic stiffness nonlinearitites. The simulation parameters remain unchanged, and are shown in Table 5.1. A three input single output model is chosen. The model setup is shown diagrammatically in Figure 5.8. The inputs records $x_1(t)$, $x_2(t)$ and $x_3(t)$ are defined as $(x_u - x_s)$, $sign(\dot{x}_u - \dot{x}_s)$ and $(x_u - x_s)^3$,

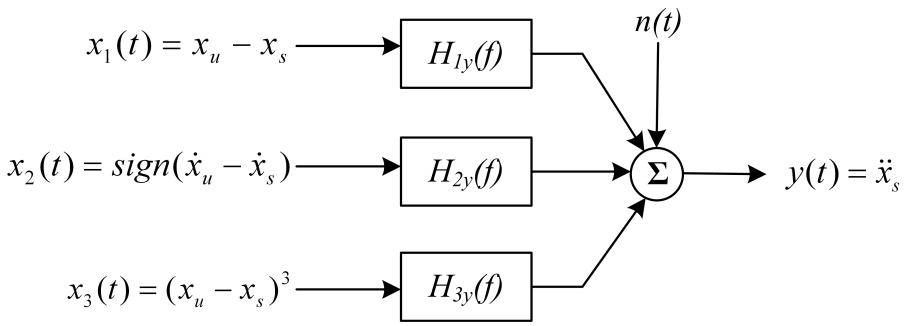

Figure 5.8: Three input single output R–MISO setup

Sampling frequency, f_s	Time points, N	Block size	Overlap	Window Type	Filter type	FRF Estimator
256 Hz	2097152	2048	50 %	Hanning	LP:50 Hz	H_1

Table 5.11: Signal processing parameters used for quarter car simulation R–MISO analysis

respectively. The output $y(t)$ is equal to $\ddot{x}_s$. The terms H_{1y}, H_{2y} and H_{3y} are the FRF's between the respective inputs and the output. The signal processing parameters used for the R–MISO analysis are shown in Table 5.11. Figure 5.9 shows results of the analysis[1]. It can be seen that the value of H_{1y} at 0 Hz, is equal to the mass normalised stiffness. Estimates of mass normalised μ_s and k_n can be obtained from the magnitudes of H_{2y} and H_{3y}.

The results in the presence of 5 % noise, are shown in Figure 5.10 and warrant further discussion. One advantage of the frequency domain approach is that the effect of noise on the R–MISO approach can be assessed using the multiple coherence function. One observation in this case is that the multiple coherence drops sharply below approximately 2 Hz. This makes the estimation of the mass normalised linear stiffness difficult. The FRF value at 0 Hz is approximately 72 N/m, which is clearly an erronous estimate.

A curve–fit is used to estimate the sprung mass normalised linear stiffness parameter in the presence of noise. The Rational Fraction Polynomials (RFP) FRF curve–fit

[1]Notation used for R–MISO analysis: H_{1y},H_{2y},H_{3y} are FRF's defined in Figure 5.8; γ^2_{1y}, ordinary coherence between $x_1(t)$ and $y(t)$; $\gamma^2_{2y.1}$, partial coherence between the conditioned record $x_{2.1}(t)$ and $y(t)$; $\gamma^2_{3y.2!}$, partial coherence between the conditioned record $x_{3.2!}(t)$ and $y(t)$; $\gamma^2_{y:x}$, multiple coherence function between all the inputs and the output.

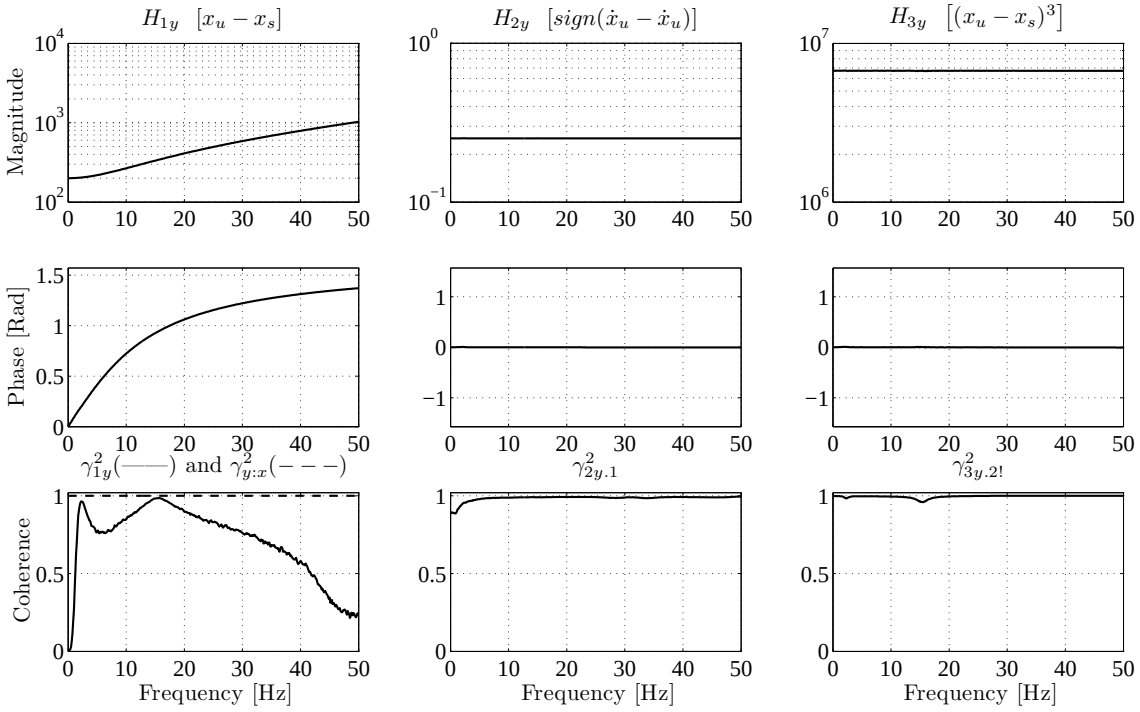

Figure 5.9: Nonlinear quarter car model R–MISO analysis results

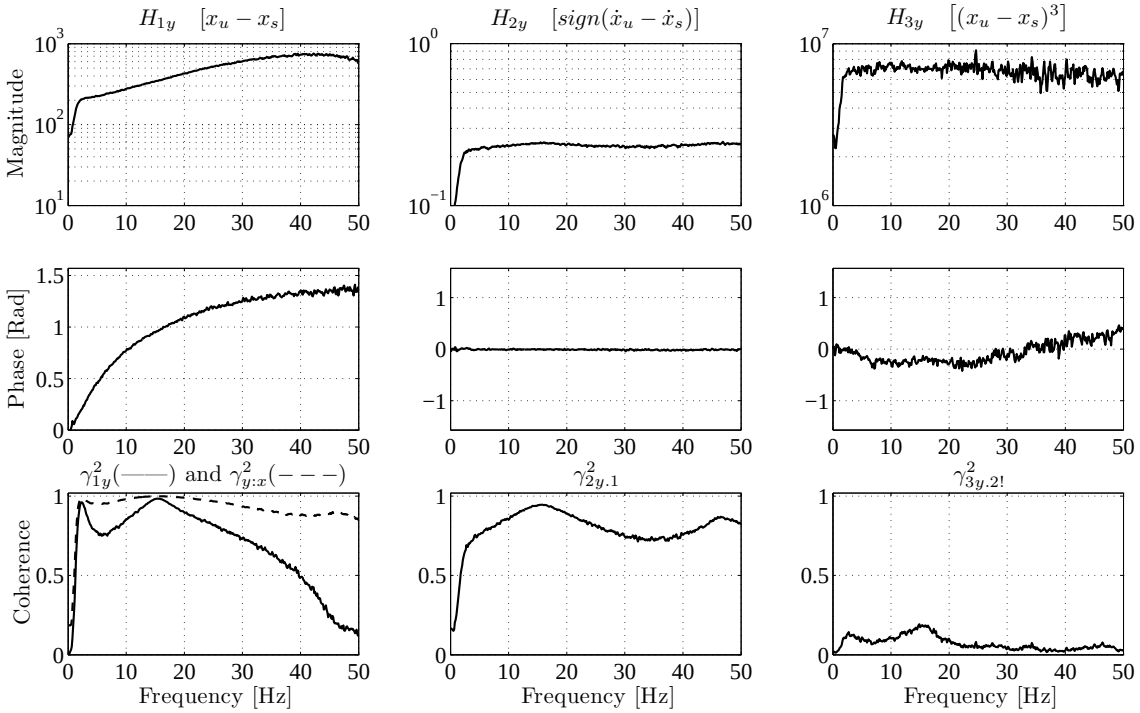

Figure 5.10: Nonlinear quarter car model R–MISO analysis results (5 % noise)

method is adopted for this purpose [184]. The RFP method is a Multiple Degree–Of–Freedom (MDOF) Experimental Modal Analysis (EMA) curve–fit method which expresses the measured FRF in terms of rational fraction polynomials as follows,

$$H(\omega) = \frac{\sum_{k=0}^{n} (j\omega)^k \alpha_k}{\sum_{k=0}^{m} (j\omega)^k \beta_k}. \tag{5.21}$$

Manipulation of equation 5.21 allows the coefficients α_k and β_k to be found using linear least squares techniques. Despite the non–parametric nature of the identified FRF, the sprung mass normalised stiffness can be estimated by normalising the numerator coefficients(α_k) by β_0. The value of α_0 after normalisation gives an estimate of the y–axis crossing point of the synthesised FRF and hence the sprung mass normalised stiffness. The RFP method in its standard form is found to give reasonable estimates of the mass normalised stiffness value when the multiple coherence is close to unity. However, it is found that the synthesised FRF is biased by errors on the measured FRF when the multiple coherence function is not close to unity. Therefore, a weighted RFP method is developed to increase the accuracy of the FRF estimates. The variance of the noise present on the FRF data can be computed from [20],

$$\text{var}\left(|H_{xy}|\right) \approx \frac{\left(1-\gamma_{xy}^2\right)}{2\gamma_{xy}^2 n_d} |H_{xy}|^2 \tag{5.22}$$

where, n_d is the number of sample records used in the spectral estimation. Using equation 5.22, a weighting function for the RFP least squares estimator, W_{xy}^2, can be formulated as follows [185],

$$W_{xy}^2 = \frac{|H_{xy}|}{\text{var}\left(|H_{xy}|\right)}. \tag{5.23}$$

A measure of the quality of the synthesised FRF fit to the actual FRF is provided using the Synthesis Correlation Coefficient (SCC) [186]. The SCC, Γ^2, is given by,

$$\Gamma^2 = \frac{\left|\sum_{\omega=\omega_1}^{\omega_2} H(\omega)\hat{H}^*(\omega)\right|^2}{\sum_{\omega=\omega_1}^{\omega_2} H(\omega)H^*(\omega) \sum_{\omega=\omega_1}^{\omega_2} \hat{H}(\omega)\hat{H}^*(\omega)} \tag{5.24}$$

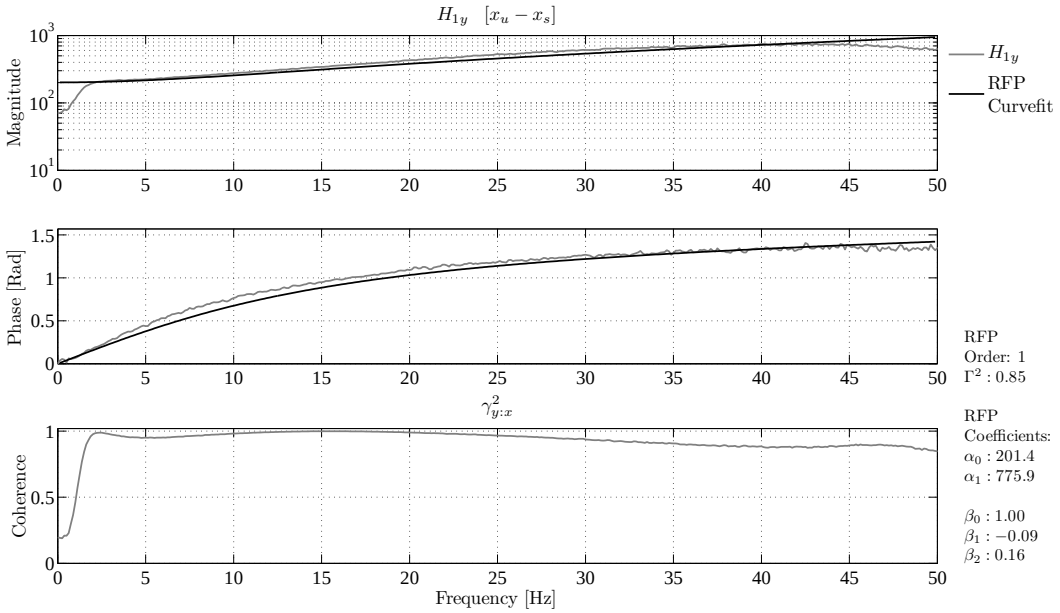

Figure 5.11: Nonlinear quarter car model with 5 % noise R–MISO weighted RFP curve–fit

where, $H(\omega)$ is the measured FRF and $\hat{H}(\omega)$ is the synthesised FRF. In the case of the constant coefficients due to the R–MISO nonlinear paths, a weighted mean is used to calculate the parameter estimates. The weighted mean is given by,

$$\overline{x} = \frac{\sum_{\omega=\omega_1}^{\omega_2} W(\omega)\,|H_{xy}(\omega)|}{\sum_{\omega=\omega_1}^{\omega_2} W(\omega)} \tag{5.25}$$

where, H_{xy} is the FRF of the nonlinear path and W is the weighting vector defined in equation 5.23, however, the variance on H_{xy} defined by equation 5.22 is developed from the partial coherence of the corresponding nonlinear path as opposed to the ordinary coherence.

Applying this approach to the nonlinear quarter car model with noise leads to the curve–fit shown in Figure 5.11. Note in areas of low multiple coherence, *i.e.* below 2 Hz and above 45 Hz, the synthesised FRF is not significantly biased by these frequency points due to the weighting on the least squares estimator. This improves the parameter estimates especially in the case when the multiple coherence drops significantly from unity. The estimated quarter car model parameters in the presence of 0 % noise and 5 % noise are summarised in Table 5.12. Good sprung mass

0% Noise

Parameter	Actual	Estimate	% Error	Γ^2
k_s/m_s	200.0	199.0	+0.5	0.89
μ_s/m_s	0.25	0.25	+0.4	1.00
k_n/m_s	6.72x10^6	6.72x10^6	+0.0	1.00

5% Noise

Parameter	Actual	Estimate	% Error	Γ^2
k_s/m_s	200.0	201.4	+0.7	0.85
μ_s/m_s	0.25	0.24	-6.1	0.99
k_n/m_s	6.72x10^6	6.80x10^6	+1.1	0.95

Table 5.12: Estimated mass normalised nonlinear quarter car model parameters using R–MISO and a RFP curve–fit

normalised parameter estimates are obtained in all cases.

Unknown shock absorber model structure

The R–MISO approach is now applied to the more complex case of the nonlinear quarter car model with Bouc–Wen shock absorber. The simulation parameters are the same as for the time domain case and are given in Table 5.7. As the exact model form is assumed unknown, a set of possible R–MISO inputs is generated. The set of basis functions for this analysis are chosen to be,

$$basis = (sign(x_u - x_s), sign(\dot{x}_u - \dot{x}_s), sign(\ddot{x}_u - \ddot{x}_s), PS_1, PS_2, PS_3) \tag{5.26}$$

where, PS_1, PS_2 and PS_3 represent the list of basis terms in the power series expansion of the doubly indexed series (for $i_{max} = j_{max} = 7$),

$$PS_1 = \sum_{i=1}^{i_{max}} \sum_{j=0}^{j_{max}} (x_u - x_s)^i (\ddot{x}_u - \ddot{x}_s)^j \tag{5.27}$$

$$PS_2 = \sum_{i=1}^{i_{max}} \sum_{j=1}^{j_{max}} (x_u - x_s)^i (\dot{x}_u - \dot{x}_s)^j \tag{5.28}$$

$$PS_3 = \sum_{i=1}^{i_{max}} \sum_{j=1}^{j_{max}} (\dot{x}_u - \dot{x}_s)^i (\ddot{x}_u - \ddot{x}_s)^j . \tag{5.29}$$

Sampling frequency, f_s	Time points, N	Block size	Overlap	Window Type	Filter type	FRF Estimator
2048 Hz	4194304	2048	50 %	Hanning	LP:50 Hz	H_1

Table 5.13: Signal processing parameters used for quarter car simulation with Bouc–Wen shock absorber R–MISO analysis

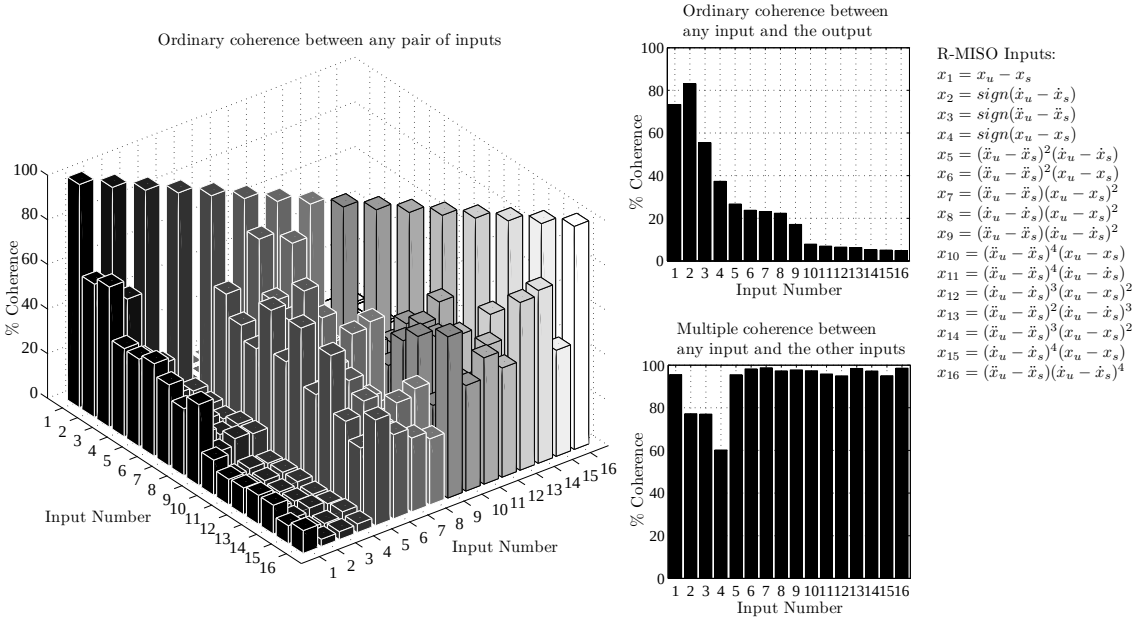

Figure 5.12: Bouc–Wen quarter car simulation R–MISO model check results

The R–MISO output is sprung mass acceleration, $\ddot{x}_s$. The signal processing parameters used for the R–MISO analysis are given in Table 5.13. The integral of each input terms ordinary coherence with the output is calculated. Terms with an integral of less than 5 % of perfect coherence are discarded and the remaining inputs are ordered in decending order, based on their percentage coherence with the R–MISO output. The model is checked, as outlined above, to ensure it is well defined before the analysis is run. The results of the model check, after basis function truncation and reordering, are shown in Figure 5.12. A total of 16 inputs are included in the model out of a possible 157 in the original basis function set. As the FRF of most interest in this case is the FRF between the relative displacement of the shock absorber ($x_u - x_s$) and the sprung mass acceleration ($\ddot{x}_s$), $x_u - x_s$ is set as input number 1 (x_1). The results of the R–MISO analysis, for inputs x_1, x_2 and x_3, are shown in Figure 5.13 (the Matlab® function *rmiso*, developed to run R–MISO analysis for an arbitrary number of inputs is documented in Appendix C).

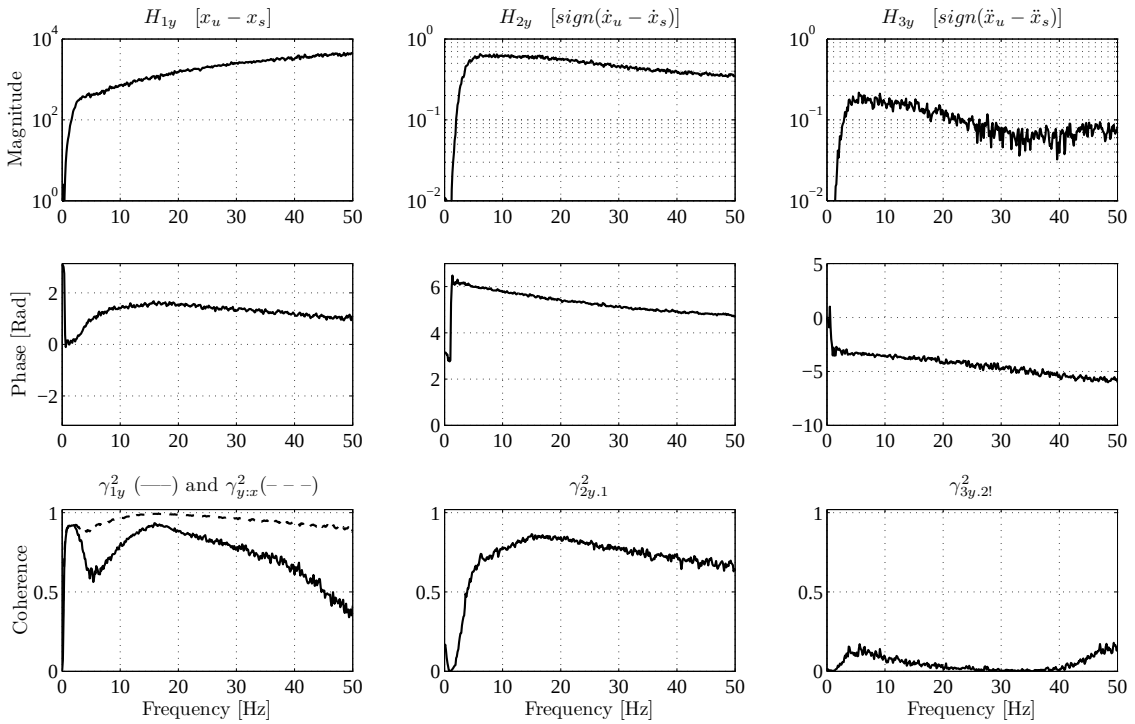

Figure 5.13: Bouc–Wen quarter car simulation R–MISO analysis results for inputs x_1, x_2, x_3

A weighted RFP curve–fit is performed as before and the results are shown in Figure 5.14. In this case the curve–fit is performed in the 0–16 Hz frequency range, as highest multiple coherences are seen close to the natural frequencies of the sprung and unsprung masses and a drop in phase from its ideal value of $\pi/2$ is seen above 16 Hz. An error of 12.1 % is seen in the estimated sprung mass normalised stiffness. This represents a significant improvement in model error when compared with the time domain estimate of the linear stiffness. A combination of time domain and frequency domain analysis of the Bouc–Wen quarter car simulation, using operational testing, produces estimates for m_s and k_s of 25.2 kg and 4430.2 N/m, respectively. These estimates compare favourably with the corresponding true values of 25 kg and 5000 N/m, considering the complexity of the identification problem.

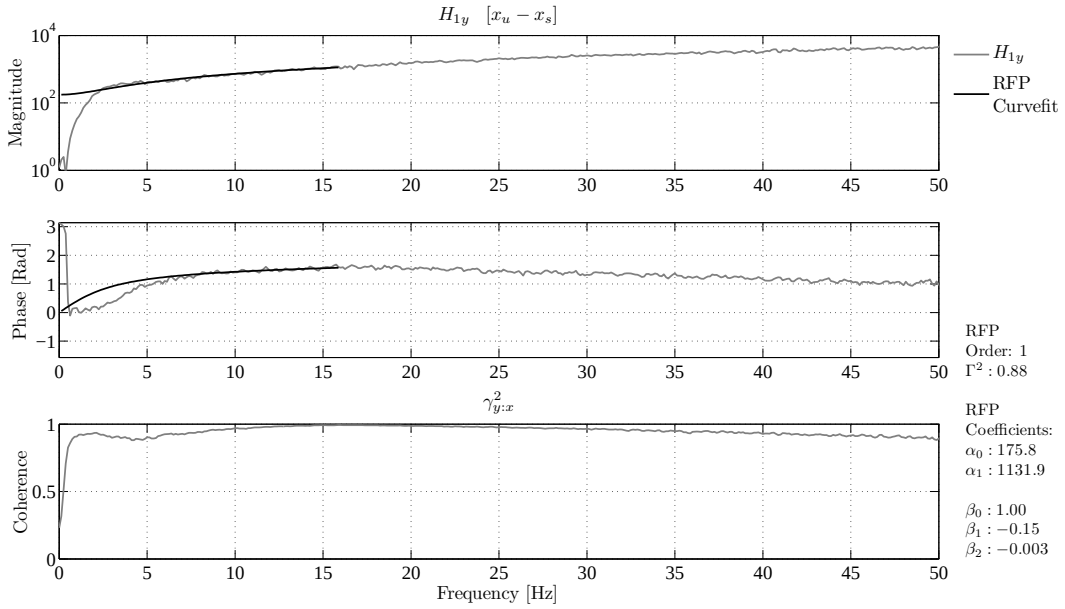

Figure 5.14: Bouc–Wen quarter car simulation R–MISO weighted RFP curve–fit

5.3 Experimental quarter car rig identification

Having implemented the boundary perturbation technique on a range of nonlinear quarter car simulations, the technique is now applied to the experimental identification of the quarter car test rig. A combination of time and frequency domain approaches allowed for the identification of a nonlinear quarter car simulation with a complex Bouc–Wen shock absorber characteristic. This time and frequency domain approach is extended here to allow operational experimental identification of the quarter car rig.

The rig is instrumented with four accelerometers, three on the unsprung mass in the transverse, fore–aft and vertical directions and one on the sprung mass in the vertical direction. The accelerometer mounting positions are shown in Figure 5.15. The transverse, fore–aft and vertical directions are referred to as the x, y and z–directions in future discussion[2]. Excitation is provided using the 72 lobe cam, shown in Figure 5.16. The cam frequency is linearly swept from 0.4–6 Hz during each experimental measurement run. Data are sampled at 256 Hz and each measurement data set contains 16384 samples. The first 60 data sets of each measurement run

[2]The following notation is used to distinguish between measurement directions; $\ddot{x}_{ux}$, unsprung mass acceleration in the x–direction; $\ddot{x}_{uy}$, unsprung mass acceleration in the y–direction; $\ddot{x}_{uz}$, unsprung mass acceleration in the z–direction; $\ddot{x}_{sz}$, sprung mass acceleration in the z–direction. Velocity and displacement follow along similar lines.

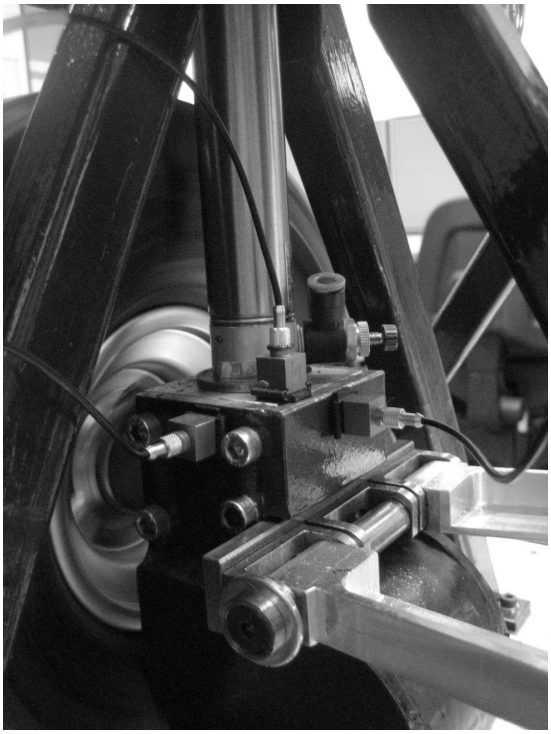

(a) Unsprung mass, showing accelerometers mounted in the transverse, fore–aft and vertical directions or x, y and z–directions, respectively

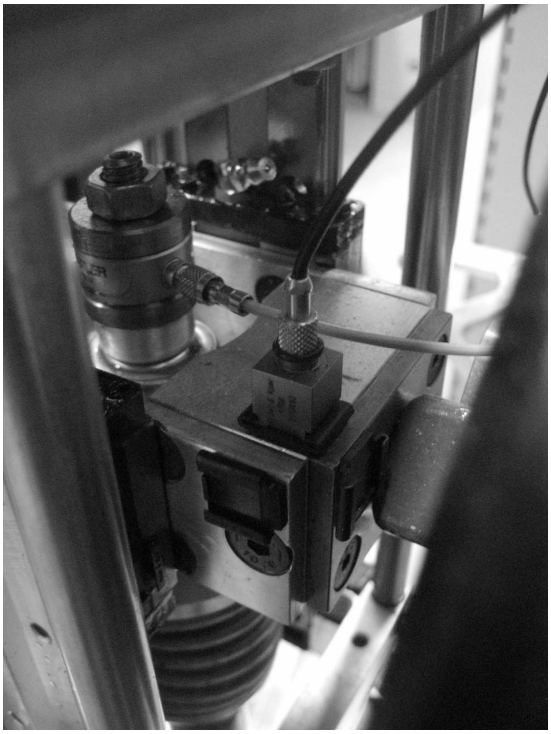

(b) Sprung mass, showing an accelerometer mounted in the vertical or z–direction

Figure 5.15: Quarter car rig accelerometer locations for operational testing

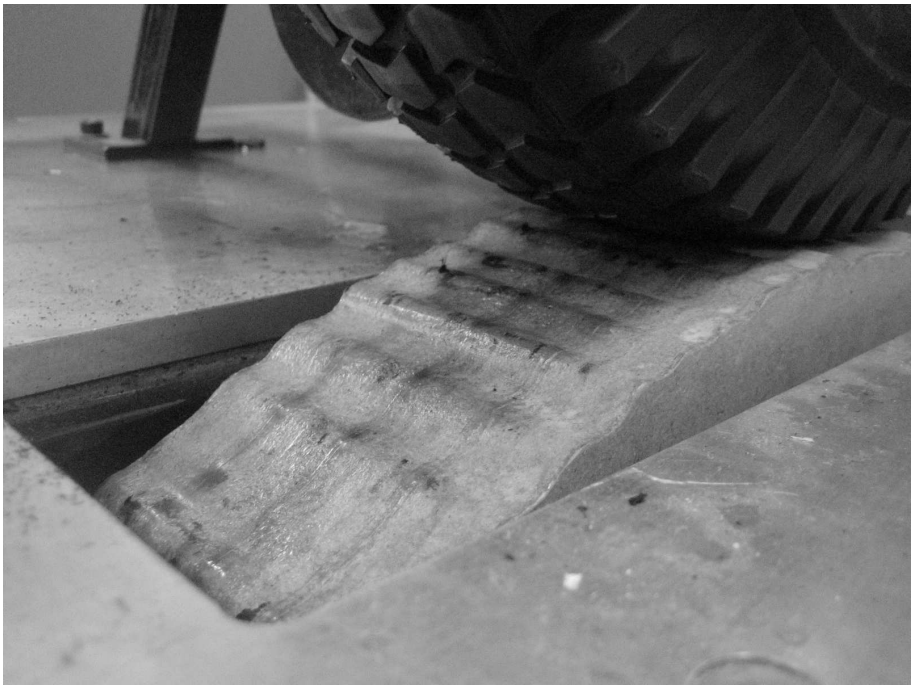

Figure 5.16: Quarter car rig 72 lobe pseudo random cam

Figure 5.17: Quarter car rig with known added mass attached to the sprung mass

are discarded to ensure components have reached a steady state operating temperature before subsequent data sets are collected for analysis. The data acquisition is repeated with a known mass added to the sprung mass. Figure 5.17 shows the added mass clamped to the sprung mass. Experiments are conducted with added mass values of 6.5, 8.0, and 10.5 % of the sprung mass magnitude.

5.3.1 Characterisation and model selection

The RFS of the quarter car rig is shown in Figure 5.18 for 10 data set averages. The stochastic nature of the RFS is due to the hysteretic nature of the system, as observed in Figure 5.5 and in the work of Cafferty *et al.* [21]. One assumption made by Cafferty *et al.* is that the significant dynamical behaviour of such a system is summarised by the 'backbone' of the RFS surface. This approximation allows a practical modelling by a memory–less system [21]. The 'backbone' of the system can be identified by averaging out the effects of hysteresis. When duplicate force values exist for a given velocity and displacement the algorithm used to develop the RFS returns an average of the values. The RFS is replotted using 400 averages and is shown in Figure 5.19.

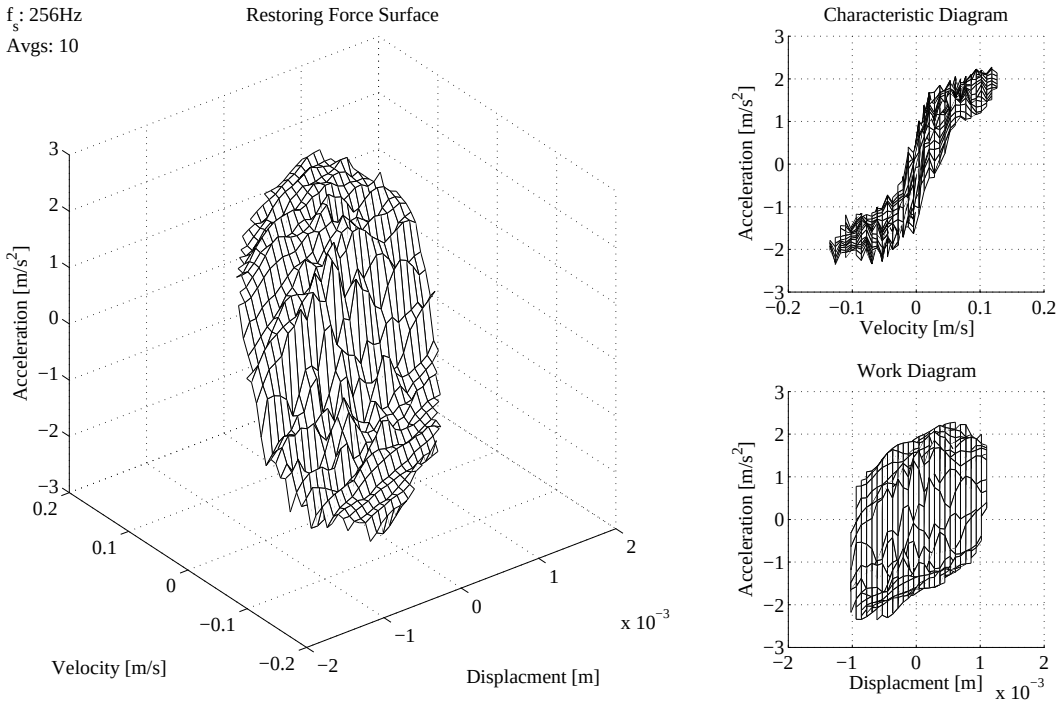

Figure 5.18: Quarter car rig restoring force surface (10 averages)

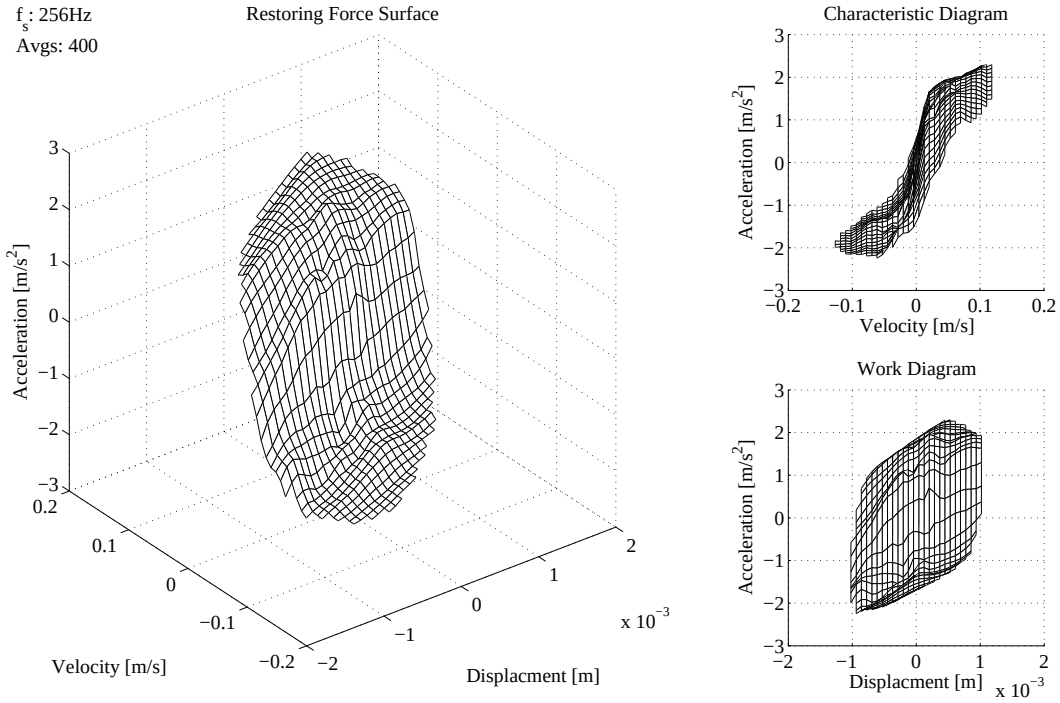

Figure 5.19: Quarter car rig restoring force surface (400 averages)

The identification of the quarter car rig, given the operationally identified restoring force surface, presents the same set of challenges faced for the identification of the Bouc–Wen simulation when the shock absorber model form is unknown, *i.e.* complex nonlinear behaviour, frequency and amplitude dependence, hysteresis, unknown shock absorber model form and in the experimental case, measurement noise. As a starting point, a spring–damper–friction model of the shock absorber is assumed. This model is chosen based on an analysis of the shock absorber RFS. The shock absorber is seen to exhibit high damping at low velocities ($-0.03 < \dot{x}_u - \dot{x}_s < 0.03$) and a lower damping rate at high velocities ($|\dot{x}_u - \dot{x}_s| > 0.03$). The spring–damper–friction model offers a relatively simple model of this type of nonlinear behaviour.

5.3.2 Operational parameter estimation

The time and frequency domain approaches, developed under controlled simulated conditions, provide a means of identifying both the suspension system sprung mass and also the true linear stiffness in the system. Here, this approach is adopted to experimentally identify the quarter car rig sprung mass, shock absorber spring stiffness and a nonlinear damping model, using operational testing.

Time domain approach

As with the nonlinear quarter car simulation, the boundary perturbation approach coupled with DPE is first used to identify the quarter car rig parameters. Nonlinear quarter car simulations showed this approach to be very robust in the estimation of the sprung mass in all simulated scenarios. Analysis of the quarter car model with Bouc–Wen shock absorber suggests that the sprung mass estimate is not particularly sensitive to the shock absorber model form used in the estimation algorithm.

The analysis is run on experimental data from the quarter car rig. After rig warm up, 60 measurement data sets are collected. A known mass (m_a) with magnitude equal to 10.5 % of the sprung mass is attached to the sprung mass. A further 60 measurement data sets are collected. Figure 5.20 shows a plot of the mean significance factor (equation 5.10) for each input across the 60 measurement data sets. It also shows mass normalised parameter estimates of the most significant input, $(\dot{x}_u - \dot{x}_s)$, for the no added mass and added mass cases. The analysis is

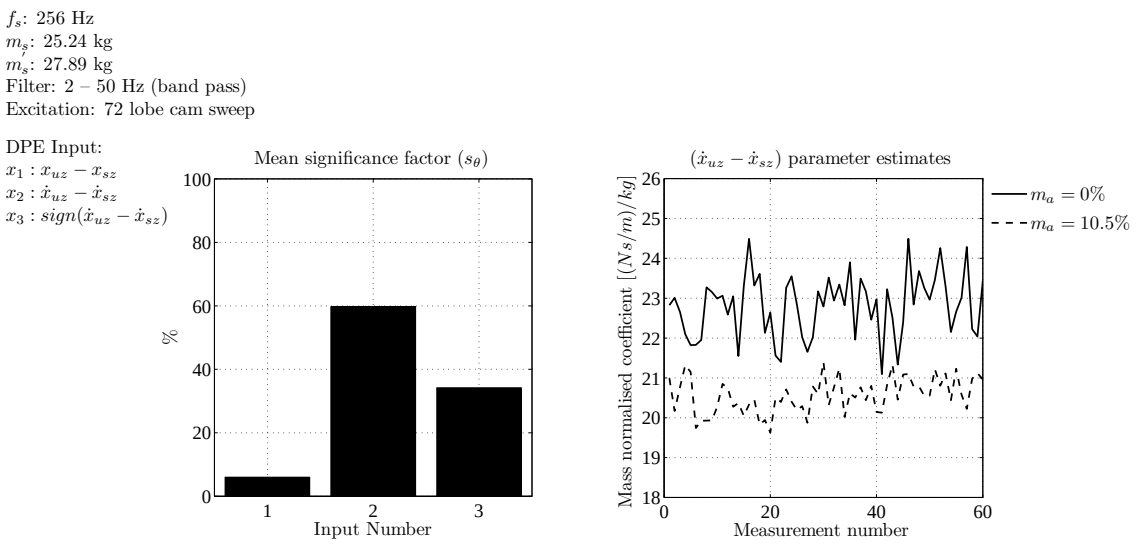

Figure 5.20: Quarter car rig boundary perturbation analysis with 10.5 % added mass

repeated for added mass values of 6.5 % and 8.0 %. The estimated suspension parameters are shown in Table 5.14. Good estimates of the sprung mass are seen in all three cases, with a mean percentage error of 3.5 %.

Frequency domain approach

The quarter car rig is designed to allow realistic multi–directional motions of the unsprung mass. The unsprung mass displacement in the z–direction, plotted against the displacement in both the x and y–directions, for a 72 lobe cam sweep are shown in Figure 5.21. The data is normalised by the maximum value of displacement in the z–direction. Significant displacements of the unsprung mass are seen in both the x and y–directions. It is, therefore, deemed necessary to include motions in the x and y–directions in the R–MISO analysis.

Due to the complex nature of the shock absorber, as observed in the RFS plot in Figure 5.19, a set of basis functions is chosen to include a wide range of nonlinear terms. The basis function has a total of 256 terms, consisting of powers and sign terms of measured acceleration, velocity and displacement signals. The basis

10.5% Added Mass

Parameter	Actual	Estimate	% Error
m_s	25.24	24.39	-3.4
k_s	5690	14225	+150.0

8.0% Added Mass

Parameter	Actual	Estimate	% Error
m_s	25.24	23.58	-6.6
k_s	5690	14127	+148.0

6.5% Added Mass

Parameter	Actual	Estimate	% Error
m_s	25.24	25.11	-0.5
k_s	5690	14418	+153.0

Table 5.14: Quarter car rig boundary perturbation analysis results with 10.5 %, 8.0 % and 6.5 % added mass

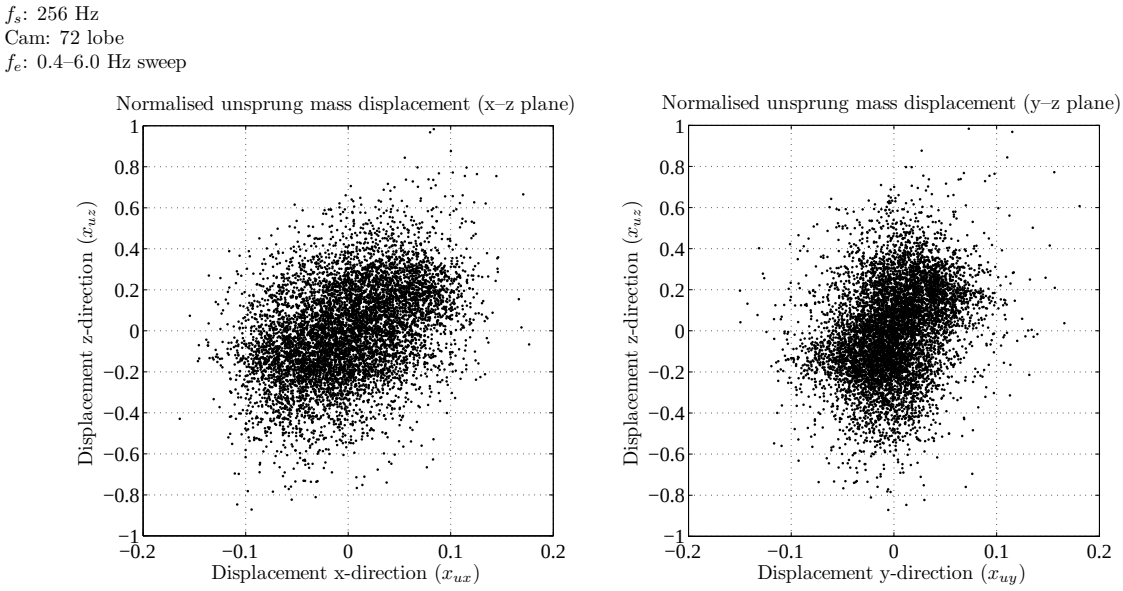

Figure 5.21: Normalised quarter car rig unsprung mass displacement in the x, y and z–directions

function is defined as,

$$\begin{aligned} basis = (&sign(x_{uz} - x_{sz}),\ sign(\dot{x}_{uz} - \dot{x}_{sz}),\ sign(\ddot{x}_{uz} - \ddot{x}_{sz}),\\ &sign(x_{uz} - x_{ux}),\ sign(\dot{x}_{uz} - \dot{x}_{ux}),\ sign(\ddot{x}_{uz} - \ddot{x}_{ux}),\\ &sign(x_{uz} - x_{uy}),\ sign(\dot{x}_{uz} - \dot{x}_{uy}),\ sign(\ddot{x}_{uz} - \ddot{x}_{uy}),\\ &sign(x_{ux} - x_{sz}),\ sign(\dot{x}_{ux} - \dot{x}_{sz}),\ sign(\ddot{x}_{ux} - \ddot{x}_{sz}),\\ &sign(x_{uy} - x_{sz}),\ sign(\dot{x}_{uy} - \dot{x}_{sz}),\ sign(\ddot{x}_{uy} - \ddot{x}_{sz}),\\ &sign(x_{ux} - x_{uy}),\ sign(\dot{x}_{ux} - \dot{x}_{uy}),\ sign(\ddot{x}_{ux} - \ddot{x}_{uy}),\\ &PS_k) \end{aligned} \tag{5.30}$$

where, the terms PS_k, for $k = 1, 2, 3..., 17.$, represent the list of basis terms in the power series expansion of the doubly indexed series (for $i_{max} = j_{max} = 7$),

$$PS_1 = \sum_{i=1}^{i_{max}} \sum_{j=0}^{j_{max}} (x_{uz} - x_{sz})^i (\ddot{x}_{uz} - \ddot{x}_{sz})^j \qquad PS_2 = \sum_{i=1}^{i_{max}} \sum_{j=1}^{j_{max}} (x_{uz} - x_{sz})^i (\dot{x}_{uz} - \dot{x}_{sz})^j$$

$$PS_3 = \sum_{i=1}^{i_{max}} \sum_{j=1}^{j_{max}} (\dot{x}_{uz} - \dot{x}_{sz})^i (\ddot{x}_{uz} - \ddot{x}_{sz})^j \qquad PS_4 = \sum_{i=2}^{i_{max}} (\dot{x}_{uz} - \dot{x}_{sz})^i$$

$$PS_5 = \sum_{i=2}^{i_{max}} (\ddot{x}_{uz} - \ddot{x}_{sz})^i \qquad PS_6 = \sum_{i=2}^{i_{max}} (x_{ux} - x_{sz})^i$$

$$PS_7 = \sum_{i=2}^{i_{max}} (\dot{x}_{ux} - \dot{x}_{sz})^i \qquad PS_8 = \sum_{i=2}^{i_{max}} (\ddot{x}_{ux} - \ddot{x}_{sz})^i$$

$$PS_9 = \sum_{i=2}^{i_{max}} (x_{uy} - x_{sz})^i \qquad PS_{10} = \sum_{i=2}^{i_{max}} (\dot{x}_{uy} - \dot{x}_{sz})^i$$

$$PS_{11} = \sum_{i=2}^{i_{max}} (\ddot{x}_{uy} - \ddot{x}_{sz})^i \qquad PS_{12} = \sum_{i=1}^{i_{max}} (x_{uz} - x_{ux})^i$$

$$PS_{13} = \sum_{i=2}^{i_{max}} (\dot{x}_{uz} - \dot{x}_{ux})^i \qquad PS_{14} = \sum_{i=2}^{i_{max}} (\ddot{x}_{uz} - \ddot{x}_{ux})^i$$

$$PS_{15} = \sum_{i=1}^{i_{max}} (x_{uz} - x_{uy})^i \qquad PS_{16} = \sum_{i=2}^{i_{max}} (\dot{x}_{uz} - \dot{x}_{uy})^i$$

$$PS_{17} = \sum_{i=2}^{i_{max}} (\ddot{x}_{uz} - \ddot{x}_{uy})^i .$$

The signal processing parameters used for the R–MISO analysis are shown in Table 5.15. All measured signals are high pass filtered to eliminate low frequency

Sampling frequency, f_s	Time points, N	Block size	Overlap	Number Data Sets	Window Type	Filter type	FRF Estimator
256 Hz	16384	2048	50 %	60	Hanning	HP:1 Hz	H_1

Table 5.15: Signal processing parameters used for quarter car rig R–MISO analysis

Input	Expression	Input	Expression
x_1	$x_{uz} - x_{sz}$	x_{14}	$sign(\dot{x}_{uz} - \dot{x}_{uy})$
x_2	$x_{uz} - x_{ux}$	x_{15}	$(\ddot{x}_{uz} - \ddot{x}_{uy})^3$
x_3	$x_{uz} - x_{uy}$	x_{16}	$(\ddot{x}_{uz} - \ddot{x}_{ux})^3$
x_4	$sign(\ddot{x}_{uy} - \ddot{x}_{sz})$	x_{17}	$sign(\ddot{x}_{ux} - \ddot{x}_{uy})$
x_5	$sign(\ddot{x}_{uz} - \ddot{x}_{uy})$	x_{18}	$(\ddot{x}_{uz} - \ddot{x}_{sz})^3$
x_6	$(\ddot{x}_{uy} - \ddot{x}_{sz})^3$	x_{19}	$sign(\dot{x}_{uy} - \dot{x}_{sz})$
x_7	$sign(\ddot{x}_{uz} - \ddot{x}_{ux})$	x_{20}	$sign(\dot{x}_{ux} - \dot{x}_{uy})$
x_8	$(\ddot{x}_{ux} - \ddot{x}_{sz})^3$	x_{21}	$(x_{ux} - x_{sz})^3$
x_9	$sign(\dot{x}_{uz} - \dot{x}_{ux})$	x_{22}	$(x_{uy} - x_{sz})^3$
x_{10}	$sign(\dot{x}_{uz} - \dot{x}_{sz})$	x_{23}	$(\ddot{x}_{ux} - \ddot{x}_{uy})^3$
x_{11}	$sign(\ddot{x}_{uz} - \ddot{x}_{sz})$	x_{24}	$sign(x_{uz} - x_{ux})$
x_{12}	$sign(\dot{x}_{ux} - \dot{x}_{sz})$	x_{25}	$(\dot{x}_{ux} - \dot{x}_{sz})^3$
x_{13}	$sign(\ddot{x}_{ux} - \ddot{x}_{sz})$		

Table 5.16: Quarter car rig R–MISO analysis inputs

drift. Low frequency drift occurs when measured acceleration signals are integrated to obtain velocity and displacement records. Any DC offset on the original signal manifests itself as a low frequency drift component on the integrated signal. All signals are zero–phase forward and reverse filtered using a 6^{th} order Butterworth filter [183, 187]. The R–MISO model check function, as used for simulated data, is run on the basis function. The coherence threshold is set to 15 %. After truncation, 25 terms remain and are listed in Table 5.16, while the results of the R–MISO check are shown in Figure 5.22. The results of the 25 input R–MISO analysis, for input paths x_1, x_2 and x_3, are shown in Figure 5.23. The weighted RFP curve–fit method is used to estimate the sprung mass normalised stiffness. The results of the curve–fit of H_{1y} are shown in Figure 5.24. The estimated value of sprung mass normalised stiffness is 227.2 N/m/kg.

The results of a combined time and frequency domain operational identification of the quarter car test rig are compared with the parameter values obtained using isolated component identification in Table 5.17. Excellent agreement is seen between

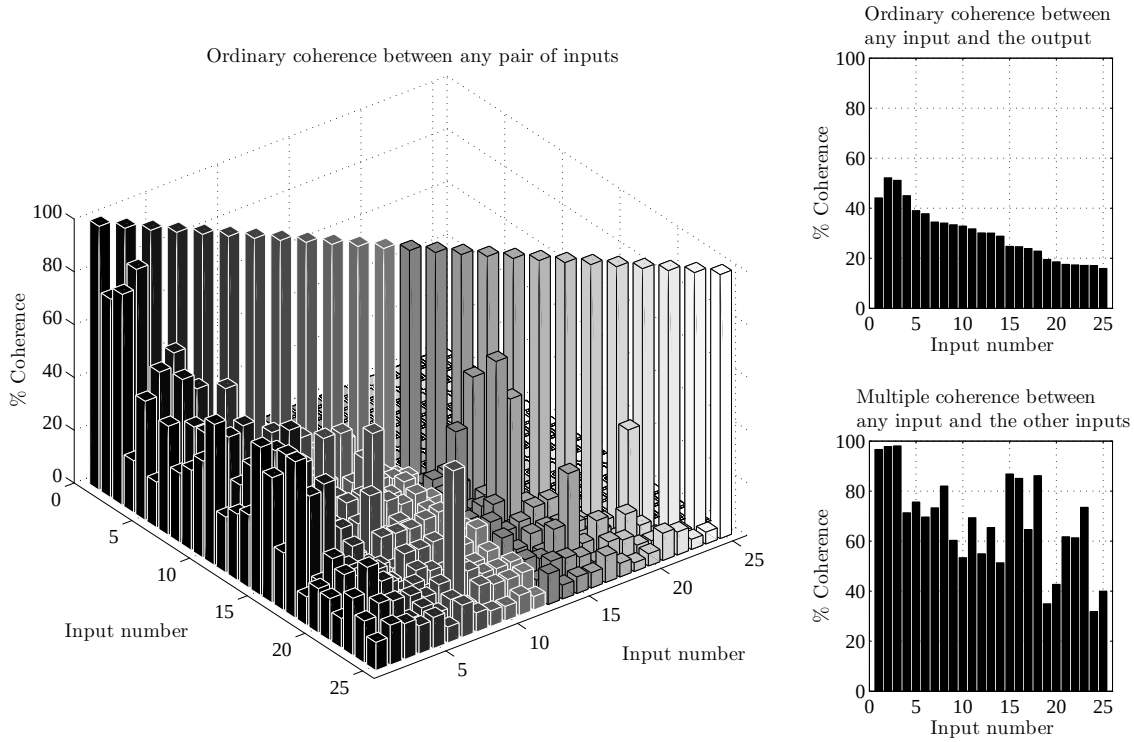

Figure 5.22: Quarter car rig R–MISO model check results (input numbers are defined in table 5.16)

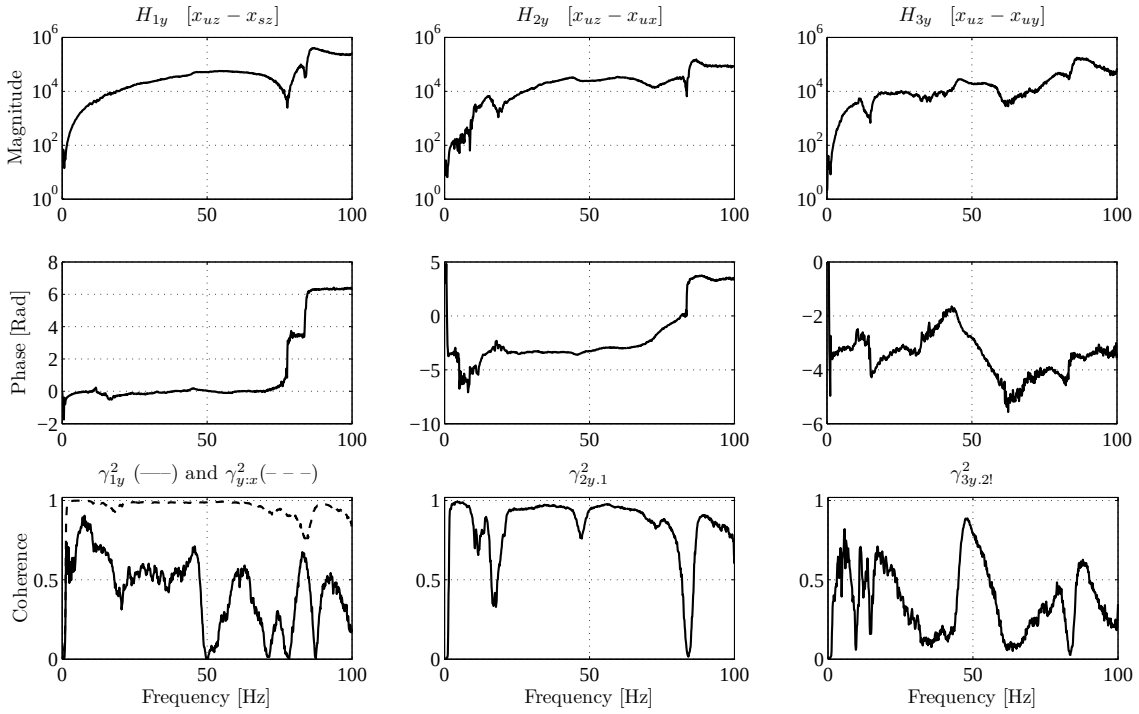

Figure 5.23: Quarter car rig R–MISO analysis results for input paths x_1, x_2 and x_3

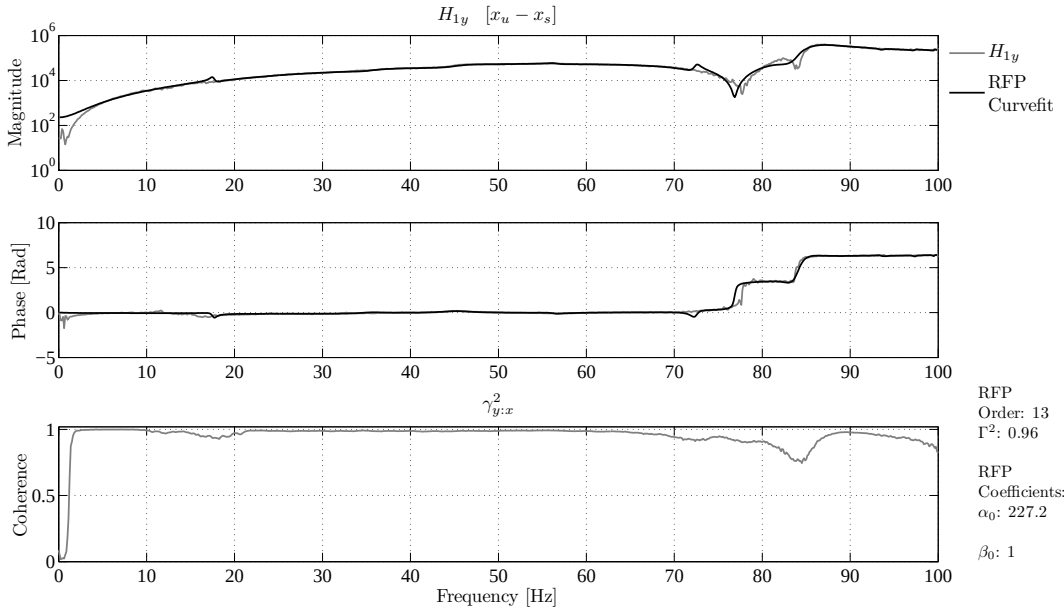

Figure 5.24: Quarter car rig R–MISO analysis weighted RFP curve–fit

Parameter	Isolated	Operational	% Error
m_s	25.24	24.36	-3.5
k_s	5690	5534.6	-2.7

Table 5.17: Quarter car rig estimated component parameters obtained using isolated component testing and operational system testing

components parameters identified using the two identification approaches.

Nonlinear damping model

Having estimated the sprung mass and linear spring parameters, the development of a damping model from operational data is now examined. It is clear, from isolated test results and a visual inspection of the shock absorber RFS, that estimation of a linear damping coefficient for the shock absorber would be inadequate to describe its nonlinear behaviour. Its significant nonlinear behaviour is represented in the RFS, therefore, it is used to develop the damping model.

Consider the operational identified shock absorber RFS shown in Figure 5.19. An indication of the damping 'backbone' of the system can be obtained by taking a narrow slice through the RFS along the plane of zero displacement. If the width of the narrow slice is chosen to be, δ, all pairs of values $((\dot{x}_u - \dot{x}_s)_i, (\ddot{x}_s)_i)$ in the raw

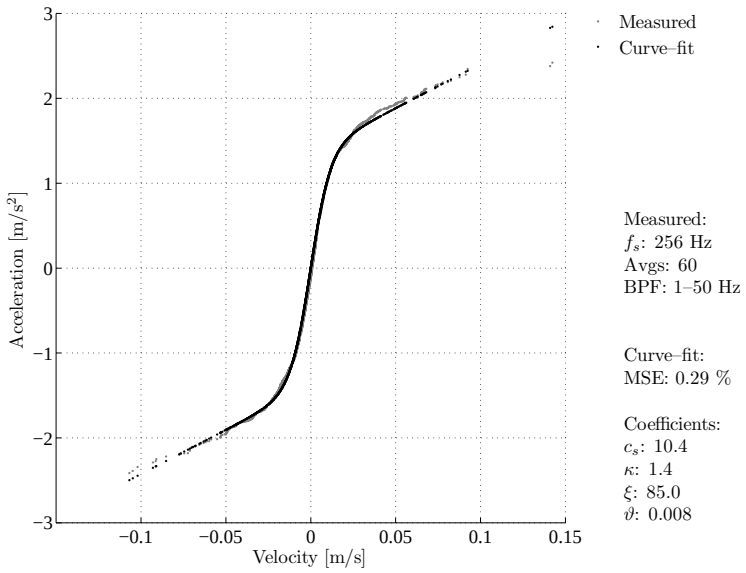

Figure 5.25: Quarter car rig nonlinear damping model from operational testing

uninterpolated RFS data, such that $|(x_u - x_s)_i| < \delta$, are recorded. Placing these values in ascending order and plotting gives a graph of $(\dot{x}_u - \dot{x}_s)$ versus $\ddot{x}_s$ which is essentially a slice through the RFS at $x_u - x_s = 0$ [11]. The 60 data sets used for the R–MISO analysis in the previous section, are used to generate the damping model. The value of δ is chosen to be 10 % of the RMS amplitude of the relative displacement across the shock absorber. Figure 5.25 shows the resulting RFS section and also a curve–fit of the data using a hyperbolic tangent shock absorber model of the form,

$$F_d = c_s(\dot{x}_u - \dot{x}_s) + \kappa \left\{ tanh\left(\xi(\dot{x}_u - \dot{x}_s) + \vartheta\right) - tanh\left(\vartheta\right) \right\}. \tag{5.31}$$

Estimation of the model parameters, c_s, κ, ξ and ϑ, requires the use of nonlinear least squares and is carried out using the Levenberg–Marquardt method (§ 2.3.4). The resulting parameter estimates are shown in Figure 5.25. A MSE value of 0.29 %, between the measured and synthesised data, indicates an excellent model fit. The model paramaters are essentially sprung mass normalised parameters. Using the operational sprung mass estimate (24.36 kg) obtained earlier, true parameter estimates for the damping model can be obtained and are shown in Table 5.18.

Parameter	Value
c_s	253.3
κ	33.5
ξ	2069.9
ϑ	0.2

Table 5.18: Quarter car rig operational damping model parameters

5.3.3 Operational model validation

The operationally identified suspension system parameters are used to generate a nonlinear quarter car simulation which is compared with measured experimental data from the quarter car test rig. As the excitation applied at the tyre patch using the pseudo random cam is unknown and unmeasurable, the method used to validate the nonlinear quarter car simulation in Chapter 4 is employed (the quarter car rig is excited with the 4 lobed cam whose profile is known and measured, allowing an equivalent excitation to be applied to the quarter car simulation).

A nonlinear quarter car simulation is developed using the operationally identified sprung mass, spring stiffness and hyperbolic tangent damping model, coupled with the nonlinear tyre model developed under isolated conditions (§ 4.1). Results in § 4.4.4 show tyre damping to have a noticeable effect on simulation accuracy, therefore, 10 % tyre damping is used corresponding to a damping value, c_u, of 169 N s/m. Validation is carried out at using approximately sinusoidal excitation, correpsonding to that generated using the quarter car rig 4 lobe cam, at 6.8 Hz and 11.2 Hz.

The simulated and measured results are shown, along with the simulation parameters, in Figure 5.26. A comparison of the measured and simulated unsprung and sprung mass RMS acceleration amplitudes and signal peak pattern, show the operational identified model to give reasonable results. This is in spite of the fact that the model is validated under very different excitation conditions to those used in the identification process. During operational identification, broadband excitation is used and the RMS amplitude of the relative displacement across the shock absorber is calculated to be 2.68x10^{-4} m. This is compared with the single frequency sine excitation for the validation test, showing corresponding RMS amplitudes of 3.44x10^{-4} m and 4.62x10^{-4} m at 6.8 Hz and 11.2 Hz, respectively. Considering the significant frequency and amplitude dependence of the shock absorber, as observed under isolated testing conditions, the operational model shows promising results.

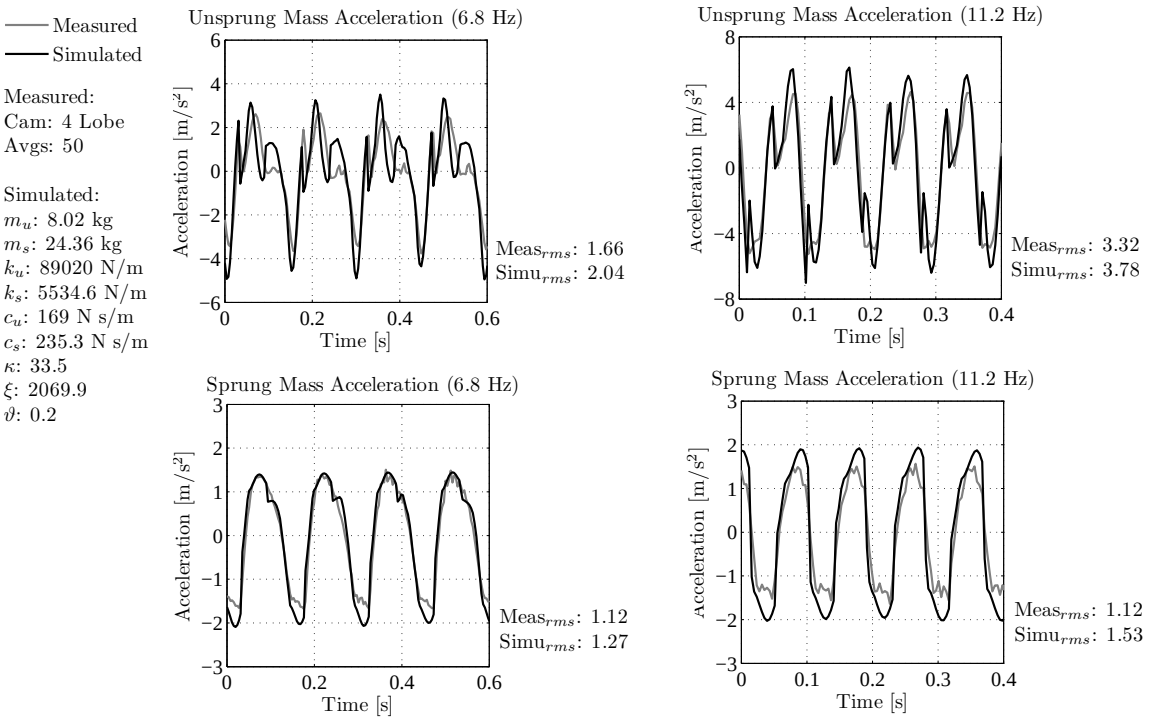

Figure 5.26: Quarter car simulation, with operationally identified parameters, comparison with measured experimental data from the quarter car test rig at 6.8 Hz and 11.2 Hz.

Chapter 6

Discussion

The results presented in Chapter 4 show the identification process for the quarter car rig using traditional force-response identification techniques. This process involved the disassembly of the test rig to facilitate isolated component testing under controlled conditions. Linear and nonlinear quarter car models, developed using the identified component parameters, are compared with measured experimental data from the quarter car test rig to assess the simulation accuracy. A discussion on these results is presented in section 6.1. Chapter 5 presents quarter car rig identification from operational testing. The techniques used are first developed using a series of nonlinear quarter car simulations before they are applied to measured experimental data from the quarter car test rig. The results of the operational suspension system identification are discussed in section 6.2.

6.1 Force–response suspension system identification

Disassembly of the quarter car test rig allows the major components (tyre, damper and spring) to be tested in isolation. Testing is carried out using an ESH® servo–hydraulic testing machine. The use of force–response testing for the identification of tyre and shock absorber models is widely reported in the literature [78, 82, 129, 188]. This approach allows controlled excitation and force measurement and aids in the development of accurate component models.

6.1.1 Suspension component identification

The tyre is tested both statically and dynamically. The tyre shows an almost linear spring characteristic under static testing. Dynamic testing is carried out using sinusoidal excitation at a range of frequencies between 1–14 Hz and amplitudes between 1–4 mm. Dynamic testing reveals a hardening/softening spring characteristic which increases with increasing tyre deflection. Observations of the tyre damping dependence on excitation amplitude and frequency are consistent with hysteretic damping [171, 172, 173]. A nonlinear point contact tyre model, consisting of a hysteretic damper in parallel with a nonlinear spring, is developed to describe the tyre behaviour. An initial validation of the model shows increasing model error at increasing excitation amplitudes. The model Mean Squared Error (MSE) is seen to be between 0.0 and 0.8 % at an excitation amplitude of 1 mm, this is seen to increase to between 2.9 and 3.1 % at an amplitude of 3 mm. The tyre response is seen to drift away from the origin with increasing amplitude of excitation. This is attributed to the asymetric nature of the preloaded tyre and is a characteristic of asymmetric systems [174]. An expression to account for this drift is included in the tyre model (equation 4.12). The revised model (equation 4.15) is shown to have a mean MSE of less than 0.2 % across the frequency and amplitude range of the experimental tests, indicating an excellent model fit.

The shock absorber is also dynamically tested using sinusoidal excitation. A novel force measurement setup, developed during this work, allows both isolated and operational testing of the shock absorber using an identical force transducer setup. Isolated testing shows the shock absorber to be highly nonlinear. The results of an initial test for harmonic distortion are shown in Figure 6.1. Strong harmonics of the single frequency excitation are seen in the response spectra, indicating significant nonlinear behaviour. Further investigation identifies the presence of static friction, asymmetry and hysteresis in the characteristic and work diagrams. The nonlinearities identified in the shock absorber are consistent with those found in experimental investigations by other authors [78, 158, 159, 189], and in particular to those of an automotive friction damper tested by Guglielmino *et al.* [138]. Static friction dominates at low piston velocities. Friction phenomena including presliding displacement, dry friction hysteresis, variable break away force and non reversibility of friction are observed in the shock absorber characteristic diagrams, as shown in Figure 6.2.

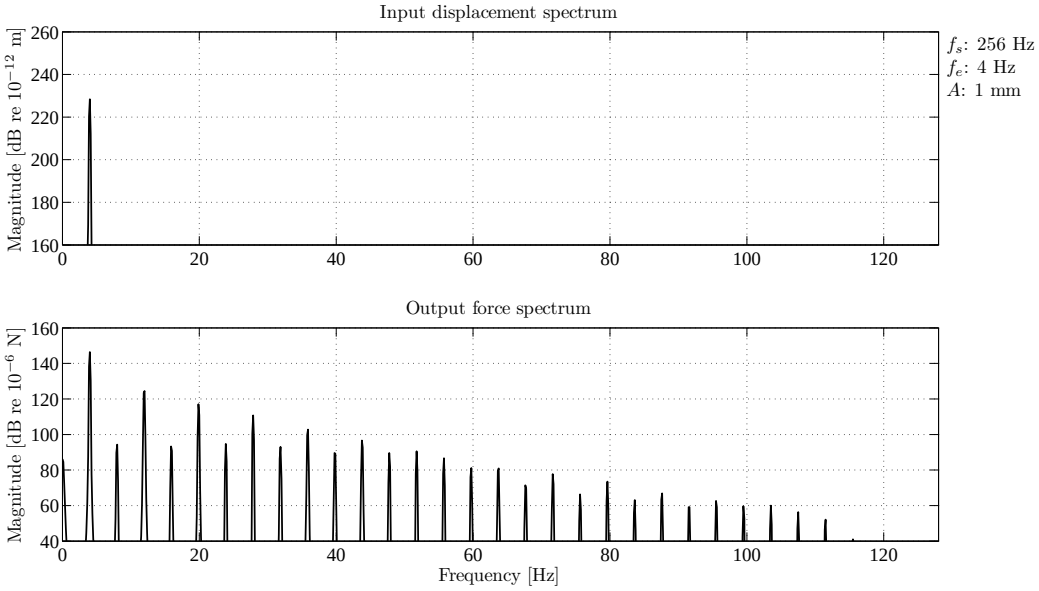

Figure 6.1: Shock absorber input and output spectra for harmonic excitation at 4 Hz

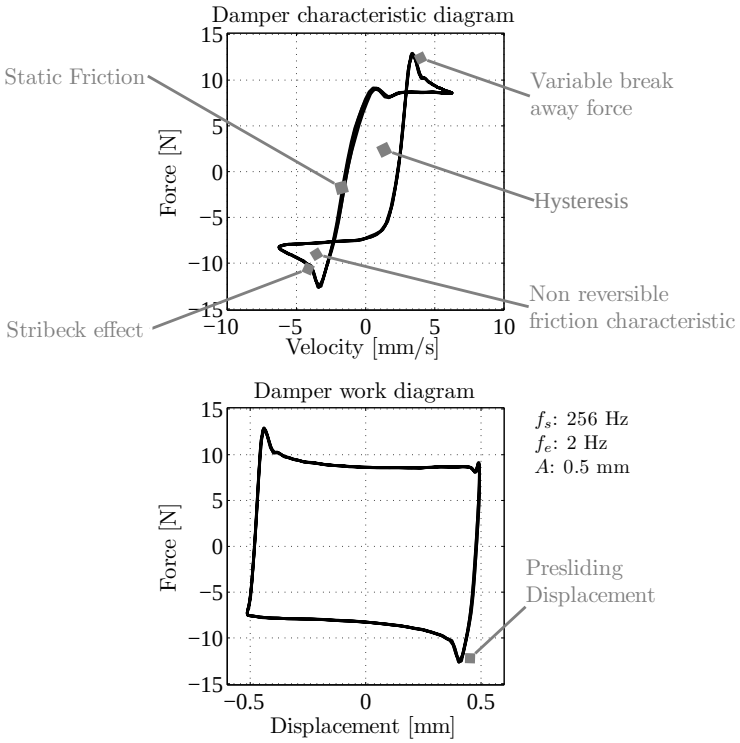

Figure 6.2: Shock absorber friction phenomena observed at an excitation frequency of 2 Hz and excitation amplitude of 0.5 mm

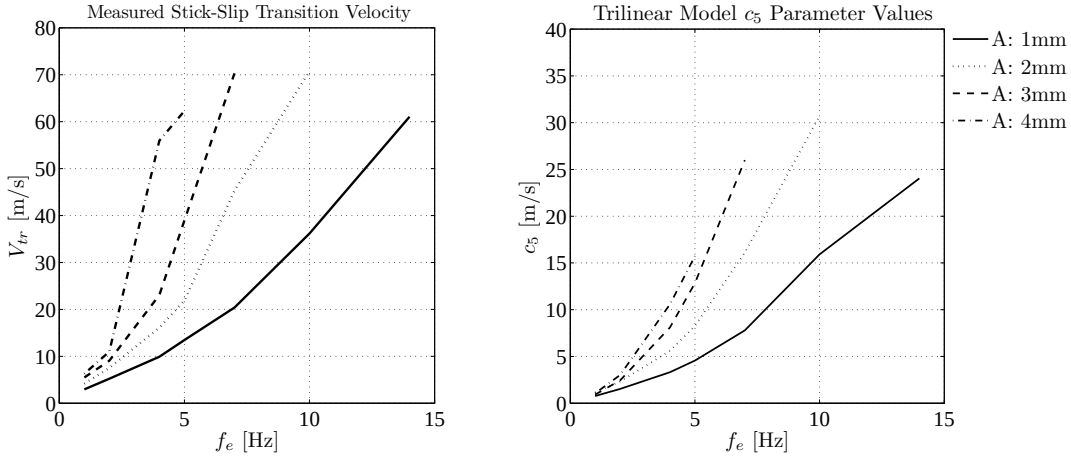

Figure 6.3: Measured Stick–slip transition velocity and optimised trilinear damper model c_5 parameter

Linear, piecewise linear and nonlinear shock absorber models are developed. The nonlinear LuGre model accurately describes the shock absorber across the range of discrete excitation frequencies and amplitudes of the experimental test. The LuGre model is, however, relatively complex compared to the linear and piecewise linear models. It is also difficult to implement in practical engineering applications [179]. The piecewise linear model provides a good compromise between model accuracy and complexity. It provides a more intuitive model of the shock absorber as model parameters can be related to shock absorber phenomena such as static friction, viscous damping in compression and rebound and stick–slip transition velocity. Figure 6.3 shows the optimised trilinear parameter c_5 plotted alongside measured stick–slip transition velocity. Note how the trilinear parameter shows similar frequency and amplitude dependence to the measured stick slip transition velocity.

The identification of a piecewise linear or nonlinear model to describe the shock absorber behaviour over the full frequency range of the experimental tests proves illusive. The approach taken to develop shock absorber models for quarter car simulation uses operational quarter car testing. The shock absorber force measurement setup allows both the measurement of shock absorber force in isolation and also in operation. This allows both linear and piecewise linear shock absorber models to be optimised at each individual excitation frequency to describe the shock absorber behaviour.

The shock absorber spring shows only a slight deviation from linear force–displacement behaviour and as a result is modelled a massless linear spring element. A linear spring stiffness of 5690 N/m is calculated and damping is found to be negligible. This spring model shows an average MSE of less than 0.6 % across the frequency and amplitude range of the experimental tests, indicating an excellent model fit.

6.1.2 Quarter car rig simulation

The identified component parameters are used to develop both linear and nonlinear quarter car simulations of the experimental test rig. The accuracy of linear quarter car simulations are first examined. The quarter car rig is excited at fifty six individual frequencies in the 1.6–24.0 Hz frequency range, using an approximately sinusoidal excitation. Linear damping models are fitted to the shock absorber characteristic at each measurement frequency. This technique allows for optimal linear damper models to be used in the linear simulations at each excitation frequency. Due to the static friction nonlinearity, the optimal viscous damping coefficients at low shock absorber velocities are extremely high ($f_e < 6$ Hz). The linear simulation is quite accurate in this low velocity static friction zone where the static friction nonlinearity dominates. The simulation accuracy may be aided by the fact that the relative motion between the unsprung and sprung masses is very small and as a result the shock absorber is effectively inactive at these low excitation velocities. As the excitation frequency increased the relative motion across the shock absorber increased and the shock absorber model became more significant in terms of simulation accuracy. Outside the static friction zone the linear simulations are found to give a reasonable approximation of the unsprung mass acceleration but overestimate the sprung mass accelerations. Figure 4.12 provides an insight into the reason behind sprung mass acceleration overestimation. Note how the optimal linear model significantly over estimates shock absorber force at higher excitation velocities. Overestimation of the shock absorber force would subsequently cause overestimation of the sprung mass acceleration.

A significant improvement in simulation accuracy is seen with the addition of nonlinear component models. The nonlinear quarter car model is assessed at two excitation frequencies, 6.8 Hz and 11.2 Hz. The shock absorber is modelled as a trilinear element and the tyre as a hardening/softening spring with parallel hysteretic damping. The accuracy of the nonlinear simulation is in part due to the accuracy with which

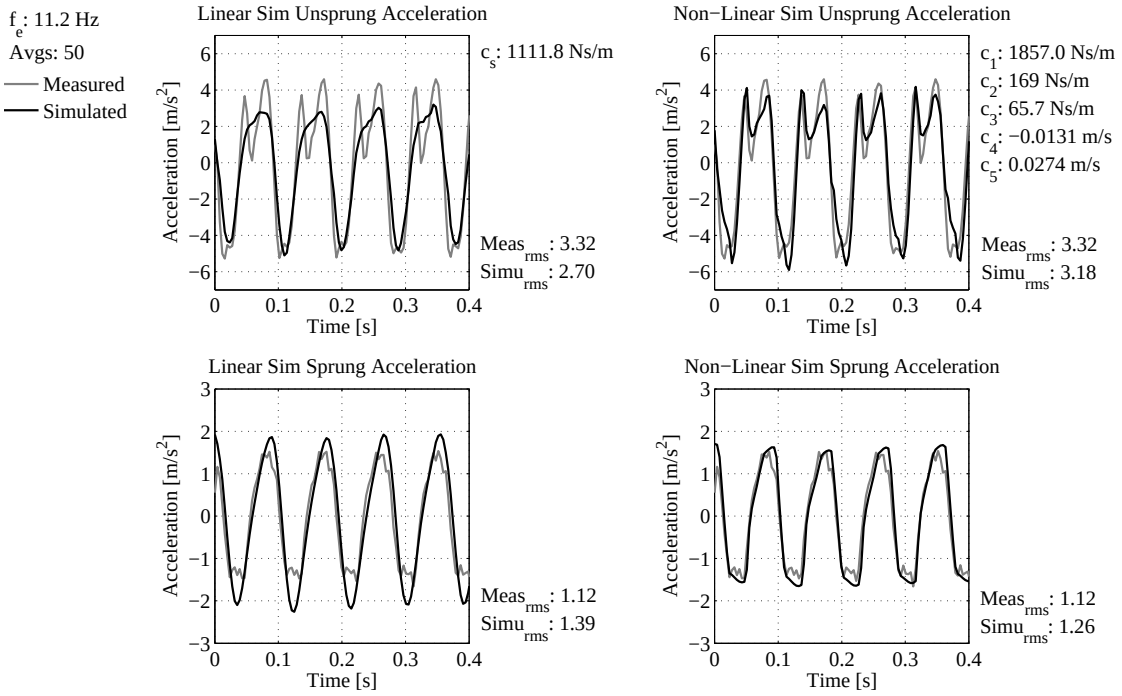

Figure 6.4: Linear and nonlinear quarter car simulation evaluation at 11.2 Hz

the trilinear shock absorber model represents the most significant nonlinearity of the shock absorber, namely the static friction. This is illustrated in Figure 4.12. The trilinear model accounts for both the high damping in the static friction zone and also the lower damping in compression and rebound outside this zone. The different influences of the trilinear and linear models on simulation results are seen at the unsprung mass acceleration peaks in Figure 4.14, replotted here in Figure 6.4. These are regions where shock absorber acceleration is close to its maximum and shock absorber velocity is close to zero. The high damping of the trilinear model in this zone causes a visible decrease in shock absorber acceleration. This is in line with the signal pattern observed from measured signals. The linear model cannot account for this phenomenon.

The effect of tyre damping on simulation accuracy is assessed at an excitation frequency of 10.4 Hz. Identical simulations are run with an optimised trilinear shock absorber model. One simulation has no tyre damping and the second has an equivalent tyre viscous damping of 138 N s/m, calculated using equation 4.5. Tyre damping is shown to have a moderate influence on the simulation accuracy. The simulation with tyre damping shows more realistic unsprung mass peak accelerations and as a result lower sprung mass acceleration. The argument put forward by a number

of authors is that tyre damping can be neglected in simulations of this type. The results show that although it has an influence on the simulation accuracy, its affect is relatively small when compared with the affect the shock absorber model has on the simulation accuracy. In developing a nonlinear quarter car model, the effectiveness of the shock absorber model should first be examined before focusing on modification of the tyre model to improve simulation accuracy [157].

Narrowband excitation, in the form of an approximately sinusoidal excitation, is used throughout this experimental and simulation work. Results show that, for this type of excitation, the nonlinear quarter car model outperforms the linear quarter car model when compared with measured data from the experimental test rig. It is noted that during the isolated shock absorber testing, the shock absorber characteristic shows significant frequency and amplitude dependence, a common observation during shock absorber experimental testing [70, 76]. Due to the narrowband nature of the excitation in this investigation, it is possible to assess the accuracy of linear and nonlinear quarter car models at individual frequencies and amplitudes. Under broadband excitation the frequency and amplitude dependence of the shock absorber may need to be accounted for.

6.2 Operational suspension system identification

The force-response approach to suspension system identification is shown to aid in the accurate development of component models. However, the laboratory experimental conditions of an isolated force-response test can differ significantly from the real life operating conditions [29]. Operational testing techniques allow component identification to be carried out around the actual loading conditions and external restraints [97]. It has been argued that *in situ* operational system characterisation and identification techniques provide a more useful model of the system, which is optimal in the real operating environment [59, 78].

The operational identification of the quarter car test rig aims to determine the suspension system sprung mass, the shock absorber spring stiffness and also a nonlinear damping model for the shock absorber. The boundary perturbation technique, developed in § 5.1, allows the estimation of suspension parameters without the need to measure the input excitation at the tyre patch. This requires two vehicle experimental tests, one with a known mass added to the vehicle sprung mass. The input

displacement to the tyre patch can be different for each experimental test run and is unmeasured. Here, the assumption is made that the input displacement spectrum is of similar magnitude for both runs, to ensure amplitude dependence of nonlinearites do not effect the parameter estimates. Both time and frequency domain approaches to the problem are examined.

6.2.1 Nonlinear quarter car simulation

The implementation of the boundary perturbation technique under controlled simulated conditions aids the development of the approach. A number of operational system identification scenarios are examined using simulated nonlinear quarter car model data. The quarter car model is chosen to have a dominant friction nonlinearity and a mild cubic stiffness.

Time domain approach

The boundary perturbation technique is used with Direct Parameter Estimation (DPE) to estimate suspension system parameters in the time domain. Exact parameter estimates are obtained in the case when all nonlinearities in the system are accounted for in the proposed system model. In the presence of 5 % uncorrelated white noise, the percentage errors in m_s, k_s and k_n are all less than 1 %, while the parameters c_s and μ_s show arrors of 7.7 % and 10.7 % respectively.

In the case where only the dominant nonlinearity is included in the model, estimates of m_s, c_s and μ_s show less than 0.1 % error. The spring stiffness, k_s, shows an over estimation by 9.6 %. The estimated linear stiffness has increased to compensate for the lack of a cubic stiffness term in the estimation process, and has effectively become an equivalent stiffness value which provides the best linear estimate of the stiffness in the model. In the presence of noise, the c_s and μ_s parameters show errors of similar magnitude to the case when all nonlinearities are included. The spring stiffness, k_s, shows an error of 9.0 %, which is 0.6 % lower than the case with no noise. The ensemble of estimates does, however, show a standard deviation of 79.1 N/m in the presence of noise, which can be compared with a value of 9.2 N/m when no noise is present on the signals. Accurate estimates of the sprung mass are obtained even in the presence of noise and an uncharacterised nonlinearity.

Hysteresis, in the form of backlash, is found to have a pronounced effect on the estimated parameter accuracy. It is interesting to note that the Restoring Force Surface (RFS) for the simulation with 10 % backlash (Figure 5.4) looks very similar to that with no backlash (Figure 5.3). Therefore, characterisation of a backlash nonlinearity using the RFS approach is not guaranteed. In the noise free case, the average parameter errors for 0.1 %, 1.0 % and 10 % backlash are 0.23 %, 1.87 % and 11.49 %, respectively. In the presence of noise and 10 % backlash the mean percentage error on the estimates is 11.64 %, although the standard deviation on the estimates is significantly greater in the presence of noise. Again less than 1 % error is seen on the sprung mass estimates in all cases. In the presence of 10 % backlash, with the backlash accounted for in the parameter estimation, very similar results are seen to the estimates with 0 % backlash.

The identification of the nonlinear quarter car model with Bouc–Wen hysteretic shock absorber, aims to examine the robustness of the estimation process when the exact shock absorber model form is unknown and is not included in the problem formulation. The hysteresis in the system can be identified from the stochastic nature of the RFS at low velocities (Figure 5.5). Accurate estimates of the sprung mass are obtained in both the noise free and noise polluted cases, with a maximum percentage error on the estimates of 0.4 %. The estimation of the linear spring and damper parameters proved difficult. In effect, the estimation procedure becomes a non–parametric method due to the absence of the exact shock absorber model form in the estimation procedure. The identified linear stiffness and linear damping parameteres show percentage errors of 121.5 % and 245.1 %, respectively. The estimated values are effectively equivalent linear stiffness and damping parameters which provide the best approximation of the system behaviour in a least squares sense. The including of a backlash parameter in the model formulation is also examined. An initial backlash parameter, estimated using the characteristic diagram in Figure 5.5, is optimised to minimise the MSE between the parameter estimation model and the simulated values. The inclusion of the backlash is seen to reduce the error on the linear stiffness and linear damping parameters to 47.1 % and 195.0 %, respectively. The MSE between the measured and predicted time histories is also reduced from 18.04 % to 11.47 % with the inclusion of backlash in the model (Figures 5.6 and 5.7).

The approach to nonlinear system identification presented by Masri *et al.* [48] is applied to the quarter car simulation with Bouc–Wen shock absorber. Given a set

of basis functions, the algorithm itself determines the required parameters to best represent the system. A basis function of 17 parameters is used. The estimated linear stiffness and damping parameters again show large percentage errors of 173.3 % and 410.1 %, respectively. The sprung mass estimate is again accurate, showing an error of 0.6 %.

Frequency domain approach

The time domain approach provides accurate estimates of sprung mass in all cases, a maximum error of 1.2 % is seen across all the simulated scenarios. Less success is obtained in the estimation of true values of stiffness and damping in the case when the exact shock absorber model form is unknown. In this case, the estimation procedure becomes non-parametric and the stiffness and damping estimates are effectively equivalent linear stiffness and linear damping values. The frequency domain approach uses Reverse Multiple Input/Single Output (R–MISO) nonlinear spectral analysis, and aims to complement the time domain methods and estimate the true value of the linear stiffness in the quarter car simulations. This approach is chosen for a number of reasons. Firstly, the availablility of ordinary coherence, partial coherence and multiple coherence functions can quickly provide an indication of how well the proposed model fits the measured data. Uncharacterised nonlinearities and noise contamination lead to drops in the coherence functions. Secondly, due to its frequency domain nature, it can identifiy frequency dependent component parameters. This is important as the shock absorber used for experimental testing in this work is shown to exhibit significant frequency dependence, as identified under harmonic excitation in isolation (§ 4.2). Thirdly, its ability to identify the system linear Frequency Response Function (FRF) in the presence of complex nonlinear behaviour is a powerful feature for the analysis of nonlinear systems.

To introduce the technique, it is first applied to the nonlinear quarter car model with friction and cubic stiffness nonlinearities. The approach estimates sprung mass normalised parameters. A three input/single output model is developed as shown in Figure 5.8. The inputs records $x_1(t)$, $x_2(t)$ and $x_3(t)$ are defined as $(x_u - x_s)$, $sign(\dot{x}_u - \dot{x}_s)$ and $(x_u - x_s)^3$, respectively. The output $y(t)$ is equal to $\ddot{x}_s$. Accurate estimates of k_s/m_s, μ_s/m_s and k_n/m_s are obtained, all showing less than 0.5 % error in the noise free case. In the presence of noise, the development of a curve–fitting technique is required for parameter estimation. Drops in coherence, especially at

frequencies close to zero, prevent direct estimation of the mass normalised stiffness from the estimated linear FRF. The Rational Fraction Polynomials (RFP) curve–fit method is adopted to improve parameter estimation accuracy. The method is further developed to include a weighting function developed from the variance on the FRF estimate. This reduces the tendance of the least square curve-fitting technique to be biased by FRF measurement points with low multiple coherence. A weighted mean is used to estimate the magnitude of the nonlinear path constant coefficients. Using this approach for the case with 5 % noise, the estimated friction parameter shows an error of 6.1 %. The linear stiffness and cubic stiffness parameteres show greater accuracy, with errors of 0.7 % and 1.1 %, respectively.

The application of the method to the more complex Bouc–Wen quarter car model is now discussed. Equation 5.16 shows that the Bouc–Wen shock absorber consists of a linear spring and linear damper in parallel with a Bouc–Wen hysteretic element. The aim is to obtain better estimates of the true linear stiffness (k_s in equation 5.16) in the suspension system as opposed to equivalent linear stiffness estimates obtained using the time domain approach. Coherence functions are used to determine the inputs to the R–MISO analysis. A set of basis functions for the analysis is chosen, consisting of a total of 157 terms. The ordinary coherence between each term in the set of possible inputs and the R–MISO output is calculated. The area under the ordinary coherence function in the frequency range of interest is calculated and expressed as a percentage of perfect coherence. Functions with a coherence level above a selected tolerance percentage are included in the problem formulation.

The selected inputs are then placed in descending order based on their ordinary coherence with the output. In this case a total of 16 terms qualified for inclusion in the analysis. The analysis is checked to ensure it is well defined before it is run, as outlined in § 5.2.2. The resulting linear FRF, between the first input path ($x_u - x_s$) and the output ($\ddot{x}_s$), is curve–fitted as before to determine the sprung mass normalised linear stiffness. The curve–fit is performed in the 0–16 Hz frequency range as the multiple coherence is seen to drop at higher frequencies and this is accompanied by a drop in phase from the ideal value of $\pi/2$ for a linear spring and damper in parallel. The estimated mass normalised linear stiffness is found to be 175.8 N/m, corresponding to a linear stiffness of 4395 N/m . The percentage error on the estimate is 12.1 %. This estimate is significantly more accuracte than the equivalent linear stiffness parameters identified using the time domain approach. For the same simulation, the best time domain estimate of the linear stiffness is 7353.5

N/m, corresponding to an error of 47 %. It is believed that a combination of the use of coherence functions to determine the optimal model formulation, coherence functions to indicate FRF accuracy and also the ability of the R–MISO analysis to estimate frequency dependent parameters, contribute to the significant improvement in linear stiffness estimate accuracy.

6.2.2 Quarter car rig identification

The time and frequency domain approaches, developed under simulated conditions, are now applied to the experimental identification of the quarter car test rig. The initial focus is on the identification of the sprung mass and the linear spring stiffness of the suspension system. The challenge here is to identify these parameters in the fully assembled quarter car test rig using only acceleration measurements recorded on the sprung and unsprung masses. The identification is carried out in the presence of a complex frequency and amplitude dependent nonlinear damper, nonlinear tyre and unmeasured multi–directional excitation at the tyre patch. This is in contrast to the spring identification carried out in § 4.3, where isolated testing and controlled experimental conditions are used. Focus then turns to the identification of a nonlinear damping model. Although accurate models of the damping mechanism are generated at discrete frequencies using isolated sinusoidal testing, the development of a general damping model applicable across a broader frequency range proves very difficult.

The quarter car test rig is excited using the 72 lobe cam for the experimental testing. The cam frequency is linearly swept from 0.4 Hz to 6 Hz over the 64 second period of the data acquisition. The 72 lobe cam is designed to excite the tyre with a series of impulses to provide a broadband excitation to the suspension system. The RFS of the quarter car rig is first generated. An initial plot of the RFS developed using 10 data set averages is shown in Figure 5.18. The stochastic nature of the surface is due to the hysteresis present in the system. Cafferty *et al.* examined the generation of RFS for an automotive damper exhibiting hysteretic behaviour [21]. It was argued in this paper that the significant dynamical behaviour of the system is summarised by the 'backbone' of the RFS. The RFS replotted for 400 data set averages, corresponding to over 7 hours of suspension operation, is shown in Figure 5.19. This approach effectively averages the separate nonlinear paths in shock absorber compression and rebound and presents a clear visual representation

of the shock absorber characteristic.

The shock absorber is shown to exhibit significant nonlinear behaviour, mainly due to complex friction related phenomena. The shock absorber requires accurate force–response testing at discrete frequencies to develop an understanding of its behaviour. It also requires the use of a complex friction model to describe its behaviour at these discrete frequencies. Therefore this presents the problem of how the shock absorber can be accurately characterised, in operation, under broadband excitation using RFS methods (an approach commonly used in the operational identification of vehicle suspension systems [70, 74, 76]). The frequency domain approach, in this investigation, uses a custom developed R–MISO setup algorithm to determine the model form which best describes the system under test. For the time domain analysis, extensive development of the methods under controlled simulated conditions, shows that the sprung mass estimate is not particularly sensitive to the accuracy of the shock absorber model.

Time domain approach

The time domain approach is first applied to estimate the quarter car rig sprung mass. The development of the boundary perturbation technique, using simulated data, revealed that accurate estimates of the sprung mass can be obtained even in a situation where the shock absorber model form is unknown and only approximated. The relatively simple spring–damper–friction shock absorber model applied to the identification of the complex Bouc–Wen shock absorber model, returned accurate sprung mass estimates with a percentage error of less than 1 %. The quarter car rig shock absorber RFS shows three distinct regions, relatively low damping at high piston velocities in compression, relatively low damping at high piston velocities in rebound and a high damping region at low velocities. These observations, suggest that a spring–damper–friction shock absorber model would provide a reasonable model of the shock absorber characteristic.

The boundary perturbation technique coupled with DPE is applied to 60 data sets acquired with no added mass attached to the sprung mass and a further 60 data sets each for added mass values of 6.5 %, 8.0 % and 10.5 % of the sprung mass. The inputs used in the DPE formulation are $(x_{uz} - x_{sz})$, $(\dot{x}_{uz} - \dot{x}_{sz})$, $(sign(\dot{x}_{uz} - \dot{x}_{sz}))$ and the output is the acceleration of the sprung mass $(\ddot{x}_{sz})$. Figure 5.20 shows the results of the analysis applied with 10.5 % added mass and is replotted here in

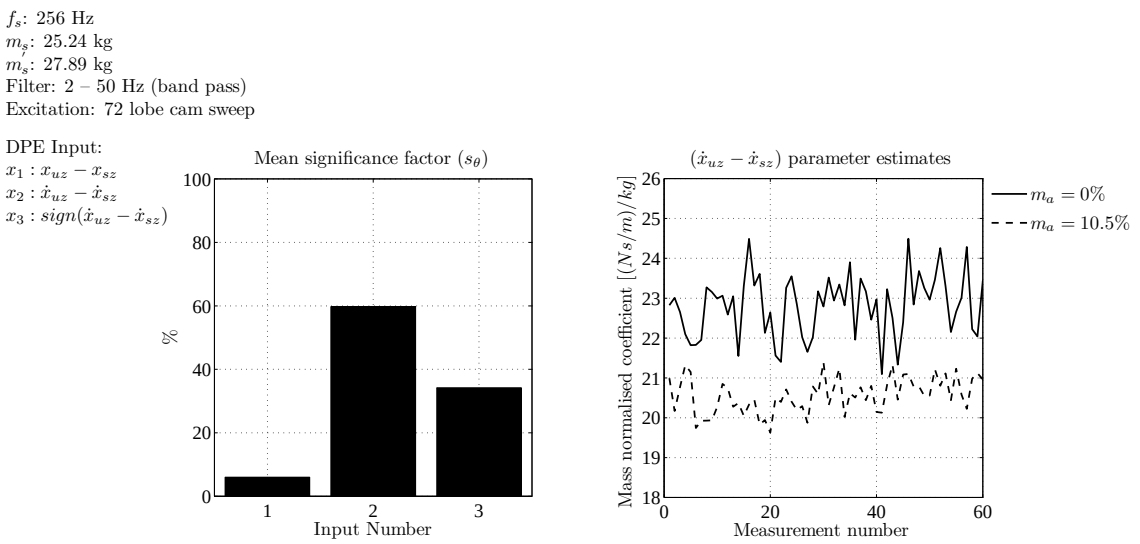

Figure 6.5: Quarter car rig boundary perturbation analysis with 10.5 % added mass

Figure 6.5. The mean significance factor for each term in the model formulation, across the 60 data sets, are shown using the bar graph. The most significant term in the model is found to be the relative velocity across the shock absorber ($\dot{x}_{uz} - \dot{x}_{sz}$), therefore, it is used to estimate the quarter car rig sprung mass. The individual mass normalised damping estimates for the 0 % added mass and 10.5 % added mass cases are also shown in Figure 6.5. The mass normalised values appear to be noisy in nature with the coefficients for 0 % and 10.5 % added mass showing standard deviations of 0.78 N s/m/kg and 0.45 N s/m/kg, respectively. The use of a larger number of data sets in the estimation may seem like a logical solution to decrease the effect of the noise and increase the accuracy of the estimated sprung mass but in a number of the experimental data sets, drift in the mass normalised coefficient estimates is observed. This drift can be seen to a certain extent in the coefficients of the 10.5 % added mass across the 60 data sets. An underlying increasing trend can be seen from approximately measurement number 5 to measurement number 60. The data is acquired over a 90 minute period so the drift may be due to ambient temperature effects on the quarter car rig, the data acquisition system or both. It may also be due to rig warm up during continuous operation. However, steps are taken to eliminate this by acquiring 120 data sets for each analysis and discarding the first 60 to ensure the rig has reached a steady state operating temperature before the data for analysis is acquired.

The boundary perturbation and DPE time domain approach is seen to give good estimates of the sprung mass in all three cases, with percentage errors for the 6.5 %, 8.0 % and 10.5 % added mass analyses equal to 0.5 %, 6.6 % and 3.4 %, respectively. These results verify the findings during the development of the method under controlled simulated conditions. It is seen, using both simulated and experimental data, that the time domain approach provides a robust method of estimating the suspension system sprung mass even in the case when a simplified representation of the actual shock absorber model characteristic is used. The estimated spring stiffness values are also quite interesting. Note how, for the three different added masses, the stiffness estimates are very similar, albeit with errors of approximately 150 % when compared with the true suspension linear stiffness. Accurate estimation of the true spring stiffness is not expected using the time domain approach. Simulated quarter car results show that the estimated stiffness is an equivalent linear stiffness when the exact shock absorber model form is not included in the model formulation.

Frequency domain approach

Having obtained good estimates of the sprung mass using three different added mass percentages, focus now turns to estimating the true linear stiffness in the quarter car test rig as opposed to an equivalent linear stiffness obtained using the time domain approach. As in the simulated quarter car case, the R–MISO approach is applied to the problem. The 60 data sets for the 0 % added mass case are used for the R–MISO analysis.

An initial investigation is carried out to determine the significance of the unsprung mass motions in the x and y–directions. The plots of the unsprung mass trajectory in the x–z plane and the y–z plane are shown in Figure 5.21. It can be seen that the peak displacements in the x and y–directions are greater than 15 % of the peak displacement in the z–direction and are, therefore, deemed significant. This adds an interesting aspect to the operational identification problem in this investigation. Many works presented in the literature use hydraulic shakers to excite the suspension systems [70, 75, 76, 107]. This provides a very controlled vertical excitation to the tyre patch and does not replicate the realistic case where multi–directional motions of the unsprung mass are observed.

A large basis function, consisting of 256 terms, is chosen for the R–MISO analysis due to the complex nonlinear behaviour of the shock absorber and the multi–directional

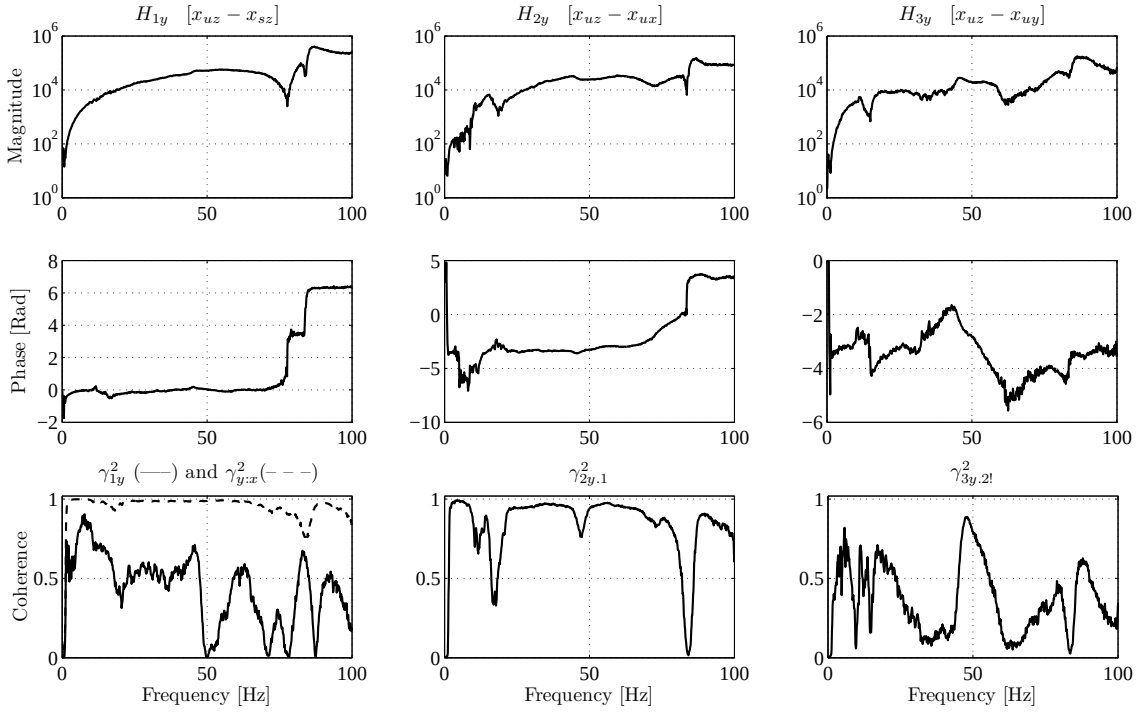

Figure 6.6: Quarter car rig R-MISO analysis results for input paths x_1, x_2 and x_3

motion of the unsprung mass. The basis function terms are outlined in equation 5.30. The number of terms to be included in the model are truncated as in the application of R–MISO to the simulated case. Due to the large number of basis terms the coherence threshold level is set at 15 % of perfect coherence. A total of 25 terms qualify for inclusion in the R–MISO analysis. The FRF's for the first 3 inputs ($x_{uz} - x_{sz}$, $x_{uz} - x_{ux}$, $x_{uz} - x_{uy}$) to the R–MISO analysis are shown in Figure 5.23 and replotted here in Figure 6.6. Note the significant increase in the multiple coherence function over the ordinary coherence function for H_{1y}, due to the inclusion of the additional linear and nonlinear terms. Greater than 90 % multiple coherence is seen in the 1.5–70 Hz frequency range.

A 13$^{\text{th}}$ order RFP model is used to curve–fit H_{1y}. The model order is chosen based on the rig resonances observed during quarter car rig Experimental Modal Analysis (EMA). Table 6.1 summarises resonant frequencies obtained via peak–picking the results of the EMA on the quarter car rig (as described in § 3.1.4, where the driving point FRF's for this analysis are plotted in Figure 3.9). A total of 13 significant resonances are observed in the EMA FRF's. Note how a number of the rig resonance can be observed in the linear paths (x_1, x_2, x_3) of the R–MISO analysis (Figure 6.6). A combination of FRF peaks, phase changes and localised coherence spikes serve

Force – F_{sz}			Force – F_{uz}			Force – F_{ux}		
$\ddot{x}_{sz}$	$\ddot{x}_{uz}$	$\ddot{x}_{ux}$	$\ddot{x}_{sz}$	$\ddot{x}_{uz}$	$\ddot{x}_{ux}$	$\ddot{x}_{sz}$	$\ddot{x}_{uz}$	$\ddot{x}_{ux}$
-	-	13	-	-	-	13	13	13
-	-	-	-	-	-	-	-	15
-	-	-	-	18	-	-	-	19
-	-	-	-	-	-	-	21	-
-	-	24	25	25	24	24	24	24
33	33	-	-	-	-	-	-	-
47	-	48	-	-	-	-	-	-
71	71	-	71	71	-	-	-	-
-	-	78	-	78	78	-	78	79
-	-	-	81	-	-	-	-	-
-	-	91	91	91	91	91	91	91
93	93	-	-	-	-	-	-	-
-	-	-	-	96	96	-	96	96

Table 6.1: Quarter car rig resonance frequencies (Hz) for hammer impact excitation on the unsprung mass in the x and z–directions and the sprung mass in the z–direction

to provide a rough indication of the presence of both lightly damped and heavily damped modes. The more dominant rig resonances are observed at 11, 15, 25, 45, 79, 82 and 89 Hz. These correspond well with the modes identified in the modal analysis test, considering that the rig resonant frequencies may vary slightly under operating conditions. In the operational analysis case when no *a priori* knowledge of the system exists, this approach may provide a starting point for the selection of a RFP curve–fit order.

The linear paths x_2 and x_3 in the R–MISO analysis are chosen to eliminate as many rig resonances as possible from x_1. These paths are chosen by trial and error using combinations of the recorded signals x_{ux}, x_{uy}, x_{uz} and x_{sz}. This simplifies the estimation of the mass normalised spring stiffness between the unsprung mass and the sprung mass. In H_{1y}, note that below 50 Hz, very subtle indicators (small highly damped peaks and small phase changes) of the resonance can be observed at approximately 15 Hz and 45 Hz, but the dominant effects of these peaks are removed from the analysis by the linear paths x_2 and x_3. This approach to the estimation of the linear FRF between the unsprung and sprung masses shows good results. This is confirmed with the curve–fit shown in Figure 5.14. A sprung mass normalised spring stiffness value of 227.2 N/m/kg is obtained from the curve–fit in a similar manner to that outlined under simulated conditions.

A comparison of the parameter estimates obtained using the time and frequency domain approach to operational identification of the quarter car test rig and parameter values obtained through isolated component identification methods is shown in Table 5.17. The mean sprung mass, obtained using three added mass values for the time domain analysis, is used to determine the true linear spring stiffness. The linear stiffness estimate of 5534.5 N/m and the sprung mass estimate of 24.36 kg, show percentage errors of 2.7 % and 3.5 %, respectively, when compared with estimates using traditional isolated component testing methods. The results show excellent agreement between operationally identified parameters and isolated parameters.

The operational analysis is extended further to develop a nonlinear model of the damping in the shock absorber. The nonlinear damping model used, termed the hyperbolic tangent model, has been applied by a number of authors to model shock absorber characteristic diagrams [21, 70]. A quarter car simulation developed using operationally identified component parameters (sprung mass, spring stiffness and nonlinear damping model) shows reasonable agreement with measured results, despite being validated under excitation conditions differing significantly from those used during the identification process. Errors in the Root Mean Square (RMS) accelerations in the 6.8 Hz case are 22.8 % and 13.4 % for the unsprung and sprung masses, respectively. At 11.2 Hz, errors of 13.8 % and 36.2 % are seen for the unsprung and sprung mass accelerations, respectively. Good agreement is seen in terms of simulated and measured signals peak pattern. One reason for the over estimation of quarter car rig accelerations in all cases is attributed to the differing relative velocities across the shock absorber during the identificaiton process and the validation tests. A RMS value of 0.022 m/s is seen during identification compared with a value of 0.034 m/s observed during validation at 11.2 Hz. As a consequence, during identification the shock absorber would operate more in the high damping static friction zone as opposed to the lower damping viscous damping zones. The identified model would in turn reflect this and would, therefore, not be optimal in the presence of higher relative velocities across the shock absorber as observed during validation.

Due to the nature of its development, the operational quarter car simulation is valid across a wide frequency range. It should be noted that the same quarter car simulation is used at both validation frequencies. This is in contrast to the nonlinear quarter car simulations developed in Chapter 4. These models feature trilinear shock absorber models optimised at 6.8 Hz and 11.2 Hz. Attempts to developed

a reasonably accurate model, applicable across a larger frequency range using isolated sinusoidal testing methods, proves illusive. For this reason it is believed the operationally identified quarter car simulation provides a more useful model of the quarter car test rig when compared with the quarter car simulations optimised at discrete frequencies.

6.3 Summary

The development of techniques for the operational identification of vehicle suspension systems in this investigation benefits from the end–to–end approach taken to the problem. The problem is addressed in a methodical and logical manner from experimental design to operational testing. There are a number of important features of the analysis methods developed in this work which have not previously been addressed by similar investigation in this field [70, 74, 75, 76, 106, 107, 111]. Firstly the quarter car test rig is designed to provide realistic suspension system operating conditions. Excitation to the tyre patch is multi–directional and significant motions of the unsprung mass in the x, y and z–directions are observed. They are deemed significant to the overall dynamics of the system and are accounted for in the analysis. This type of realistic excitation input to the tyre patch has not previously been included in operational suspension system identification works in the literature. The operational identification approach developed in this investigation represents a move towards on–road vehicle suspension system identification. The time and frequency domain methods would require little modification to allow their application to such a problem.

The quarter car rig is also shown to have resonances close to those observed during full vehicle chassis testing [163]. The ability of the techniques developed here to deal with these resonances is key to the success of the methods. The most common excitation type used in the literature of operational suspension system identification is slow swept sine at low frequencies (0–15 Hz). Therefore, modes of the chassis excited under normal operating conditions are not excited during the analysis, eliminating their effect. In this work the tyre is excited using a rotating cam which provides a series of impulses to the tyre. Although the excitation of a rotating cam is inherently periodic, no attempt is made to limit the bandwidth of the excitation. Analysis of the FRF's generated using R–MISO analysis show multiple coherences

above 0.9 across most of the frequency range of the analysis (0–100 Hz), giving a strong indication that the excitation applied to the suspension system is broadband in nature.

The shock absorber used in the quarter car rig shows significant nonlinear behaviour, and it is generally accepted that automotive shock absorbers exhibit complex nonlinear behaviour [1, 158, 159]. RFS methods have been used, in many investigations focusing on the operational identification of suspension systems, to characterise the nonlinearities in the system. This is usually in the presence of controlled shaker excitation allowing the use of single frequency excitation or slow swept sines to observe nonlinear behaviour and select an appropriate model form. This approach works well under controlled laboratory conditions, but under real operating conditions and broadband excitation, it cannot be applied. The use of R–MISO analysis eliminates the need to estimate a shock absorber model form based on observations of the RFS. A large set of basis functions can be generated and the analysis can select the terms in the set to best represent the nonlinearities in the system. This is important when the shock absorber exhibits strong nonlinear behaviour. That said, the RFS is still a very useful tool in the operational identification process. It can be used to quickly assess the degree of nonlinearity in the system. It is used to good effect in this work to select a model form for the time domain analysis. This is possible as the time domain approach is not particularly sensitive to the accuracy of the shock absorber model chosen for the analysis.

In conclusion this work identifies actual suspension parameters using in–operation measurements, while the comprehensive approach to the operational identification problem allows for the validation of these parameters using parameters identified under controlled isolated testing conditions.

Chapter 7

Conclusions

This work presented the development of an new approach to the identification of vehicle suspension parameters using operational measurements. Due to the complexity of the system, time and frequency domain algorithms were developed. An end–to–end approach was taken to the problem which involved a combination of focused experimental design, well established force–response testing methods, vehicle suspension experimental testing and simulation, before finally implementing operational system identification. This allowed for the development of a comprehensive understanding of the dynamics of the system under test. It also provided a means of validating the suspension parameters obtained using operational testing methods using traditional force–response testing techniques. The outcomes of this work are summarised as follows,

- A new approach to the operational identification of suspension system parameters was developed. A combination of time and frequency domain methods were used to extract sprung mass, linear stiffness and nonlinear damping model parameters from a quarter car experimental test rig. Only acceleration measurements of the quarter car rig unsprung and sprung masses were used as inputs to the identification process.
- Component parameters identified using this new approach under operational conditions showed excellent agreement with those identified under controlled laboratory conditions using force–response testing.
- The operational identification approach was developed under conditions de-

signed to replicate on–road vehicle testing conditions in the laboratory. This represents a move away from operational identification using shaker excitation and a move towards more applicable on–road vehicle identification.

- A quarter car suspension test rig was designed and built to facilitate experimental suspension system testing. A novel shock absorber force measurement set–up was developed allowing the measurement of shock absorber force under both isolated and operational shock absorber testing conditions.

- The quarter car rig was dissembled and the major components of the rig (tyre, damper and spring) were identified in isolation using traditional force–response testing methods. Models of the major components were developed and formed the basis for the development of an accurate nonlinear quarter car simulation of the suspension test rig.

7.1 Future work

Research into techniques for extracting system models under real operating conditions has become more prominent in the literature in recent years. In this work, new techniques have been developed for the operational testing of automotive suspension systems. The time and frequency domain approach developed here provides a foundation for the further development of *in situ* suspension system testing techniques. Key advancements which will further drive this area of research in the future are as follows,

- This work attempted to replicate on–road vehicle conditions in the laboratory. The move towards full vehicle, on–road testing will be a key stage in the development of operational suspension system identification. Very few investigations of this nature have been carried out and reported in the literature.

- The effect of full vehicle pitch, roll and yaw motions on the identification process will need to be examined. This may be a case of measuring these motions and including them in the identification algorithm in much the same way that the unsprung mass displacement in three directions were included in this investigation.

- The operational identification of the tyre is an area which requires further research. A combination of operational identified shock absorber and operationally identified tyre would provide a means of developing a full vehicle simulation using operational testing techniques.

Bibliography

[1] S. Duym, R. Stiens, and K. Reybrouck, "Evaluation of shock absorber models," *Vehicle System Dynamics*, vol. 27, no. 2, pp. 109 – 127, 1997.

[2] A. Simms and D. Crolla, "The influence of damper properties on vehicle dynamic behaviour," *SAE Technical Paper Series, 2002-01-0319*, 2002.

[3] Y. Goh, J. Booker, and C. McMahon, "Uncertainty modelling of a suspension unit," *Proceedings of the Institution of Mechanical Engineers, Part D: Journal of Automobile Engineering*, vol. 219, no. 6, pp. 755 – 771, 2005.

[4] C. Halfmann, O. Nelles, and H. Holzmann, "Modeling and identification of the vehicle suspension characteristics using local linear model trees," *IEEE Conference on Control Applications - Proceedings*, vol. 2, pp. 1484 – 1489, 1999.

[5] W. Fleming, "Overview of automotive sensors," *IEEE Sensors Journal*, vol. 1, no. 4, pp. 296 – 308, 2001.

[6] D. L. Cronin, "Macpherson strut kinematics.," *Mechanism and Machine Theory*, vol. 58, no. 610, pp. 631 – 644, 1981.

[7] C. Kim, P. Ro, and H. Kim, "Effect of the Suspension Structure on Equivalent Suspension parameters," *Proceedings of the Institution of Mechanical Engineers, Part D: Journal of Automobile Engineering*, vol. 213, pp. 457–470, 1999.

[8] L. Svedung, "Multi-body dynamics of vehicle suspensions," Master's thesis, University of Melbourne, 2000.

[9] W. Matschinsky, *Road Vehicle Suspensions*. London, UK: Professional Engineering Publishing, 1998.

[10] C. M. Close, D. K. Frederick, and J. C. Newell, *Modelling and analysis of dynamic systems*. New York, USA: John Wiley & Sons, 3 ed., 2002.

[11] K. Worden and G. Tomlinson, *Nonlinearity in Structural Dynamics, Detection, Identification and Modelling*. Bristol, UK: Institute of Physics Publishing, 2001.

[12] J. Fitzpatrick and H. Rice, "A multiple input output method for the identification of nonlinear vibrating systems," in *Euromech 280*, (Ecully, France), pp. 91–102, A A Balkema, 1992.

[13] P. Eykhoff, *System Identification*. London, UK: John Wiley & Sons, 1974.

[14] C. Yang, D. E. Adams, and S. Ciray, "System identification of nonlinear mechanical systems using embedded sensitivity functions," *Journal of Vibration and Acoustics, Transactions of the ASME*, vol. 127, no. 6, pp. 530 – 541, 2005.

[15] L. Ljung, *System Identification, Theory for the end user*. New Jersey, USA: Prentice Hall PTR, 2 ed., 1999.

[16] W. Press, S. Teukolsky, W. Vetterling, and B. Flannery, *Numerical Recipes in C++: the art of scientific computing*. New York, USA: Cambridge University Press, 2002.

[17] J. Schoukens and R. Pintelon, *Identification of linear systems, a practical guideline to accurate modeling*. Oxford, UK: Pergamon Press, 1991.

[18] J. Bendat, *Non-Linear Systems Techniques and Applications*. New York, USA: Wiley-Interscience, 1998.

[19] K. Mohammad, K. Worden, and G. Tomlinson, "Direct parameter estimation for linear and non-linear structures," *Journal of Sound and Vibration*, vol. 152, no. 3, pp. 471 – 499, 1992.

[20] J. Bendat, "Statistical errors in measurement of coherence functions and input/output quantities," *Journal of Sound and Vibration*, vol. 59, no. 3, pp. 405 – 21, 1978.

[21] S. Cafferty, K. Worden, and G. Tomlinson, "Characterization of automotive shock absorbers using random excitation," *Proceedings of the Institution of Mechanical Engineers, Part D: Journal of Automobile Engineering*, vol. 209, no. 4, pp. 239 – 248, 1995.

[22] H. Rice and J. Fitzpatrick, "A generalised technique for spectral analysis of non-linear systems," *Mechanical Systems and Signal Processing*, vol. 2, no. 2, pp. 195 – 207, 1988.

[23] J. Bendat and A. Piersol, *Random Data, Analysis and Measurement Procedures*. New York, USA: Wiley-Interscience, 2000.

[24] J. Bendat and A. Piersol, *Engineering Applications of Correlation and Spectral Analysis*. New York, USA: Wiley-Interscience, 1993.

[25] D. Ewins, *Modal Analysis, Theory and Practice*. Somerset, UK: Research Studies Press Ltd., 1984.

[26] R. Allemang and D. Brown, "Experimental modal analysis," in *Harris' shock and vibration handbook* (C. Harris and A. Piersol, eds.), New York, USA: McGraw-Hill, 5 ed., 2002.

[27] H. Rice and J. Fitzpatrick, "A procedure for the identification of linear and non-linear multi-degree-of-freedom systems," *Journal of Sound and Vibration*, vol. 149, no. 3, pp. 397 – 411, 1991.

[28] N. Mø ller, R. Brincker, H. Herlufsen, and P. Andersen, "Modal testing of mechanical structures subject to operational excitation forces," in *Proceedings 25th International Conference on Noise and Vibration Engineering*, pp. 763–770, 2000.

[29] C. Devriendt and P. Guillaume, "The use of transmissibility measurements in output-only modal analysis," *Mechanical Systems and Signal Processing*, vol. 21, no. 7, pp. 2689 – 2696, 2007.

[30] R. Brincker, L. Zhang, and P. Andersen, "Modal identification of output-only systems using frequency domain decomposition," *Smart Materials and Structures*, vol. 10, no. 3, pp. 441 – 445, 2001.

[31] S. Gade, N. Mø ller, H. Herlufsen, and H. Konstantin-Hansen, "Frequency Domain Techniques for Operational Modal Analysis," in *Proceedings of the International Operational Modal Analysis Conference*, pp. 261–272, 2005.

[32] C. Devriendt and P. Guillaume, "Identification of modal parameters from transmissibility measurements," *Journal of Sound and Vibration*, vol. 314, no. 1-2, pp. 343 – 56, 2008.

[33] C. Devriendt, G. De Sitter, S. Vanlanduit, and P. Guillaume, "Operational modal analysis in the presence of harmonic excitations by the use of transmissibility measurements," *Mechanical Systems and Signal Processing*, vol. 23, no. 3, pp. 621 – 635, 2009.

[34] L. Garibaldi, "Application of the conditioned reverse path method," *Mechanical Systems and Signal Processing*, vol. 17, no. 1, pp. 227 – 235, 2003.

[35] G. Kerschen, K. Worden, A. Vakakis, and J.-C. Golinval, "Past, present and future of nonlinear system identification in structural dynamics," *Mechanical Systems and Signal Processing*, vol. 20, no. 3, pp. 505 – 92, 2006.

[36] D. Ewins, "Influence of nonlinearties on modal tests," in *Euromech 280*, (Ecully, France), pp. 3 – 11, A A Balkema, 1992.

[37] F. Ehrich and H. Abramson, "Nonlinear vibration," in *Harris' shock and vibration handbook* (C. Harris and A. Piersol, eds.), New York, USA: McGraw-Hill, 5 ed., 2002.

[38] T. Caughey, "Equivalent Linearization Techniques," *Journal of the acoustical society of America*, vol. 35, no. 11, pp. 1706–&, 1963.

[39] H. Rice, "Identification of weakly non-linear systems using equivalent linearization," *Journal of Sound and Vibration*, vol. 185, no. 3, pp. 473 – 473, 1995.

[40] S. Masri and T. Caughey, "A nonparametric identification technique for nonlinear dynamic problems," *Transactions of the ASME. Journal of Applied Mechanics*, vol. 46, no. 2, pp. 433 – 47, 1979.

[41] E. F. Crawley and A. C. Aubert, "Identification of nonlinear structural elements by force-state mapping.," *AIAA journal*, vol. 24, no. 1, pp. 155 – 162, 1986.

[42] G. Kerschen, J. Golinval, and K. Worden, "Theoretical and experimental identification of a non-linear beam," *Journal of Sound and Vibration*, vol. 244, no. 4, pp. 597 – 613, 2001.

[43] K. Worden, "Data processing and experiment design for the restoring force surface method, part i: integration and differentiation of measured time data," *Mechanical Systems and Signal Processing*, vol. 4, no. 4, pp. 295 – 319, 1990.

[44] K. Worden, "Data processing and experiment design for the restoring force surface method, part ii: Choice of excitation signal," *Mechanical Systems and Signal Processing*, vol. 4, no. 4, pp. 321 – 344, 1990.

[45] D. S. and S. J., "Design of excitation signals for the restoring force surface method," *Mechanical Systems and Signal Processing*, vol. 9, pp. 139–158 (20), 1995.

[46] C. Meskell and J. Fitzpatrick, "Errors in parameter estimates from the force state mapping technique for free response due to phase distortion," *Journal of Sound Vibration*, vol. 252, pp. 967–974, 2002.

[47] P. A. Atkins, J. R. Wright, and K. Worden, "An extension of force appropriation to the identification of non-linear multi-degree of freedom systems," *Journal of Sound and Vibration*, vol. 237, no. 1, pp. 23 – 43, 2000.

[48] S. Masri, J. Caffrey, T. Caughey, A. Smyth, and A. Chassiakos, "Identification of the state equation in complex non-linear systems," *International Journal of Non-Linear Mechanics*, vol. 39, no. 7, pp. 1111 – 27, Sept. 2004.

[49] G. Box and G. Jenkins, *Time Series Analysis, Forecasting and Control*. San Francisco: Holden Day, 1970.

[50] S. Chen, S. Billings, and W. Luo, "Orthogonal least squares methods and their application to non-linear system identification," *International Journal of Control*, vol. 50, no. 5, pp. 1873 – 1896, 1989.

[51] M. Feldman, "Non-linear system vibration analysis using hilbert transform–i. free vibration analysis method 'freevib'," *Mechanical Systems and Signal Processing*, vol. 8, no. 2, pp. 119 – 127, 1994.

[52] M. Feldman, "Non-linear system vibration analysis using hilbert transform–ii. forced vibration analysis method 'forcevib'," *Mechanical Systems and Signal Processing*, vol. 8, no. 3, pp. 309 – 318, 1994.

[53] M. Feldman, "Non-linear free vibration identification via the hilbert transform," *Journal of Sound and Vibration*, vol. 208, no. 3, pp. 475 – 489, 1997.

[54] J. Bendat and A. Piersol, "Spectral analysis of non-linear systems involving square-law operations," *Journal of Sound and Vibration*, vol. 81, no. 2, pp. 199 – 213, 1982.

[55] J. Bendat and A. Piersol, "Decomposition of wave forces into linear and non-linear components," *Journal of Sound and Vibration*, vol. 106, no. 3, pp. 391 – 408, 1986.

[56] C. M. Richards and R. Singh, "Identification of multi-degree-of-freedom non-linear systems under random excitations by the 'reverse path' spectral method," *Journal of Sound and Vibration*, vol. 213, no. 4, pp. 673 – 708, 1998.

[57] J. Fitzpatrick, H. Rice, C. Richards, and R. Singh, "Comments on identification of multi-degree-of-freedom non-linear systems under random excitations by the 'reverse path' spectral method [and reply]," *Journal of Sound and Vibration*, vol. 237, no. 2, pp. 357 – 60, 2000.

[58] C. Richards and R. Singh, "Comparison of two non-linear system identification approaches derived from "reverse path" spectral analysis," *Journal of Sound and Vibration*, vol. 237, no. 2, pp. 361 – 376, 2000.

[59] D. Adams and R. Allemang, "Frequency domain method for estimating the parameters of a non-linear structural dynamic model through feedback," *Mechanical Systems and Signal Processing*, vol. 14, no. 4, pp. 637 – 656, 2000.

[60] H. Van Der Auweraer, "Structural dynamics modeling using modal analysis: Applications, trends and challenges," in *IEEE Instrumentation and Measurement Technology Conference*, vol. 3, (Budapest, Hungary), pp. 1502 – 1509, 2001.

[61] D. Ewins, "Basics and state-of-the-art of modal testing," *Sadhana*, vol. 25, pp. 207–220, 2000.

[62] P. W. A. Zegelaar, "Modal analysis of tire in-plane vibration," *SAE Technical Paper Series, 971101*, 1997.

[63] C. Meskell and J. Fitzpatrick, "Parameter identification in a system with both linear and coulomb damping," in *Modern practice in stress and vibration analysis* (M. Gilchrist, ed.), Rotterdam, Netherlands: A.A. Balkema, 1997.

[64] H. Esmonde, J. Fitzpatrick, H. Rice, and F. Axisa, "Analysis of non-linear squeeze film dynamics. part i. physical theory and modelling," in *American Society of Mechanical Engineers, Pressure Vessels and Piping Division (Publication) PVP*, vol. 189, (Nashville, TN, USA), pp. 171 – 177, 1990.

[65] H. Esmonde, F. Axisa, J. Fitzpatrick, and H. Rice, "Analysis of non-linear squeeze film dynamics. part ii. experimental measurement and model verification," in *American Society of Mechanical Engineers, Pressure Vessels and Piping Division (Publication) PVP*, vol. 189, (Nashville, TN, USA), pp. 179 – 184, 1990.

[66] H. Esmonde, J. Fitzpatrick, H. Rice, and F. Axisa, "Modelling and identification of nonlinear squeeze film dynamics," *Journal of Fluids and Structures*, vol. 6, no. 2, pp. 223 – 248, 1992.

[67] P. F. Liagre and J. M. Niedzwecki, "Estimating nonlinear coupled frequency-dependent parameters in offshore engineering," *Applied Ocean Research*, vol. 25, no. 1, pp. 1 – 19, 2003.

[68] A. Parker, *A method of characterisation of the nonlinear vibration transmissibility of cushioning materials*. PhD thesis, Victoria University, 2007.

[69] C. Meskell, J. Fitzpatrick, and H. Rice, "Application of force-state mapping to a non-linear fluid-elastic system," *Mechanical Systems and Signal Processing*, vol. 15, no. 1, pp. 75 – 85, 2001.

[70] K. Worden, D. Hickey, M. Haroon, and D. E. Adams, "Nonlinear system identification of automotive dampers: A time and frequency-domain analysis," *Mechanical Systems and Signal Processing*, vol. 23, no. 1, pp. 104 – 126, 2009.

[71] C. Bao, H. Hao, Z.-X. Li, and X. Zhu, "Time-varying system identification using a newly improved hht algorithm," *Computers and Structures*, vol. 87, no. 23-24, pp. 1611 – 1623, 2009.

[72] S. Duym, "An alternative force state map for shock absorbers," *Proceedings of the Institution of Mechanical Engineers, Part D: Journal of Automobile Engineering*, vol. 211, no. 3, pp. 175–179, 1997.

[73] S. W. R. Duym and J. F. M. Schoukens, "Selection of an optimal force-state map," *Mechanical Systems and Signal Processing*, vol. 10, no. 6, pp. 683 – 695, 1996.

[74] D. Hickey, M. H. Haroon, D. E. Adams, and K. Worden, "Investigating nonlinear behaviour within a vehicle suspension system using time and frequency domain techniques," in *Applied Mechanics and Materials*, vol. 5-6, (Bath, United kingdom), pp. 285 – 294, 2006.

[75] M. Haroon and D. E. Adams, "Component restoring force identification for damage identification in vehicle suspension systems," *International Journal of Vehicle Systems Modelling and Testing*, vol. 3, no. 1-2, pp. 25 – 46, 2008.

[76] M. Haroon, D. Adams, Y. Luk, and A. Ferri, "A time and frequency domain approach for identifying nonlinear mechanical system models in the absence of an input measurement," *Journal of Sound and Vibration*, vol. 283, pp. 1137–1155, 2005.

[77] M. Weigel, W. Mack, and A. Riepl, "Nonparametric shock absorber modelling based on standard test data," *Vehicle System Dynamics*, vol. 38, no. 6, pp. 415 – 432, 2002.

[78] W. Schiehlen and B. Hu, "Spectral simulation and shock absorber identification," *International Journal of Non-Linear Mechanics*, vol. 38, no. 2, pp. 161 – 171, 2003.

[79] C. Boggs, M. Ahmadian, and S. Southward, "Efficient empirical modelling of a high-performance shock absorber for vehicle dynamics studies," *Vehicle System Dynamics*, vol. 48, no. 4, pp. 481 – 505, 2010.

[80] D. Kowalski, M. Rao, J. Blough, and S. Gruenberg, "Dynamic testing of shock absorbers under non-sinusoidal conditions," *Proceedings of the Institution of Mechanical Engineers, Part D: Journal of Automobile Engineering*, vol. 216, no. 5, pp. 373 – 384, 2002.

[81] S. Duym, "Simulation tools, modelling and identification, for an automotive shock absorber in the context of vehicle dynamics," *Vehicle System Dynamics*, vol. 33, no. 4, pp. 261 – 85, 2000.

[82] R. Basso, "Experimental characterization of damping force in shock absorbers with constant velocity excitation," *Vehicle System Dynamics*, vol. 30, no. 6, pp. 431 – 442, 1998.

[83] M. Rao and S. Gruenberg, "Measurement of equivalent stiffness and damping of shock absorbers," *Experimental Techniques*, vol. 26, no. 2, pp. 39 – 42, 2002.

[84] Y. Ko, G. Heydinger, and D. Guenther, "Evaluation of a shock model for vehicle simulation," *SAE Technical Paper Series, 2007-01-0845*, 2007.

[85] E. R. Wang, X. Q. Ma, S. Rakhela, and C. Su, "Modelling the hysteretic characteristics of a magnetorheological fluid damper," *Proceedings of the Institution of Mechanical Engineers, Part D: Journal of Automobile Engineering*, vol. 217, no. 7, pp. 537 – 550, 2003.

[86] B. Spencer Jr. and S. Dyke, "Phenomenological model for magnetorheological dampers.," *Journal of Engineering Mechanics*, vol. 123, no. 3, pp. p230 –, 1997.

[87] G. Yao, F. Yap, G. Chen, W. Li, and S. Yeo, "Mr damper and its application for semi-active control of vehicle suspension system," *Mechatronics*, vol. 12, no. 7, pp. 963 – 973, 2002.

[88] X. Q. Ma, E. R. Wang, S. Rakheja, and C.-Y. Su, "Modeling hysteretic characteristics of mr-fluid damper and model validation," in *Proceedings of the IEEE Conference on Decision and Control*, vol. 2, (Las Vegas, NV, United States), pp. 1675 – 1680, 2002.

[89] K.-G. Sung, Y.-M. Han, J. Sohn, and S.-B. Choi, "Road test evaluation of vibration control performance of vehicle suspension featuring electrorheological shock absorbers," *Proceedings of the Institution of Mechanical Engineers, Part D: Journal of Automobile Engineering*, vol. 222, no. 5, pp. 685 – 698, 2008.

[90] M. Gobbi, P. Guarneri, G. Rocca, and G. Mastinu, "Test rig for characterization of automotive suspension systems," *SAE Technical Paper Series, 2008-01-0692*, 2008.

[91] M. Gobbi, G. Mastinu, and F. Giorgetta, "Sensors for measuring forces and moments with application to ground vehicle design and engineering," in *American Society of Mechanical Engineers, Design Engineering Division (Publication) DE*, vol. 118 A, (Orlando, FL, United States), pp. 161 – 168, 2005.

[92] M. Gobbi, G. Mastinu, and M. Pennati, "Indoor testing of road vehicle suspensions," *Meccanica*, vol. 43, no. 2, pp. 173 – 184, 2008.

[93] H. Nozaki and Y. Inagaki, "Technology for measuring and diagnosing the damping force of shock absorbers and the constant of coil springs when mounted on a vehicle," *JSAE Review*, vol. 20, no. 3, pp. 413 – 419, 1999.

[94] C. Kim and P. Ro, "Reduced-order modelling and parameter estimation for a quarter-car suspension system," *Proceedings of the Institution of Mechanical Engineers, Part D: Journal of Automobile Engineering*, vol. 214, no. 8, pp. 851 – 864, 2000.

[95] J. Langdon, "Design and Adaptive Control of a Lab Based Tire Coupled Quarter-car Suspension Test Rig for the Accurate Re-creation of Vehicle Response," Master's thesis, Virginia Polytechnic Institute and State University, 2007.

[96] D. Allison and R. Sharp, "On the low frequency in-plane forced vibrations of pneumatic tyre/wheel/suspension assemblies," *Vehicle System Dynamics*, vol. 27, no. 1 supp 1, pp. 151 – 162, 1997.

[97] M. Basseville, A. Benveniste, M. Goursat, L. Hermans, L. Mevel, and H. Van der Auweraer, "Output-only subspace-based structural identification: from theory to industrial testing practice," *Transactions of the ASME. Journal of Dynamic Systems, Measurement and Control*, vol. 123, no. 4, pp. 668 – 76, 2001.

[98] E. Pierro, E. Mucchi, L. Soria, and A. Vecchio, "On the vibro-acoustical operational modal analysis of a helicopter cabin," *Mechanical Systems and Signal Processing*, vol. 23, no. 4, pp. 1205 – 17, 2009.

[99] I. Zaghbani and V. Songmene, "Estimation of machine-tool dynamic parameters during machining operation through operational modal analysis," *International Journal of Machine Tools & Manufacture*, vol. 49, no. 12-13, pp. 947 – 57, 2009.

[100] J. Brownjohn, F. Magalhaes, E. Caetano, and A. Cunha, "Ambient vibration re-testing and operational modal analysis of the humber bridge," *Engineering Structures*, vol. 32, no. 8, pp. 2003 – 2018, 2010.

[101] B. Peeters, M. Olofsson, and P. Nilsson, "Test based dynamic characterizing of a complete truck by operational modal analysis," in *2nd International Operational Modal Analysis Conference*, vol. 2, (Copenhagen, Denmark), pp. 437 – 444, 2007.

[102] R. Brincker, N. Mø ller, and P. Andersen, "Output only modal testing of a car body subject to engine excitation," in *Proceedings of the International Modal Analysis Conference*, vol. 1, pp. 786–792, 2000.

[103] P. Mohanty and D. J. Rixen, "Modified era method for operational modal analysis in the presence of harmonic excitations," *Mechanical Systems and Signal Processing*, vol. 20, no. 1, pp. 114 – 130, 2006.

[104] P. Mohanty and D. Rixen, "Operational modal analysis in the presence of harmonic excitation," *Journal of Sound and Vibration*, vol. 270, no. 1-2, pp. 93 – 109, 2004.

[105] P. Mohanty and D. Rixen, "A modified ibrahim time domain algorithm for operational modal analysis including harmonic excitation," *Journal of Sound and Vibration*, vol. 275, no. 1-2, pp. 375 – 390, 2004.

[106] M. Haroon, D. E. Adams, and Y. W. Luk, "A technique for estimating linear parameters using nonlinear restoring force extraction in the absence of an input measurement," *Journal of Vibration and Acoustics, Transactions of the ASME*, vol. 127, no. 5, pp. 483 – 492, 2005.

[107] C. G. McGee, M. Haroon, D. E. Adams, and Y. W. Luk, "A frequency domain technique for characterizing nonlinearities in a tire-vehicle suspension system," *Journal of Vibration and Acoustics, Transactions of the ASME*, vol. 127, no. 1, pp. 61 – 76, 2005.

[108] M. Haroon and D. E. Adams, "Time and frequency domain nonlinear system characterization for mechanical fault identification," *Nonlinear Dynamics*, vol. 50, no. 3, pp. 387 – 408, 2007.

[109] M. Haroon and D. E. Adams, "Identification of damage in a suspension component using narrowband and broadband nonlinear signal processing techniques," in *Proceedings of SPIE - The International Society for Optical Engineering*, vol. 6532, (San Diego, CA, United states), 2007.

[110] M. Haroon and D. Adams, "Development of component-level damage evolution models for mechanical prognosis," *Journal of Applied Mechanics*, vol. 75, no. 2, pp. 021017 – 1, 2008.

[111] P. Li, R. Goodall, P. Weston, C. Seng Ling, C. Goodman, and C. Roberts, "Estimation of railway vehicle suspension parameters for condition monitoring," *Control Engineering Practice*, vol. 15, no. 1, pp. 43 – 55, 2007.

[112] P. Ventura, C. Ferreira, C. Neves, R. Morais, A. Valente, and M. Reis, "An embedded system to assess the automotive shock absorber condition under

vehicle operation," in *Proceedings of IEEE Sensors*, (Lecce, Italy), pp. 1210 – 1213, 2008.

[113] C. Ferreira, P. Ventura, R. Morais, A. L. Valente, C. Neves, and M. C. Reis, "Sensing methodologies to determine automotive damper condition under vehicle normal operation," *Sensors and Actuators, A: Physical*, vol. 156, no. 1, pp. 237 – 244, 2009.

[114] M. Rozyn and N. Zhang, "A method for estimation of vehicle inertial parameters," *Vehicle System Dynamics*, vol. 48, no. 5, pp. 547 – 565, 2010.

[115] M. C. Best, "Identifying tyre models directly from vehicle test data using an extended kalman filter," *Vehicle System Dynamics*, vol. 48, no. 2, pp. 171 – 187, 2010.

[116] L. Hermans and H. Van Der Auweraer, "Modal testing and analysis of structures under operational conditions: Industrial applications," *Mechanical Systems and Signal Processing*, vol. 13, pp. 193–216, 1999.

[117] W. J. Fleming, "New automotive sensors - a review," *IEEE Sensors Journal*, vol. 8, no. 11, pp. 1900 – 1921, 2008.

[118] J. Kelly, H. Kowalczyk, and H. Oral, "Track simulation and vehicle characterization with 7 post testing," *SAE Technical Paper Series, 2002-01-3307*, 2002.

[119] C. Paré, "Experimental Evaluation of Semiactive Magneto- Rheological Suspensions for Passenger Vehicles," Master's thesis, Virginia Polytechnic Institute and State University, 1998.

[120] M. Ahmadian and C. Paré, "A quarter-car experimental analysis of alternative semiactive control methods," *Journal of Intelligent Material Systems and Structures*, vol. 11, no. 8, pp. 604 – 612, 2000.

[121] M. Ahmadian, F. D. Goncalves, and C. Sandu, "An experimental analysis of suitability of various semiactive control methods for magneto rheological vehicle suspensions," in *Proceedings of SPIE - The International Society for Optical Engineering*, vol. 5760, (San Diego, CA, United States), pp. 208 – 216, 2005.

[122] K. Farong and F. Zongde, "An experimental investigation into the design of vehicle fuzzy active suspension," in *Proceedings of the IEEE International Conference on Automation and Logistics, ICAL 2007*, (Jinan, China), pp. 959 – 963, 2007.

[123] J. Ziegenmeyer, "Estimation of Disturbance Inputs to a Tire Coupled quarter car suspension test rig," Master's thesis, Virginia Polytechnic Institute and State University, 2007.

[124] S. Chantranuwathana and H. Peng, "Adaptive robust force control for vehicle active suspensions," *International Journal of Adaptive Control and Signal Processing*, vol. 18, no. 2, pp. 83 – 102, 2004.

[125] Y. Ando and M. Suzuki, "Control of active suspension systems using the singular perturbation method," *Control Engineering Practice*, vol. 4, no. 3, pp. 287 – 293, 1996.

[126] K. Yi and B. S. Song, "Observer design for semi-active suspension control," *Vehicle System Dynamics*, vol. 32, no. 2, pp. 129 – 148, 1999.

[127] J. Watton, K. Holford, and P. Surawattanawan, "The application of a programmable servo controller to state control of an electrohydraulic active suspension," *Proceedings of the Institution of Mechanical Engineers, Part D: Journal of Automobile Engineering*, vol. 218, no. 12, pp. 1367 – 1377, 2004.

[128] J. Lee, H. Yoo, and J. Lee, "High frequency characteristics of a front wheel suspension," *Vehicle System Dynamics*, vol. 28, no. 4-5, pp. 261 – 271, 1997.

[129] F. Gauterin and C. Ropers, "Modal tyre models for road noise improvement," *Vehicle System Dynamics*, vol. 43, no. SUPPL., pp. 297 – 304, 2005.

[130] F. Giorgetta, M. Gobbi, and G. Mastinu, "On the testing of vibration performances of road vehicle suspensions," *Experimental Mechanics*, vol. 47, no. 4, pp. 485 – 495, 2007.

[131] M. Gobbi, F. Giorgetta, P. Guarneri, G. Rocca, and G. Mastinu, "Experimental study and numerical modelling of the dynamic behaviour of tyre/suspension while running over an obstacle," in *American Society of Mechanical Engineers, Design Engineering Division (Publication) DE*, (Chicago, IL, United States), pp. 195–204, 2006.

[132] J. Perisse and J. Hamet, "A comparison of the 2D ring and 3D orthotropic plate for modelling of radial tire vibrations," *29th International Congress on Noise Control Engineering*, 2000.

[133] H. Haga, "Evaluation of tyre models for durability loads prediction using a suspension-on-a-drum environment," *Vehicle System Dynamics*, vol. 43, no. SUPPL, pp. 281 – 296, 2005.

[134] R. Roberson and R. Schwertassek, *Dynamics of Multibody Systems*. Berlin, Germany: Springer-Verlag, 1988.

[135] G. Jazar, R. Alkhatib, and M. F. Golnaraghi, "Root mean square optimization criterion for vibration behaviour of linear quarter car using analytical methods," *Vehicle System Dynamics*, vol. 44, pp. 477–512, 2006.

[136] R. Majjad, "Estimation of suspension parameters," in *IEEE Conference on Control Applications - Proceedings*, (Hartford, CT, USA), pp. 522 – 527, 1997.

[137] A. Yousefi, A. Akbari, and B. Lohmann, "Low order robust controllers for active vehicle suspensions," in *Proceedings of the IEEE International Conference on Control Applications*, (Munich, Germany), pp. 693 – 698, 2007.

[138] E. Guglielmino, T. Sireteanu, C. W. Stammers, G. Gheorghe, and M. Giuclea, *Semi-active Suspension Control Improved Vehicle Ride and Road Friendliness*. London, UK: Springer-Verlag, 2008.

[139] R. S. Sharp and D. A. Crolla, "Road vehicle suspension system design - a review," *Vehicle System Dynamics*, vol. 16, no. 3, pp. 167 – 192, 1987.

[140] H. Imine, Y. Delanne, and N. M'Sirdi, "Road profile input estimation in vehicle dynamics simulation," *Vehicle System Dynamics*, vol. 44, no. 4, pp. 285 – 303, 2006.

[141] H. Kowalczyk, "Damper tuning with the use of a seven post shaker rig," *SAE Technical Paper Series, 2002-01-0804*, 2002.

[142] S. Türkay and H. Akçay, "A study of random vibration characteristics of the quarter-car model," *Journal of Sound and Vibration*, vol. 282, pp. 111–124, 2005.

[143] L. Etman, R. Vermeulen, J. Van Heck, A. Schoofs, and D. Van Campen, "Design of a stroke dependent damper for the front axle suspension of a truck

using multibody system dynamics and numerical optimization," *Vehicle System Dynamics*, vol. 38, no. 2, pp. 85 – 101, 2002.

[144] G. Verros, S. Natsiavas, and C. Papadimitriou, "Design Optimization of Quarter-car Models with Passive and Semi-active Suspensions under random road excitation," *Journal of Vibration and Control*, vol. 11, pp. 581–606, 2005.

[145] G. Georgiou, G. Verros, and S. Natsiavas, "Multi-objective optimization of quarter-car models with a passive or semi-active suspension system," *Vehicle System Dynamics*, vol. 45, no. 1, pp. 77 – 92, 2007.

[146] M. M. Elmadany and Z. S. Abduljabbar, "Linear quadratic gaussian control of a quarter-car suspension," *Vehicle System Dynamics*, vol. 32, no. 6, pp. 479 – 497, 1999.

[147] P. Lugner, H. Pacejka, and M. Plochl, "Recent advances in tyre models and testing procedures," *Vehicle System Dynamics*, vol. 43, no. 6-7, pp. 413 – 436, 2005.

[148] A. Schmeitz, *A Semi-Emperical Three-Dimensional Model of the Pneumatic Tyre Rolling over Arbitrary Uneven Road Surfaces*. PhD thesis, Delft University of Technology, 2004.

[149] P. Zegelaar, *The dynamic response of tyres to brake torque variations and road unevenesses*. PhD thesis, Delft University of Technology, 1998.

[150] L. R. Miller, "Tuning passive, semi-active, and fully active suspension systems," in *Proceedings of the IEEE Conference on Decision and Control Including The Symposium on Adaptive Processes*, pp. 2047 – 2053, 1988.

[151] T. Gillespie, S. Karamihas, D. Cebon, M. Sayers, M. Nasim, W. Hansen, and N. Ehsan, "Effects of heavy vehicle characteristics on pavement response and performance," *National Cooperative Highway Research Program Report*, no. 353, pp. 1 – 126, 1993.

[152] S. P. Wilson, N. K. Harris, and E. J. OBrien, "The use of bayesian statistics to predict patterns of spatial repeatability," *Transportation Research Part C: Emerging Technologies*, vol. 14, no. 5, pp. 303 – 315, 2006.

[153] S. Türkay and H. Akçay, "Effect of tire damping on the ride performance potential of active suspension systems," in *Proceedings of the SICE Annual Conference*, (Tokyo, 113, Japan), pp. 1209 – 1216, 2007.

[154] A. A. Popov and Z. Geng, "Modelling of vibration damping in pneumatic tyres," *Vehicle System Dynamics*, vol. 43, no. SUPPL, pp. 145 – 155, 2005.

[155] J. Levitt and N. Zorka, "Influence of tire damping in quarter car active suspension models," *Journal of Dynamic Systems, Measurement and Control, Transactions of the ASME*, vol. 113, no. 1, pp. 134 – 137, 1991.

[156] S. Türkay and H. Akçay, "Influence of tire damping on the ride performance potential of quarter-car active suspensions," *Proceedings of the IEEE Conference on Decision and Control*, pp. 4390 – 4395, 2008.

[157] D. Maher and P. Young, "An insight into linear quarter car model accuracy," *Vehicle System Dynamics*, DOI 10.1080/00423111003631946, 2010.

[158] D. Kowalski, M. Rao, J. Blough, S. Gruenberg, and D. Griffiths, "The effects of different input excitation on the dynamic characterization of an automotive shock absorber," *SAE 01NVC-120*, 2001.

[159] M. D. Rao, S. Gruenberg, H. Torab, and D. Griffiths, "Vibration testing and dynamic modeling of automotive shock absorbers," in *Proceedings of SPIE - The International Society for Optical Engineering*, vol. 3989, (Newport Beach, CA, USA), pp. 423 – 429, 2000.

[160] C. Rajalingham and S. Rakheja, "Influence of suspension damper asymmetry on vehicle vibration response to ground excitation," *Journal of Sound and Vibration*, vol. 266, no. 5, pp. 1117 – 1129, 2003.

[161] J. Lee and D. Thompson, "Dynamic stiffness formulation, free vibration and wave motion of helical springs," *Journal of Sound and Vibration*, vol. 239, no. 2, pp. 297 – 320, 2001.

[162] V. Wowk, *Machinery Vibration: Balancing*. New York, USA: McGraw-Hill, 1994.

[163] P. Verboven, P. Guillaume, and B. Cauberghe, "Multivariable frequency-response curve fitting with application to modal parameter estimation," *Automatica*, vol. 41, no. 10, pp. 1773 – 82, 2005.

[164] P. Verboven, P. Guillaume, S. Vanlanduit, and B. Cauberghe, "Assessment of nonlinear distortions in modal testing and analysis of vibrating automotive structures," *Journal of Sound and Vibration*, vol. 293, no. 1-2, pp. 299 – 319, 2006.

[165] "Vibration measurement and analysis," *Brüel & Kjær Lecture Note: BA 7676-12*, 1998.

[166] H. Herlufsen, "Dual channel fft analysis (part 1)," *Brüel & Kjær Technical Review*, no. 1, 1984.

[167] D. F. Moore, *The friction of pneumatic tyres*. Amsterdam, Netherlands: Elsevier Scientific Publishing Company, 1975.

[168] J. R. Kilner, "Pneumatic tire model for aircraft simulation.," *Journal of Aircraft.*, vol. 19, no. 10, pp. 851 – 857, 1982.

[169] M. Sayers and S. Karamihas, "Interpretation of road roughness profile data - final report," *Technical Report UMTRI9619, University of Michigan Transportation Research Institute*, 1996.

[170] K. J. Kitching, D. J. Cole, and D. Cebon, "Performance of a semi-active damper for heavy vehicles," *Journal of Dynamic Systems, Measurement, and Control*, vol. 122, no. 3, pp. 498–506, 2000.

[171] R. Steidel, *An Introduction to Mechancial Vibrations*. New York, USA: John Wiley & Sons, 1989.

[172] R. Blake, "Basic vibration theory," in *Harris' shock and vibration handbook* (C. Harris and A. Piersol, eds.), New York, USA: McGraw-Hill, 5 ed., 2002.

[173] S. Rao, *Mechanical Vibrations*. Singapore: Prentice Hall, 2005.

[174] C.-T. Huang and S.-Y. Kuo, "Drift response of a bilinear hysteretic system to periodic excitation under sustained load effects," *International Journal of Non-Linear Mechanics*, vol. 41, no. 4, pp. 530 – 542, 2006.

[175] D. P. Hess and A. Soom, "Friction at a lubricated line contact operating at oscillating sliding velocities," *Journal of Tribology*, vol. 112, no. 1, pp. 147–152, 1990.

[176] Y. Zhu and P. Pagilla, "Static and dynamic friction compensation in trajectory tracking control of robots," *Robotics and Automation, 2002. Proceedings. ICRA '02. IEEE International Conference on*, vol. 3, pp. 2644–2649, 2002.

[177] M. Lorenz, B. Heimann, J. Tschimmel, and V. Hartel, "Applying semi-active friction damping to elastic supports for automotive applications," *Advanced*

Intelligent Mechatronics, 2003. AIM 2003. Proceedings. 2003 IEEE/ASME International Conference on, vol. 1, pp. 377–382 vol.1, July 2003.

[178] C. Canudas de Wit, H. Olsson, K. Astrom, and P. Lischinsky, "A new model for control of systems with friction," *Automatic Control, IEEE Transactions on*, vol. 40, pp. 419–425, Mar 1995.

[179] J. Wojewoda, A. Stefanski, M. Wiercigroch, and T. Kapitaniak, "Hysteretic effects of dry friction: modelling and experimental studies," *Philosophical Transactions of the Royal Society A: Mathematical, Physical and Engineering Sciences*, vol. 366, no. 1866, pp. 747 – 765, 2008.

[180] M. Sun and R. J. Sclabassi, "Errors in synchronous data acquisition and averaging," in *Proceedings of the IEEE International Conference on Systems Engineering*, (Pittsburgh, PA, USA), pp. 172 – 175, 1990.

[181] M. Sun, D. L. Bonaddio, J. Mi, and R. J. Sclabassi, "An analysis of the effects of jitter in data acquisition on synchronous averaging," *IEEE Transactions on Systems, Man and Cybernetics*, vol. 21, no. 2, pp. 456 – 463, 1991.

[182] C. Woody, "Characterization of an adaptive filter for the analysis of variable latency neuroelectric signals," *Medical and Biological Engineering and Computing*, vol. 5, pp. 539–554, 1967.

[183] R. Hamming, *Digital Filters*. New Jersey, USA: Prentice–Hall, 3 ed., 1989.

[184] M. H. Richardson and D. L. Formenti, "Parameter estimation from frequency response measurements using rational fraction polynomials," in *Proceedings of the International Modal Analysis Conference*, (Orlando, FL, USA), pp. 167 – 181, 1982.

[185] P. Verboven, P. Guillaume, B. Cauberghe, S. Vanlanduit, and E. Parloo, "A comparison of frequency-domain transfer function model estimator formulations for structural dynamics modelling," *Journal of Sound and Vibration*, vol. 279, no. 3-5, pp. 775 – 98, 2005.

[186] R. J. Allemang, "The modal assurance criterion - twenty years of use and abuse," *S V Sound and Vibration*, vol. 37, no. 8, pp. 14 – 23, 2003.

[187] F. Gustafsson, "Determining the initial states in forward-backward filtering," *IEEE Transactions on Signal Processing*, vol. 46, 1996.

[188] W. Liao and C. Lai, "Harmonic analysis of a magnetorheological damper for vibration control," *Smart Materials and Structures*, vol. 11, no. 2, pp. 288 – 296, 2002.

[189] R. Eyres, A. Champneys, and N. Lieven, "Modelling and dynamic response of a damper with relief valve," *Nonlinear Dynamics*, vol. 40, no. 2, pp. 119 – 147, 2005.

[190] E. Berger, "Friction modeling for dynamic system simulation," *Applied Mechanics Reviews*, vol. 55, no. 6, pp. 535 – 577, 2002.

[191] B. Armstrong and C. De Wit, *Friction Modeling and Compensation, The Control Handbook*. London, UK: CRC Press, 1996.

Appendix A

Tyre identification

The pneumatic tyre serves an important purpose in suspension systems, with respect to the isolation of road induced vibration. There are a variety of tyre models in the literature with different levels of complexity. Tyre model complexity is determined by the frequency range of interest of the study [147]. In this research, the experimental identification of a tyre, taken from a quarter car suspension experimental test rig is documented. Experimental testing of the tyre is carried out in isolation using an ESH® servo–hydraulic testing machine.

Characterisation

The tyre force under loading is measured using the ESH® machine load cell. The load cell has a capacity of 100 kN. Maximum loads of less than 350 N are expected during tyre testing. For this reason the ESH® machine load cell is recalibrated in this region using a Brüel & Kjær® type 8200 force transducer, which has a compressive load capacity of 5 kN.

Static compression tests are used to determine the linear stiffness of the tyre. Testing is carried out at two tyre inflation pressures, 1.1 Bar and 2.0 Bar. The test setup can be seen in Figure A.1. Figure A.2 shows force deflection plots for both inflation pressures. The tyre is compressed by 10 mm in both cases and the corresponding force is measured simultaneously. It is found that the tyre can be approximated with reasonable accuracy by a linear spring. As expected higher inflation pressure

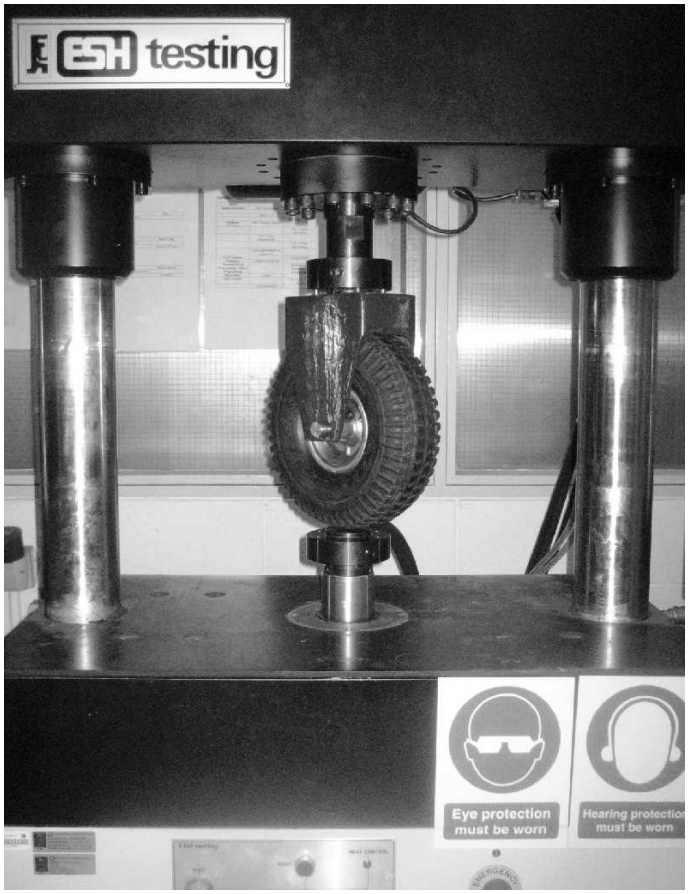

Figure A.1: Tyre dynamic test setup

leads to a higher tyre stiffness value. Linear regression leads to static linear stiffness values (k_{ls}) of 81.42 N/mm and 63.32 N/mm for the 2.0 Bar and 1.1 Bar tests, respectively.

Static testing cannot be used to identify tyre damping. Dynamic testing is required to test the damping properties of the tyre and also to determine if the linear spring assumption holds under dynamic loading. The test setup is the same as for the static testing. The quarter car rig has a combined sprung and unsprung mass of 33.2 kg, which equates to a static load on the tyre of approximately 325 N. This preload is applied to the tyre in the ESH® machine before each test is carried out. This allows for the characterisation of the tyre dynamics in its actual operating range.

The tyre is tested at four inflation pressures (P), 1.1, 1.5, 1.8 and 2.0 Bar. The static deflections under preload are 6.0, 4.8, 4.2 and 3.5mm, respectively. The tests are carried out at selected frequencies between 1 Hz and 14 Hz, and at selected amplitudes between 1 mm and 4 mm. Figure A.3 shows two typical work diagrams (force–

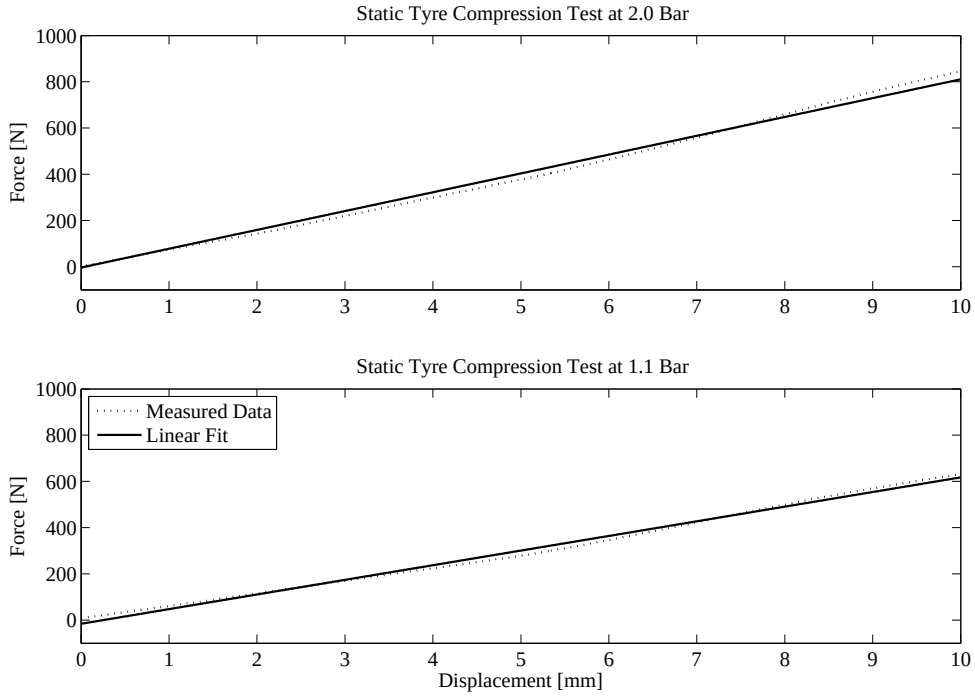

Figure A.2: Tyre static test results at 2.0 Bar (top) and 1.1 Bar (bottom), showing linear fit lines

displacement) for sinusoidal displacement excitation of the form $x = A\sin(2\pi f_e t)$. Note the hardening/softening spring characteristic visible in both diagrams. The tyre shows a hardening/softening spring characteristic at all frequencies and amplitudes.

Hysteresis loops are also observed in the work diagrams. The area enclosed by the loop denotes the energy dissipated by the tyre in one cycle of motion. The type of damping (viscous or hysteretic) can be found by investigating the frequency dependence of the energy dissipation. It has been found experimentally that the energy loss per cycle, due to internal friction, is independent of frequency [172] or decreases slightly with increasing frequency [171]. The energy loss per cycle is also approximately proportional to the square of the amplitude [173]. Table A.1 shows energy loss per cycle for a tyre inflation pressure of 1.5 Bar. It is noted that in general the energy loss per cycle does not increase significantly with increasing frequency and at higher frequencies it decreases slightly with increasing frequency. The energy loss per cycle is also approximately proportional to the square of the excitation amplitude. This leads to the assumption that the major damping mechanism of the tyre is hysteretic damping.

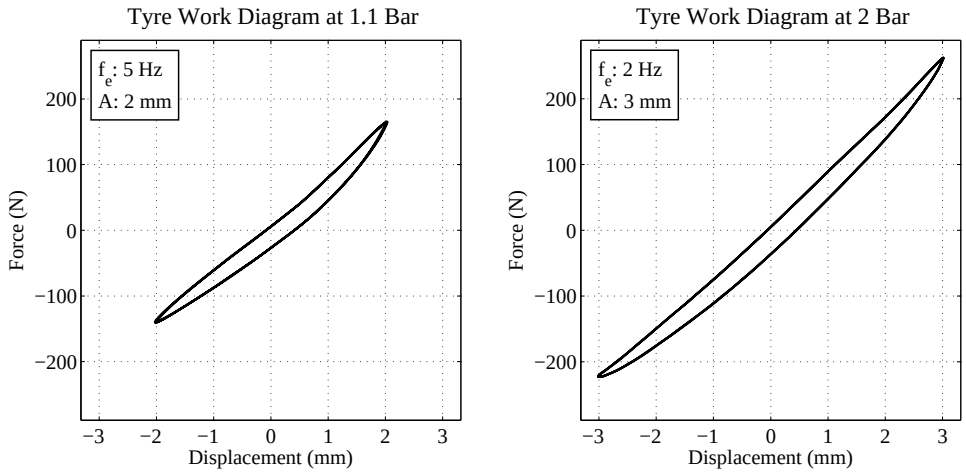

Figure A.3: Tyre work diagrams at $f_e = 5$ Hz, $A = 2$ mm, 1.1 Bar (left) and $f_e = 2$ Hz, $A = 3$ mm, 2.0 Bar (right)

Tyre Inflation Pressure 1.5 Bar

A	1mm	2mm	3mm	4mm
f_e	ΔW	ΔW	ΔW	ΔW
1hz	27.12	100.57	208.16	329.85
2hz	27.45	101.35	211.37	341.23
4hz	28.29	104.11	214.79	343.31
5hz	27.24	102.57	211.98	-
7hz	27.14	101.26	205.83	-
10hz	24.45	89.51	-	-
14hz	21.92	-	-	-

Table A.1: Tyre energy loss per cycle [mJ]

Model selection

Both linear and nonlinear tyre models are developed. The tyre is modelled as a linear spring and also as a hardening/softening nonlinear spring system. The linear tyre force, F_l, and nonlinear tyre force, F_l, are given by,

$$F_l = k_l x \tag{A.1}$$

$$F_n = k_n(x + c_t x^2) \tag{A.2}$$

where k_l and k_n are the linear and nonlinear spring constants, x is the tyre deflection and c_t is a constant which determines magnitude of the nonlinearity. First and second order polynomials are fitted to the tyre work diagrams, in a least squares sense, to determine the values of k_l and k_n, respectively. It is found that $k_l \approx k_n$ in all cases. Therefore, a linear approximation of the hardening/softening nonlinear spring model can be obtained by setting c_t equal to zero. Figure A.4 shows two typical second order polynomial curve fits to the measured data. Note that the measured data are not symmetrical about the origin but tends to be offset along the negative y-axis. This type of drift is a characteristic of asymmetric systems. Such systems are prone to bias their response toward a preferred or weak direction [174]. The f_o value on the plot legend represents the offset of the polynomials fitted to the data.

Tyre damping

Consider a linear spring and hysteretic damper connected in parallel. The force displacement relation, assuming approximately harmonic excitation, can be expressed as [173],

$$F = (k + ih)x \tag{A.3}$$

where,

$$k + ih = k\left(1 + i\frac{h}{k}\right) = k(1 + i\eta). \tag{A.4}$$

The term $k + ih$ is known as the complex stiffness and $\eta = h/k$ is a constant, indicating a dimensionless measure of damping. Complex stiffness represents both the elastic and the damping force at the same time [171]. An equivalent viscous damping

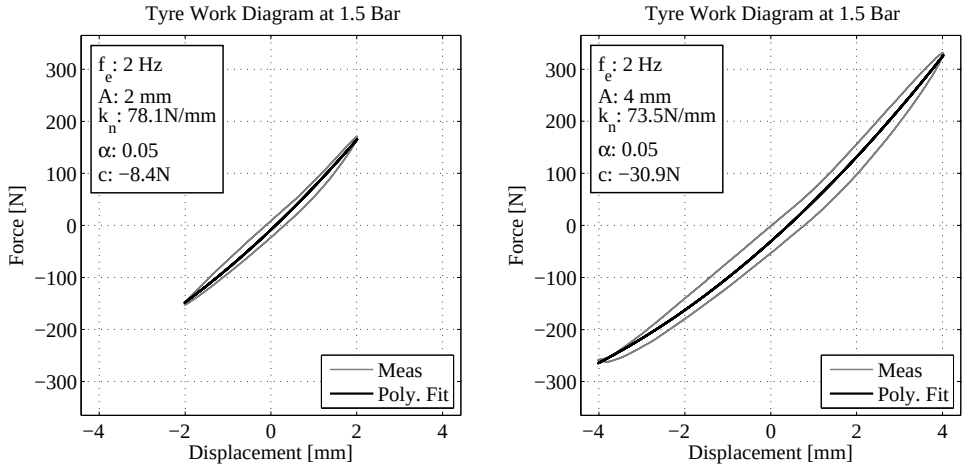

Figure A.4: Tyre work diagrams with second order polynomial curve fit at $f_e = 2$ Hz, $A = 2$ mm, 1.5 Bar (left) and $f_e = 2$ Hz, $A = 4$ mm, 1.5 Bar (right)

ratio and viscous damping constant can be calculated for hysteretic damping using,

$$\zeta_{eq} = \frac{\eta}{2} \tag{A.5}$$

$$c_{eq} = \frac{\eta k}{\omega}. \tag{A.6}$$

In terms of η, the energy loss per cycle is independent of frequency and can be expressed as

$$\Delta W = \pi k \eta X^2. \tag{A.7}$$

Tyre parameter dependence

Table A.2 [1] shows the values k_n, c_t and η obtained for each tyre test. The excitation frequency, f_e, excitation amplitude, A, and inflation pressure, P, dependence of k_n, c_t and η are now investigated further. Examining Table A.2 and Figure A.5, it can be observed that the tyre stiffness k_n increases in a linear fashion with ex-

[1] Missing data outside ESH® machine capability

Tyre Inflation Pressure 2.0 Bar

A	1mm			2mm			3mm		
f_e	k_n	c_t	η	k_n	c_t	η	k_n	c_t	η
1hz	92.36	0.018	0.092	86.43	0.035	0.086	79.06	0.044	0.083
2hz	93.13	0.019	0.096	87.63	0.036	0.090	80.00	0.046	0.084
4hz	94.79	0.021	0.096	88.66	0.036	0.091	86.43	0.049	0.089
5hz	95.38	0.021	0.093	89.30	0.036	0.087	85.94	0.054	0.080
7hz	96.82	0.023	0.095	90.31	0.037	0.089	86.63	0.055	0.081
10hz	97.76	0.019	0.085	91.48	0.035	0.079	-	-	-
14hz	100.36	0.020	0.082	-	-	-	-	-	-

Tyre Inflation Pressure 1.8 Bar

A	1mm			2mm			3mm		
f_e	k_n	c_t	η	k_n	c_t	η	k_n	c_t	η
1hz	86.40	0.033	0.097	82.84	0.039	0.092	80.80	0.049	0.087
2hz	86.44	0.032	0.099	83.19	0.036	0.096	81.39	0.048	0.089
4hz	88.60	0.033	0.100	84.75	0.036	0.097	82.57	0.050	0.089
5hz	88.83	0.033	0.096	85.04	0.036	0.087	82.80	0.050	0.085
7hz	90.00	0.033	0.098	85.30	0.036	0.089	83.37	0.050	0.087
10hz	92.22	0.033	0.087	87.41	0.036	0.079	-	-	-
14hz	93.72	0.034	0.085	-	-	-	-	-	-

Tyre Inflation Pressure 1.5 Bar

A	1mm			2mm			3mm		
f_e	k_n	c_t	η	k_n	c_t	η	k_n	c_t	η
1hz	83.32	0.072	0.102	79.69	0.061	0.099	76.80	0.052	0.095
2hz	81.64	0.047	0.104	78.07	0.053	0.101	75.98	0.050	0.097
4hz	84.64	0.049	0.104	81.08	0.056	0.101	78.38	0.052	0.096
5hz	83.67	0.063	0.100	81.44	0.059	0.097	79.14	0.055	0.092
7hz	84.88	0.064	0.102	81.63	0.059	0.099	79.70	0.056	0.094
10hz	87.09	0.065	0.090	83.51	0.060	0.088	-	-	-
14hz	88.23	0.064	0.088	-	-	-	-	-	-

Tyre Inflation Pressure 1.1 Bar

A	1mm			2mm			3mm		
f_e	k_n	c_t	η	k_n	c_t	η	k_n	c_t	η
1hz	74.92	0.117	0.119	71.68	0.082	0.117	69.61	0.065	0.112
2hz	74.54	0.103	0.121	70.54	0.076	0.119	68.67	0.062	0.115
4hz	77.78	0.105	0.120	73.93	0.079	0.117	71.37	0.065	0.113
5hz	76.94	0.100	0.116	72.73	0.076	0.113	70.74	0.064	0.109
7hz	79.20	0.103	0.113	75.18	0.079	0.115	72.47	0.066	0.110
10hz	79.54	0.100	0.107	76.01	0.079	0.104	-	-	-
14hz	81.98	0.104	0.104	-	-	-	-	-	-

Table A.2: Identified tyre parameters for a range of excitation frequencies, amplitudes and inflation pressures

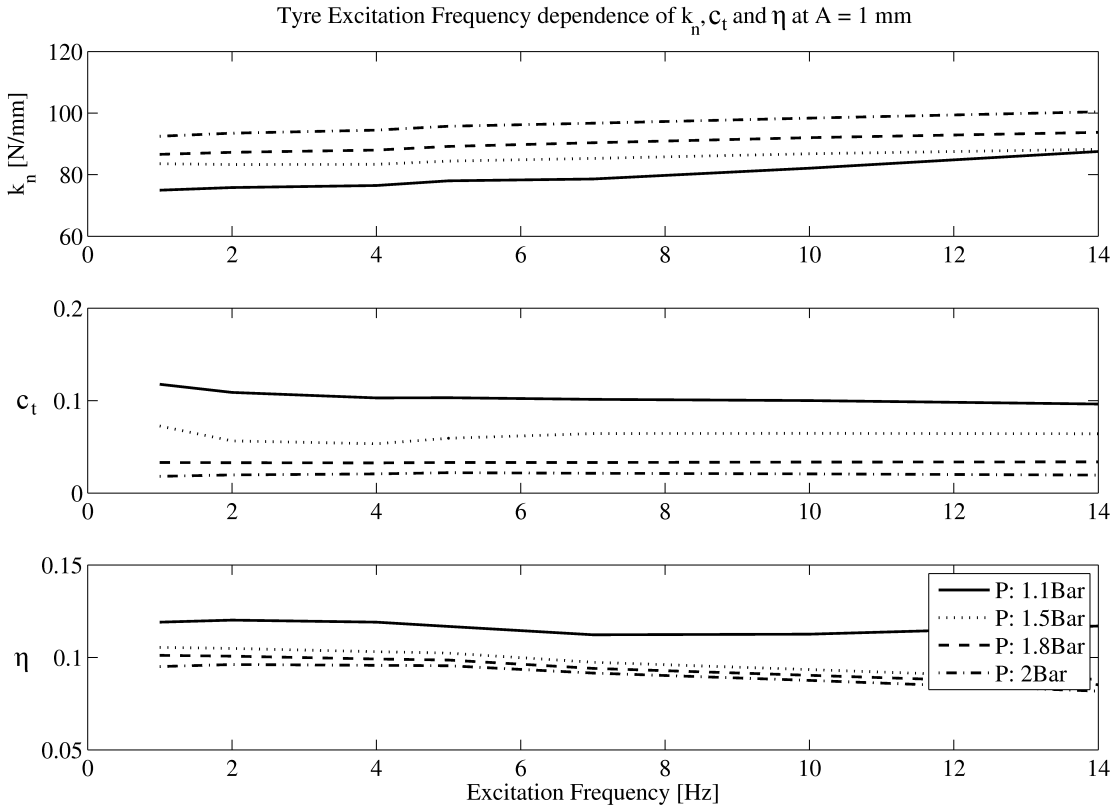

Figure A.5: Tyre parameter frequency dependance for $A = 1$mm

citation frequency, c_t remains almost constant with increasing excitation frequency and η tends to decrease slightly with excitation frequency. Structural damping as mentioned above is independent of excitation frequency. From equation A.4 it can be seen that $\eta = h/k$, which indicates that in the case of the tyre an increase in frequency would indeed cause a decrease in η, due to the frequency dependence of the tyre stiffness.

Tyre stiffness, k_n, decreases with increasing excitation amplitude as seen in Figure A.6. This figure also shows that the tyre shows more pronounced hardening/softening spring effects at higher amplitudes, as indicated by an increasing c_t value. It can be concluded that the hardening/softening nonlinearity of the tyre is only dependent on excitation amplitude and not frequency. The hysteresis loss, η, decreases with increasing amplitude. Both η and c_t are also found to decrease with increasing tyre pressure, while tyre stiffness naturally increases with inflation pressure.

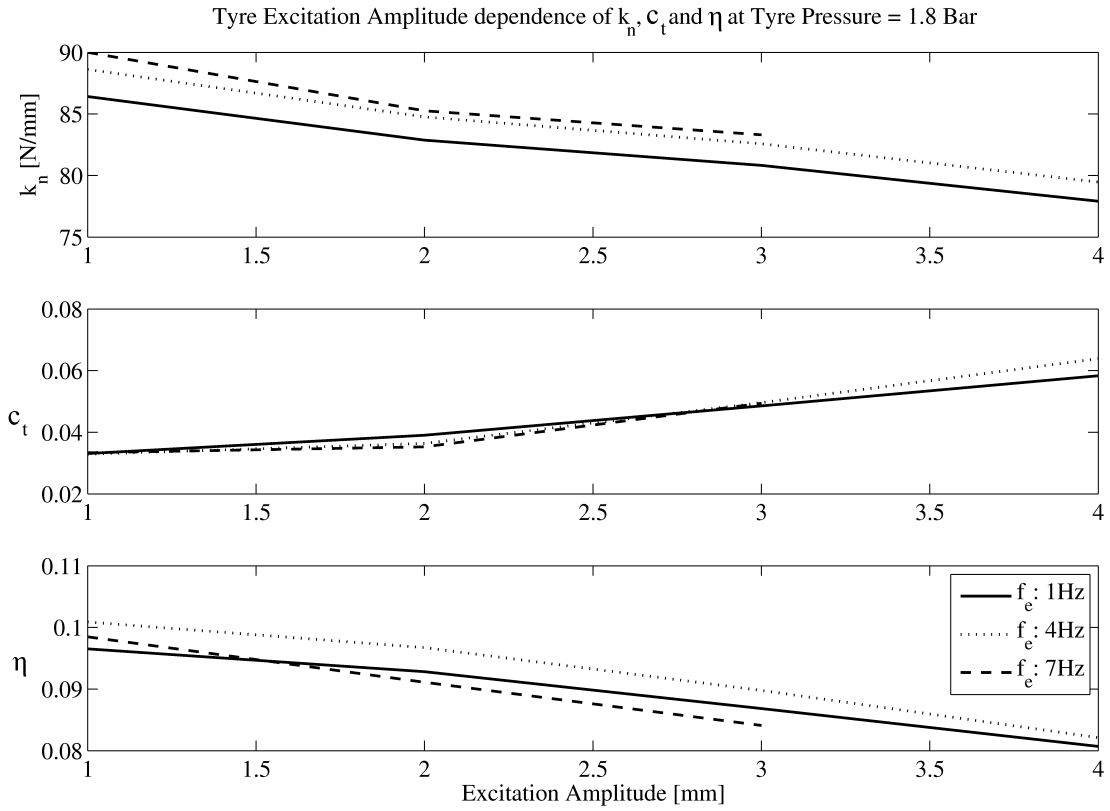

Figure A.6: Tyre parameter amplitude dependence for $P = 1.8$ Bar

Parameter estimation

From the analysis of the measured results presented above, it is found that a number of factors effect the tyre properties. Assuming a constant inflation pressure of 1.8 Bar, first order polynomials can be fitted to Figure A.5 and Figure A.6 giving an expression for k_n, in terms of A and f_e,

$$k_n = -2.79A + 0.5f_e + 89.02. \tag{A.8}$$

Similarly at constant pressure, c_t and η depend only on excitation amplitude, therefore as above the following expressions are determined from Figure A.6,

$$c_t = 0.0085A + 0.0234 \tag{A.9}$$

$$\eta = -0.0067A + 0.1071. \tag{A.10}$$

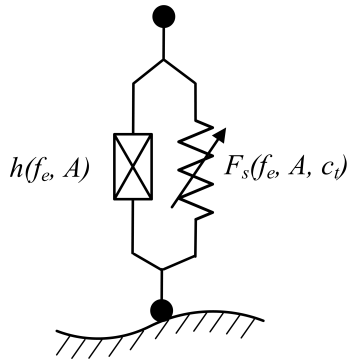

Figure A.7: Proposed point contact tyre model

The proposed point contact tyre model consists of a hysteresis damper in parallel with a nonlinear spring, as shown in Figure A.7. Using equation A.6 an equivalent viscous damping coefficient can be found to represent the hysteretic damping in the tyre. Therefore the equation for the force displacement relation can be expressed as

$$F_t = F_s + F_d \tag{A.11}$$

$$= k_n(x + c_t x^2) + c_{eq}(\dot{x}) \tag{A.12}$$

where, F_t, F_s and F_d represent the tyre force, the spring force and the damping force, respectively.

Model Refinement

The proposed model is implemented in Matlab® and a series of simulations are carried out to determine the accuracy of the model. Two typical simulation work diagrams are shown in Figure A.8. They are plotted with the corresponding measured values for comparison. In order to have an objective measure of 'goodness of fit', the Mean Squared Error (MSE) is introduced,

$$MSE(\hat{x}) = \frac{100}{N\sigma_x^2}\sum_{i=1}^{N}(x_i - \hat{x}_i)^2 \tag{A.13}$$

where, N is the number of data points and σ_x^2 is the variance of the measured data record. Experience with this norm suggests that a value less than 5 % indicates a good model, while less than 1 % indicates excellence [70]. Table A.3 shows the MSE for the simulation results. The simulation error is seen to increase with increasing

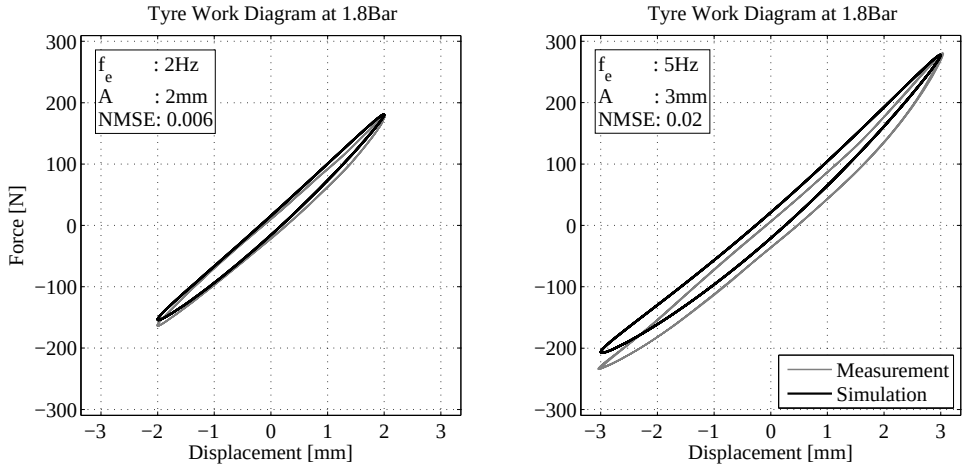

Figure A.8: Initial tyre model fit to measured data at $f_e = 2$ Hz, $A = 2$ mm, 1.8 Bar (left) and $f_e = 5$ Hz, $A = 3$ mm, 1.8 Bar (right)

Tyre Inflation Pressure 1.8 Bar				
A	1mm	2mm	3mm	4mm
f_e	MSE	MSE	MSE	MSE
1hz	0.5	0.6	1.4	3.0
2hz	0.0	0.6	1.2	3.1
4hz	0.1	0.5	1.2	2.9
5hz	0.2	0.6	1.5	-
7hz	0.4	0.4	1.5	-
10hz	0.6	0.6	-	-
14hz	0.8	-	-	-

Table A.3: Nonlinear tyre model MSE

excitation frequency and amplitude. Further investigation revealed that the main source of error in the nonlinear model is due to the offset observed in measured data. Note in Figure A.8, at $f_e = 5$Hz and $A = 3$mm, the simulation is centred around zero force, while the measured data shows a negative offset along the y-axis. This is also noted in Figure A.4 as the polynomials fitted to the data did not pass through the origin. The absolute value of the offset f_o, in Newtons, is found to increase with increasing excitation amplitude while remaining relatively

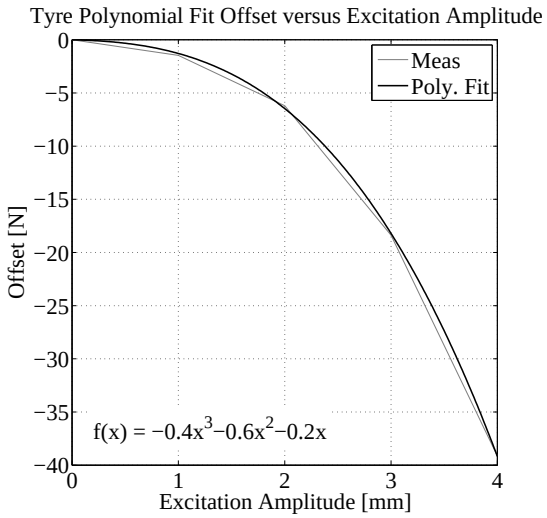

Figure A.9: Tyre polynomial fit offset versus excitation amplitude

independent of excitation frequency. The relationship between f_o and excitation amplitude is shown graphically in Figure A.9 for a tyre inflation pressure of 1.8 bar. A third order polynomial fit is also shown in Figure A.9. This polynomial is used to represent the relationship between offset and excitation amplitude allowing the nonlinear spring model, given by equation A.2, to be modified to yield

$$F_s(x) = k_n(x + c_t x^2) + f_o(A) \tag{A.14}$$

$$f_o(A) = -0.44A^3 - 0.61A^2 - 0.23A \tag{A.15}$$

where, k_o is a nonlinear function of excitation amplitude. The modified nonlinear tyre model therefore becomes

$$F_t = F_s + F_d \tag{A.16}$$

$$= k_n(x + c_t x^2) + f_o(A) + c_{eq}(\dot{x}) \tag{A.17}$$

where F_t, F_s and F_d represent the tyre force, the spring force and the damping force, respectively.

Model validation

Evaluation of this modified nonlinear tyre model revealed a significant improvement over the original nonlinear tyre model. Table A.4 shows the MSE for a range of

Tyre Inflation Pressure 1.8 Bar				
A	1mm	2mm	3mm	4mm
f_e	MSE	MSE	MSE	MSE
1hz	0.3	0.1	0.1	0.1
2hz	0.1	0.2	0.1	0.3
4hz	0.0	0.1	0.1	0.2
5hz	0.2	0.2	0.2	-
7hz	0.2	0.2	0.4	-
10hz	0.1	0.2	-	-
14hz	0.1	-	-	-

Table A.4: Revised nonlinear tyre model MSE

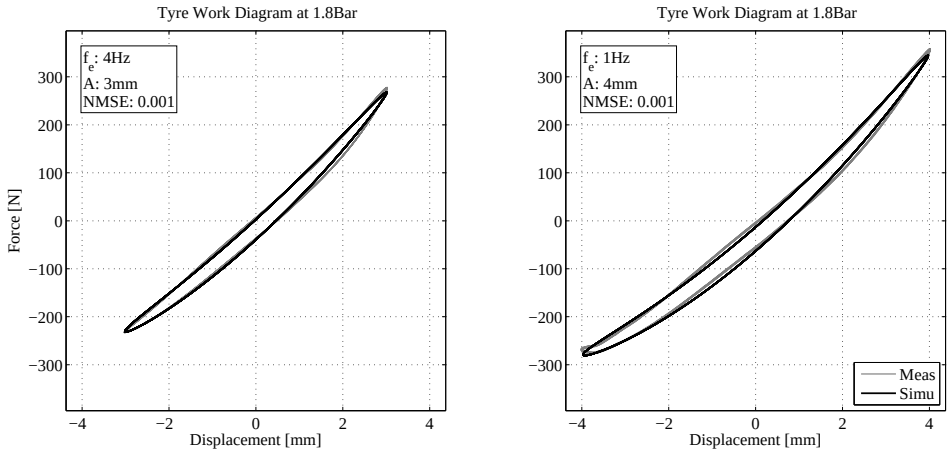

Figure A.10: Proposed tyre model fit to measured data at $f_e = 4$ Hz, $A = 3$ mm, 1.8 Bar (left) and $f_e = 1$ Hz, $A = 4$ mm, 1.8 Bar (right)

excitation frequencies and amplitudes at a pressure of 1.8 Bar. The inclusion of the offset, f_o, significantly improves the model accuracy at larger excitation amplitudes. The average MSE across all measurement frequencies and amplitudes is found to be 0.17. This is compared with an average MSE of 1.0 for the original nonlinear tyre model. The tyre model fit is shown for two example measurements in Figure A.10.

Appendix B

Shock Absorber Identification

Many works in the literature highlight the complex nonlinear nature of vehicle shock absorbers [78, 82, 158, 159]. Their identification is usually carried out experimentally using mechanical test stands [78] and harmonic excitation [77, 158]. It has been common practice to model the damping of a shock absorber as a linear viscous damper, as in the linear quarter car model. This linear model is now commonly replaced with two and three slope models to account for the major nonlinearities of the shock absorber [1]. Here, the identification of a shock absorber used in a quarter car suspension experimental test rig is documented. The shock absorber is a coil–over air damper. The spring is removed and the damper dynamically tested in isolation to characterise its behaviour. Experimental testing of the damper is carried out using an ESH® servo–hydraulic testing machine.

Characterisation

Figure B.1 shows a close up of the shock absorber test set–up, which is based on the methods used by Centro Ricerche FIAT (CRF) of Torino, Italy, as presented in a case study by Worden and Tomlinson [11]. A novel force measurement system is developed allowing the measurement of shock absorber force during isolated and operational testing (in the quarter car test rig), using an identical force transducer set–up. A force measurement set–up of this nature has, to the author's knowledge, not been previously reported in the literature. The set–up, shown in Figure B.2, uses a Kistler® 9021A load washer sandwiched between two 5 mm thick steel washers. A

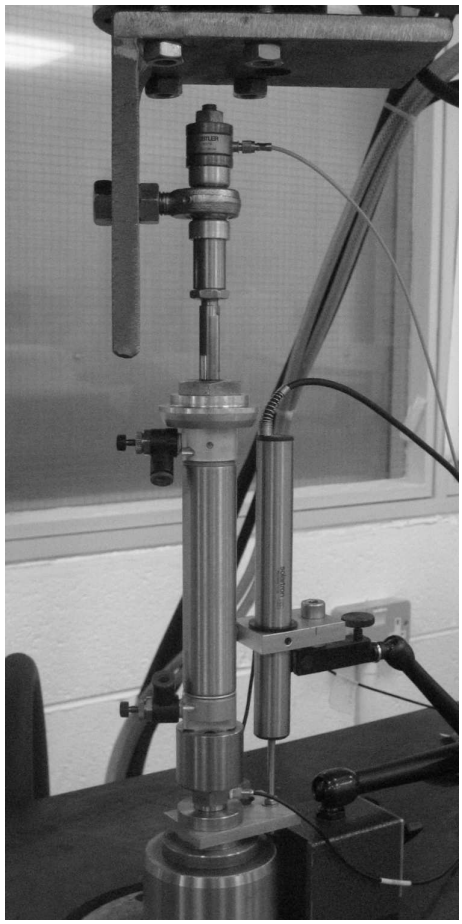

Figure B.1: Shock absorber experimental test set–up

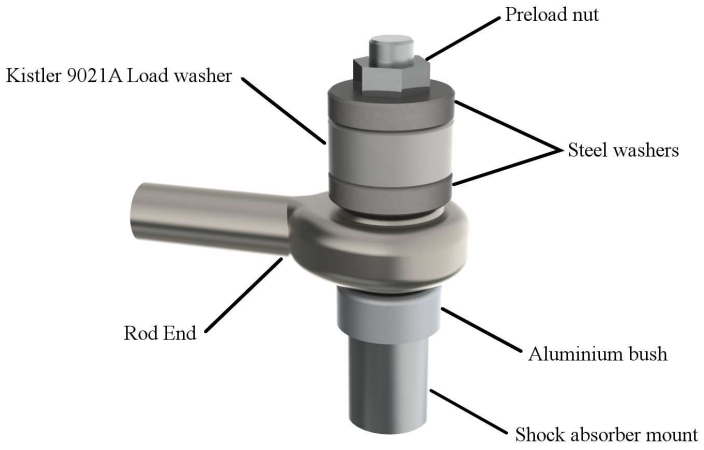

Figure B.2: Custom shock absorber force measurement setup

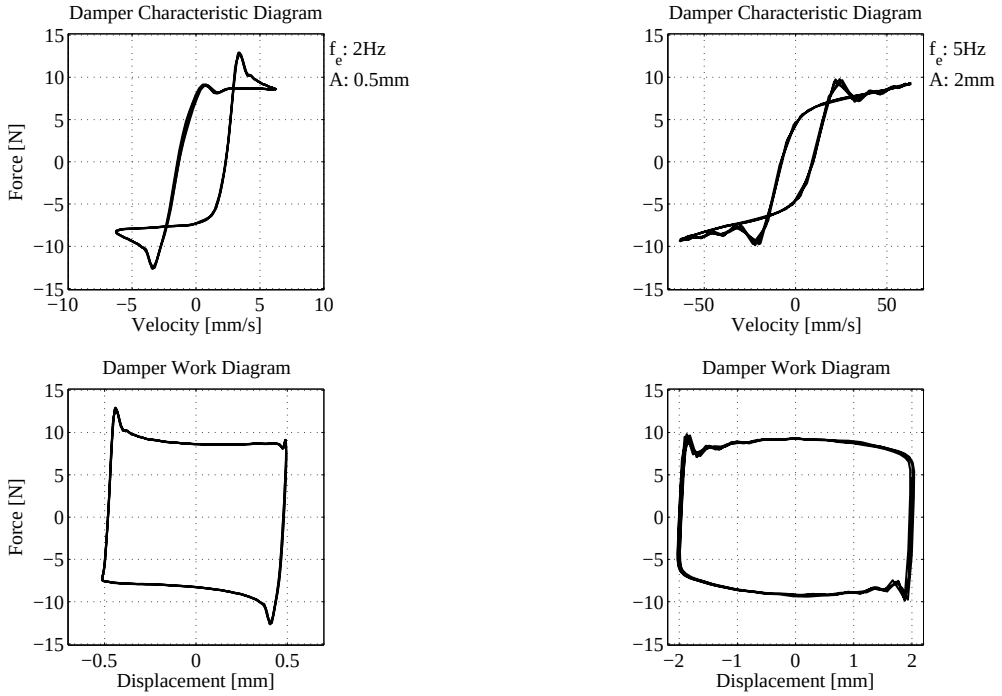

Figure B.3: Shock absorber characteristic and work diagrams at $f_e = 2$ Hz, $A = 0.5$ mm (left) and $f_e = 5$ Hz, $A = 2$ mm (right)

high precision rod end provides the shock absorber attachment to the sprung mass. The complete set–up is mounted on a steel shaft running through the rod end, steel washers and load washer. A preload of 6 kN is applied to the load washer using the preload nut. The complete set–up is dynamically calibrated using a Brüel & Kjær® Type 8200 force transducer on the ESH® machine. The Type 8200 force transducer can only be used in the ESH® machine where displacements are in the vertical direction only. It is not designed to handle the multi–directional loading which exists during quarter car rig operation. The type 9021A set–up is designed so that it can be used in both the ESH® machine and the quarter car rig, without any danger of damaging the transducer. Both transducers can be seen in position during testing in Figure B.1.

Figure B.3 shows typical characteristic diagrams (force–velocity) and work diagrams (force–displacement) for the damper, subject to displacement excitation of the form $x = A\sin(2\pi f_e t)$. Initial observation of the characteristic diagram indicate the presence of static friction in the damper. This can be seen as the shock absorber velocity increases from zero. Note the sharp increase in force (sticking) followed by a decrease in force (slipping). Due to the low velocity of the damper at 2 Hz 0.5

mm, the friction force dominates, a common property of coulomb friction [11]. The characteristic diagram shows stick-slip behaviour with the breakaway force (*i.e.* the force required to stop sticking and initiate slipping) equal to approximately ±13 N. As the velocity increases the friction force exhibits velocity dependence (stribeck effect). The damper force decreases as the velocity increases to its maxima of ±6.3 mm/s. The force, as the velocity decreases from its maximum is lower than the corresponding force as the velocity increases to its maximum. This phenomenon, known as frictional lag, was observed experimentally by Hess and Soom [175]. Note that as the velocity returns to zero from the maxima, the damper again enters the stick state at approximately ±0.6 mm/s. The velocity dependence friction model is the most prominent in system dynamics literature and is given by the equation [190]

$$\mu\left(V_{rel};\mu_0,\mu_1,\alpha\right) = \mu_0 + \mu_1 exp\left(-\alpha\left|V_{rel}\right|\right) \tag{B.1}$$

where μ_0 governs the large relative velocity behaviour, μ_1 governs the low velocity behaviour and α governs the rate of change of friction with change in relative velocity.

Pre–sliding displacement of approximately 83 μm can also be seen in the work diagram (Figure B.3). This spring like behaviour in stiction is due to relative displacement between the cylinder wall and the piston seal prior to slipping. The pre–sliding displacement increases with excitation frequency to a value of approximately 153 μm at 14 Hz, 0.5 mm amplitude. It also increases with amplitude and a value of 110 μm is recorded at 2 Hz, 4 mm amplitude. This indicates that pre–sliding displacement is dependent on the acceleration of the damper piston in the sticking phase of motion.

Figure B.4 shows the excitation amplitude and frequency dependence of static friction, pre–sliding displacement and pre–sliding to sliding transition velocity. As expected static friction is greatest at low amplitudes and low frequencies. Static friction is also seen to increase at higher frequencies. The rate of increase is larger for larger excitation amplitudes. The effect of excitation frequency on pre–sliding displacement is seen to increase with increasing amplitude. At low amplitudes (< 1 mm) the frequency dependence of the pre–sliding displacement is almost negligible. The frequency dependence of the pre–sliding displacement becomes more significant at larger excitation amplitudes. The sticking to slipping transition velocity shows similar trends to the pre–sliding displacement.

Different combinations of excitation frequency and amplitude are used to compare the damper characteristic at equivalent excitation velocities. Figure B.5 shows the

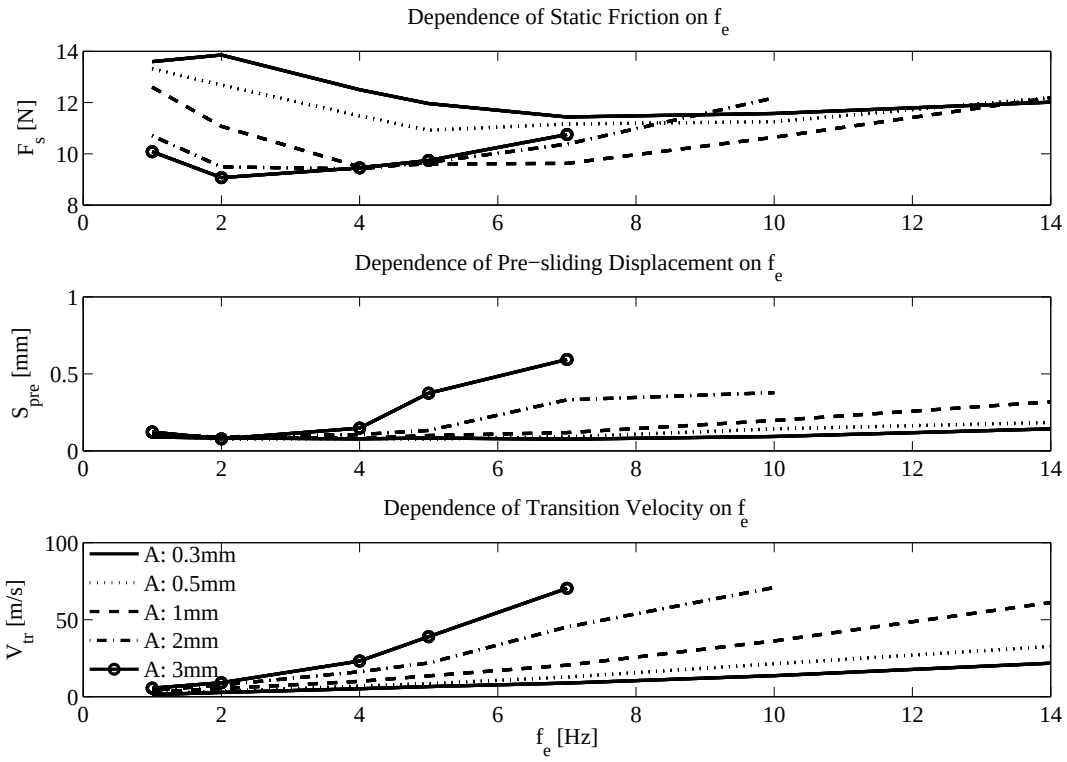

Figure B.4: Frequency and amplitude dependence of friction phenomena observed in the shock absorber characteristic diagrams

results of two such comparisons. A reasonable correlation is seen in the first plot. The second plot however highlights a dependence on shock absorber acceleration. The transition velocity at 10 Hz is significantly greater than that at 5 Hz, despite the fact that the piston velocities are equal. The transition velocities are approximately 24 mm/s and 38 mm/s, at 5 Hz and 10 Hz respectively. This acceleration dependence is also apparent, but to a lesser extent, in the first plot.

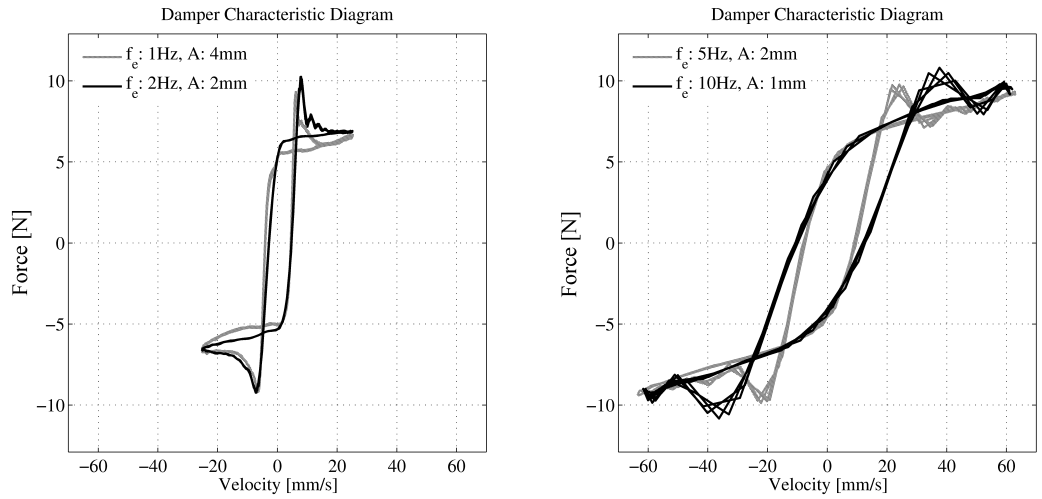

Figure B.5: Shock absorber acceleration dependence

Model selection

Commonly used static friction models are shown in Figure B.6. The friction model which best represents the phenomena observed from damper test results is the stribeck–coulomb–viscous Friction model. The stribeck effect is the negatively sloped characteristic taking place at low velocities [191]. Static friction models cannot sufficiently describe all the dynamic effects of friction, such as pre–sliding displacement, friction lag and variable break away force [176, 177].

Friction behaviour can be divided into two regimes, pre–sliding and sliding. In the pre–sliding regime the friction force is a hysteretic function of the position. In the sliding regime the friction is a nonlinear function of velocity. A dynamic friction model is required to model such behaviour. One such model, called the LuGre model, was developed by Canudas de Wit *et al.* [178]. The LuGre model supports hysteretic behaviour due to friction lag, spring like behaviour in stiction and gives a varying break away force depending on the rate of change of the applied force. It is a combination of the static friction model and the Dahl friction model. The LuGre

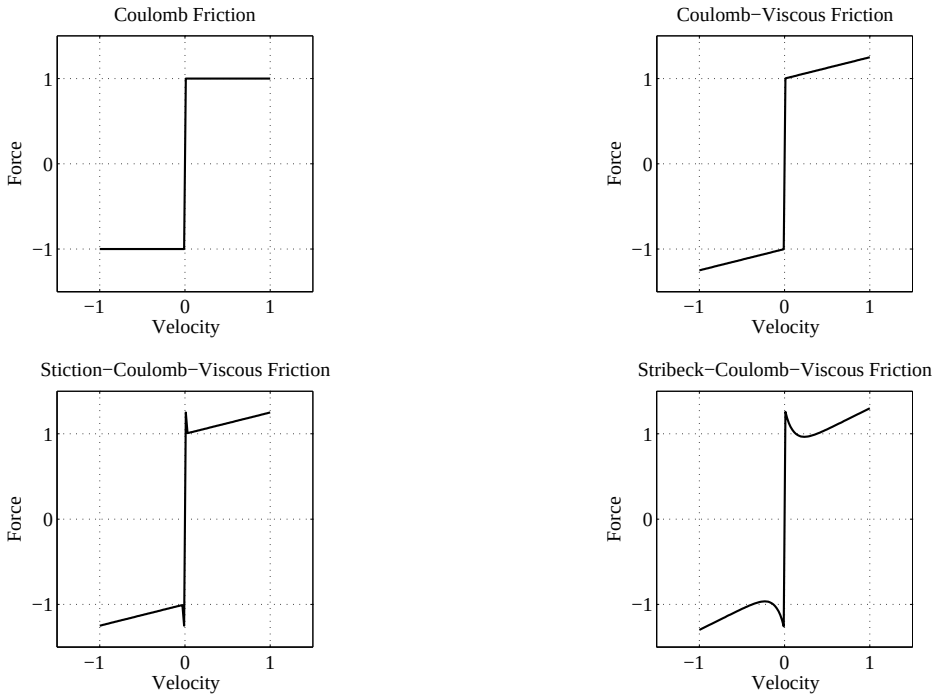

Figure B.6: Examples of static friction models

model is a bristle type friction model and is given by,

$$\frac{dz}{dt} = v - \sigma_0 \frac{|v|}{g(v)} z \tag{B.2}$$

$$g(v) = F_c + (F_s - F_c)e^{-(v/v_s)^2} \tag{B.3}$$

$$F = \sigma_0 z + \sigma_1 \dot{z} + f(v) \tag{B.4}$$

where z is the average unmeasurable deflection of the bristles, σ_0 is the bristle stiffness and σ_1 is the bristle velocity dependent damping coefficient [178]. F_s and F_c represent the static friction force and the Coulomb friction force, respectively. The term v_s is the stribeck velocity and the function $g(v)$ characterises the stribeck effect. The function $f(v)$ is a function which represents lubrication and viscous friction effects. The function $f(v)$ in the model allows for the inclusion of the damper viscous damping characteristics as the piston velocity and displacement increases.

Figure B.7 shows the LuGre model with optimised parameters to fit the experimental data for an excitation frequency of 4 Hz and an amplitude of 4 mm. Optimisation is carried out in Matlab® using the pattern search optimisation function *patternsearch*. Pattern search algorithms are a subclass of direct search algorithms, the minimiser

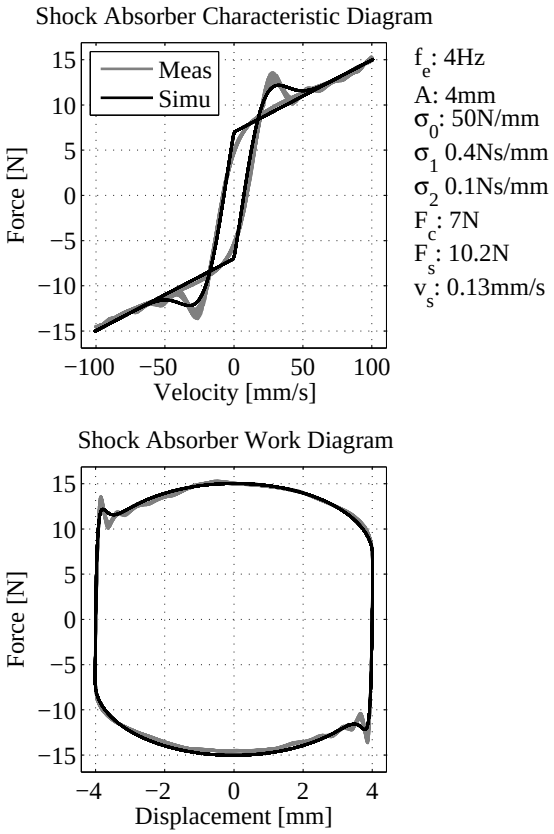

Figure B.7: LuGre friction model approximation of measured data

of a continuous function is sought without the use of derivatives. This function is chosen due to its ability to find global minima unlike other derivative based optimisation functions which may return local minima. The optimised model shows a good fit with measured data. It models the asymmetric behaviour of the damper in acceleration and deceleration well and also includes hysteresis effects and pre–sliding displacement. Dynamic friction models such as the LuGre model are known to be complex and hard to implement in practical engineering applications [179].

Significant hysteresis can also be observed in Figure B.3 at low velocities. Figure B.8 shows energy dissipated per cycle (ΔW) for various amplitudes plotted against excitation frequency. ΔW is seen to increase in an approximately linear fashion with excitation frequency at the larger amplitudes of excitation, indicating that the damping mechanism is viscous damping. At the lower amplitudes (0.5 mm and 1 mm) the energy dissipation does not show strong dependence on excitation frequency. This is believed to be due to friction in the damper. At low amplitudes of excitation, friction damping would account for most damping force due to the relatively small

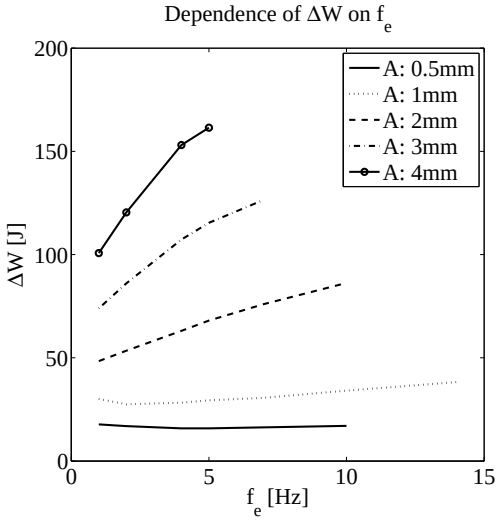

Figure B.8: Damper energy dissipation dependence on excitation frequency

motion of the piston and hence movement of the fluid within the damper. Hysteresis modelling in dampers has received much attention in the literature. The Bouc–Wen hysteresis model is often used in the modelling of magnetorheological dampers. The force, $F(t)$, of a Bouc–Wen damper in parallel with a spring and viscous damper is given by,

$$F = c_s\dot{x}(t) + k_s x(t) + \alpha\nu(t) \tag{B.5}$$

where the evolutionary variable ν is governed by

$$\dot{\nu}(t) = B\dot{x}(t) - \beta\left|\dot{x}(t)\right|\nu(t)\left|\nu(t)\right|^{n-1} - \gamma\dot{x}(t)\left|\nu(t)\right|^{n}. \tag{B.6}$$

The shape of the hysteric loop is governed by the coefficients B, α, β, γ and n. Optimal parameters of the model are found using pattern search optimisation. Figure B.9 shows the Bouc–Wen simulation results superimposed on experimental results for an excitation frequency of 4 Hz and an amplitude of 4 mm. The Bouc–Wen model shows a good fit with measured results. It does not however model the stiction observed in the measured data.

Due to the asymmetric nature of many shock absorbers, piecewise linear models have been increasingly used in place of linear models. A trilinear model is selected to model the shock absorber based on the observation of three distinct regions in the characteristic diagrams in Figure B.3. A viscous damping characteristic at high velocities in compression and rebound and a static friction zone at low shock absorber

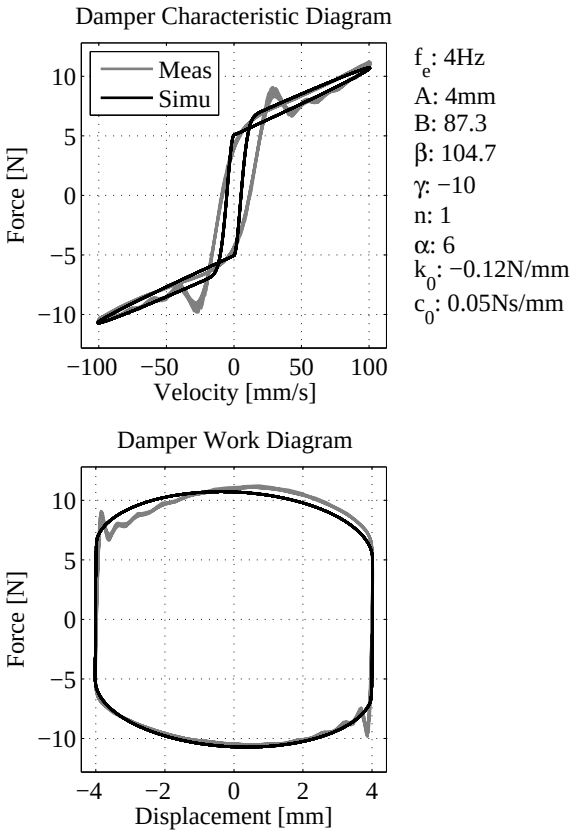

Figure B.9: Optimized Bouc–Wen damper model

velocities. The equations representing the trilinear characteristic are given by [78],

$$f_d(\dot{z}) = \begin{cases} c_3(\dot{z} - c_5) + c_1 c_5 & \text{for } \dot{z} > c_5, \\ c_1 \dot{z} & \text{for } c_4 \leq \dot{z} \leq c_5, \\ c_2(\dot{z} - c_4) + c_1 c_4 & \text{for } \dot{z} < c_4 \end{cases} \tag{B.7}$$

where, f_d is the damper force, $\dot{z}$ is damper piston velocity and the parameters c_1, c_2, c_3, c_4, c_5 to be identified, are shown in Figure B.10. The equations of the trilinear model are more intuitive than the Bouc–Wen or LuGre models. It allows a reasonable approximation of both friction and pre–sliding displacement.

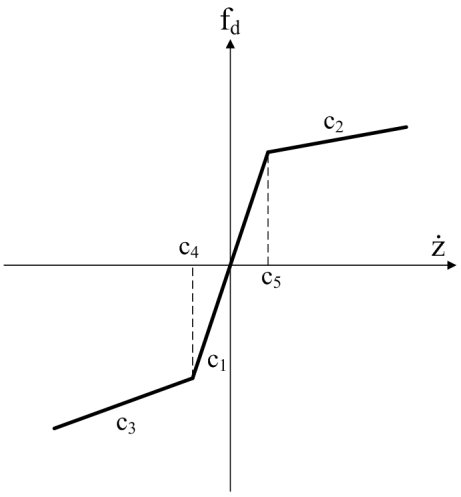

Figure B.10: Damper piecewise linear function (adapted from [78])

Parameter estimation

It is evident from the complex nature of the damper characteristic diagram that a simple linear model will not accurately represent the damper. Initial investigations are carried out to identify the optimal parameters of the LuGre and Bouc–Wen models across the frequency and amplitude range of the experimental tests. The Bouc–Wen hysteresis model and LuGre friction model are found to accurately model the major phenomena of the damper at discrete frequencies and amplitudes. Attempts are made to determine generalised parameters for these models across a wide range of frequencies and amplitudes. Both direct search methods and the genetic algorithm are used to identify global optimisation minima for each experimental data set. The identified parameters do not show a strong pattern across the frequency and amplitude range of the experimental data. This can be seen in Figure B.11, which shows optimised LuGre model coefficient dependence on the excitation frequency. As a result, it proved difficult to identify generalised optimisation parameters for all experimental frequencies and amplitudes.

Focus turns to the more intuitive trilinear damper model to identify the shock absorber. The trilinear model parameters can be directly related to phenomena identified in the shock absorber characteristic diagrams. The friction which dominates at low velocities can be related to parameter c_1 which represents the trilinear damping at low velocities. The sticking to sliding transition velocity to parameters c_4 and c_5 while the viscous damping outside the static friction zone can be related to parameters c_2 and c_3. Optimised trilinear damper coefficients are identified at

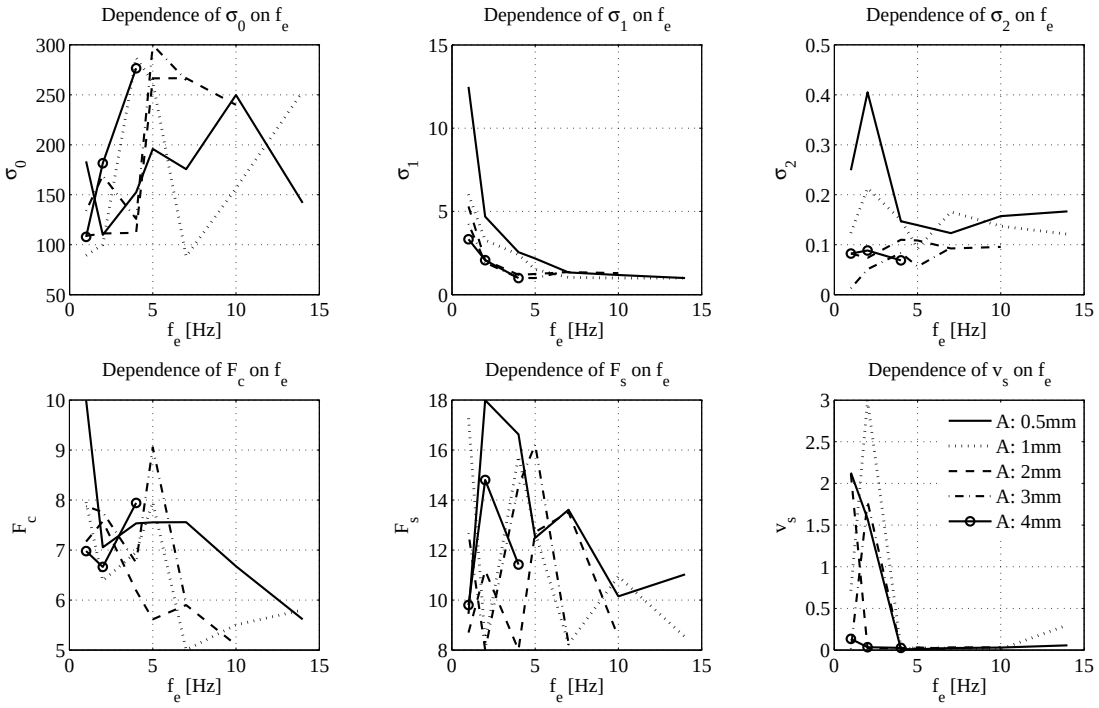

Figure B.11: Optimsed LuGre model coefficient dependence on f_e

each experimental data set. The dependence of the trilinear damper coefficients on excitation frequency and amplitude can be seen in Figure B.12. At low excitation frequencies and amplitudes the presence of friction in the damper has a larger effect on the identified coefficients. Large values of c_1 and negative values of c_2 are seen at low amplitudes and low frequencies due to these friction effects. At higher piston velocities, coefficients c_2 and c_3 show a slight decrease with increasing frequency and amplitude. The absolute values of c_4 and c_5 increase with increasing frequency and amplitude. Notice the similarities between parameters c_4 and c_5 and the sticking to slipping transition velocity in Figure B.4. Although the parameters of the model are intuitive it also proves difficult to identify expressions for the parameters across the frequency and amplitude range of the experimental tests.

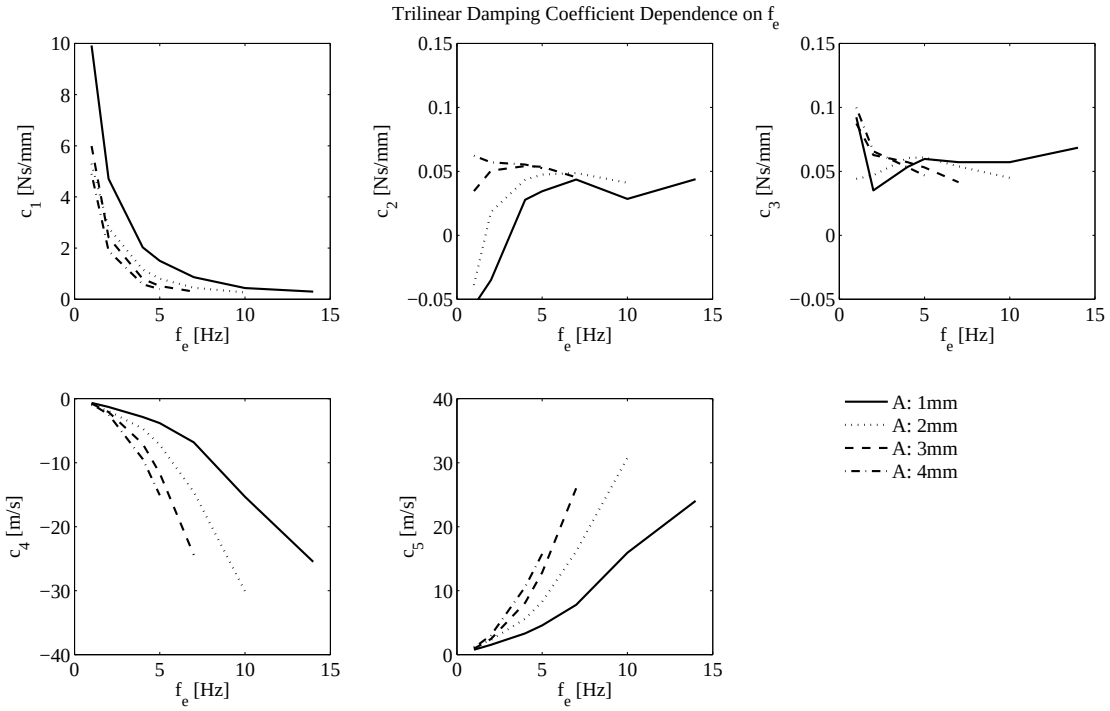

Figure B.12: Damper coefficient dependence on f_e

Appendix C

Matlab algorithms

Matlab R-MISO function

```
function [A F CC OC PC MC] = rmiso_v2(x,y,fs,varargin)
%RMISO performs a reverse MISO analysis with multiple inputs
% --INPUT ARGUMENTS
% - x(Nxm) input vector
% N - number of data points in each signal
% m - Number of input signals
% - y(Nx1) output vector
% --OUTPUT ARGUMENTS
% - A(N/2+1,m) Frequency spectra
% - F(N/2+1,1) Frequency vector
% - CC(N/2+1,m) Cumulative coherence
% - OC(N/2+1,m) Ordinary coherence
% - PC(N/2+1,m) Partial coherence
% - MC(N/2+1,1) Multiple coherence

% Damien Maher
% Mechanical and Manufacturing Engineering
% Dublin City University
% 08.02.10
% Matlab 7.1.0.246 (R14) Service Pack 3
```

```
% --OPTIONS
options.overlap = 50; % percent
options.N = 2048;
options = parseargs(options,varargin{:});
% --SIGNAL POST PROCESSING PARAMETERS
N = options.N;
olap = options.overlap/100;
win = window(@hann ,N);
overLap = round(length(win).*olap);
% Add y to end of x
x = [x,y];
size_x = size(x,2);
%--CALCULATING ALL AUTOSPECTRA AND CROSSSPECTRA
for j = 1:size_x
for k = 1:size_x
[Sxy_0(:,(j-1)*size_x + k), F] =
cpsd(x(:,j),x(:,k),win,overLap,[],fs);
end
end
% --LINEAR FRF'S, CONDITIONED AUTOSPECTRA & CROSSSPECTRA
for r = 1:size_x-1
for ii = 1:size_x
eval(strcat('Lxy(:,(r-1)*size_x + ii) = Sxy_', num2str(r-1),
'(:,(r-1)*size_x + ii)./Sxy_', num2str(r-1),
'(:,(r-1)*size_x + r);'));
end

for ii = 1:size_x
for jj = 1:size_x
if ii == jj
eval(strcat('Sxy_',num2str(r), '(:,(ii-1)*size_x + jj) =
Sxy_', num2str(r-1), '(:,(ii-1)*size_x + jj) -
(abs(Lxy(:,(r-1)*size_x + jj)).^2).*Sxy_',
num2str(r-1), '(:,(r-1)*size_x + r);'))
else
eval(strcat('Sxy_', num2str(r), '(:,(ii-1)*size_x + jj) =
```

```
Sxy_', num2str(r-1), '(:,(ii-1)*size_x + jj) -
Lxy(:,(r-1)*size_x + jj).* Sxy_', num2str(r-1),
'(:,(ii-1)*size_x + r);'))
end
end
end
end
% --ORDINARY COHERENCE FUNCTIONS
OC = zeros(size(Sxy_0,1), size_x-1);
for ii = 1:size_x-1
OC(:,ii) = (abs(Sxy_0(:,ii*size_x)).^2)./
(Sxy_0(:,(ii-1)*size_x+ii).*Sxy_0(:,size_x^2));
end
% --PARTIAL COHERENCE FUNCTIONS
PC = zeros(size(Sxy_0,1), size_x-1);
for ii = 1:size_x-1
eval(strcat('PC(:,ii)=(abs(Sxy_',num2str(ii-1),
'(:,ii*size_x)).^2)./(Sxy_',num2str(ii-1),
'(:,(ii-1)*size_x+ii).*Sxy_',num2str(ii-1),
'(:,size_x^2));'));
end
% --CUMULATIVE COHERENCE FUNCTIONS
CC = zeros(size(Sxy_0,1), size_x-1);
for ii = 1:size_x-1
eval(strcat('CC(:,ii) = (abs(Sxy_',num2str(ii-1),
'(:,ii*size_x)).^2)./(Sxy_',num2str(ii-1),
'(:,(ii-1)*size_x+ii).*Sxy_0(:,size_x^2));'));
end
% --MULTIPLE COHERENCE FUNCTIONS
MC = zeros(size(Sxy_0,1), 1);
for ii = 1:size_x-1
MC = [MC + CC(:,ii)];
end
% --GENERATING FRFS A1, A2
A = zeros(size(Sxy_0,1), size_x-1);
A(:,size_x-1) = Lxy(:,((size_x)^2)-size_x);
for kk = 2:size_x-1
```

```
i = kk;
A(:,size_x-kk) = Lxy(:,((size_x)^2)-size_x*kk);

while i > 1
A(:,size_x-kk) = A(:,size_x-kk) - Lxy(:,((size_x)^2)-
size_x*kk-(kk-i+1)).*A(:,size_x-(kk-i+1));
i = i - 1;
end
end
%--EOF
```

Matlab least squares function

```
function [X, covarX, signifX, sizeA, rankA] = lssvd(A,Y)
%LSSVD Solves the overdetermined set of equations (Ax = Y) in a
%least squares sense using singular value decomposition, where:
% - A = [M x N]
% - x = [M x 1]
% - Y = [N x 1]
% --INPUT ARGUMENTS
% - A [M x N]
% - Y [N x 1]
% --OUTPUT ARGUMENTS
% - X [M x 1], LS solution vector
% - covarX, covariance matrix
% - signifX, significance factors of elements of X
% - sizeA, size of matrix A
% - rankA, rank of matrix A

% Damien Maher
% Mechanical and Manufacturing Engineering
% Dublin City University
% 19.10.10
% Matlab 7.1.0.246 (R14) Service Pack 3

%--SVD
[U,E,V] = svd(A,0);
% remove values in E less than tol
tol = length(Y)*eps*E(1,1);
index = find(diag(E)< tol);
rE = diag(1./diag(E));
rE(index,index) = 0;
X = V*rE*(U'*Y);
%--COVARIANCE MATIX
covarX = V*(rE^2)*V';
%--SIGNIFICANCE FACTORS
for ii = 1:min(size(A))
```

```
var_1(ii) = var(X(ii).*A(:,ii));
end
signifX = 100.*var_1./sum(var_1);
%--SIZE AND RANK OF A
rankA = rank(A);
sizeA = min(size(A));
```

Appendix D

QcAT - Quarter car Analysis Tool

Quarter car Analysis Tool (QcAT) is a custom experimental test and simulation analysis tool developed in Matlab®. QcAT gives the user control of the complete data acquisition-analysis-presentation process from a single Graphical User Interface (GUI). The acquisition tab allows the user to enter experimental and simulation parameters. QcAT implements ActiveX control of both Pulse® and Labview® to set data acquisition and experimental test rig parameters. A basic motor control loop uses the National Instruments ® USB-6009 I/O module to set the motor speed via a control voltage to the motor inverter. After acquisition data can be visualised and further processed in QcAT or exported for presentation. A diagram summarising the hardware/software implementation is shown in Figure D.1.

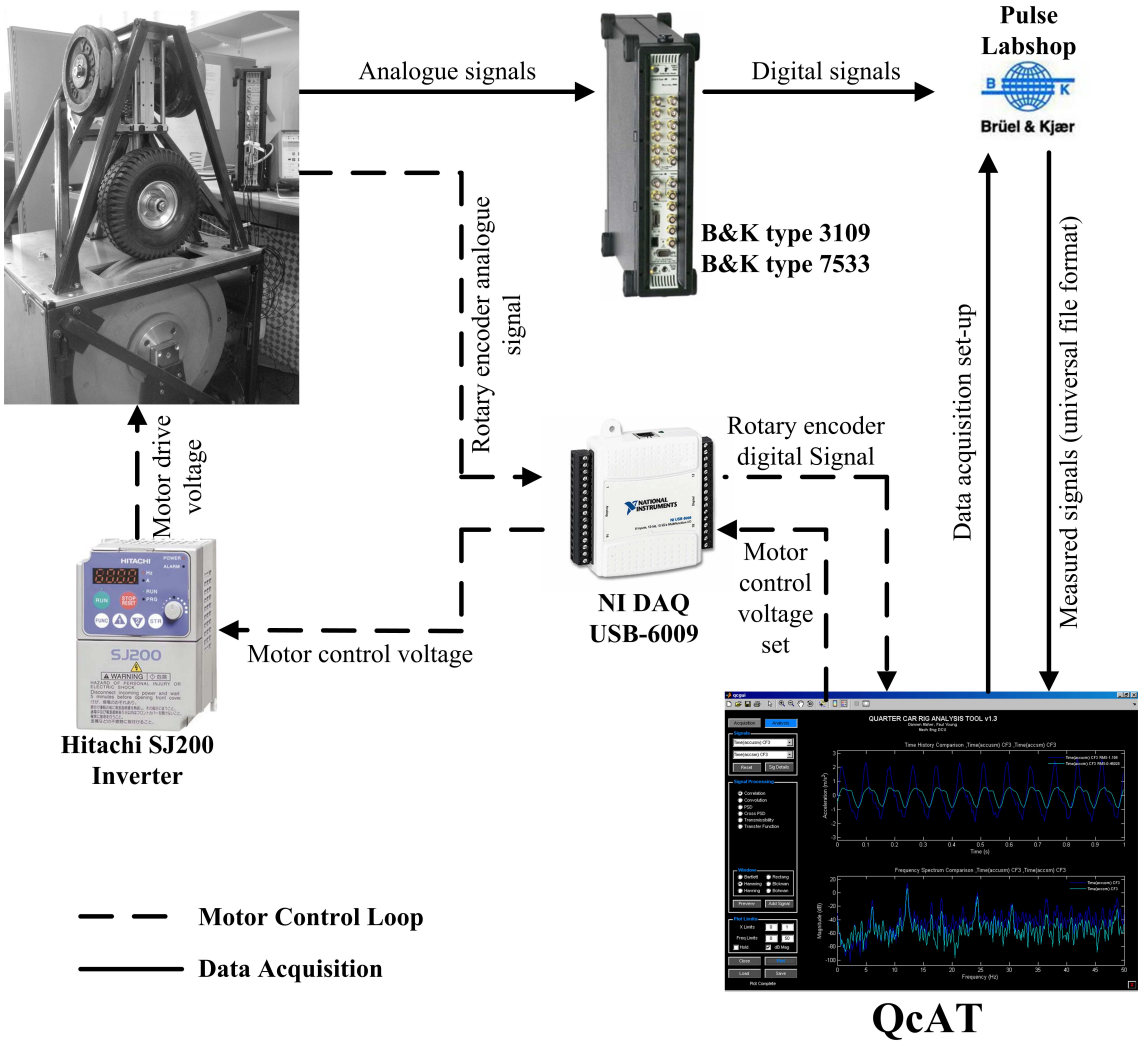

Figure D.1: Experimental testing hardware/software implementation

Data acquisition and simulation setup

Data acquisition and simulation setup are controlled inside the acquisition tab. The acquisition tab is shown in Figure D.2. The analysis options are divided into three sections;

Simulation setup allows the user to control the simulation parameters. Option are available for the setup of quarter car parameters, including the selection of a nonlinear shock absorber, nonlinear tyre and simulation input.

Measurement setup controls the settings of the Pulse® data acquisition system and quarter car rig. The length of the experimental test can be controlled

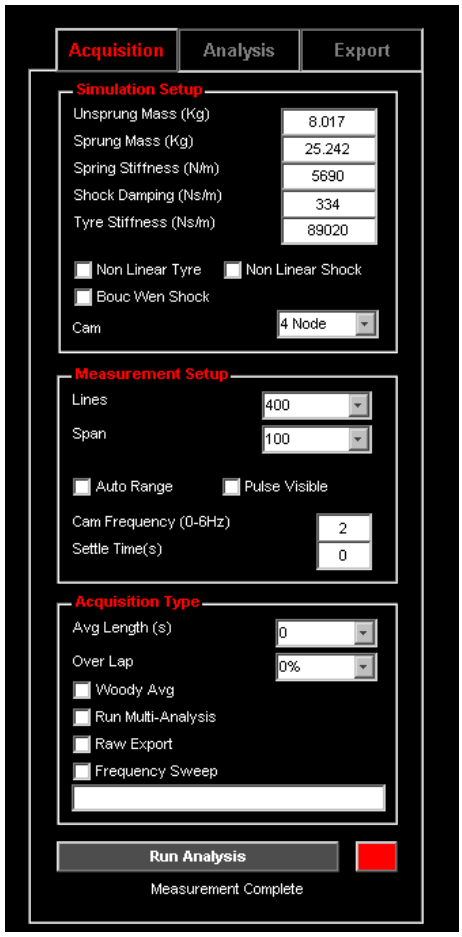

Figure D.2: Data acquisition and simulation options

along with transducer auto-ranging, quarter car rig cam frequency and rig warm up time.

Acquisition type allows the user to set averaging properties, multiple experimental test runs, frequency sweeps. Additional arguments for the various analysis methods can be entered in the text box. The user can choose to filter the results or export raw data following data acquisition.

Data analysis and presentation

Following data acquisition, acquired experimental and simulation data are automatically loaded into the analysis tab for further processing. The analysis tab is shown in Figure D.3. Data can be analysed directly after acquisition or saved to universal file format for future analysis. Saved data sets can also be loaded into the analysis

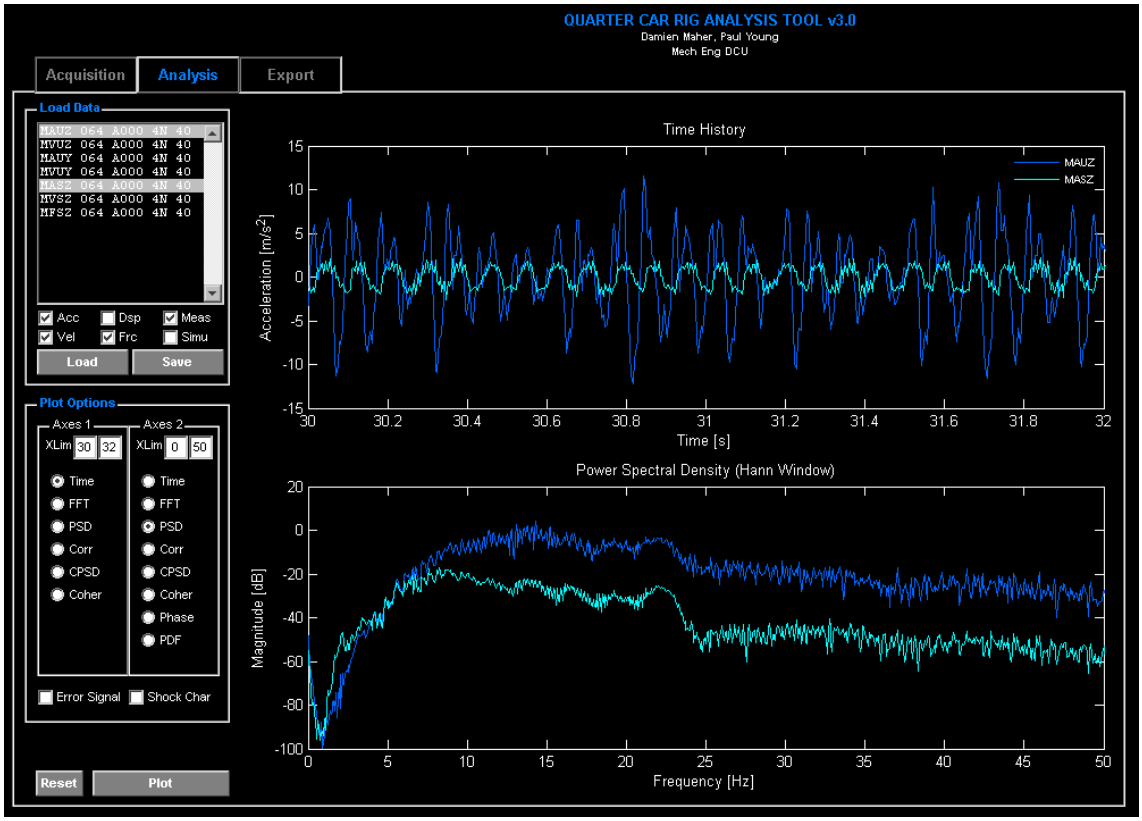

Figure D.3: Analysis tab

tab.

The data available for analysis populates the load data frame as shown in Figure D.4a. This represents a menu of what signals are available in the loaded data sets. Single or multiple signals can be selected for analysis. The signal name gives details of the data contained in the signal. For example, the first entry in the load data form is '`MAUZ 064 A000 4N 40`'. This represents a measured unsprung mass acceleration in the z direction, the time history is 64 seconds long, with zero averages and acquired using a 4 lobed cam at a frequency of 0.4 Hz. Plotting options are set using the plot options frame, shown in Figure D.4b. The user can chose from a number of different time and frequency domain representations of the data.

The presentation of data acquired and analysed in QcAT is achieved using the export tab. Multiple data sets can be loaded and exported to a figure for presentation purposes. Figure D.5 shows the export setup screen and Figure D.6 shows the output generated by QcAT.

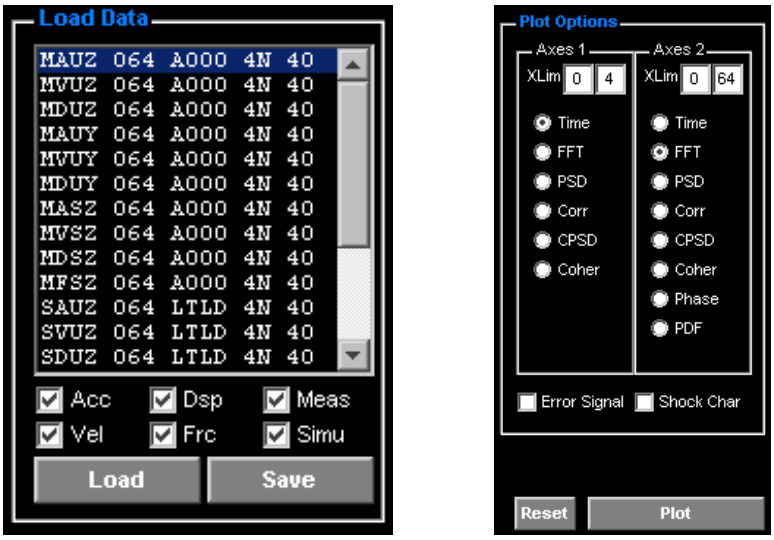

(a) Load Data (b) Plot Options

Figure D.4: Data load and analysis options

Figure D.5: Export setup

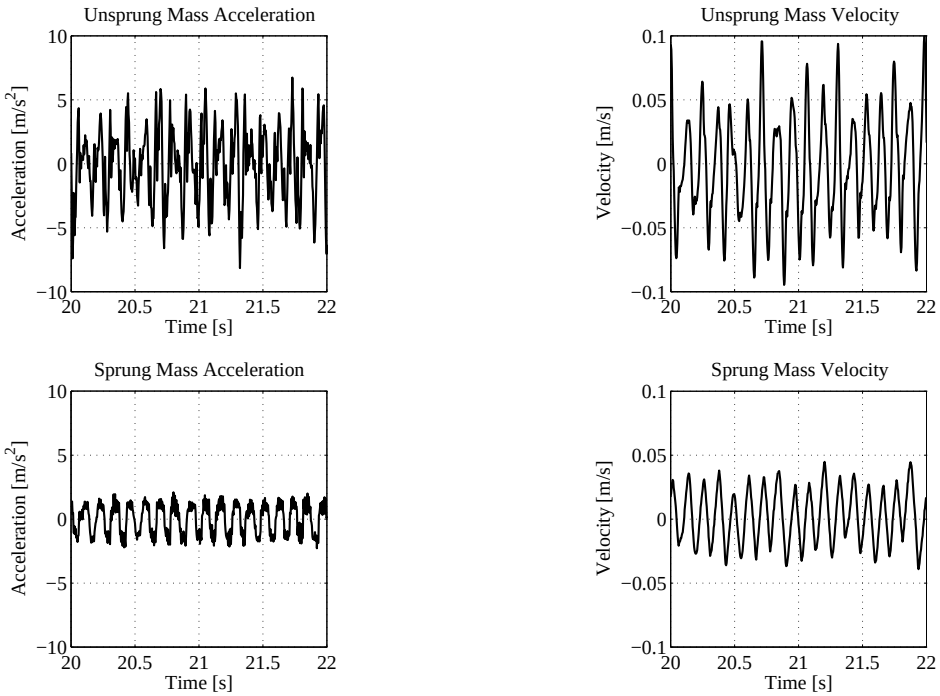

Figure D.6: Automated figure generation

Version history

v1.0 QcAT is initially developed for the purpose of quickly carrying out simulations for comparison with experimental data. The acquisition of experimental data is controlled using an implementation of Visual Basic for Applications® (VBA) inside Pulse®. Control of the quarter car rig is implemented in Labview® via a USB-6009 input/output module.

v1.1 A stand alone Visual Basic®(VB) executable application to control Pulse® and Labview® is developed. This allows a VB experimental setup graphical user interface to be developed which can be called directly from QcAT.

v1.2 An option to use an electromagnetic shaker, to excite the quarter car rig, is included in the simulation and experimental options in QcAT. Figure D.7 shows a screen shot of QcAT v1.2. Cam excitation options are on the left and shaker excitation options on the right.

v2.0 The need to have Visual Basic®, Labview®, Matlab®, and Pulse® open in order to conduct experimental tests is eliminated by implementing Matlab® ActiveX control of Pulse® and the rig control hardware. The user interface is

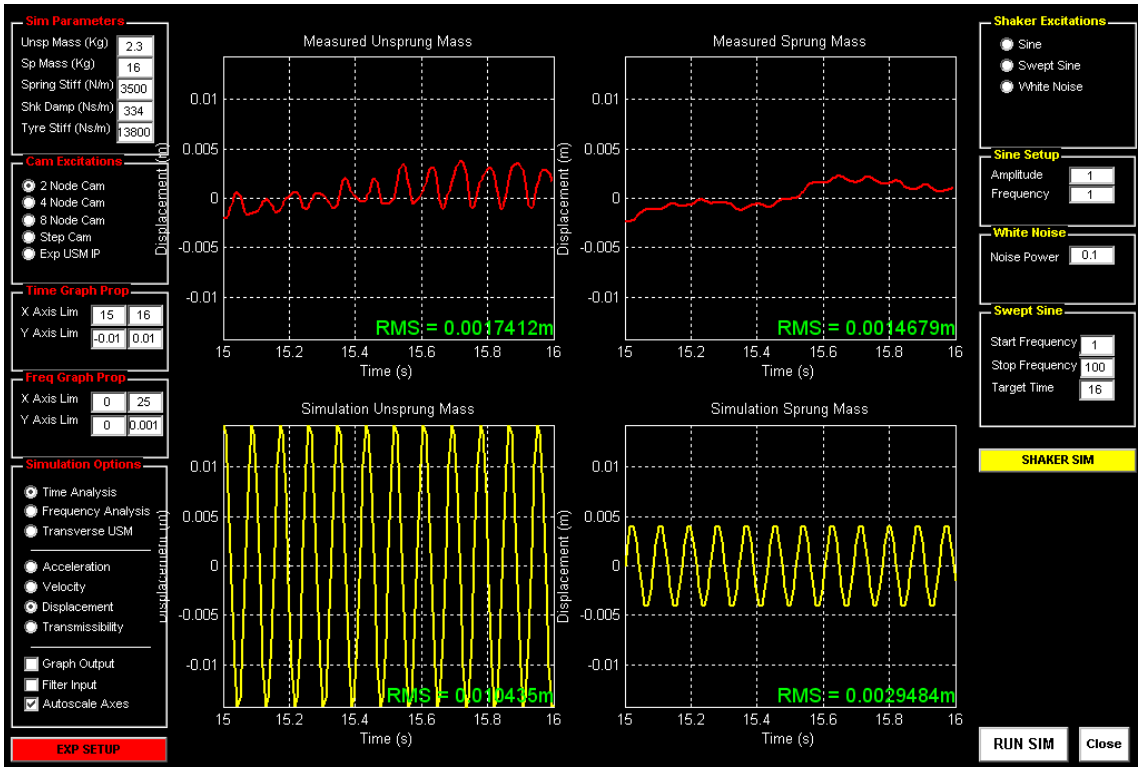

Figure D.7: QcAT v1.2

redesigned to accommodate this change. All experimental data sets are now stored in universal file format 58b. This facilitates accurate documentation of experimental and simulation results.

v2.1 Options are added for transducer auto-ranging, cam sweep input, automated multiple experimental test runs and signal averaging.

v2.2 A simulation tab is added to conduct simulations separately from experimental data and the analysis tab is expanded to include more analysis options, as shown in Figure D.8.

v2.3 Acquisition of lateral unsprung mass acceleration is added. A 3D visualisation tool is implemented to allow animation of simulated and measured quarter car rig motion, as shown in Figure D.9

v3.0 Complete revision of user interface. Analysis tab developed to allow analysis and visualisation of multiple data sets simultaneously. Export tab added to allow presentation of the data outside QcAT.

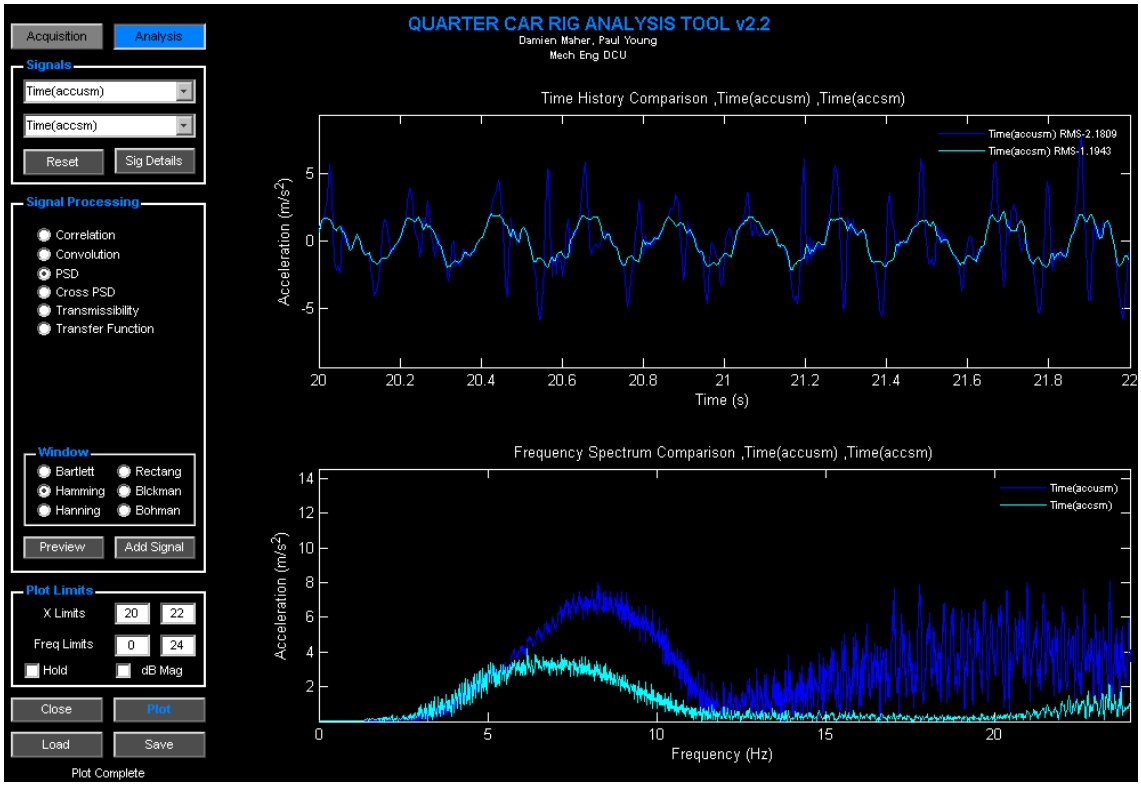

Figure D.8: QcAT v2.2 Analysis Tab

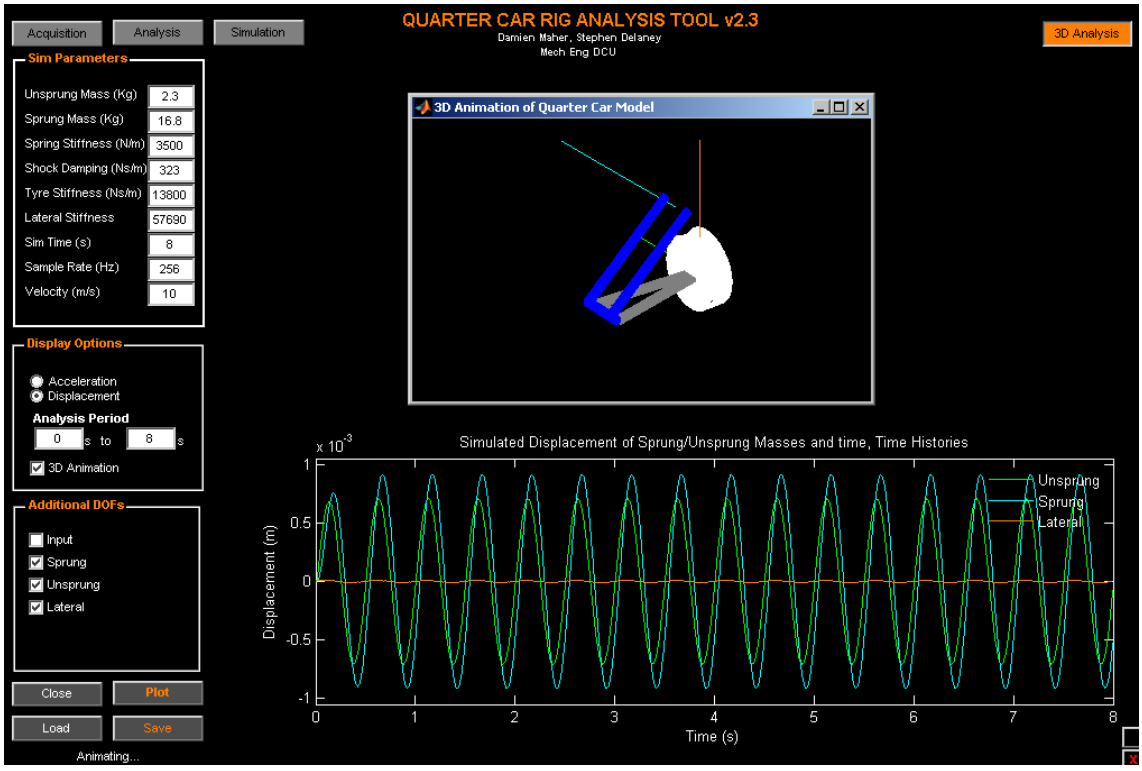

Figure D.9: QcAT v2.3 3D analysis and visualisation

Appendix E

Universal File Formats

Universal File formats (UF) were originally developed by the Structural Dynamics Research Corporation (SDRC) in the late 1960s to facilitate data transfer between computer aided test (CAT) and computer aided design (CAD) software and in an effort to facilitate computer aided engineering (CAE).

The formats were originally developed as 80 character ASCII records that occur in a specific order according to each UF format. As computer files became routinely available, single UF formats were concatenated into computer file structures. Recently, a hybrid UF file structure (UF Dataset 58 Binary) was developed for experimental data that allows data to be stored in a more efficient binary format. The use of the Universal File Format as a *de facto* standard has been of great value to the experimental dynamics (vibration and acoustic) community, particularly in the area of modal analysis.

Universal Dataset Number: 58

```
Universal Dataset
Number:  58
Name:  Function at Nodal DOF
Status:  Current
Owner:  Test
Revision Date:  23-Apr-1993


 Record 1:   Format(80A1)
             Field 1               - ID Line 1
 Record 2:   Format(80A1)
             Field 1               - ID Line 2
 Record 3:   Format(80A1)
             Field 1               - ID Line 3
 Record 4:   Format(80A1)
             Field 1               - ID Line 4
 Record 5:   Format(80A1)
             Field 1               - ID Line 5
 Record 6:   Format(2(I5,I10),
             2(1X,10A1,I10,I4))
             DOF Identification
             Field 1               - Function Type
                                   0 - General or Unknown
                                   1 - Time Response
                                   2 - Auto Spectrum
                                   3 - Cross Spectrum
                                   4 - Frequency Response Function
                                   5 - Transmissibility
                                   6 - Coherence
                                   7 - Auto Correlation
                                   8 - Cross Correlation
                                   9 - Power Spectral Density
                                   10 - Energy Spectral Density
                                   11 - Prob Density Function
                                   12 - Spectrum
```

```
                    13 - Cumulative Freq Distribution
                    14 - Peaks Valley
                    15 - Stress/Cycles
                    16 - Strain/Cycles
                    17 - Orbit
                    18 - Mode Indicator Function
                    19 - Force Pattern
                    20 - Partial Power
                    21 - Partial Coherence
                    22 - Eigenvalue
                    23 - Eigenvector
                    24 - Shock Response Spectrum
                    25 - Finite Impulse Resp Filter
                    26 - Multiple Coherence
                    27 - Order Function
Field 2             - Function Id Number
Field 3             - Version or sequence number
Field 4             - Load Case Id Number
                    0 - Single Point Excitation
Field 5             - Response Entity Name
                    ('NONE' if unused)
Field 6             - Response Node
Field 7             - Response Direction
                    0 - Scalar
                    1 - +X Translation
                    -1 - -X Translation
                    2 - +Y Translation
                    -2 - -Y Translation
                    3 - +Z Translation
                    -3 - -Z Translation
                    4 - +X Rotation
                    -4 - -X Rotation
                    5 - +Y Rotation
                    -5 - -Y Rotation
                    6 - +Z Rotation
                    -6 - -Z Rotation
```

	Field 8	- Reference Entity Name
		(‘NONE’ if unused)
	Field 9	- Reference Node
	Field 10	- Reference Direction
		(same as field 7)
Record 7:	Format(3I10,3E13.5)	
	Data Form	
	Field 1	- Ordinate Data Type
		2 - real, single precision
		4 - real, double precision
		5 - complex, single precision
		6 - complex, double precision
	Field 2	- Number of data pairs
		for uneven abscissa
		spacing, or number of
		data values for even
		abscissa spacing
	Field 3	- Abscissa Spacing
		0 - uneven
		1 - even
		(no abscissa values stored)
	Field 4	- Abscissa minimum
		(0.0 if spacing uneven)
	Field 5	- Abscissa increment
		(0.0 if spacing uneven)
	Field 6	- Z-axis value
		(0.0 if unused)
Record 8:	Format	
	(I10,3I5,2(1X,20A1))	
	Abscissa Data	
	Characteristics	
	Field 1	- Specific Data Type
		0 - unknown
		1 - general
		2 - stress
		3 - strain

```
                                    5 - temperature
                                    6 - heat flux
                                    8 - displacement
                                    9 - reaction force
                                    11 - velocity
                                    12 - acceleration
                                    13 - excitation force
                                    15 - pressure
                                    16 - mass
                                    17 - time
                                    18 - frequency
                                    19 - rpm
                                    20 - order
            Field 2                 - Length units exponent
            Field 3                 - Force units exponent
            Field 4                 - Temperature units exponent
            Field 5                 - Axis label
                                    ('NONE' if not used)
            Field 6                 - Axis units label
                                    ('NONE' if not used)
Record 9:   Format
            (I10,3I5,2(1X,20A1))
            Ordinate Numerator
            Data Characteristics
Record 10:  Format
            (I10,3I5,2(1X,20A1))
            Ordinate Denominator
            Data Characteristics
Record 11:  Format
            (I10,3I5,2(1X,20A1))
            Z-axis Data
            Characteristics
Record 12:
            Data Values
```

Case	Ordinate Type	Precision	Abscissa Spacing	Format
1	real	single	even	6E13.5
2	real	single	uneven	6E13.5
3	complex	single	even	6E13.5
4	complex	single	uneven	6E13.5
5	real	double	even	4E20.12
6	real	double	uneven	2(E13.5,E20.12)
7	complex	double	even	4E20.12
8	complex	double	uneven	E13.5,2E20.12

Appendix F

Engineering drawings